

ASSESSMENT OF CHANGES IN THE DIELECTRIC PROPERTIES OF
MULTIDRUG RESISTANT CANCER CELLS BY ELECTROROTATION
TECHNIQUE

A THESIS SUBMITTED TO
THE GRADUATE SCHOOL OF NATURAL AND APPLIED SCIENCES
OF
MIDDLE EAST TECHNICAL UNIVERSITY

BY

GARSHA BAHRIEH

IN PARTIAL FULFILLMENT OF THE REQUIREMENTS
FOR
THE DEGREE OF MASTER OF SCIENCE
IN
ELECTRICAL AND ELECTRONICS ENGINEERING

AUGUST 2014

Approval of the thesis:

**ASSESSMENT OF CHANGES IN THE DIELECTRIC PROPERTIES OF
MULTIDRUG RESISTANT CANCER CELLS BY ELECTROROTATION
TECHNIQUE**

submitted by **GARSHA BAHRIEH** in partial fulfillment of the requirements for
the degree of **Master of Science in Electrical and Electronics Engineering**
Department, Middle East Technical University by,

Prof. Dr. Canan Özgen
Dean, Graduate School of **Natural and Applied Sciences**

Prof. Dr. Gönül Turhan Sayan
Head of Department, **Electrical and Electronics Engineering**

Assoc. Prof. Dr. Haluk Külâh
Supervisor, **Electrical and Electronics Eng. Dept., METU**

Examining Committee Members:

Prof. Dr. Tayfun Akın
Electrical and Electronics Engineering Dept., METU

Assoc. Prof. Dr. Haluk Külâh
Electrical and Electronics Engineering Dept., METU

Prof. Dr. Ufuk Gündüz
Biology Dept., METU

Prof. Dr. Nevzat Güneri Gencer
Electrical and Electronics Engineering Dept., METU

Assoc. Prof. Dr. Yeşim Serinağaoğlu Doğrusöz
Electrical and Electronics Engineering Dept., METU

Date: **29.08.2014**

I hereby declare that all information in this document has been obtained and presented in accordance with academic rules and ethical conduct. I also declare that, as required by these rules and conduct, I have fully cited and referenced all material and results that are not original to this work.

Name, Lastname: Garsha Bahrieh

Signature:

ABSTRACT

ASSESSMENT OF CHANGES IN THE DIELECTRIC PROPERTIES OF MULTIDRUG RESISTANT CANCER CELLS BY ELECTROROTATION TECHNIQUE

Bahrieh, Garsha
M. Sc., Department of Electrical and Electronics Engineering
Supervisor: Assoc. Prof. Dr. Haluk Klah

August 2014, 236 pages

With recent advances in microfabrication technologies different methodologies are employed to study the dielectric properties of the biological systems. These include electrorotation (ER), dielectrophoresis, microelectrical impedance spectroscopy, and impedance flow cytometry. Among them, ER is utilized as a high accuracy approach in determining the membrane and interior dielectric properties of single cells.

In addition, in cancer therapy, cancer cells are developing resistance toward the chemotherapeutic drugs and their biophysical properties are showing variations. Therefore, study of changes in the physical and electrical properties of resistant cells is important to make differentiation between drug sensitive and resistant cells.

This thesis presents the design, fabrication, and implementation of ER devices with 3D electrodes for the dielectric characterization of cells. In addition, as an experimental application of the extracted dielectric properties of the cells (by ER), the DEP method is utilized.

1st generation of the ER chips with pyramidal planar (2D) electrodes was utilized for the proof of concept and study of the feasibility of dielectric characterization of cells using ER technique. First analyses were carried out using yeast cells and

imatinib resistant human leukemia cells (K562-IMA). 3D FEM analyses and experimental results showed that the use of 2D (planar) structures can lead to errors in the measurement. In 2D structures, because of the negligible height of the electrodes (~300nm) compared to the biological cells (~10-25 μm), the variation of the rotational torque (ROT-T) is significant along the z-axis. In addition, due to high current density passing through the 2D electrodes, the thermal heating of the electrodes was significant. This can result in variations in the medium temperature due to the thermal resistive heating of the electrodes. Therefore, variations in the conductivity of the medium were unavoidable. It can alter the ER characterization results, because of the high sensitivity of the ER method to the conductivity of the medium. 3D electrode structures can provide a high sustainability of the ROT-T along the z-axis, by encompassing the whole cell body and eliminating the fringing electric field effect on the cells rotation. In these electrodes, due to increased volume of the electrodes, the current density passing through the electrodes drops significantly. Therefore, the thermal heating reduces by more than an order of magnitude, which guarantees consistency of the medium conductivity during the ER experiments.

The second generation of the ER devices with 3D pyramidal electrodes were designed and fabricated to overcome the problems with the planar ER devices. These devices were fabricated with 3D electrodes on az glass substrate. However, there were a number of problems which were faced in the experimental analyses of these devices. Firstly, due to the glass substrate, assessment of the rotation of the cells was difficult. Moreover, small reservoir size and hydrophobicity of the parylene had made entrance of the cells into the electrode area difficult. In addition, due the complexity of the fabrication process and limited number of ER chips on each wafer, the 2nd generation of the ER chips was unsuitable for the practical uses.

The third generation of the ER devices, with 3D electrodes was designed to overcome the problems in the previous generations. The fabrication process of these devices needs a single mask. In addition, to study the electrode geometry effects in the ER method, ER devices with six different electrode geometries were designed and fabricated. In order to make a comparison between the electrical characteristics of the each electrode type, experimental and numerical investigations

were carried out. For this purpose, 3D rotational torque and effective electric field distributions were characterized using experimental and FEM analyses (COMSOL). The ER devices with polynomial electrodes were chosen to have the most practical compromise between the uniformity and sustainability of the generated rotational torque. Using polynomial quadrupole electrodes, 9 different cell populations, including K562 human leukemia cells and MCF7 breast cancer cells and their multidrug resistance (MDR) counterparts were characterized. For this purpose, the rotational behavior of the cells was studied in four different medium conductivities (1-8 mS/m) in the frequency range of 1-100 kHz. Subsequent to determination of peak rotation frequencies in all media, an automated MATLAB program was used to calculate the dielectric properties of the cells. It was observed that, sensitive and MDR cancer cells show significant variation in their dielectric properties, which can be used to identify and separate MDR cells from sensitive ones through DEP-based methods.

In addition, to investigate the feasibility of separation of the cancerous cells and their multidrug resistance (MDR) derivation from the human leukocyte cell mixture, DEP chips were designed and fabricated. These chips have five active electrodes and total of 12 potentially floating electrodes, which had 3D structures, located in the parylene microchannel side walls. 3D COMSOL simulations were utilized in the design and studying the separation performance of the DEP chips. In addition, FEM analyses were implemented in the optimization of fluidic flow rates and applied voltages. Using 3D simulations, the separation efficiency of the designed DEP devices was calculated as 100%. The initial experimental analysis of fabricated DEP devices with K562-IMA cells showed a successful separation of the cell under both n-DEP and p-DEP forces to the intended channels.

In conclusion, three generations of the ER devices with more than eight different electrode geometries were designed and fabricated. 3D FEM simulations and experimental analyses were utilized in the characterization of the ER devices. The polynomial electrodes were chosen to have the most practical compromise between the rotational torque uniformity and magnitude. Using the polynomial electrodes, different cell populations, including K562 leukemia cancer cells and its imatinib (0.2, 0.3, and 0.5 μM) and doxorubicin (0.1, 0.3, and 0.5 μM) resistant counterparts

and MCF7 and its 1 μ M doxorubicin resistant derivation were characterized. As an application for extracted dielectric properties of the cells, DEP chips with novel potentially floating electrode configuration was designed and fabricated. Results show that sensitive and resistant cancer cells can be separated from each other via DEP-based methods, and ER is a powerful and sensitive dielectric characterization technique for the biological cells.

Keywords: Electrorotation, cell characterization, dielectrophoresis (DEP), 3D-electrode, multidrug resistance (MDR).

ÖZ

ÇOKLU İLAÇ DİRENÇLİLİĞİ GELİŞTİRMİŞ KANSER HÜCRELERİNİN DİELEKTRİK ÖZELLİKLERİNİN ELEKTROROTASYON TEKNİĞİ İLE BELİRLENMESİ

Bahrieh, Garsha
Yüksek Lisans, Elektrik Elektronik Mühendisliği Bölümü
Danışman: Doç. Dr. Haluk Külâh

Ağustos, 2014, 236 sayfa

Son yıllarda, mikrofabrikasyon teknolojilerindeki ilerlemelerle birlikte, biyolojik parçacıkların dielektrik özelliklerinin belirlenmesinde kullanılacak farklı teknikler geliştirilmiştir. Bunlardan bazıları, elektrotasyon (ER), dielektroforez (DEP), mikroelektrik impedans spektrofotometrisi ve impedans akış sitometrisi olarak sıralanabilir. Bu teknikler arasında, elektrotasyon, hücre zarı ve sitoplazmik dielektrik özelliklerin tekil hücre bazında, yüksek hassasiyette belirlenmesinde etkin bir yöntem olarak kullanılmaktadır.

Kanser hücreleri kanser tedavisi sırasında biyofiziksel özelliklerini değiştirerek kemoterapatik ilaçlara karşı direnç kazanmaktadır. Bu sebeple, ilaca dirençli hücrelerin fiziksel ve elektriksel özelliklerindeki değişimlerin incelenmesi, dirençli hücreyi dirençsiz olandan ayırmak adına oldukça önem kazanmıştır.

Bu çalışmada, 3-boyutlu elektrot yapısına sahip ER çiplerinin tasarım, üretim ve biyolojik hücrelerin dielektrik özelliklerinin belirlenmesinde kullanımı araştırılmıştır. Bunun yanı sıra, elde edilen dielektrik özellikler, hücrelerin DEP tekniği ile ayrıştırılmasında kullanılmıştır.

ER tekniğinin dielektrik karakterizasyonda kullanılabilirliğini kanıtlamak için birinci nesil ER çipleri, Si taban üzerine işlenen 2-boyutlu düzlemsel piramit elektrotlardan oluşmuştur. Analizler ilk olarak maya hücrelerinde ve imatinib dirençli insan lösemi hücrelerinde (K562-IMA) gerçekleştirilmiştir. 3-boyutlu FEM analizleri ve deneysel sonuçlar, 2 boyutlu elektrot yapılarının çeşitli ölçüm

hatalarına yol açtığını göstermiştir. 2 boyutlu elektrot yapılarında, elektrot yüksekliği (~300 nm) hücre büyüklüğüne (~1-25 µm) göre çok daha az olduğundan, dikey ekseninde (z-ekseni) rotasyon kuvveti (ROT-T) ciddi ölçüde değişmektedir. Bunun yanı sıra, 2 boyutlu elektrotlarda akım yoğunluğunun fazla olması nedeniyle ciddi bir termal ısınma gözlenmiştir. Termal ısınmanın fazla olması çözelti sıcaklığını arttırmakta, dolayısıyla, çözelti iletkenliği ölçüm sürecince değişim göstermektedir. ER tekniği, çözelti iletkenliği ile doğrudan ilişkili olduğundan, termal ısınma ER sonuçlarını ciddi ölçüde etkilemektedir. Diğer yandan, 3 boyutlu elektrotlar ROT-T'nin z-ekseni boyunca sabit kalmasını sağlayıp, elektrik alan saçaklanmalarını engelleyebilmekte ve elektrik alanın tüm hücre çapı üzerinde homojen etki etmesini sağlamaktadır. Ayrıca, elektrot hacminin artması nedeniyle, 3 boyutlu elektrotlarda birim alandaki akım yoğunluğu azalmakta ve termal ısınmanın büyük oranda önüne geçilmektedir. Böylece, çözelti iletkenliği ölçüm süresi boyunca sabit kalmaktadır.

İkinci nesil, 3 boyutlu piramit elektrot yapısındaki ER çipleri, 2 boyutlu elektrot yapılarındaki problemleri çözmek için tasarlanmış ve cam pul üzerinde üretilmiştir. Ancak, bu çiplerin testleri sırasında çeşitli problemlerle karşılaşmıştır. Örneğin, cam taban kullanıldığı için hücrelerin dönüş hızını mikroskop altında gözlemlemek zorlaşmıştır. Ayrıca, rezervuar küçüklüğü, parilen hidrofobikliği gibi diğer bir takım problemler testlerde sıkıntılara yol açmıştır. Bu çiplerin üretiminin de 4 maske içermesi ve görece kompleks olması nedeniyle ER testlerinde kullanılmamıştır.

Üçüncü nesil ER çipleri 2. nesil çiplerde yaşanan problemleri aşmak için tasarlanmış ve Si taban üzerine tek maske kullanılarak üretilmiştir. Ayrıca, elektrot yapısının ER sonuçlarına etkisini incelemek üzere 6 farklı elektrot geometrisi tasarlanmış ve üretilmiştir. Farklı elektrot geometrilerinin ER karakterizasyonu, nümerik ve deneysel olarak araştırılıp karşılaştırılmıştır. 3 boyutlu dögüsel kuvvetin ve elektrik alan dağılımının nümerik karakterizasyonu FEM (COMSOL) analizleri ile ve deneysel olarak incelenmiştir. Sonuç olarak, polinomik elektrot yapısına sahip 3 boyutlu ER çiplerinin dögüsel kuvvetin homojenliği ve sürekliliği açısından en iyi sonucu verdiği gözlenmiştir. Polinomik dörgü elektrot yapısı kullanılarak 9 farklı hücrenin (K562 lösemi hücresi ve dirençli tipleri (0.2, 0.3, 0.5

μM imatinib) ile MCF7 meme kanseri hücresi ve dirençli tipleri (0.1, 0.3, 0.5 μM doxorubicin)) dielektrik karakterizasyonu gerçekleştirilmiştir. Her bir hücrenin dögüsel elektrik alan kuvveti altındaki rotasyon hızları 4 farklı iletkenlikteki (1-8 mS/m) çözelti içinde, 1-100 kHz frekans aralığında taranmıştır. Her bir çözelti içindeki en yüksek rotasyon frekansının belirlenmesinin ardından, hücrelerin dielektrik özellikleri, geliştirilen MATLAB programı yardımıyla otomatik olarak hesaplanmıştır. Sonuçlar, hassas ve dirençli kanser hücrelerinin dielektrik özelliklerinin ciddi şekilde değiştiğini ve bunun hücreleri DEP tabanlı metotlarla ayırtmada kullanılabileceğini göstermiştir.

Bu çalışmada ayrıca, elde edilen sonuçların bir uygulaması olarak, dirençli hassas kanser hücrelerinin beyaz kan hücrelerinden ayırtılmasında kullanılmak üzere DEP çipi tasarlanmış ve üretilmiştir. Bu çipte, parilen tabanlı mikroakışkan kanal duvarlarına yerleştirilen 5'i aktif ve 12'si pasif üç boyutlu elektrotlar kullanılmıştır. Çipin tasarımı ve ayırtma performansının nümerik incelemeleri için 3-boyutlu COMSOL benzetimleri gerçekleştirilmiştir. Bunun yanı sıra, akış hızı ve voltaj değerlerinin optimizasyonu için FEM analizleri gerçekleştirilmiştir. Üç boyutlu benzetimler, tasarlanan DEP çipinin kanser hücrelerinin kan hücrelerinden %100 verimle ayırtılabileceğini göstermektedir. Yapılan ön deneylerde, K562-IMA hücrelerinin uygulanan n-DEP veya p-DEP kuvvetlerinden etkilenecek farklı kanallara yönlendirilebildiği gözlenmiştir.

Sonuç olarak, bu çalışmada sekizden fazla elektrot geometrisine sahip 3 farklı nesil ER çipi tasarlanmış ve üretilmiştir. ER çiplerinin karakterizasyonu için 3D FEM benzetimleri ve deneysel analizler gerçekleştirilmiştir. Polinomik elektrot yapılarının dögüsel kuvvetin homojenliği ve büyüklüğü açısından en iyi sonucu verdiği gözlenmiştir. Polinomik elektrot yapısındaki çipler kullanılarak, hassas ve dirençli K562 lösemi hücreleri ile hassas ve dirençli MCF7 meme kanseri hücrelerinin dielektrik karakterizasyonu gerçekleştirilmiştir. Elde edilen dielektrik özelliklerin bir uygulaması olarak, özgün bir elektrot yapısına sahip DEP ayırtma çipi tasarlanmış ve üretilmiştir. Elde edilen sonuçlar, hassas ve dirençli kanser hücrelerinin DEP metodu ile birbirinden ayırtılabileceğini, ve ER metodunun, biyolojik hücreler için, güçlü ve hassas bir dielektrik karakterizasyon tekniği olduğunu göstermektedir.

Anahtar Kelimeler: Elektrotasyon, hücre karakterizasyonu, dielektroforez (DEF), 3 boyutlu elektrot, çoklu ilaç direnci (ÇİD)

To my father, Morteza

My mother, Jaleh

and

“Sona”

ACKNOWLEDGEMENTS

I would like to thank to my supervisor Associate Professor Haluk Kulah, for his continuous guidance, support, and trust throughout my master studies. In addition, I want to thank him because of his endless effort to teach the disciplined way of study and research to me. He has taught me that the difference between the perfection and imperfection of a task is the tiny details that are ignored by most of the people. I am sure that, I will benefit from his heritage throughout my life.

I am grateful to Prof. Dr. Tayfun Akin, because I believe that this study was not achievable without the provided facilities and opportunities by him.

I am deeply thankful to my senior colleague, Dr. Hatice Ceylan Koydemir for her endless guidance, assistance, support, and also for her patience in answering my questions. In addition, I am grateful to her, because of her contribution in fabrication of my devices.

I would like to thank Dr. Ebru Özgür for her continuous support in every stage of this study, and her huge effort in helping me to combine the biology, MEMS, and electronics engineering. In addition, I am deeply thankful because of her efforts and patience in improving my writing skills. I am also thankful to Dr. Özge Zorlu, and Dr. Yekbun Adıgüzel for their help and assistance. Also I am grateful to Dr. Özge Zorlu for his contribution in fabrication of my devices.

I would like to thank Aziz Koyuncuoğlu and Taylan Töral for their efforts in fabrication of the utilized device in this study.

I would like to thank Murat Erdem, for providing the biological cells, almost anytime time during the day and night.

I am especially thankful to all of my previous and present lab friends in the BioMEMS, PowerMEMS, and MEMS groups, including: Salar Chamanian, Hasan Uluşan, Yağmur Demircan, Kaveh Gharehbaghi, Mustafa Kangül, Özgen Sümer Laçın, Gürhan Özkayar, Parisa Naghinazhadahmadi, Ahmet Erdal Yılmaz, Rui

Çolaço, Levent Beker, Ulas Aykutlu, Yunus Terzioglu, Soner Sönmezoğlu, Selçuk Keskin, and Serdar Tez, for their kind friendship.

I would like to express my deepest thankfulness and gratitude to my father, Morteza Bahrieh, my mother, Jaleh Sadid, my brother, Niusha and my sister, Prosha for their support throughout my life, and for their trust and faith in me.

I would like to thank to my dearest, Sona Mokhtari for her endless love, trust, and support. I thank her, for making every moment of my life, an enjoyable and memorable moment.

I would like to thank The Scientific and Technological Research Council of Turkey (TUBITAK) for the scholarship and support for me.

TABLE OF CONTENTS

ABSTRACT	v
ÖZ.....	ix
ACKNOWLEDGEMENTS	xiv
TABLE OF CONTENTS	xvi
LIST OF TABLES	xx
LIST OF FIGURES.....	xxii
CHAPTERS.....	1
1. INTRODUCTION.....	1
1.1 Impedance Flow Cytometry (IFC).....	4
1.2 Microelectrical Impedance Spectroscopy (μ -EIS).....	11
1.3 Dielectrophoresis.....	16
1.3.1 Fitting the DEP spectra to the cell model.....	17
1.3.2 DEP Crossover Frequency.....	18
1.3.3 DEP Motion Analyses	20
1.4 Electrorotation.....	21
1.4.1 Fitting the experimental ER spectrum to cell model.....	24
1.4.2 Peak Rotation Frequency.....	26
1.4.3 Novel ER Devices	28
1.5 Research Objectives and Thesis Organization.....	32
2. THEORY.....	37
2.1 Dipole Formation.....	37
2.2 Applied Effective Moment on the Dipole.....	38

2.3	Electrorotation	41
2.4	Cell Modeling	43
2.4.1	Theory	43
2.4.2	DEP and ER Spectra of Neutrophils	46
3.	DIELECTRIC CHARACTERIZATION	51
3.1	The Slope and Intercept Method.....	52
3.2	First Level Approximations	54
3.3	Second Level Approximations	55
3.4	Third Level Approximations	57
3.5	Fourth Level Approximations.....	59
3.6	An Automated MATLAB Algorithm for Cell Characterization	61
3.6.1	Inputs for the MATLAB program.....	61
3.6.2	Outputs of the MATLAB Program	63
3.7	Dielectric properties of K562 human leukemia cells	66
4.	DESIGN AND SIMULATIONS	69
4.1	Design Criteria for the ER devices	69
4.2	The 1 st Generation of the ER Devices	70
4.3	The 2 nd Generation of the ER Devices	74
4.4	The 3 rd Generation of the ER Devices	77
4.4.1	Introduction	78
4.4.2	Finite Element Modeling.....	79
4.4.3	Cell Preparation.....	80
4.4.4	Experimental	80
4.4.5	ER Devices with Pyramidal Electrodes	82
4.4.6	ER Devices with Polynomial Electrodes	86
4.4.7	ER Devices with Prolate Elliptical Electrodes.....	91
4.4.8	ER Devices with Oblate Elliptical Electrodes	95

4.4.9	ER Devices with Circular Electrodes	100
4.4.10	ER Devices with Bone Electrodes	104
4.5	Discussion	106
4.6	Conclusion	111
5.	FABRICATION	115
5.1	Fabrication of the 1 st Generation of the ER Devices.....	115
5.2	Fabrication of the 2 nd Generation of the ER Devices.....	117
5.3	Fabrication of the 3 rd Generation of the ER Devices	122
6.	RESULTS AND DISCUSSION	127
6.1	Experimental Test Setup for the ER Measurements	127
6.2	Cell Preparation.....	131
6.3	Dielectric Characterization of K562 and K562 MDR Cells	132
6.3.1	Dielectric Characterization of K562 Cells.....	133
6.3.2	Dielectric Characterization of K562/IMA Cells.....	135
6.3.3	Dielectric Characterization of K562/DOX Cells.....	139
6.3.4	Conclusion	142
6.4	Dielectric Characterization of MCF7 and MCF7/DOX-1 μ M Cells	144
7.	DIELECTROPHORESIS	149
7.1	DEP Theory.....	149
7.2	Cell Modeling	151
7.2.1	Simulation of DEP Responses of the Cells	151
7.3	Design Criteria	153
7.3.1	Design.....	154
7.3.2	Simulations	157
7.4	Fabrication.....	162
7.5	Conclusion	164
8.	CONCLUSION	167

REFERENCES.....	171
APPENDICES	
A. DOUBLE SHELL CELL MODEL IN MATLAB.....	183
B. AUTOMATED MATLAB BASED SOFTWARE FOR EXTRACTING THE DIELECTRIC PROPERTIES OF THE CELLS USING ELECTROROTATION METHOD.....	191
C. JOULE HEATING ANALYSES OF THE 3D ER ELECTRODES.....	207
D. FINITE ELEMENT SIMULATIONS	209
D.1 DEP Devices	209
D.1.1 Electrical Model.....	209
D.1.1.1 Subdomain Conditions	212
D.1.1.2 Boundary Conditions.....	213
D.1.2 Microfluidic Model	214
D.2.1 Subdomain Conditions.....	215
D.2.2 Boundary Conditions	216
D.1.3 Constants.....	217
D.1.4 Solving	217
D.2 ER Devices	219
D.2.1 Subdomain Conditions.....	219
D.2.2 Boundary Conditions	220
D.2.3 Constants.....	221
D.2.4 Solving	222
E. FABRICATION PROCESS FLOW.....	223

LIST OF TABLES

TABLES

Table 1. 1: Literature survey of utilized methods in characterization of biologic particles.	30
Table 2. 1: Dielectric properties of neutrophils.....	46
Table 3. 1: Dielectric properties of K562 cells (Labeed et al. [5]).....	67
Table 3. 2 : Dielectric properties of K562 cells.	68
Table 4. 1: Comparison of the sustainability of the effective electric field for different electrode geometries. Results present percentage of the circular area compared to the total measurement area with maximum of 5%, 10%, and 20% variations in the effective electric field compared to device center.....	107
Table 4. 2: Comparison between the FEM modeling and experimentally obtained characteristics of the various electrode geometries. The variance of the simulation data is compared based on the magnitude of the effective electric field at $z= 5\mu\text{m}$. For the experimental data the variance is calculated based on the average rotation rates for the cell positioned at $z<30\mu\text{m}$	109
Table 6. 1 : Extracted dielectric properties of drug sensitive K562 human leukemia cells, using ER method.....	135
Table 6. 2 : Extracted dielectric properties of K562/IMA human leukemia cells,using ER method.	138
Table 6. 3: Extracted dielectric properties of K562/IMA human leukemia cells, using ER method.	142
Table 6. 4: Extracted dielectric properties of MCF7 and MCF7/DOX- 1000 nM human breast cancer cells, using ER method.	147
Table 7. 1: Dielectric properties of the utilized cells in this study.....	152
Table 7. 2: Design parameters of the DEP devices	157

Table 7. 3: Calculated $Re(F_{CM})$ and C_{DEP} for the cells in the separation frequency of 160 MHz. 160

Table 7. 4: Optimized boundary conditions for the DEP devices..... 160

Table E. 1: Detailed fabrication flow of the 1st generation of the ER devices..... 223

Table E. 2: Detailed fabrication flow of the 2nd generation of the ER devices..... 225

Table E. 3: Detailed fabrication flow of the 3rd generation of the ER devices. 232

LIST OF FIGURES

FIGURES

Figure 1. 1: Showing the division BioMEMS field into the lab-on-a-chip and μ TAS. (Figure from Wikipedia/BioMEMS).....	1
Figure 1. 2: Growing market place of BioMEMS devices since 2011. (Figure from www.yole.fr)	2
Figure 1. 3: Electrical model of an IFC system with bottom electrodes. (A) Capacitance and resistance modeling of the microfluidic IFC system in the presence of a biological cell. (B) Simulated complex impedance spectrum of a 10 μ m diameter cell using a SPICE model [21].	6
Figure 1. 4: (A) Schematic diagram of the device showing the cross-section of the IFC system, together with the optical system. Inset shows the photograph of the microchannel with microelectrodes. (B) Equivalent electrical modeling of the IFC system in presence of the biological cell [18].	7
Figure 1. 5: Schematic of an IFC system with top and bottom electrodes. (A) Electrical model of the microfluidic IFC system in presence of a biological particle. (B) Expected measured signal from each pair of electrodes [23].	8
Figure 1. 6: Schematic diagram of the IFC system, with optical detection apparatus. A dual laser excitation and detection is implemented for simultaneous measurement of electrical and optical properties of the cells [24].	9
Figure 1. 7: Microfluidic system for measurement of dielectric properties of the cell membrane. (A) Schematic view of the device. “-p” shows the negative pressure in the outlet channel for aspirating the medium. (B) Experimental results showing the measured impedance signal at 7 different frequencies [27].	11
Figure 1. 8: A μ -EIS system with micro-pillars to capture single cells. (A) 3D presentation of the cell capturing procedure. (B) Top view of the device [37].....	12

Figure 1. 9: A μ -EIS device, with hydrodynamic cell trapping system. (A) The experimental setup. Electrical connections are made using a PCB, which enables data acquisition. (B) Photograph of the fabricated prototype with the PDMS ports mounted on the inlet and the outlet. (C) Photograph of the microchannel, while the device is under operation. (D) Schematic view of the trapping region, with differential measurement electrodes. (E) Image of the trapped beads with $15\mu\text{m}$ size. (F) Image of the trapped single Hela cell [38]..... 13

Figure 1. 10 : Schematic view of the μ -EIS device, with four impedance analysis sides. The close-up view shows a trapped cell inside the microchannel due to application of negative pressure (suction) [35]..... 14

Figure 1. 11 : Schematic view of the impedance spectrometry device, with electrode micro-well. Cell driven by the medium flow is trapped at the micro-well area, due to n-DEP force [34]..... 15

Figure 1. 12: Number of publications on DEP in the 1st decade of 21st century [43]. 16

Figure 1. 13 : Categorized DEP publications on three subjects of theory, technology, and applications, since 1995 [43]..... 17

Figure 1. 14: DEP device for dielectric characterization of the leukocytes. (A) Photograph of the device with microfluidic reservoirs, and electrical connections. (B) Castellated electrode arrays for determination of crossover frequency. (C) Device under operation. Arrows and circles show eosinophils and erythrocytes, respectively [57]..... 19

Figure 1. 15: Schematic view of the ER device. The direction of the rotating electric field upon application of sinusoidal voltage applied in phase quadrature, and the rotation of cells toward the direction of induced moment are shown. 22

Figure 1. 16: Photograph of the ER device with different electrode geometries. (A) Oblate elliptical, (B) Circular, (C) Prolate elliptical, (D) Pyramidal, and (E) Polynomial. 22

Figure 1. 17: Experimental study of the distribution of the rotational torque on the ER devices. (A) Polynomial quadrupole electrodes. (B) Position of the studied cells on inter-electrode region of the polynomial electrodes. (C) Extracted rotation

rate map. Averaging and smoothing method is applied to the measurement data [66].	24
Figure 1. 18: Extraction of ER spectrum of the cells to determine the dielectric properties. (A) Schematic of the ER test setup. (B) ROT spectra for MDA231 cells (\diamond), T-lymphocytes (0), and erythrocytes (Δ) in the medium with conductivity of 56 mS/m. Each data point is an average of four measurements [1].	25
Figure 1. 19: Diagram of an experimental setup for automated ER measurements [88].	29
Figure 1. 20: The schematic of the ER devices, with eight electrodes. The DEP electrodes are utilized to trap the cells in the center of the device, using n-DEP force. Applied sinusoidal signal in phase quadrature through the ER electrodes is used to induce the rotational torque on the cells [70].	30
Figure 2. 1: Representation of the dipole formation upon application of an electric field on the particle.	38
Figure 2. 2: Interior structures of a single cell. (Figure from www.slideshare.net).	43
Figure 2. 3: Equivalent electrical model of a single cell. (Figure from www.biotele.com)	44
Figure 2. 4: Multilayer shell approach for determining the effective permittivity of the double-shell model. (A) A cell with 3 layers. (B) Determination of effective permittivity of the layers 1 and 2. (C) Determination of effective permittivity of the layers 1 effective and 3.	45
Figure 2. 5: A single neutrophil with segmented cell nucleus.	46
Figure 2. 6: The graphical user interface of the implemented MATLAB algorithm for calculating the frequency dependent response of cells inside an AC electric field.	47
Figure 2. 7: Double-shell modeling of imaginary and real part of F_{CM} for the neutrophils.	48
Figure 2. 8: Imaginary and real part of F_{CM} inside three media with different conductivities.	49
Figure 3. 1: Input Panel for the MATLAB program.	62
Figure 3. 2: The slope and the intercept of the fitted data.	63
Figure 3. 3: The output section for dielectric properties of the cell membrane.	64

Figure 3. 4: Determining the interior conductivity of the cell by two distinct averaging methods. Blue colored section indicates averaging based on three data sets. Green colored section indicated the averaging based on the calculated data in each medium.	65
Figure 3. 5: Fitted lines for peak rotation frequencies of an unreal cell.	66
Figure 3. 6: Summary of calculation steps, in the MATLAB program.	66
Figure 3. 7: Graph of imaginary part of the F_{CM} , inside media with varying conductivities	67
Figure 3. 8: Calculated dielectric properties of the K562 cell.	68
Figure 4. 1: Layout of the 1 st generation of the ER devices, with magnified electrode region.	71
Figure 4. 2: Fabricated prototype of the ER device with planar pyramidal electrodes.	72
Figure 4. 3: FEM simulation of the generated resistive heating in the ER devices with planar electrodes.	73
Figure 4. 4: The FEM analyses of the total current density passing through the planar electrodes.	73
Figure 4. 5: FEM simulation of the EEF in the inter-electrode region of the 2 nd generation of the ER devices. The red arrow shows the direction of the electric field at an arbitrary time instant.	75
Figure 4. 6: FEM simulation of the electric field gradient intensity on the 2 nd generation of the ER devices. (A) Distribution of (∇E^2) on the ER chip. (B) The region in the vicinity of the electrode tips has the maximum value of the (∇E^2) which reduces toward the electrodes center.	75
Figure 4. 7: Designed layout for the 2 nd generation of the ER chips.	76
Figure 4. 8: Fabricated prototypes from 1 st and 2 nd generation of the ER devices. .	76
Figure 4. 9: Photograph of the fabricated prototypes of the ER device with different electrode shapes. (A) oblate elliptical, (B) circular, (C) prolate elliptical, (D) pyramidal, and (E) polynomial.	78
Figure 4. 10: Designed layout of the devices with pyramidal electrodes, together with the magnified inter-electrode region.	82

Figure 4. 11: Segmented inter-electrode region in the ER devices with pyramidal electrodes.....	83
Figure 4. 12: Experimentally measured rotation rates mapped to the ER devices with pyramidal electrodes. (A) SEM photographs of the measurement region. The orientations of the electrodes show the position of the electrodes in the mapped data. (B) Surface plot and (C) Counter-plot of the rotation of the cells at $z < 30 \mu\text{m}$	83
Figure 4. 13 : Experimentally measured rotation rates mapped on the devices pyramidal electrodes. (A) SEM photographs of the measurement region. The orientations of the electrodes show the position of the electrodes in mapped data. (B) Surface plot and (C) Counter-plot of the rotation of the cells at $z \cong 100 \mu\text{m}$	84
Figure 4. 14 : Height presentation of the effective electric field distribution on the devices with pyramidal electrodes.	84
Figure 4. 15: 3D simulation of distribution of the EEF on the $z = 15 \mu\text{m}$ plane.....	85
Figure 4. 16: Designed layout of the devices with polynomial electrodes, together with the magnified inter-electrode region.	86
Figure 4. 17: Segmented inter-electrode region in the ER devices with polynomial electrodes.....	87
Figure 4. 18: Experimentally measured rotation rates mapped to the devices with polynomial electrodes. (A) SEM photographs of the measurement region. The orientations of the electrodes show the position of the electrodes in the mapped data. (B*) Surface plot and (C) Counter-plot of the rotation of the cells at $z < 30 \mu\text{m}$	88
Figure 4. 19: Experimentally measured rotation rates mapped to the devices with polynomial electrodes. (A) SEM photographs of the measurement region. The orientations of the electrodes show the position of the electrodes in the mapped data. (B) Surface plot and (C) Counter-plot of the rotation of the cells at $z \cong 100 \mu\text{m}$	88
Figure 4. 20: Height presentation of the effective electric field distribution of the devices with polynomial electrodes.....	89
Figure 4. 21: 3D simulation of distribution of the EEF on the $z = 15 \mu\text{m}$ plane of the polynomial electrodes.....	90

Figure 4. 22: Designed layout for the devices with the prolate elliptical electrodes, together with the magnified inter-electrode region..... 91

Figure 4. 23: Segmented inter-electrode region of the ER devices with prolate elliptical electrodes. 92

Figure 4. 24: Experimentally measured rotation rates mapped to the devices with prolate elliptical electrodes. (A) SEM photographs of the measurement region. The orientations of the electrodes show the position of the electrodes in the mapped data. (B) Surface plot and (C) Counter-plot of the rotation of the cells at $z < 30 \mu\text{m}$ 93

Figure 4. 25: Experimentally measured rotation rates mapped to the devices with prolate elliptical electrodes. (A) SEM photographs of the measurement region. The orientations of the electrodes show the position of the electrodes in the mapped data. (B) Surface plot and (C) Counter-plot of the rotation of the cells at $z = 100 \mu\text{m}$ 93

Figure 4. 26: Height presentation of the effective electric field distribution on the devices with prolate elliptical electrodes. 94

Figure 4. 27: 3D simulation of distribution of the EEF on the $z = 15 \mu\text{m}$ plane of the prolate elliptical electrodes. 95

Figure 4. 28: The designed layout of the ER devices with the oblate elliptical electrode geometry..... 96

Figure 4. 29: Segmented inter-electrode region of the ER devices with the oblate elliptical electrodes. 97

Figure 4. 30: Experimentally measured rotation rates mapped on the devices with oblate elliptical electrodes. (A) SEM photographs of the measurement region. The orientations of the electrodes show the position of the electrodes in the mapped data. (B) Surface plot and (C) Counter-plot of the rotation of the cells at $z < 30 \mu\text{m}$ 97

Figure 4. 31: Experimentally measured rotation rates mapped on the devices with oblate elliptical electrodes. (A) SEM photographs of the measurement region. The orientations of the electrodes show the position of the electrodes in the mapped data. (B) Surface plot and (C) Counter-plot of the rotation of the cells at $z \cong 100 \mu\text{m}$ 98

Figure 4. 32: Height presentation of the effective electric field distribution of the devices with oblate elliptical electrodes.....	98
Figure 4. 33: 3D simulation of distribution of the EEF on the $z = 15 \mu\text{m}$ plane of the oblate elliptical electrodes.....	99
Figure 4. 34: The designed layout of the ER devices with the circular electrode geometry.....	100
Figure 4. 35: Segmented inter-electrode region of the ER devices with circular electrodes.....	101
Figure 4. 36: Experimentally measured rotation rates mapped on the devices with circular electrodes. (A) SEM photographs of the measurement region. The orientations of the electrodes show the position of the electrodes in the mapped data. (B) Surface plot and (C) Counter-plot of the rotation of the cells at $z < 30 \mu\text{m}$	102
Figure 4. 37: Experimentally measured rotation rates mapped on the devices with circular electrodes. (A) SEM photographs of the measurement region. The orientations of the electrodes show the position of the electrodes in the mapped data. (B) Surface plot and (C) Counter-plot of the rotation of the cells at $z = 100 \mu\text{m}$	102
Figure 4. 38: Height presentation of the effective electric field distribution on the devices with circular electrodes.....	103
Figure 4. 39: 3D simulation of distribution of the EEF on the $z = 15 \mu\text{m}$ plane of the circular electrodes.....	104
Figure 4. 40: The designed layout of the ER devices with the bone electrode geometry.....	105
Figure 4. 41: Height presentation of the effective electric field distribution on the devices with bone electrodes.....	105
Figure 5. 1: Fabrication flow of the 1 st generation of the ER devices using a single mask.....	116
Figure 5. 2: Utilized mask for the fabrication of the 1 st generation of the ER devices.	116
Figure 5. 3: Fabricated prototypes of the 1 st generation of the ER devices.....	117
Figure 5. 4: Fabrication flow of the 2 nd generation of the ER devices.....	118

Figure 5. 5: Mask 1 used for patterning of the Ti/Au layer.	119
Figure 5. 6: Mask 2 for determining the Cu electroplating areas.	120
Figure 5. 7 : Mask 3 for determining the reservoir area in the inter-electrode region of the pyramidal electrodes.	120
Figure 5. 8: Designed layout for the fabrication of the ER devices on a common wafer with the DEP devices.	121
Figure 5. 9: Fabricated prototypes of the 2 nd generation of the ER devices with magnified electrode and reservoir region.....	122
Figure 5.10 : Fabrication flow of the 3 rd generation of the ER devices with 3D electrodes, using a single mask.	123
Figure 5. 11: Layout of the designed mask for the fabrication of the 3 rd generation of the ER devices.	124
Figure 5. 12 : SEM photograph of the ER devices with 3D electrodes. (A) Pyramidal, (B) Polynomial, (C) Prolate elliptical, (D) Oblate elliptical, and (E) Circular electrodes.	125
Figure 6. 1: ER test setup. Micropipette is used for loading 3 μ l of cell suspension into the PDMS reservoir. Rotational torque is generated on the cells by energizing the polynomial electrodes with sinusoidal signals in phase quadrature. The rotations of the cells are recorded using a video microscope for further analyses.....	129
Figure 6. 2: Utilized four channel function generator for generating four sinusoidal signals in phase quadrature.	129
Figure 6. 3 : Photograph of the experimental test setup with magnified view of the device under test.....	131
Figure 6. 4: K562 cells under the ER characterization tests.	133
Figure 6. 5: Rotation rates of K562 sensitive cells in the frequency range of 1 kHz to 0.1 MHz, inside four media with different conductivities.	134
Figure 6. 6: Straight line fitted to the data points of peak rotation frequency and cell radius versus medium conductivity. The membrane capacitance and effective conductance are calculated using the slope and intercept of the fitted line.	134
Figure 6. 7: K562/IMA-0.5 μ M cells under the ER characterization tests with quadrupole polynomial electrodes.	136

Figure 6. 8: Rotation rates of K562/IMA-0.2 μM cells in the frequency range of 1 kHz to 0.1 MHz, inside four media with different conductivities.....	136
Figure 6. 9: Rotation rates of K562/IMA-0.3 μM cells in the frequency range of 1 kHz to 0.1 MHz, inside four media with different conductivities.....	137
Figure 6. 10: Rotation rates of K562/IMA-0.5 μM cells in the frequency range of 1 kHz to 0.1 MHz, inside four media with different conductivities.....	137
Figure 6. 11: Straight line fitted to the data points of peak rotation frequency and cell radius versus medium conductivity. For each cell population, the membrane capacitance and effective conductance are calculated using the slope and intercept of the fitted line, respectively.	138
Figure 6. 12 : K562/DOX-0.5 μM cell under the ER measurements.....	139
Figure 6. 13: Rotation rates of K562/DOX-0.1 μM cells in the frequency range of 1 kHz to 0.1 MHz, inside four media with different conductivities.....	140
Figure 6. 14: Rotation rates of K562/DOX-0.3 μM cells in the frequency range of 1 kHz to 0.1 MHz, inside four media with different conductivities.....	141
Figure 6. 15: Rotation rates of K562/DOX-0.3 μM cells in the frequency range of 1 kHz to 0.1 MHz, inside four media with different conductivities.....	141
Figure 6. 16: Straight line fitted to the data points of peak rotation frequency and cell radius versus medium conductivity. For each cell population, the membrane capacitance and effective conductance are calculated using the slope and intercept of the fitted line, respectively.	142
Figure 6. 17: MATLAB simulation of K562 sensitive and resistant cells for DEP spectrum analysis, in medium with conductivity of 1 mS/m and relative permittivity of 78.....	144
Figure 6. 18: MCF7/DOX-1000 nM cells under the ER measurements.	145
Figure 6. 19: Rotation rates of MCF7/Sensitive cells in the frequency range of 1 kHz to 0.1 MHz, inside four media with different conductivities.....	145
Figure 6. 20 : Rotation rates of MCF7/DOX-1000 nM cells in the frequency range of 1 kHz to 0.1 MHz, inside four media with different conductivities.	146
Figure 6. 21 : Straight line fitted to the data points of peak rotation frequency and cell radius versus medium conductivity. For each cell population, the membrane	

capacitance and effective conductance are calculated using the slope and intercept of the fitted line, respectively.....	146
Figure 7. 1: Simulated $\text{Re}(F_{\text{CM}})$ for the blood cells and the cancer cells, with magnified view of the proposed separation region at the $f=160$ MHz.....	153
Figure 7. 3: Schematic view of the designed DEP device with 3D isolated electrodes, together with the critical dimension of the device, in μm	155
Figure 7. 4: Designed layout of the DEP devices together with the critical dimensions of the devices.	156
Figure 7. 5: 3D FEM simulation of the distribution of the gradient of the electric field intensity in the DEP separation region of the device.....	159
Figure 7. 6: Use of finite element simulations to study the separation efficiency of the cells.	161
Figure 7. 7: Fabrication process flow of the DEP devices, using four masks.	162
Figure 7. 8: (A) Fabricated prototype of the DEP devices. (B) Magnified view of the sputtered Ti/Au electrodes before electroplating and (C) SEM photograph of the 3D electroplated floating electrodes.	164
Figure C. 1: Current density passing through the electrodes and medium in the ER devices with 3D electrodes.	208
Figure C. 2: Generated joule heating the ER devices with 3D polynomial electrodes.	208
Figure D. 1: Subdomain properties of the DEP devices.....	213
Figure D. 2: Defined electrical boundary conditions for the DEP devices.....	214
Figure D. 3: Defined subdomain conditions for the DEP devices in the microfluidic module.....	215
Figure D. 4: Microfluidic boundary settings for the DEP devices.....	216
Figure D. 5: Defined constant values for the electric model.	217
Figure D. 6: Designed FEM module of the polynomial structures.	220
Figure D. 7: Subdomain properties of the ER devices.....	220
Figure D. 8: Defined boundary condition for the inter-electrode region.	221
Figure D. 9: Defined constant values for the ER model.	221

CHAPTER 1

INTRODUCTION

Advances in semiconductor technologies since the 1970s have paved the way for fabrication of the devices with micron dimensions. These devices, which were combinations of mechanical structures with embedded electronics, were categorized under the MicroElectroMechanical systems (MEMS). MEMS technology has borrowed its fabrication capabilities from the growing semiconductor field and has applied it to different fields of the science, such as biology, chemistry, and mechanics. With the application of the MEMS technology in biological sciences a new field has born under the title of BioMEMS (Fig. 1.1).

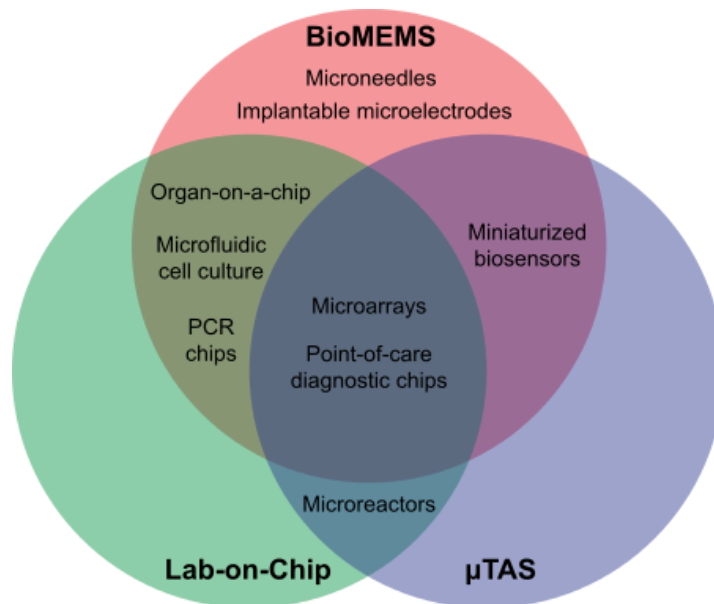


Figure 1. 1: Showing the division BioMEMS field into the lab-on-a-chip and μ TAS.
(Figure from Wikipedia/BioMEMS)

This field has borrowed the most advanced microfabrication techniques from its parental field, MEMS, and has applied them to the micro world of the biological particles such as cells, viruses, and bacteria. With advances in BioMEMS field, new fields were born like micro total analysis systems (μ TAS) and lab-on-chips (LOC), which have extended use of BioMEMS field to the specific areas of biology. With recent advances in the microfluidics, BioMEMS has enabled fast prototyping of the medical devices with higher accuracy and sensitivity, and with lower fabrication costs and energy consumption. In addition, it has enabled new methods of manipulation of biological particles by production of micron sized channels, which can be used as replicates of human capillary environment. Following the maturation of the theory and the technology in recent years, fabricated biomedical devices using the MEMS technology has found their ways to commercial market (Fig. 1.2).

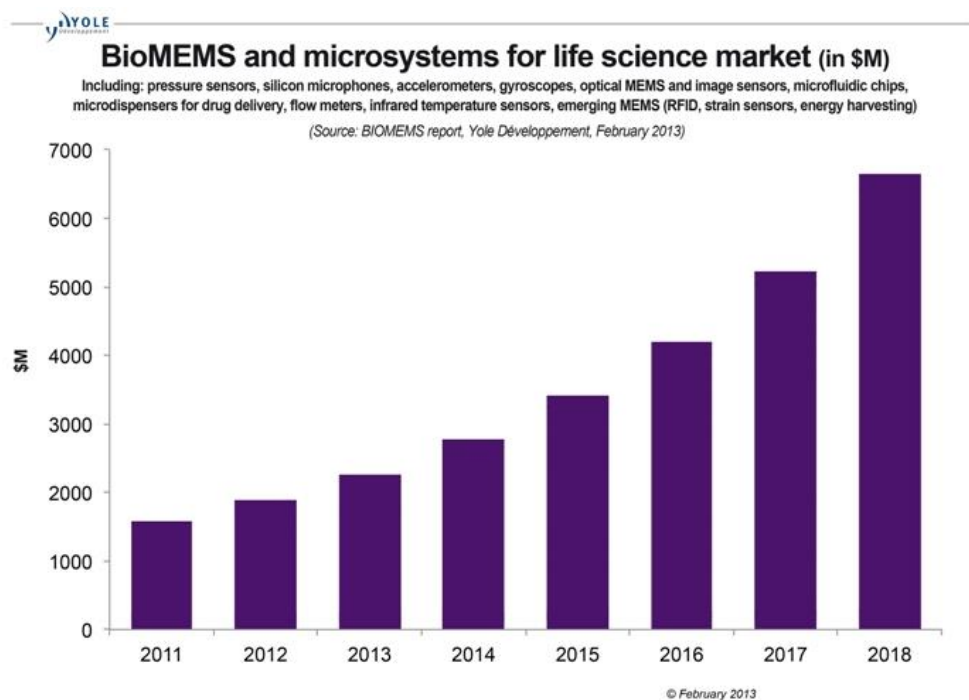


Figure 1. 2: Growing market place of BioMEMS devices since 2011.
 (Figure from www.yole.fr)

With growing interest in the application of the MEMS technology in the biology, study of biophysical properties of the cells has gained further importance. Cells are the most basic and functional part of the complex living systems and study of

biophysical (electrical and mechanical) properties of the cells can provide an inspection to physical and chemical status of biological organisms. In the past two decades, a number of new approaches were used in studying the relation between the diseases and variations in mechanical and electrical properties of the cells. It was known that there are many complex feed-back mechanism within the cells that help them adapt themselves to the changes in their external environment or any excitation. These feed-back mechanisms can be explored and specified by studying the changes in physical parameters of the cells. Among others, dielectric properties of the cells hold significant importance, as they carry the footprints of each cell type and variations in cells dielectric properties could be utilized as a tool for detecting changes in their physical status. In addition, variations in the dielectric properties of different cells make separation, manipulation, and detection of the cells possible based on their electrical signals.

First attempts to measure the dielectric properties of cells backs to early 1910's. However, the most practical study of cells dielectric properties starts with the modeling of the biological cells using a single-shell cell model in 1950's and use of Coulter counters in 1956 [13]. Recent advances in MEMS technology have enabled the single cell analyses. Different methodologies are employed in studying the dielectric properties of the biological particles, including electrorotation (ER) [1–6], dielectrophoresis [5,6,14–16], microelectrical impedance spectroscopy (μ -EIS) [7,8], and impedance flow cytometry (IFC) [9–12]. All these methods are utilizing the advantages of the microfluidic channels and microelectrode arrays.

One of the MEMS enabled fields is dielectrophoresis (DEP), which was introduced following the advances in fabrication of microfluidic systems and microelectrodes inside the microchannels. DEP has gained a high significance by providing the ability of separating and manipulating of cells and particles based on their electrical properties as well as differences in their size. Therefore, accurate determination of cells dielectric properties is essential in the design and implementation of DEP chip.

This thesis presents the dielectric characterization of human leukemia cancer cells (K562), breast cancer cells (MCF7), and their multidrug resistance (MDR) derivations (doxorubicin and imatinib resistance), using electrorotation method.

The target behind the dielectric characterization of these cells was deliberating on feasibility of application of DEP method in separation and detection of MDR in cancerous cells. Moreover, the relation between the developments of MDR with changes in dielectric properties of the cells were investigated for imatinib and doxorubicin resistant K562 cells. For the characterization purpose, ER devices with 3D electrodes were utilized. Experimental and FEM analysis were used for studying the 3D torque distribution on the ER devices with different 3D electrode geometries. Analyses have shown various advantages of the 3D electrode over generally used planar (2D) electrodes. As an experimental application of the extracted dielectric properties of the cells, the DEP devices were designed and fabricated. It is aimed to achieve high efficiency in separation of the human leukemia cells and its MDR derivations from the leukocytes mixture, using these devices. As the first step, the separation efficiency of the fabricated devices was studied using the FEM analyses. The results show 100% efficiency for separating the K562 cells from the leukocytes mixture.

In this chapter, different methodologies used in the dielectric characterization of the biological cells will be summarized. In each section, brief background information is provided together with a literature survey on the developed techniques. Sections 1.1 through 1.3 introduce the dielectric characterization methods, including the impedance flow cytometry (IFC), microelectrical impedance spectrometry (μ -EIS), and dielectrophoresis. Advantages and the feasibility of each method are discussed with examples of proposed prototypes for each method. In Section 1.4, electrorotation (ER) method is investigated as a single cell dielectric characterization method. Different approaches in utilization of the ER method in the dielectric characterization of single cells are discussed. Finally, objectives of this research and organization of the thesis are presented.

1.1 Impedance Flow Cytometry (IFC)

MEMS based IFCs are the miniaturized types of the Coulter counters. Coulter counters are intensively being used in clinical applications, especially for cell counting. In addition to the cell counting, the flow cytometry method has been used as a dielectric characterization method. The conventional Coulter counter devices

are able to identify the cells based on distinctive volume differences using DC analyses. However, recently more advanced Coulter counters have been commercialized which are capable of performing RF analyses. These devices are equipped with both electronics for DC and RF measurements, making them capable of measuring the electric properties of the cells independent of their volume. Following the advances in microfluidic technologies, these Coulter counters are being demonstrated on the LOC devices, by impedance flow cytometry method. Impedance flow cytometry is a non-invasive, label-free method, which is used in the study of electrical signature of the biological particles. These devices enable discrimination of the cells without needing any magnetic or fluorescent markers. The electrical impedance of the cell is studied over a wide frequency range to reveal the electric properties. By performing multiple frequency measurements, one can also reveal the frequency-dependency of the cells dielectric properties. Information on cell size, as well as membrane and cytoplasmic composition can be obtained by studying the dominant factors in each frequency range.

To utilize this method, a comprehensive modeling is essential for the response of the system in AC or DC electric field. A well settled model of the response of the IFC systems in each frequency range is proposed by Gawad et al. [17] Figure 1.3 shows the electrical response of a conventional IFC system in different frequency ranges. It is important to note that the modeled system uses the bottom electrode configuration. Similar modeling is utilized for studying the electrical response of the IFC systems, in the presence of a cell between the electrodes [18–20]. As shown in this model, in the low-frequency band, the measured electrical signal is significantly dominated by the double-layer formation in the vicinity of the electrodes. The double-layer presents a capacitive characteristic, which is shorted in frequencies above 100 kHz. Generally the dielectric properties of the cells can be determined by performing measurements in the range of 0.5 - 100 MHz. The same effect is seen for the resistive membrane of the cell. With an increase in the frequency, the membrane capacitance increasingly shorts out the membrane resistance and the dielectric properties of the cell interior are sensed by the electrodes. In order to eliminate the interfering signals from the conductive medium, use of two pairs of electrodes is a commonly implemented configuration.

The first pair of the electrodes senses the current changes due to the presence of a cell between the electrodes, while the second pair of the electrodes operates as a reference, measuring the current passing through the pour medium. This system enables the differential measurement method and eliminates the common signals, such as resistivity of the medium.

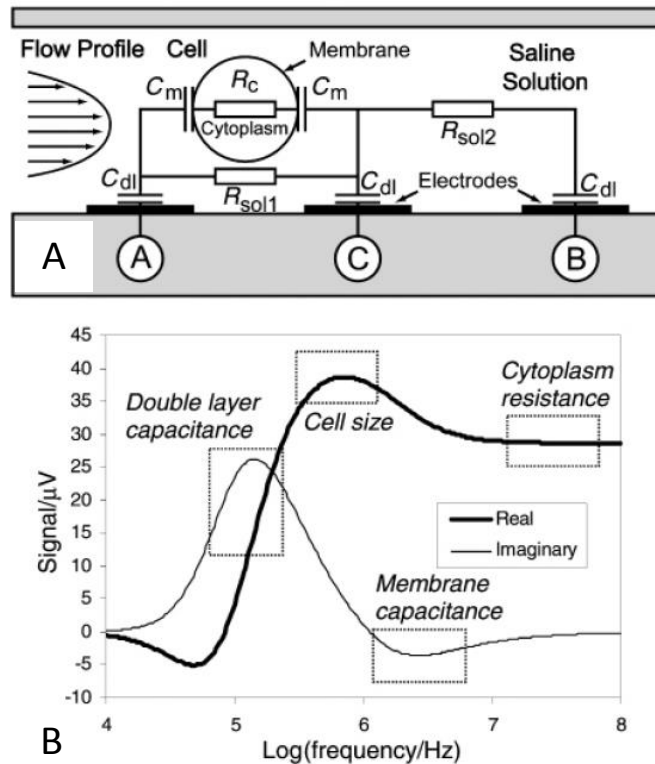


Figure 1. 3: Electrical model of an IFC system with bottom electrodes. (A) Capacitance and resistance modeling of the microfluidic IFC system in the presence of a biological cell. (B) Simulated complex impedance spectrum of a 10 μm diameter cell using a SPICE model [21].

Same bottom electrode configuration was used in studies of Benazzi et al. [18]. In addition, they have implemented an optical apparatus for performing fluorescent measurement, to increasing the accuracy of the system. Their device includes two pairs of electrodes (measuring and reference) for electrical measurements and an optical measurement side, capable of operating in three optic wavelength ranges (Fig. 1.4).

Proposed microfluidic system benefits from simultaneous electrical and optical measurements for providing a comparison between recorded signals from each source. This system was used in characterization and detection of three algae groups (*Isochrysis galbana*, *Rhodospirillum rubrum*, *Synechococcus* sp.).

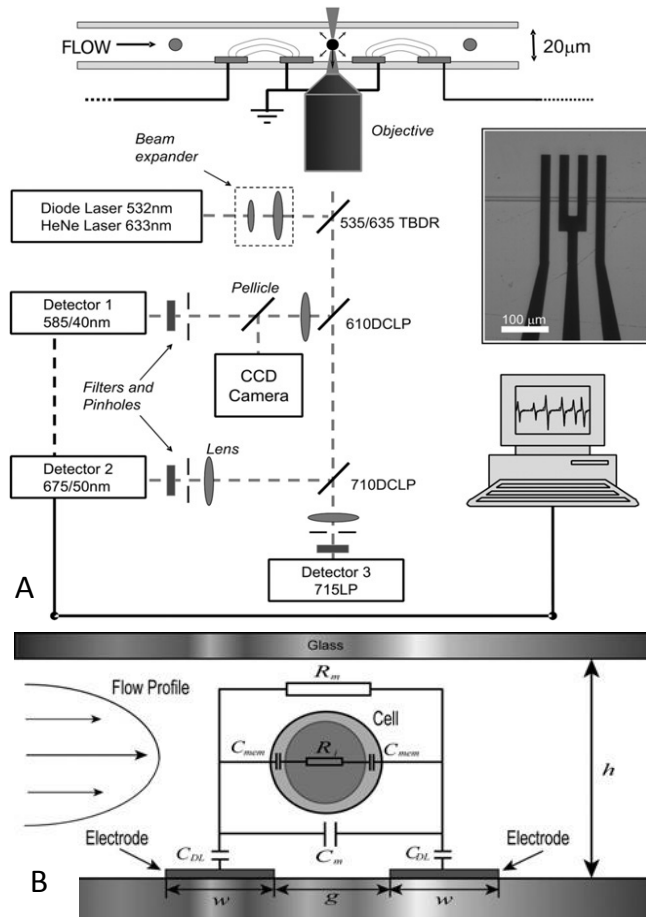


Figure 1. 4: (A) Schematic diagram of the device showing the cross-section of the IFC system, together with the optical system. Inset shows the photograph of the microchannel with microelectrodes. (B) Equivalent electrical modeling of the IFC system in presence of the biological cell [18].

Use of optical system with three operational wavelengths makes discrimination of each algae group possible. Although, it was shown that this micro-sensor has a comparable accuracy compared to commercial flow cytometers; the identification range of the device is limited to particle above 2 μm.

In addition to bottom electrode configuration, bottom and top electrodes were used in the IFC systems [20,22]. Cheung et al. has used two pairs of bottom and top

electrodes in their IFC chips for characterization and discrimination between different particles and cells including RBCs, ghosts, and polystyrene beads. The opacity (ratio of the RF signal to the DC signal) and the phase information were used for cell discrimination [18]. The proposed device with a high frequency band amplification circuit with multi-frequency quadrature modulation in the frequency range of 350 kHz – 20 MHz is capable of discriminating 1000 cells/sec. The working principle of the chips and the cell modeling are shown in Fig. 1.5.

Holmes et al. has proposed an IFC chip with simultaneous optical verification using a fluorescence measuring system [19]. The device (Fig. 1.6) has the same electrode structure with the Cheung et al. This device measures the electrical signals of cells passing through the channel followed. The electrical measurements were followed with an optical measurement of the fluorescent properties of the cells. This setup realizes the simultaneous comparison between the optical and electrical signals, by application of a confocal-optical detection with dual laser beams.

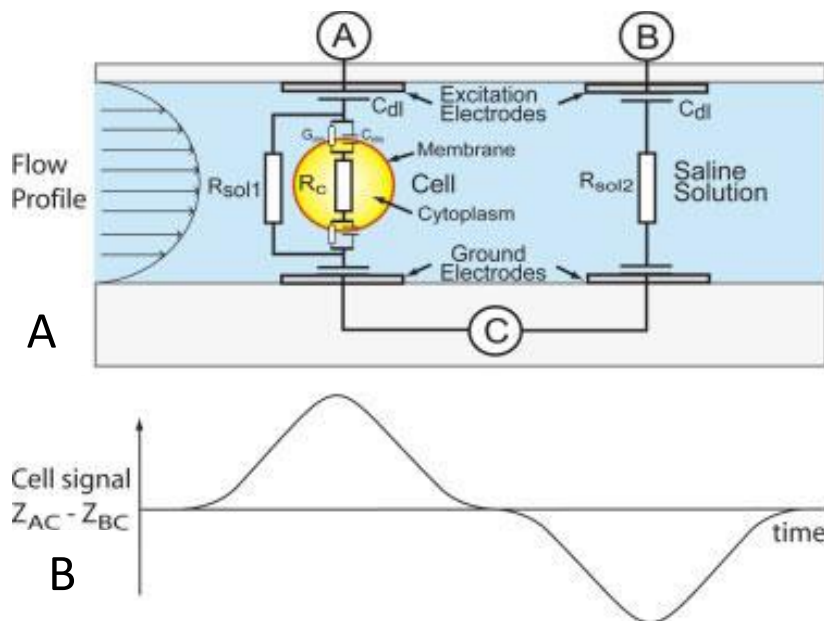


Figure 1. 5: Schematic of an IFC system with top and bottom electrodes. (A) Electrical model of the microfluidic IFC system in presence of a biological particle. (B) Expected measured signal from each pair of electrodes [23].

In above, examples of device with lateral bottom electrodes and both bottom and top measuring electrodes were presented. IFC chips with top and bottom electrodes provide a better output signal by encompassing the whole cell body, and eliminating

fringing field effects on the cells. However, fabrication of top and bottom electrodes needs complex micro-fabrication processes. Another method in the IFCs is use of optical measurements as a complementary approach. IFCs with fluorescent measuring apparatus provide higher accuracy compared to the conventional IFC systems. In addition, it can be used as a proof of concept for electrical discrimination between the cells with distinct optical properties. A disadvantage accompanied with utilization of optical systems is an increase in the complexity and cost of the system.

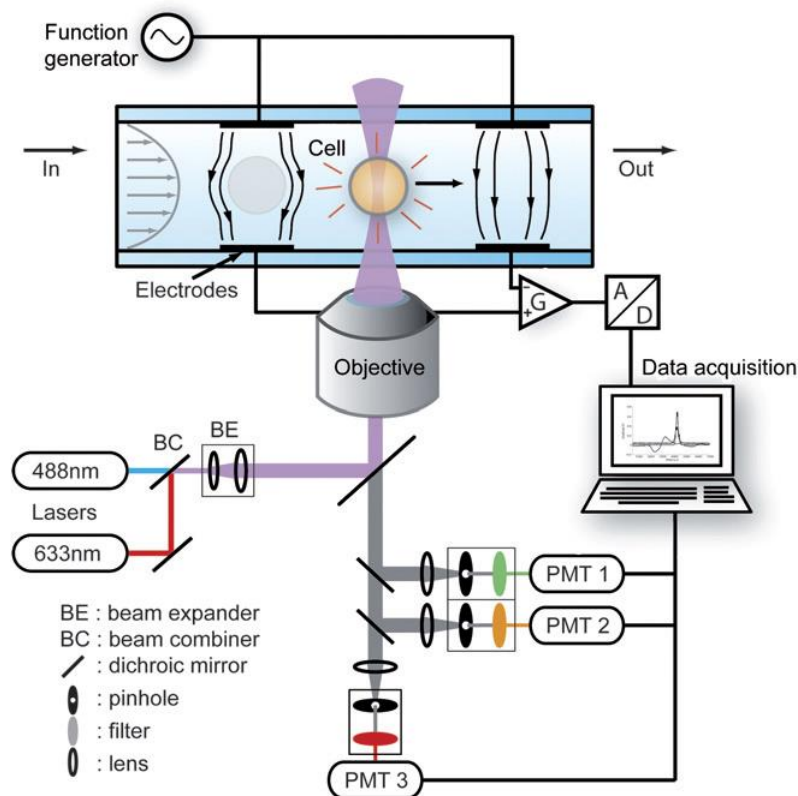


Figure 1. 6: Schematic diagram of the IFC system, with optical detection apparatus. A dual laser excitation and detection is implemented for simultaneous measurement of electrical and optical properties of the cells [24].

The current technology is unable to provide miniaturization and integration of the optical measurement systems into the microchips, therefore huge external devices are being used for the purpose. Another issue in IFC systems is electrode polarization, which causes difficulties in interpretation of the recorded electrical signals. Different solutions were proposed for overcoming this problem. A

noteworthy approach is presented in studies of Küttel et al. [25] and Demierre et al. [26]. They have characterized and used liquid electrodes in DEP and IFC microchips. Küttel et al. had implemented liquid lateral electrodes for impedance spectrometry. The excitation electric field was generated using metal electrodes, far from the measurement channel. Then, the generated electric field was guided through a conductive access channel to the main measurement area. This configuration is shown to eliminate the polarization problem in conventional IFC chips. Another approach in dealing with the electrode polarization is use of non-polarizable electrode. Zheng et al. have introduced a new approach for determining the cells' membrane and cytoplasmic electric properties, using non-polarizable electrodes [27]. In this method, cells were driven inside the microchannel using a hydraulic pressure, and were squeezed into a chamber, which was smaller than the cell size (Fig. 1.7). The dielectric properties of the cells were measured at seven different frequencies in a range of 1-400 kHz by Ag/AgCl electrodes (non-polarizable electrodes). The current variance caused by the presence of a cell in the microchannel was measured using a pair of Ag/AgCl electrodes, inserted from the inlet and outlets. To reveal the dielectric properties of the cells, measured current was amplified and demodulated. For calculating the specific membrane capacitance and cytoplasmic conductivity of the cells, mechanical and electrical models of the squeezed cells were developed. For cell discrimination purpose, this system considers combination of differences in specific membrane capacitance, cytoplasmic conductivity, and cell size. The authors had made a comparison between the performance of the Coulter counters which were solely dependent on the discrimination in the cell size, and the proposed system, which studies the cells membrane and the cytoplasmic properties for the discrimination purpose. It was shown that, for cells with comparable sizes, the detections and discrimination performance was improved from 66% in conventional Coulter counters to 93% in these devices.

As discussed above, different methods are utilized in miniaturization of the Coulter counters. Huge effort has been put on embedding the IFCs into the LOCs, for the dielectric characterization of single cells. Although there have been significant improvements in this field, especially in the utilization of IFCs in point of care

applications, IFC chips have not been commercialized as the medical devices. One of the important issues is increasing the performance and accuracy of IFC chips. Use of fluorescent markers in combination with electrical methods is shown to enhance the performance of the cell discrimination. However, the optical apparatus cannot be embedded into the micro devices.

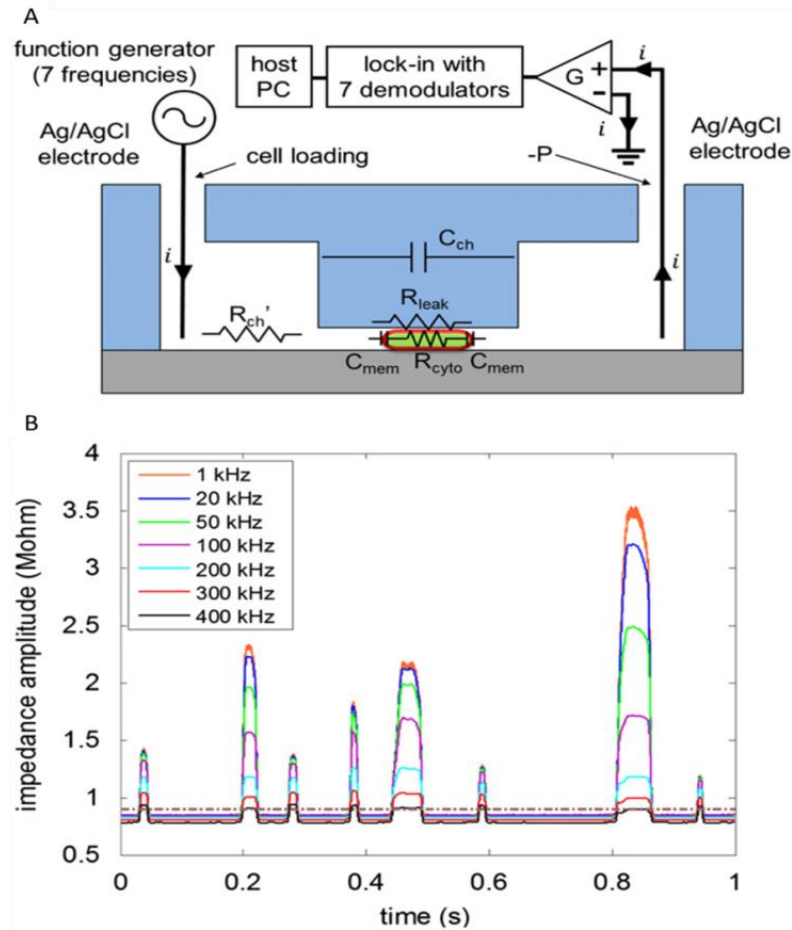


Figure 1. 7: Microfluidic system for measurement of dielectric properties of the cell membrane. (A) Schematic view of the device. “-p” shows the negative pressure in the outlet channel for aspirating the medium. (B) Experimental results showing the measured impedance signal at 7 different frequencies [27].

1.2 Microelectrical Impedance Spectroscopy (μ -EIS)

Microelectrical impedance spectroscopy (μ -EIS) is a single cell analysis method, in which the frequency dependent impedance of the cells is measured. Frequency dependent impedance analyses provide insights to the biophysical compounds of the

cell membrane and interior. In addition, μ -EIS has found significance in the cytosensors or cell-based biosensors, which utilize the biological cells as sensing element, revealing any internal or external excitations [28–33]. For this aim, the frequency of the applied electrical signals to the immobilized cells between a pair of electrodes is swept on a specific frequency band, and then the current passing through the electrodes is recorded. The changes in the recorded signal reveal the dependency of the electrical properties of the cells on the electrical frequency. It is obvious that there are many similarities between the μ -EISs and IFCs. An important difference discriminating these methods is the necessity of an immobilization mechanism in the μ -EIS. For studying the frequency response of a cell, impedance spectroscopy is generally accomplished using a trapping or immobilization mechanism. Therefore, in this section we will focus on the different trapping methods used in impedance spectrometry. Different approaches in immobilization of a single cell in the measurement area are surveyed in the below section.

For immobilization purpose, different methodologies are utilized including hydrodynamic trapping [7], n-DEP [34], negative pressure trapping [35], micro-holes [36], and micro-pillars [37]. In the below section feasibility of each method will be studied, by investigating available examples in the literature.

Jang et al. has used SU-8 microstructures (micro-pillars) inside a microfluidic channel to trap single cells [37]. The schematic of the fabricated chip is shown in Fig. 1.8.

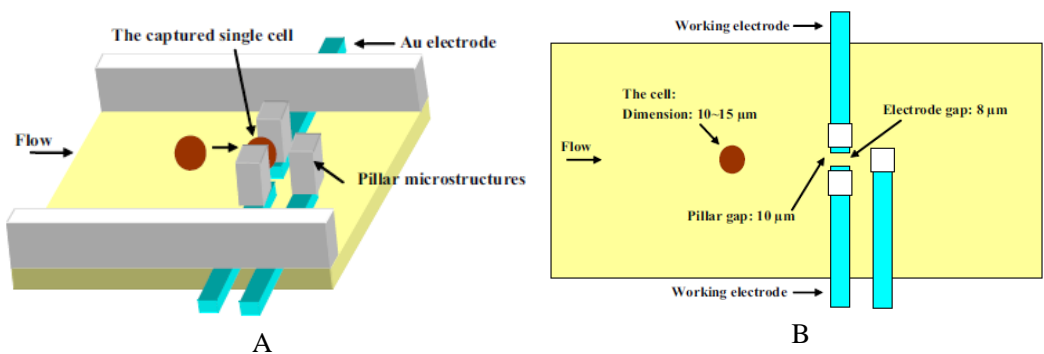


Figure 1. 8: A μ -EIS system with micro-pillars to capture single cells. (A) 3D presentation of the cell capturing procedure. (B) Top view of the device [37].

Introduced flow from the inlets, drive the cells toward micro-pillar side, where a pair of measuring electrodes is placed in the lateral side of the micro-pillars. This system is utilized in the impedance analyses of the Hela cells in the low frequency band of 1-100 kHz.

Use of a hydrodynamic cell trapping system for single cell analyses was proposed by Malleo et al. [38]. Proposed system was used in the study of time dependent chemical perturbation effect on Hela cells (Fig. 1.9). Measurements were accomplished using a pair of closely positioned electrodes, acting as a reference (empty) and a measuring electrode (containing trapped cell). In addition, it was used in the study of effects of medium conductivity in recorded impedance of the cells.

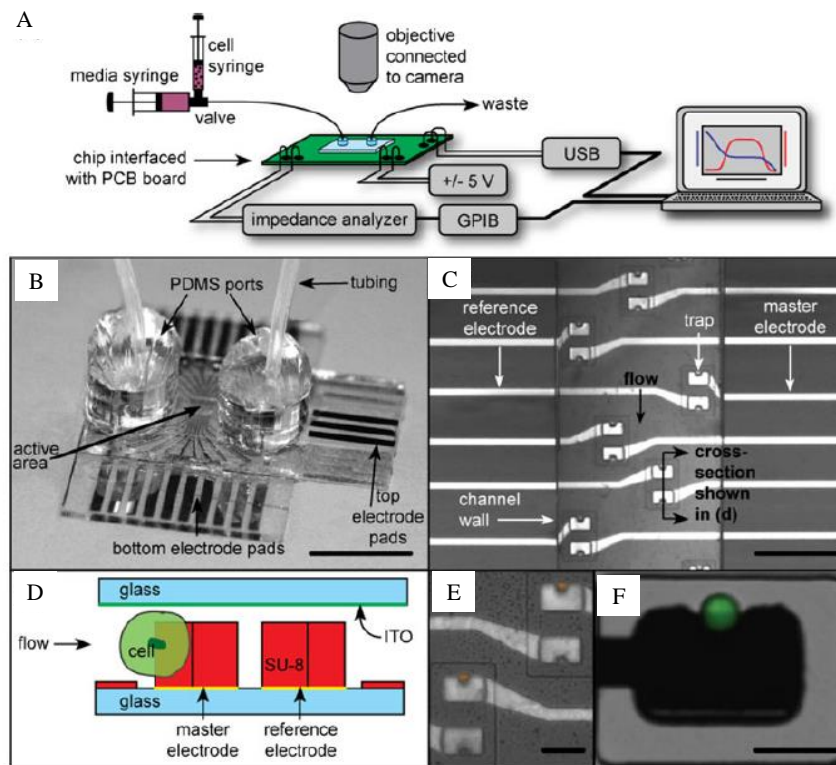


Figure 1. 9: A μ -EIS device, with hydrodynamic cell trapping system. (A) The experimental setup. Electrical connections are made using a PCB, which enables data acquisition. (B) Photograph of the fabricated prototype with the PDMS ports mounted on the inlet and the outlet. (C) Photograph of the microchannel, while the device is under operation. (D) Schematic view of the trapping region, with differential measurement electrodes. (E) Image of the trapped beads with $15\mu\text{m}$ size. (F) Image of the trapped single Hela cell [38].

An example of a trapping system with negative pressure is presented by Cho et al. [39]. The system is used to study the highly and poorly metastatic neck and head cancer cells over a frequency range of 40 Hz – 10 MHz. Their fabricated device on a glass substrate with PDMS capping consist of two flow channels with 8 pair of the electrodes on each channel (Fig. 1.10). Generated negative pressure (suction) was used to immobilize the cell between the measuring electrodes.

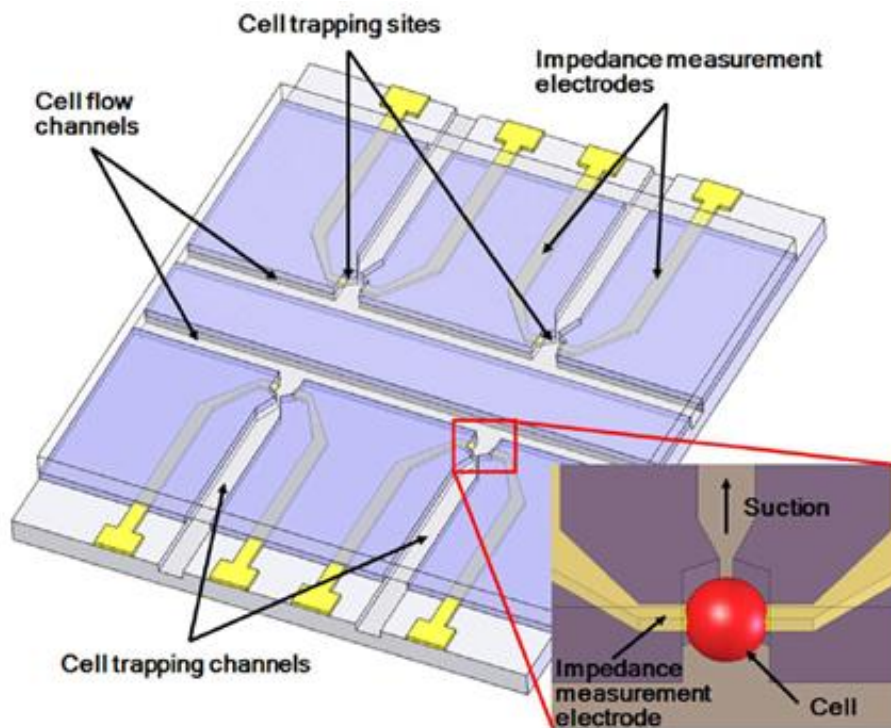


Figure 1. 10 : Schematic view of the μ -EIS device, with four impedance analysis sides. The close-up view shows a trapped cell inside the microchannel due to application of negative pressure (suction) [35].

In addition to utilization of mechanical structure in cell trapping, AC signals are applicable in immobilization of the cells. Utilization of AC electrokinetics for trapping the cells is presented by Lan et al. [34]. They used the alternating current electrothermal (ACET) effect combined with negative dielectrophoresis (n-DEP) for trapping the cells inside the electrode micro-wells (Fig. 1.11). ACET is a phenomenon, which is used in the transport of a medium with high conductivity under a non-uniform electric field. The motion of the medium is due to the produced resistive heating in the electrode area. Transported particles in the

medium are trapped inside the n-DEP area. This method was applied to the HeLa cells, for impedance measurements in the frequency range of 1-100 kHz.

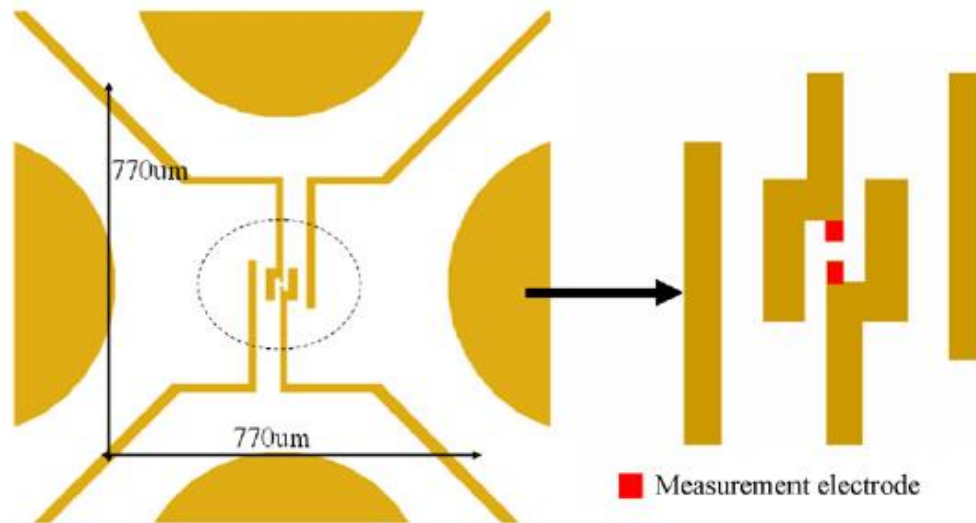


Figure 1. 11 : Schematic view of the impedance spectrometry device, with electrode micro-well. Cell driven by the medium flow is trapped at the micro-well area, due to n-DEP force [34].

The μ -EIS provides a label free impedance analysis of the cells. Although, it is not a general method in exact determination of the cells dielectric properties, it is capable of monitoring the changes in electric signals of the cells due to the external excitation by chemicals or drugs. Another factor making it as a preferred method in drug analyses is the ability to simultaneously monitor the changes in electrical properties of the cells. In μ -EIS systems, positioning of the cells between the electrodes carries a high importance due to the dependency of the measurements to the cell position. A general problem faced in this method is current leakage. To overcome current leakage modification on the electrodes are reported for exact positioning of the cells between the measuring electrodes. Among the different methodologies utilized in cell positioning, hydrodynamic immobilization and use of pillars are shown to have higher efficiency. An important drawback of AC electrokinetic methods such as n-DEP, which utilize multiple signals for cell trapping, is the alternation of the measured electrical response of the cells. In other words, the applied electric field to generate the n-DEP force, results in changes in

electrical properties of the cells. Therefore, the recorded signals do not reflect the actual electric properties of the cells.

1.3 Dielectrophoresis

Dielectrophoresis (DEP) is the motion of the polarizable particles under presence of a non-uniform electric field. The motion of the particles is a result of interaction of the induced dipole with the non-uniform electric field. DEP is generally utilized in separation and manipulation of various particles and cells. In addition, it is a powerful tool for detection and separation of circulating tumor cells (CTCs). Since the development of the DEP theory by Pohl (1951, 1958, and 1961) [40–42] to describe the DEP force applied on the particles in a non-uniform electric field, there have been an extensive literature produced on the DEP theory. In the first decade of the 21st century more than 2000 publications have been published on the theory, status of developed technology, and applications of DEP (Fig. 1.12) [43]. With matured literature and technology, now most of the effort is directed to applications of DEP in biosensors and LOCs. About 75% of 300 articles, published every year, are now focused on particle separation applications of the DEP (Fig. 1.13). Now, most of the effort is directed to the medical applications of the DEP, and production of commercialized devices for point of care applications.

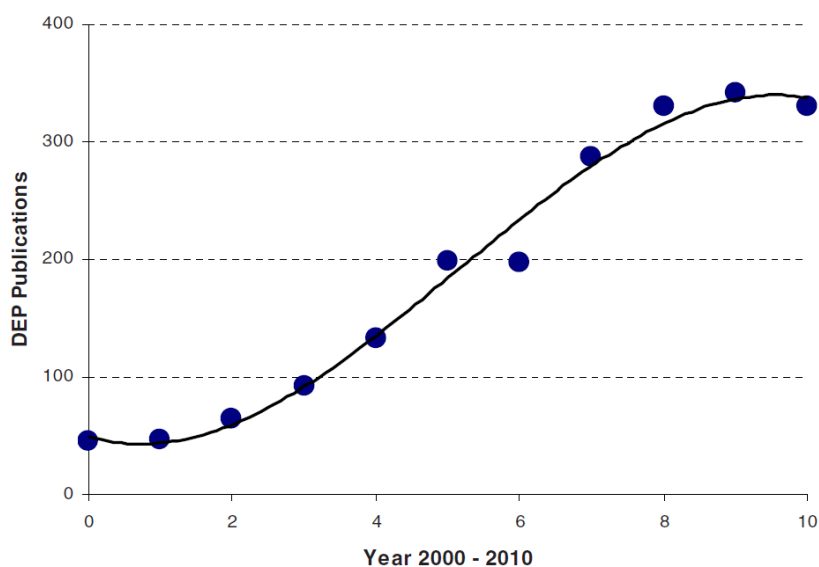


Figure 1. 12: Number of publications on DEP in the 1st decade of 21st century [43].

With advances in the technology, in addition to the biological particles, DEP is now applied to the nanoparticles, such as carbon nanotubes, nanowires, and oxide

nanoparticles [44–47]. Beside, DEP has further potential to be utilized in the dielectric characterization of various particles, especially biological cells.

Different approaches are available in the literature on characterization of the biological particles using the DEP method. These methods include fitting the DEP collection rate of the cells to the single or double shell cell model [48–50], the slope and the intercept method for determining the cell membrane dielectric properties [6,51–53], levitation and mobility analysis [54,55], and DEP crossover frequency analysis [51,56,57].

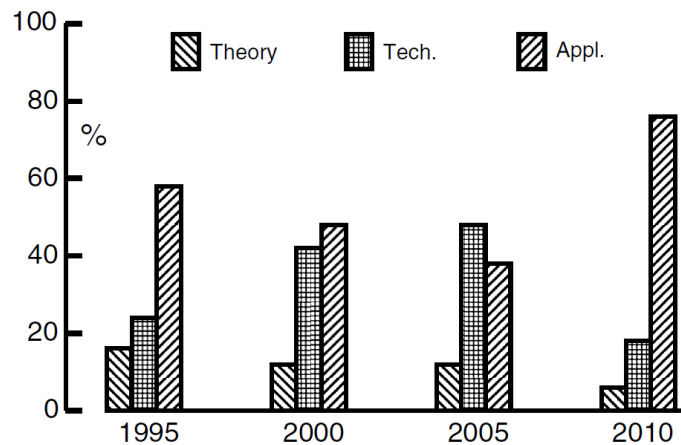


Figure 1. 13 : Categorized DEP publications on three subjects of theory, technology, and applications, since 1995 [43].

Following Sections will introduce the different dielectric characterization approaches using the DEP method.

1.3.1 Fitting the DEP spectra to the cell model

Unlike other single cell characterization methods, DEP studies the responses of a group of cells. For this purpose, collection rates of the cells in different frequencies are investigated, which enables depicting the DEP spectrum of the cells over a specific frequency band. Duncan et al. have used the DEP collection method to study the transfer rate of different ions in drug sensitive and MDR leukemia cancer cells (K562) [48]. They have used ion channel blocker agents to study the contribution of chloride, potassium, and calcium ions to the cytoplasmic conductivity of the sensitive and the MDR cells. Cells are characterized by manual

counting of the cells collected at the needle electrodes. The dielectric properties of the cells are determined by fitting the measured spectra to the single-shell model. It has been shown that, the contribution of potassium and calcium ion remain constant in sensitive and MDR cells, while the chloride activity has increased three times in resistant cells. Chin et al. has used the same method to detect apoptosis after drug injection (staurosporine) to the K562 cell, by studying the changes in the dielectric properties of the cells [49]. For this purpose, collection rates of cells in a frequency range of 10 kHz to 3 MHz are fitted to the single-shell model. Labeed et al. has studied the influence of the MDR modulators on reversal of MDR mechanism using the DEP spectrum method [50]. Many studies have shown that the mechanism of development of MDR could be reversed after treatment with MDR modulators. For this purpose, the dielectric properties of K562 and its MDR derivatives were studied using DEP and flow cytometry, both before and after treatment with the MDR reversal agent (XR9576). It has shown that, although there are significant differences between the electrical properties of sensitive and MDR cells, there is no significant change after treatment with the MDR reversal agent.

A more accurate approach to determine the cells dielectric properties is fitting the measured DEP spectra to the double-shell cell model. This method is able to determine the dielectric properties of the cell nucleus. Implementation of double-shell model is presented in studies of Haung et al. [58]. They have utilized a polynomial quadrupole electrode configuration to study the DEP responses of the viable and nonviable yeast cells. The measurement was performed in the frequency range of 1 kHz – 10 MHz.

1.3.2 DEP Crossover Frequency

In addition to extract the DEP spectra, determination of the DEP crossover frequencies can be used to extract the dielectric properties of the cells. At the crossover frequency, the effective DEP force applied to the particle becomes zero; therefore the lateral movements of the particles are ceased. For this purpose, DEP response of the particles is studied over a wide frequency band and the frequencies in which the motion of the cells is ceased is found.

Vykoukal et al. has used this method to study the dielectric properties of leukocyte subpopulations, using a DEP device with gold electrodes patterned on the polymer substrate [57] (Fig. 1.14). They have shown that the T-lymphocytes, B-lymphocytes, monocytes, and granulocytes have distinct membrane dielectric properties. This could be utilized in separation and discrimination of leukocytes using label-free systems, based on the size and dielectric properties of the cell. Pethig et al. [51] has used the same method in the determination of membrane capacitance and conductance of insulin secreting cells. They determined the DEP crossover frequencies of the cells using polynomial quadrupole electrodes, in five distinct media with varying conductivities. Obtained crossover frequencies were used in the slope and intercept method. In this method, a straight line is fitted to the data points of the crossover frequencies versus the medium conductivity. The cell membrane capacitance and conductance can be calculated, using the slope and intercept of the fitted line, respectively.

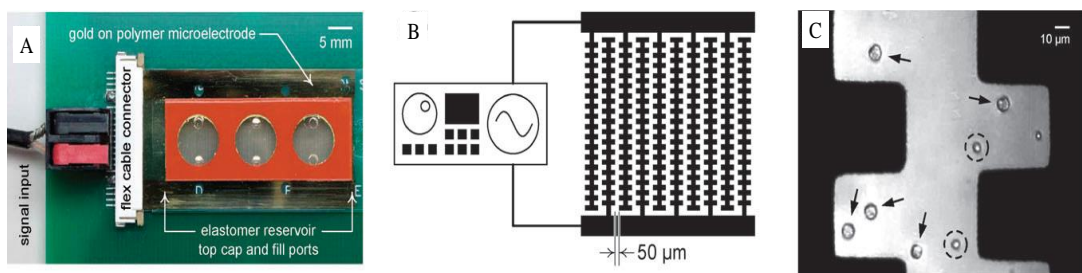


Figure 1. 14: DEP device for dielectric characterization of the leukocytes. (A) Photograph of the device with microfluidic reservoirs, and electrical connections. (B) Castellated electrode arrays for determination of crossover frequency. (C) Device under operation. Arrows and circles show eosinophils and erythrocytes, respectively [57].

Broche et al. presented the dielectric characterization of oral squamous cell carcinoma (OSCC) (H357) and human HPV-16 transformed keratinocyte cell line (UP33), using the DEP crossover frequency method [56]. The DEP collection data and DEP crossover frequencies of the cells were measured in the frequency range of 1 kHz – 16 MHz. Results approve that the dielectric properties of these two cell lines differs significantly, which facilitates the separation and detection of the H357 and the UP33 cells using DEP method.

In addition to the dielectric properties of the cell membrane, this method can be utilized in the calculation of the dielectric properties of the cell interior [6]. This method is highly sensitive to any motion induced on the cells other than the DEP motion. Therefore, during the measurements all other external stimuli should be eliminated. Moreover, the exact determination of crossover frequency is not possible, and only a frequency range can be specified in which cell motion due to DEP force is ceased.

1.3.3 DEP Motion Analyses

Another method that is used in the DEP based dielectric characterization of the particles is the study of DEP induced motion of the particles. This method needs a highly uniform distribution of the electric field, where the magnitude of the electric field can be assumed as constant. Then, by estimating the effective electric field on the cells, the velocity of the cells can be related to the dielectric properties of the cells. Haapalainen et al. utilized this method for dielectric characterization of the particles based on their DEP mobility [54]. For this purpose hyperbolic quadrupole electrodes were utilized, which produces a linear change in electric field distribution throughout the measurement area. It is claimed that the dielectric properties of polystyrene-carboxylate micro-beads are determined by measuring the velocity of the particles. In this study, they have assumed that the magnitude of the electric field gradient intensity remains constant over the measurement area; however it can be shown by FEM analyses that the variance in electric field magnitude can exceed the 20% of central electric field in hyperbolic quadrupole electrodes. In addition, manual measurement of the speed of the moving cells can be a time consuming task. In order to automatize the velocity measurements, Gascoyne et al. developed an image processing software to study the lateral motion of a mixed sample of mammalian cells in low medium conductivity [59]. The applied frequency is swept from 500 Hz to 100 kHz and relative motion of cells is processed to reveal the dielectric properties of the cells. Although, the exact properties of the cells are not calculated, they have determined the frequencies, at which different cells can be separated.

In addition to mentioned methods, different methodologies are developed to study the dielectric properties of the cells. A common approach in DEP studies is investigating the DEP response of a group of the cells and single cell analysis is not possible using the DEP method. Although it is a rapid method in cell characterization, it is not able to reveal the accurate properties of the biological cells. Fitting the DEP spectra to the single or double-shell model depends extremely on the fitting parameters. Therefore, deviations from the exact cell model, can lead to significant errors in the results. In addition, measurement of the crossover frequencies of the cells, results in a range of frequencies in which the DEP motion of cells cease and specifying a single frequency is not possible. The viscous damping forces will eliminate the movements of the cells around the crossover frequency. To avoid this fact, a very strong electric field gradient is necessary. However, a strong electric field can cause damages in the cells. Moreover, to determine the crossover frequency of the cells, it is necessary to eliminate all other forces such as hydrodynamics, which can lead to lateral movements of the cells.

1.4 Electrorotation

Electrorotation is a non-invasive dielectric characterization method, which is used to study the cells' dielectric properties. ER is categorized under the AC electrokinetics phenomena. AC electrokinetic is the motion of the micron size particles, induced by application of AC signals. ER is the circular motion of the polarizable particles due to application of an external rotating electric field (Fig. 1.15). The rotation of the particles is a result of interaction of induced dipole on the particles with the rotating electric field. Therefore, the rotational torque is proportional to effective electric field (EEF) distribution. The rotating electric field is generated by application of signals with equal amplitudes with $360^\circ/n$ phase shifted apart to n electrodes [60,61]. Electrodes are arrayed symmetrically around the measurement area. In the literature, extensively quadrupole electrodes with 90° phase shifts are used for the characterization. Different electrode geometries including circular (pin) [3], pyramidal [53], and polynomial [1,4,52] structures are used for generating the rotating electric field (Fig. 1.16).

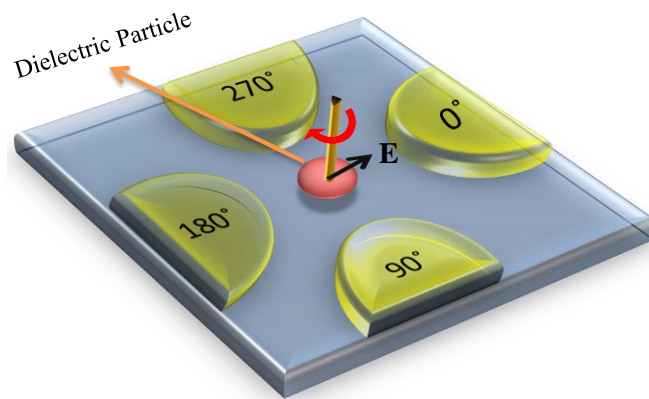


Figure 1. 15: Schematic view of the ER device. The direction of the rotating electric field upon application of sinusoidal voltage applied in phase quadrature, and the rotation of cells toward the direction of induced moment are shown.

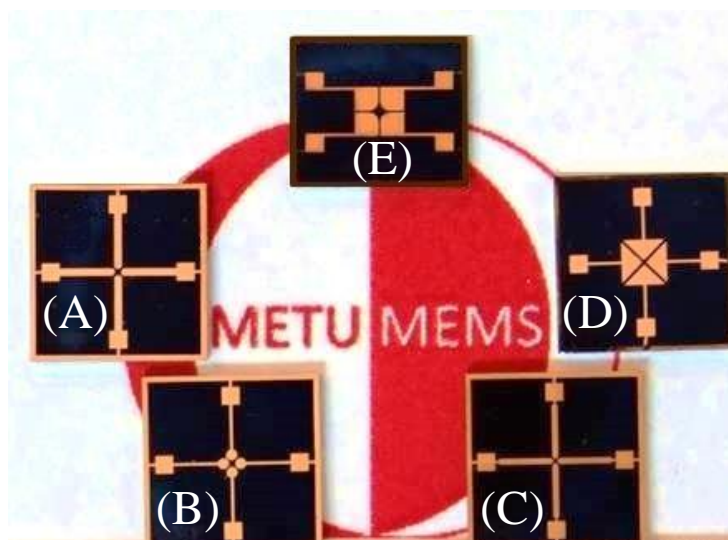


Figure 1. 16: Photograph of the ER device with different electrode geometries. (A) Oblate elliptical, (B) Circular, (C) Prolate elliptical, (D) Pyramidal, and (E) Polynomial.

The reproducibility and reliability of the measured rotation rates depend on a number of experimental and physical conditions including consistency of the ionic concentration and temperature of the medium, and uniformity and sustainability of the induced rotational torque (ROT-T) on the particles [62]. It is known that the induced rotational torque on the particles under a rotating electric field is spatial-

dependent. Therefore, to achieve high accuracy in the measurements and assure reproducibility of the collected ER data, a highly uniform EEF distribution with a constant magnitude is desirable over the measurement area. Enhancements in the uniformity of the EEF on the x-y plane is reported by investigation of the EEF distribution and numerical optimizations of the electrode structures [63–67]. These studies were focused on the surface distribution of EEF on the planar electrodes. In these studies, cells are assumed to be positioned on the device surface [67]. However, in practical ER measurement, cells are repelled from the device surface because of: (i) levitations forces inside the suspending medium and (ii) non-uniformities of the EEF along the z-direction (in planar structures due to the fringing electric field effect). This leads to manipulation of the particles by DEP forces (along the z-axis). Non-uniformity and variances of the EEF along the z-direction is considered as a significant drawback of the planar electrodes, which are due to the negligible height of the planar electrodes ($\sim 300\text{nm}$) compared to the biological cell size ($\sim 10\ \mu\text{m}$). Previous attempts to extract the experimental ROT-T map on the ER devices are limited to the polynomial [66] and circular [68] electrodes, which both have planar structures. Hughes and et al. [66] has studied rotation of 203 elliptical latex beads ($3\ \mu\text{m} \times 5\ \mu\text{m}$) on the devices with polynomial planar electrodes to extract the ROT-T map. The measurements were limited to the inter-electrode region of $400\ \mu\text{m} \times 400\ \mu\text{m}$, which is shown in Fig. 1.17. Figure 17(B) shows the position of the measured cells in the device surface with $\pm 1\ \mu\text{m}$ accuracy. In order to increase the consistency of the obtained results, they have used a number of averaging and smoothing methods. The extracted rotational torque map is shown in Fig. 1.17(C).

Rotation rate of the cells are frequency dependent, and reflects the dielectric properties of the cells interior and membrane. Unlike the DEP method, ER is used in the single cell analysis. This method is capable of determining the exact dielectric properties of the cells membrane and the interior. The frequency dependent rotation speeds of particles in media with different conductivities can be used to estimate their surface and interior dielectric properties, including membrane capacitance (C_M), effective membrane conductance (G_M), and intracellular conductivity (σ_i), at the single cell level. ER have been successfully used in the

dielectric characterization of biological cells, including erythrocytes [3,69], leukocytes [70–74], fibroblasts [75], variety of cancer cells [76–78], and bacterial cells [79].

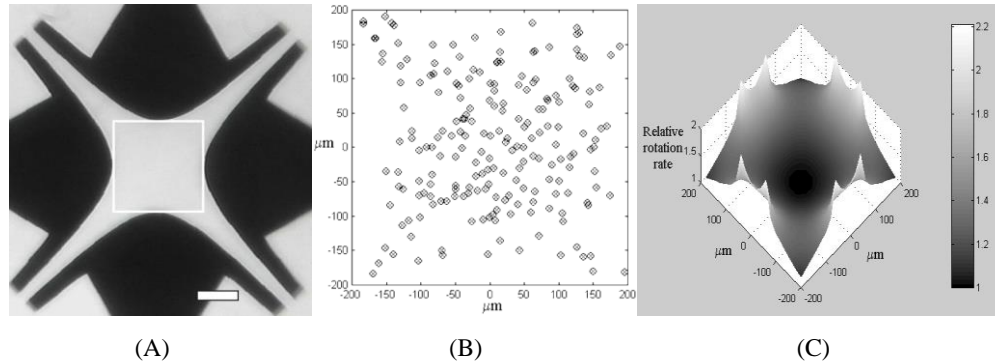


Figure 1. 17: Experimental study of the distribution of the rotational torque on the ER devices. (A) Polynomial quadrupole electrodes. (B) Position of the studied cells on inter-electrode region of the polynomial electrodes. (C) Extracted rotation rate map. Averaging and smoothing method is applied to the measurement data [66].

Different methodologies were utilized in extracting the cells dielectric properties, using the ER method. These methods are based on fitting the experimental ER spectrum to the single or double-shell model or use of the governing ER equation based on the peak rotation frequencies.

1.4.1 Fitting the experimental ER spectrum to cell model

In this method the ER experiment is performed in a medium with a specific conductivity. Then, the ER spectrum of the cells is extracted by studying the rotational responses of the cells over a wide frequency range. Then the ER spectrum of the cells is fitted to the single [80] or double shell model [81] of the biologic cells.

Becker et al. demonstrated dielectric characterization of metastatic human breast cancer cell lines (MDA231) [1]. They have used a quadrupole polynomial electrode array with 400 μm tip-tip distance for the ER experiments. The ER response of the cells was measured in the frequency range of 10 kHz – 100 MHz to

form the ER spectrum of the cells. Dielectric properties of the cells were extracted by fitting the ER spectrum of the cells to the single shell cell model (Fig. 1.18). They have shown that the dielectric properties of MDA231 cells vary from the erythrocytes and T lymphocyte cells, which enable use of the DEP method in detection and separation of breast cancer cell from normal blood sample. In addition, they demonstrated separation of MDA231 cells from the normal blood sample using the DEP method.

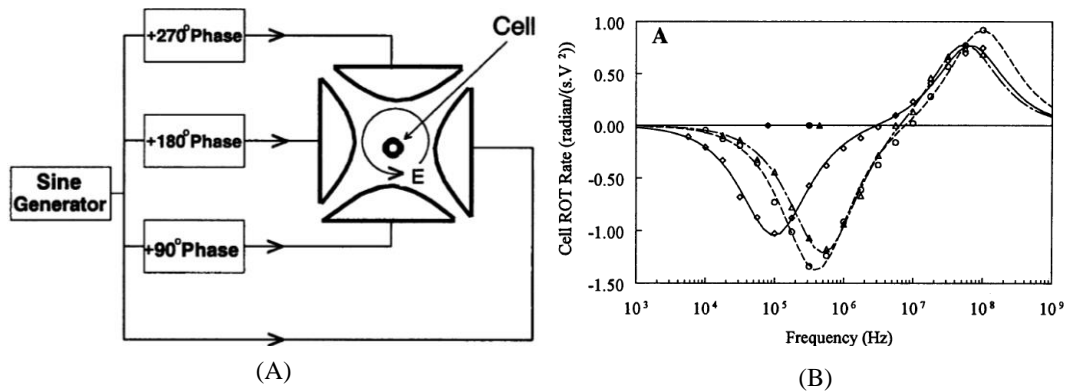


Figure 1. 18: Extraction of ER spectrum of the cells to determine the dielectric properties. (A) Schematic of the ER test setup. (B) ROT spectra for MDA231 cells (\diamond), T-lymphocytes (\circ), and erythrocytes (Δ) in the medium with conductivity of 56 mS/m. Each data point is an average of four measurements [1].

Gisma et al. presented the characterization of neurospora slime and the Myeloma Tib9 cell line using the simultaneous application of the DEP and the ER methods [82]. They have used the single-shell cell model for extracting the dielectric properties of the cells. Then by comparing the obtained results from both DEP and ER experiments, they have concluded that the single shell cell model cannot interpret the exact model of the cells. They had suggested use of three-shell model in determining the dielectric properties of the cells from the DEP or ER spectra. They have used a simple measurement setup, by gluing platinum wires to the glass slide. The electrode length was 15mm and the gap between the electrodes was about 0.2 mm.

Use of the double shell cell model is presented in studies of Griffith et al. [74]. They presented use of gold planar electrodes to study the dielectric properties of

human neutrophils upon activation with phorbol myristate acetate (PMA). They have used double-shell model to interpret the biophysical parameters of the cells during activation with PMA. It is important to note that due to large nucleus size in neutrophils, use of single-shell method can result in misinterpretation of dielectric properties of the cells. Therefore, double-shell model can describe the role of a large nucleus in effective cell permittivity.

In fitting the ER spectra to the cells model, rotation rate of the cells is sampled in 10-20 frequency steps over the measurement range, which is generally ranging from 100s of Hz to 10s of MHz. Although use of the single or double shell methods are well settled method in the dielectric characterization of the cells; it suffers from high dependency of the cells dielectric properties on the fitting algorithm. Therefore, small divergence from the actual cell model can alter the determined dielectric properties significantly. A more convenient and accurate method is the exact determination of the peak rotation frequencies of the cells and use of the effective complex permittivity equation to calculate the dielectric properties of the particles.

1.4.2 Peak Rotation Frequency

In this method, the peak rotation frequencies of the biological cells are determined in media with varying conductivities. Then, using the mathematical expression of the effective complex permittivity of the cells, the dielectric properties of the cells are calculated. There is a wealth of literature in the characterization of the cells using the peak rotation frequencies, and a comprehensive description can be found in the recent publication of Lei et al. [6]. They have modified the theory for extracting the cell dielectric properties from the low frequency peak rotation frequencies. In addition, optimizations are performed on utilization of the effective complex permittivity of the cells. Different levels of approximation, that enables calculation of the cell membrane and interior dielectric properties based on conductivity of the medium and the limitations on the measured peak rotation frequency was presented. An early study of the ER was presented by Arnold et al. [83]. They have investigated the dielectric properties of the latex particles with diameters of 5-10 μm , in the media with conductivities ranging from 2 to 16 $\mu\text{S/cm}$.

They have studied the rotational response of the particles in the frequency range 30 – 1000 kHz, to determine the peak rotation frequencies. Moreover, they have studied the dependence of the peak rotation frequency on conductivity of the medium and the frequency of the electric field. In these methods, both low and high frequency rotation peaks can be used in the determination of dielectric properties. A most commonly used approach is, determination of the low frequency peak rotation frequencies of the cells inside more than three mediums with varying conductivities. Subsequent to specification of the peak rotation frequency, a straight line is fitted to the data points of the peak rotation frequencies and cell radius versus the medium conductivity. The slope and intercept of the obtained line is used to calculate the cells' effective membrane capacitance and conductance. This method has been utilized to characterize the membrane and interior dielectric properties of various cells in the literature [51–53,84–87].

Pethig et al. [51] has determined the membrane capacitance and membrane conductance values for insulin secreting cells. ER peak rotation and DEP crossover frequencies of the cells are measured in five distinct medium conductivities (11.5 -101.4 mS/m) to be used in slope and intercept method. Chuang et al. [87] reported use of the same method in characterization of HL-60 cells activated by nanoparticles. They have studied the effect of nanoparticle uptake on dielectric properties of HL-60 cells.

This method provides a more accurate and reproducible results than previous ER methods. However, dealing with complex equations to extract the interior dielectric properties of the cells, can be confusing. Because of the nonlinear nature of the equations, analytical methods cannot lead to a valid solution. Therefore, a special attention should be directed to applied approximations on the parental equation of the effective complex permittivity of cell. These approximations are applied on the conductivity of the medium and the frequency range, in which cells are tested, aiming to simplify the core equations. In the slope and intercept method, generally low frequency (DC limit) approximations are applied, which confines the conductivity of the medium and the extracted peak rotation frequency range. In

order to obtain reliable results, the measurement should be carried out in the specified range by the theory [6].

1.4.3 Novel ER Devices

In addition to discussed methods, new techniques are being introduced in implementation of the ER method in dielectric characterization of the single cells. These techniques combine the microfluidics and different AC electrokinetic phenomena, in order to enhance the performance, accuracy, and speed of the ER method.

One of these approaches is the development of video or image processing programs for automated ER experiments, to overcome the difficulties related to tedious manual measurements. In this method, video processing algorithms are being developed to recognize the rotation of the cells under the ER. In addition, these programs are able to provide numerical results, like the rotation rate, cell position, and cell size [88–91].

De Gasperis et al. has developed a video processing algorithm with real-time vision algorithm for the automated analyses of the cell motion and rotation [88]. This system is able to extract the cell rotation spectra for the frequencies ranging from 1 kHz to 200 MHz in less than 5 minutes. In order to increase the accuracy of the system, laser tweezers were used for trapping and immobilization of the cells. Figure 1.19 shows the experimental setup for automated ER measurements. One of the challenging issues in ER tests is the immobilization of cells in their position while a rotating electric field is applied. Because of non-uniformities in the applied electric field, cells or particles present a lateral movement toward or away from the electrodes under influence of the DEP force. It is important to confine the position of the cells while performing ER measurements, in order to stabilize the amplitude of the rotational torque. This increases the reliability of the collected data and eliminates the influence of non-uniformities of the electric field on the cells rotation. Different methodologies are suggested and developed for immobilizing cells including use of laser tweezers [73,92–96] and DEP-cages [93,96,97].

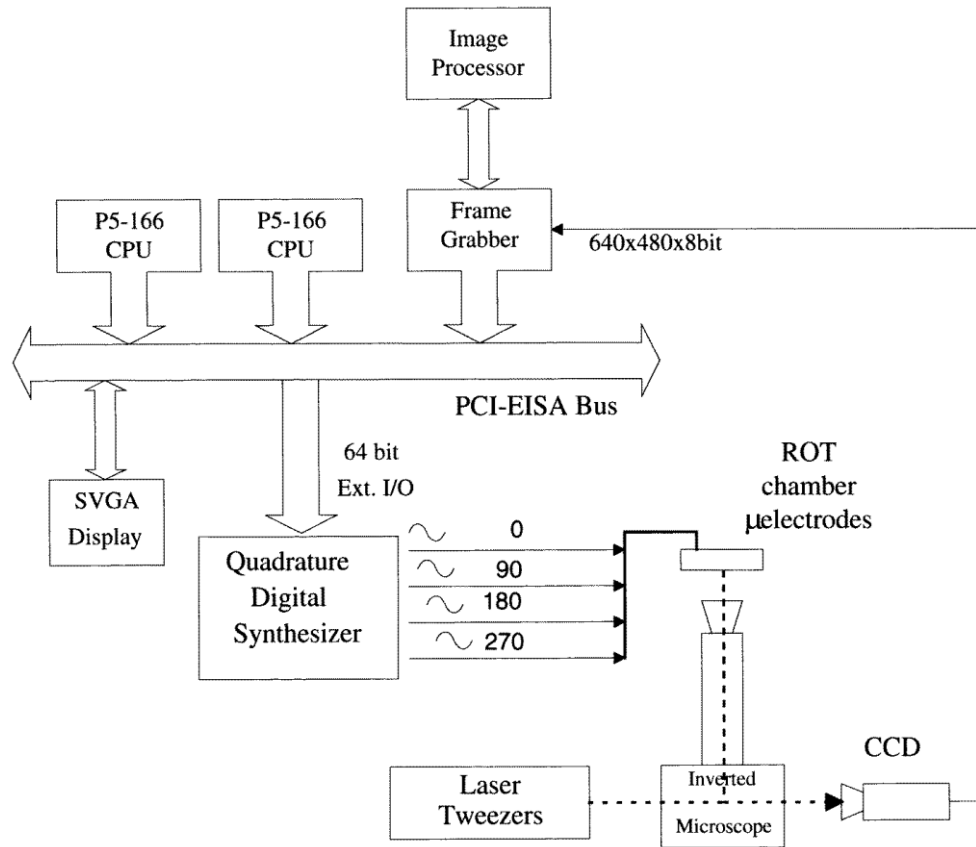


Figure 1. 19: Diagram of an experimental setup for automated ER measurements [88].

Among these methods DEP-cages are more appropriate for on chip purposes. Although use the laser tweezers is an approved method in controlling the position of the cells, it is not cost effective. In addition, due to installed external apparatus, it reduces the flexibilities of the ER systems. The most recent utilization of DEP-cage is presented in studies of Han et al. [70]. They have used simultaneous n-DEP with ER to perform the characterization. Figure 1.20 presents the schematic of the ER device, with eight 3D electrodes. They have used the proposed device in successful characterization of human leukocyte subpopulations. Although simultaneous use of n-DEP and electrorotation technique can increase the reliability of obtained data by eliminating the lateral movements of the cells due to p-DEP forces, it can alter the ER spectra of the cells due to simultaneously applied DEP signals. In other words, the cells are experiencing a combination of two sets of electrical signals and their responses to each signal vary from each other. Therefore, the recorded rotation

rates of the cells can be affected from the applied DEP signals. Table 1.1 summarizes the utilized methods in dielectric characterization of the different cell lines and biological particles.

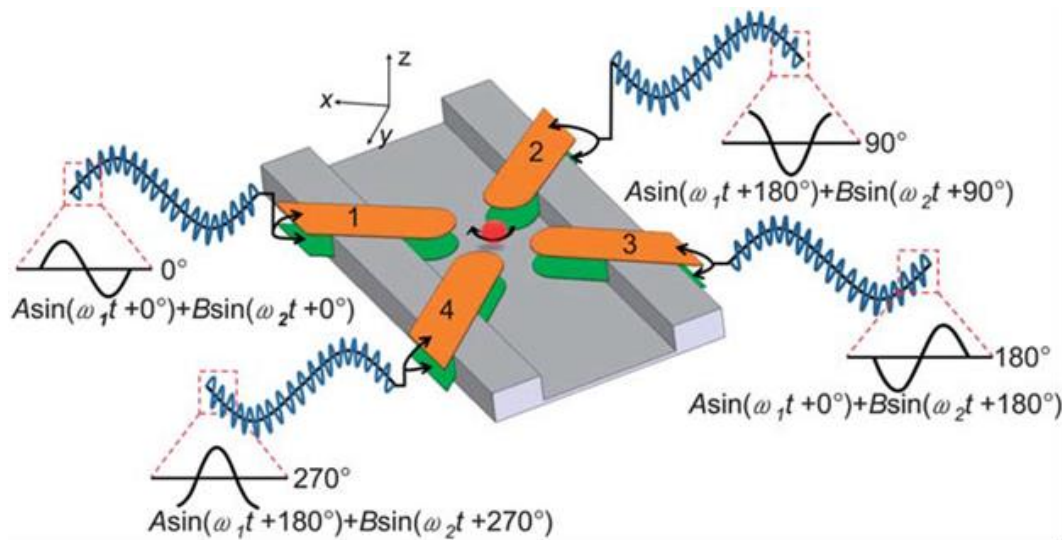


Figure 1. 20: The schematic of the ER devices, with eight electrodes. The DEP electrodes are utilized to trap the cells in the center of the device, using n-DEP force. Applied sinusoidal signal in phase quadrature through the ER electrodes is used to induce the rotational torque on the cells [70].

Table 1. 1: Literature survey of utilized methods in characterization of biologic particles.

Method	Studied Cell	Test condition	Sub-Method	Ref.
μ-EIS	HeLa cell	1-100 kHz	Micro-pillars	[37]
	HeLa cells	300kHz	Hydrodynamic	[38]
	Metastatic neck and head cancer	40-10 MHz	Negative-pressure	[35]
	Hela	1-100kHz	(ACET) and (n-DEP)	[34]
	L929 cell	1 Hz - 1MHz	Insulator well	[36]
IFC	Human erythrocytes and latex beads (5-8 μm)	100 kHz - 15 MHz	μ-CPC	[12]
	Polystyrene beads and RBCs	350 kHz- 20 MHz	-	[9]

Table 1. 1 (continued)

IFC	T-lymphocytes, monocytes and neutrophils	0.5-30MHz	FAC	[11]
	g-RBC, p-RBC, and u-RBC	10 kHz to 1 MHz	Liquid electrodes	[25]
	Mixture of three algae (Galbana, Rhodospirillum rubrum, Synechococcus sp.)	1 kHz - 100 MHz	FAC	[18]
DEP	Insulin secreting cells	48.7-101.4 mS/m	DEP crossover (Polynomial)	[5]
	RBCs	1 kHz -2 MHz	-	[98]
	Leukocyte subpopulations	10 kHz to 1 MHz	DEP crossover freq.	[57]
DEP	Sensitive and MDR K562 cells	2.5 mS/m	Collection rate (single shell)	[48]
	K562	10 kHz - 3 MHz	Collection rate & PI dye	[14]
	K562 and MDR (DOX) + MDR reversal agent	10kHz - 3MHz 2.5 mS/m	Collection rate & flow cytometry	[50]
	Polystyrene-carboxylate micro beads	-	DEP mobility	[54]
	Oral squamous cell carcinoma (OSCC) (H357) and human HPV-16 transformed keratinocyte cell line UP33	1 kHz- 16 MHz	DEP crossover and collection rate	[56]
	Mixed population of mammalian cells	500 Hz - 100kHz	Collection rate & image processing	[59]
	Yeast cells	1 kHz - 10 MHz	DEP collection rate & ER	[58]
	Latex beads	30 – 1000 kHz, 2 - 16 μ S/cm	-	[99]
	MDA231	10 kHz – 100 MHz	Single shell model	[83]
	Neurospora slime and the Myeloma Tib9 cell line	1 kHz -10 MHz, 3.6 - 35.5 mS/m	Single and three shell model	[82]

Table 1. 1 (continued)

ER	Human neutrophils upon activation with phorbol myristate acetate (PMA)	1 Hz -20 MHz	Double shell model	[74]
	Insulin secreting cells	10 kHz - 10 MHz, 11.5 - 101.4 mS/m	slope and intercept	[5]

1.5 Research Objectives and Thesis Organization

This thesis presents the design, fabrication, characterization, and implementation of ER devices with 3D electrodes for the dielectric characterization of biological cells. In addition, it presents design and fabrication of a DEP chip, for separation of cancer cells from the human leukocytes mixture.

The main objective of this thesis is the exact determination of the dielectric properties of the cancer cells and their MDR derivatives, for studying the feasibility of application of the DEP method in the separation of these cells. For this purpose, following studies are carried out:

Following steps presents, systematic approach in realizing ER device for dielectric characterization of cancer cells and their MDR counterparts:

- Study of the theory of the ER and classification of the ER methods to evaluate the feasibility of determining the exact dielectric properties of cells, using ER method.
- Development of the test procedure and designing the test setup.
- ER tests with the first generation of the ER chips (with planar pyramidal electrodes) and investigation of the ability to control the motion of the cells under ER phenomena. The initial tests were performed using yeast cells.
- Studying the accuracy and reproducibility of ER measurements on planar electrodes, and move toward 3D electrodes.
- 3D electrostatic analyses (COMSOL) of distribution of the electric field on the ER devices with 3D electrodes, followed with optimizations on the electrode geometries and other effective parameters.

- Design and fabrication of the 2nd generation of ER devices with 3D pyramidal electrodes. The fabrication of these devices was accomplished using four masks.
- Improvements in the test setup to eliminate the problems related to the alternating phase of the applied electrical signals in phase quadrature.
- Development of the methods to extract the dielectric properties of cells from their frequency dependent rotation rates.
- Test and experimental study of performance of the 3D ER electrodes.
- Design and fabrication of the 3rd generation of the ER devices with six different electrode geometries (3D electrodes).
- Torque characterization of the ER devices with different electrode geometries, to come up with the best electrode type for the ER tests.
- Improvements in the utilized equation for determination of the dielectric properties of the cells from their rotational spectra. Four different levels of approximation are utilized for calculating the dielectric properties of the cells.
- Development of an automated MATLAB algorithm for calculation of the dielectric properties of the cells using the obtained results from the ER experiments.
- Utilization of ER devices with 3D polynomial electrodes in dielectric characterization of following cells.
 - K562 human leukemia cells
 - Imatinib resistant K562 with three levels of resistance (0.2, 0.3, and 0.5 μM) to imatinib.
 - Doxorubicin resistant K562 with three levels of resistance (0.1, 0.3, and 0.5 μM) to doxorubicin.
 - MCF7 human breast cancer cells.
 - Doxorubicin resistant MCF7 with 1000 nM resistance.

Following steps are followed in the design and fabrication of the DEP devices with 3D contactless electrodes, which benefits from floating potential electrodes:

- Study of the theory of DEP and its various applications in cell separation.

- MATLAB simulations for determining the response of blood and cancer cells under the application of an AC electric field with varying frequency.
- Design and simulations of the DEP devices with potentially floating electrodes, for separation of cancer cells from leukocyte mixture. The COMSOL simulations show 100% efficiency in separation of cancerous cells using these devices.
- Initial tests with the DEP devices and successful separation of K562/IMA and K562/DOX under p-DEP and n-DEP.

The organization of the thesis is as follows:

Chapter 2 provides the necessary background theory and important equations governing the AC electrokinetics. Moreover, the electrical modeling of the biological cells is provided. Then the response of biological cells in AC electric fields is studied using an automated MATLAB algorithm.

Chapter 3 describes the utilized methods in relating the frequency dependent rotation rate of the cells to their structural dielectric composition. Then, using the equation of the effective complex permittivity of cell, different levels of approximations are introduced for dielectric characterization of biological cells. In this Section, the automated MATLAB program is presented. This program is used for calculation of dielectric properties of cell membrane and interior.

Chapter 4 presents the design and simulation of the different ER devices, utilized in this study. Then a comparison is made on the electrical characteristics of the planar electrodes (1st generation) and the 3D electrodes (2nd and 3rd generations). In addition to the FEM analyses, experimental studies of the rotational rate of the cells are performed.

Chapter 5 presents the utilized microfabrication techniques in the fabrication of the different generations of the ER devices.

Chapter 6 presents the dielectric characterization of the cancer cells using the 3rd generation of the ER devices. The dielectric properties of 9 cell lines were determined using the ER technique. These cells are K562 human leukemia cells

and its multidrug resistance (MDR) counterparts, including the imatinib resistant (K562/IMA-0.2, 0.3, 0.5 μM) and doxorubicin resistant cells (K562/DOX-0.1, 0.3, and 0.5 μM). In addition, the dielectric properties of the human breast cancer cells (MCF7) and its doxorubicin resistant (MCF7/DOX-1000 nM) derivation were measured using this technique.

Chapter 7 presents the design, simulation, and the fabrication of MEMS based dielectrophoresis (DEP) device for separation of the K562 human leukemia cancer cells and its multidrug resistance (MDR) counterparts from the human leukocytes mixture.

Finally, in chapter 8, thesis conclusion discussing the accomplished tasks in this study and possible future works are presented.

CHAPTER 2

THEORY

The rotation of the dielectric particles is generally described by the dipole moment theory. By using this method, one can formulize the rotational torque expression for spherical particles inside an AC electric field. For this purpose, exact knowledge of the dipole formation and the mechanism related to the torque generation is essential.

2.1 Dipole Formation

The starting point to describe the rotational motion of particles under an AC electric field is to comprehend the mechanism of dipole formation. The induced dipole on a particle, placed in an AC electric field, consists of equal but opposite distribution of $+q$ and $-q$ charges in the cell membrane or interior layers (Fig. 2.1).

Under a non-uniform distribution of the electric field, two charges will experience different forces. If the dipole size is small enough to satisfy the following assumption, $|\bar{d}| \rightarrow 0$ then the well-known expression for the dipole force is obtained:

$$\bar{F}_{dipole} = \bar{p} \cdot \nabla \bar{E} \quad (1)$$

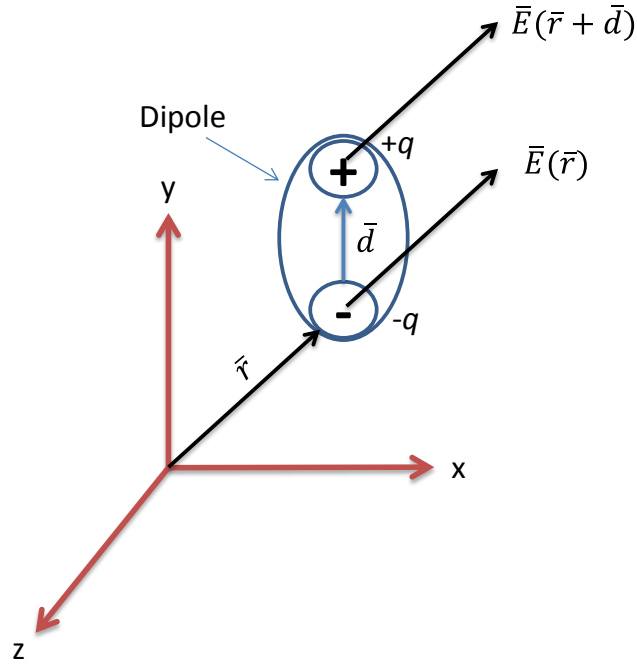


Figure 2. 1: Representation of the dipole formation upon application of an electric field on the particle.

It can be inferred from Eq. 1 that the dipole force is exerted on the particle only if the external field has a non-uniform distribution ($\nabla \bar{E} \neq 0$). The above equation is an approximation of the force exerted on a physical particle, known as the dielectrophoretic approximation. This approximation is generally satisfied in the practical application, due to the larger size of the electrodes compared to biological particles. In other words, above expression is valid if the size of the non-uniformities of the electric field is larger than the particle size.

2.2 Applied Effective Moment on the Dipole

Consider a homogenous particle of radius R with the permittivity and the conductivity of ϵ_p and σ_p , respectively. The particle is immersed in a liquid medium with the permittivity, conductivity, and the dynamic viscosity of ϵ_m , σ_m , and η , respectively. If the external electric field $\bar{E}(t)$, is introduced as:

$$\bar{E}(t) = E_0(\cos \omega t a_x + \sin \omega t a_y) \quad (2)$$

where, a_x and a_y are the unit vectors along the x and y axis, the particle presents a circular rotating behavior. We could rewrite the Eq. 2 based on the phasor expression as below:

$$\bar{E}(t) = E_0(a_x - j a_y) \quad (3)$$

The generated electrostatic potential Φ_{dipole} due to the presence of the dipole with the effective moment of \bar{p}_{eff} inside the medium, is described as [100]:

$$\Phi_{dipole} = \frac{p_{eff} \cos \theta}{4\pi \varepsilon_m R^2} \quad (4)$$

where, R and θ are the angle and the radial distance from the origin in the polar-coordinates, respectively. For the case of spherical dielectric particles, the effective dipole moment can be described by below expression:

$$p_{eff} = 4\pi K R^3 E_0 \quad (5)$$

K is the Clausius-Mossotti factor (F_{CM}) and represents the polarizability of the particle compared to the suspension medium. In other words, F_{CM} describes the frequency dependent response of a polarizable particle in interaction with an AC electric field. This factor depends on the dielectric properties of the particle and the medium and the frequency of the electric field. The F_{CM} can be calculated using below expression for the spherical lossless dielectric particles:

$$F_{CM} = \frac{\varepsilon_p - \varepsilon_m}{\varepsilon_p + 2\varepsilon_m} \quad (6)$$

However, above equation generally does not describe the polarizability of the biological particles. Biological particles are categorized under the dielectric particles with loss in an AC electric field. There are many dissipation mechanism and relaxation phenomena correlated with the frequency of the electric field, which determine the behavior of the biological particles. Therefore, the effective conductivity and permittivity of the biological particles depend on the frequency of the applied AC electric field. For these particles, the dipole moment changes to the complex effective dipole moment, therefore the Clausius-Mossotti factor becomes a

function of the complex permittivities of the particle and the medium. Hence, the general form of the Clausius-Mossotti factor should be employed to interpret the behavior of the dielectric particles with ohmic or dielectric loss in an AC electric field (Eq. 7).

$$F_{CM}(\omega) = \frac{\varepsilon_p^* - \varepsilon_{med}^*}{\varepsilon_p^* + 2\varepsilon_{med}^*} \quad (7)$$

where, ε_p^* and ε_{med}^* are the complex permittivity of the particle and the medium, respectively. It is important to note that, Eq. 7 changes to the general expression of behavior of a dielectric particle by substituting the expressions of complex permittivity of the particle and the cells, which are shown as below:

$$\varepsilon_p^* = \varepsilon_p - j \frac{\sigma_p}{\omega} \quad (8a)$$

$$\varepsilon_m^* = \varepsilon_m - j \frac{\sigma_m}{\omega} \quad (8b)$$

Equations 8a and 8b reveal the dependence of the dielectric properties of the cell on the frequency of the electric field (ω). When a dielectric particle is placed in an AC electric field, depending on the frequency of the electric field and the permittivity and conductivity of the particle and the medium, varying moments are induced on the particle. In addition, different dissipation levels and relaxation mechanisms are dominant in each frequency range, which assess the behavior of the dielectric particle. In order to emphasize on these mechanisms we can rewrite the Eq. 7 by substituting Eq. 8a and b:

$$F_{CM}(\omega) = \frac{\sigma_p - \sigma_m}{\sigma_p + 2\sigma_m} \cdot \frac{j\omega\tau_0 + 1}{j\omega\tau_{MW} + 1} \quad (9)$$

where,

$$\tau_{MW} = \frac{\varepsilon_p + 2\varepsilon_m}{\sigma_p + 2\sigma_m} \quad (10a)$$

$$\tau_0 = \frac{\varepsilon_p - \varepsilon_m}{\sigma_p - \sigma_m}. \quad (10b)$$

In the above equation, τ_{MW} is the characteristic relaxation time constant and is a simple explanation of the Maxwell-Wagner interfacial polarization theory, and τ_0 is the charge relaxation time constant. Low or high frequency behavior of the cells under application of an AC electric field with angular frequency of ω can be studied at $\omega \rightarrow 0$ or $\omega \rightarrow \infty$, respectively.

In the low frequency or DC limit approximations, the conductivities of the particle and the medium are the determinant elements of the Clausius-Mossotti factor. However, in the high frequency range, the permittivities of the particle and the medium have the dominant role on the Clausius-Mossotti factor.

$$\lim_{\omega \rightarrow 0} [F_{CM}(\omega)] = \frac{\sigma_p - \sigma_m}{\sigma_p + 2\sigma_m} \quad (11a)$$

$$\lim_{\omega \rightarrow \infty} [F_{CM}(\omega)] = \frac{\varepsilon_p - \varepsilon_m}{\varepsilon_p + 2\varepsilon_m} \quad (11b)$$

2.3 Electrorotation

The rotational torque exerted on a dielectric particle under application of a uniformly rotating AC electric field can be expressed based on the effective dipole moment expression (Eq. 5). The time dependent torque applied to the particle can be expressed using below equation:

$$\bar{T}(t) = \bar{p}_{eff}(t) \times \bar{E}(t) \quad (12)$$

The above equation consists two sections, a time-averaged term with a constant magnitude and a time-varying term with a frequency equal to the twice of the frequency of the applied electric field. Jones et al. has stated that, for the particles with sizes in the range of 1-1000 μm , the motions induced by the time-varying component of the electric field is extremely damped by the viscosity of the medium [60,100]. Therefore, only the time-averaged component can play a significant role in the rotation of the particle. The time averaged rotational torque exerted on a particle is expressed using below equation:

$$\langle \bar{T}(t) \rangle = -4\pi\varepsilon_m R^3 \text{Im}(F_{CM}(\omega)) E_0^2 \quad (13)$$

In the above equation, the dependence of the rotational torque on the applied frequency is determined by the imaginary part of the Clausius-Mossotti factor. A more general case is to consider a homogenous dielectric particle with ohmic loss rotating in a conductive medium. If the medium is subjected to a uniformly rotating AC electric field, the induced rotational torque on the particle can be determined using below expression:

$$\bar{T} = \frac{6\pi\varepsilon_m R^3 E_0^2 (1 - \tau_1/\tau_2) \omega \tau_{MW}}{\left(1 + 2 \frac{\varepsilon_m}{\varepsilon_p}\right) \left(1 + \frac{\sigma_m}{2\sigma_p}\right) [1 + (\tau_{MW})^2]} \quad (14)$$

In the above equation, τ_1 and τ_2 are the charge relaxation time constants of the medium and the particle, respectively. In practical applications, the rotation of the cells is the result of the force balance between the rotational torque and the viscous damping acting on the particle. In the steady-state condition, there will be equilibrium between the rotational torque and the damping forces in the medium. Generally ER is applied to the particles with radii of less than 250 μm ; therefore the laminar viscous torque formula can be used, which is:

$$T_{damp} = -8\pi\eta R^3 \Omega \quad (15)$$

where, Ω is the angular velocity of the particle. By imposing the equilibrium condition of $\bar{T} + T_{damp} = 0$, the generally used expression for the rotation speed of the cell under ER phenomena can be obtained as below:

$$\Omega = -\frac{\varepsilon_m \text{Im}(F_{CM}) E_0^2}{2\eta} \quad (16)$$

By substituting the Eq. 9 in the above equation, the full expression of the rotation speed of a particle in relation to the dielectric properties of the medium and the particle can be presented as below:

$$\Omega = -\frac{3\varepsilon_m \sigma_m \sigma_p (\tau_2 - \tau_1) E_0^2}{2\eta (\sigma_p + 2\sigma_m) (\varepsilon_p + 2\varepsilon_m)} \left[\frac{\omega \tau_{MW}}{(\omega \tau_{MW})^2 + 1} \right]. \quad (17)$$

According to the above equation, the ER spectrum of a multi-layered particle consist a set of positive and negative rotation peaks. The ER spectrums of the

protoplast cells generally consist of two peak rotation frequencies. The positions of the peaks depend on the dielectric properties of the cells and the medium, and are specified by the characteristic relaxation time constant.

2.4 Cell Modeling

2.4.1 Theory

Cells are the most basic functional units of the complex biological systems. In addition, the molecular composition of the cell membrane and the interior are subject to complex regulation mechanisms, which help cells to adjust their living conditions. Cells are composed of different layers including cell membrane, cytoplasm, nucleus and many other sub-cellular structures (Fig. 2. 2). Modeling of the complex structure of the cells with its equivalent electric models needs a deep knowledge in the physics of each layer. Different approaches are used in the modeling of the biological cells with its equivalent electrical circuits (Fig. 2. 3).

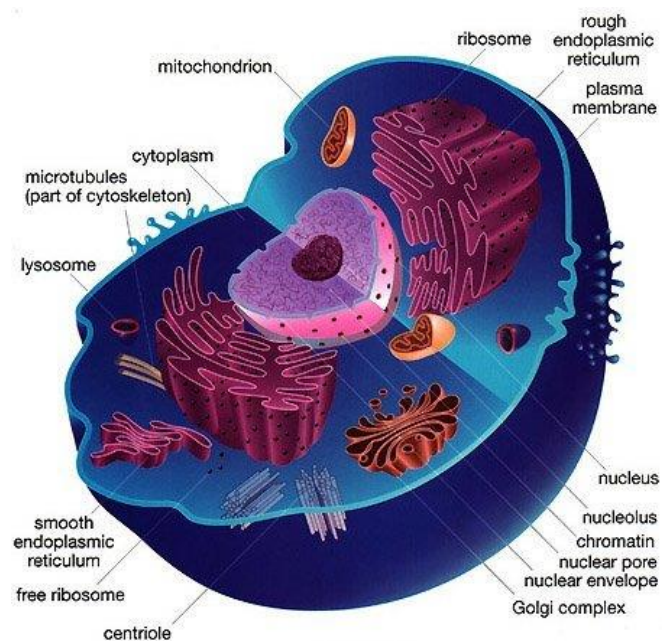


Figure 2. 2: Interior structures of a single cell.

(Figure from www.slideshare.net)

A more general approach is the use of multi-shell model of the cells [101]. In this method, each layer of the cell is replaced by its equivalent electrical element and each layer of the cell is assumed to be positioned concentrically.

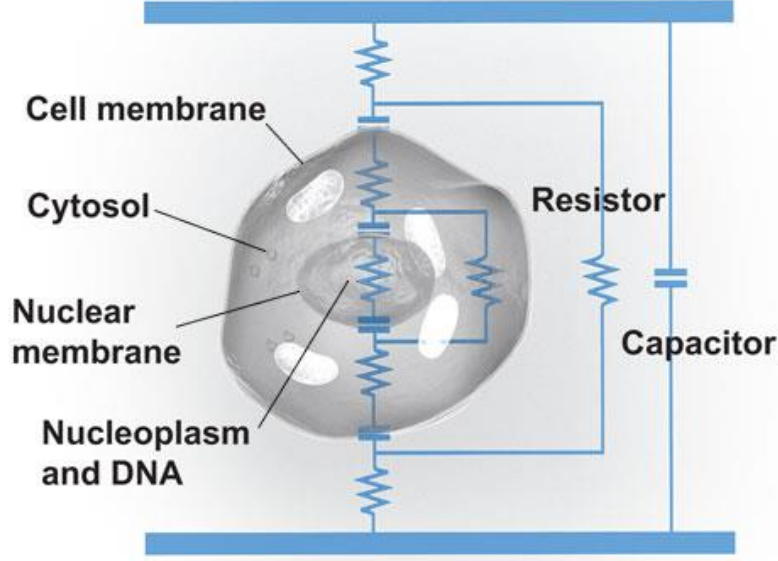


Figure 2. 3: Equivalent electrical model of a single cell.

(Figure from www.biotele.com)

In the single-shell cell model, the cell is modeled as a cell interior, consisting of cytoplasm and nucleus, and a resistive cell membrane. For a cell with radius R and membrane thickness of δ the equivalent complex permittivity of the cell is described by below expression:

$$\tilde{\varepsilon}_p^* = \tilde{\varepsilon}_p + j\tilde{\sigma}_p = \varepsilon_{mem}^* \left[\frac{(R/(R - \delta))^3 + 2(\varepsilon_i^* - \varepsilon_{mem}^*)/(\varepsilon_i^* + 2\varepsilon_{mem}^*)}{(R/(R - \delta))^3 - (\varepsilon_i^* - \varepsilon_{mem}^*)/(\varepsilon_i^* + 2\varepsilon_{mem}^*)} \right] \quad (18)$$

where, ε_{mem}^* and ε_i^* are the complex permittivities of the cell membrane and the cell interior, respectively. In addition, $\tilde{\varepsilon}_p$ and $\tilde{\sigma}_p$ represent the effective permittivity and conductivity of the particle. For the mammalian cells, the membrane thickness is at least three orders smaller than the cell radius, therefore the $R - \delta$ term can be replaced with radius of the cell with a high degree of confidence in the above equation. For studying the frequency response of a cell, which is modeled using the single-shell model and exposed to an AC electric field, the expression of the effective complex permittivity of the cell is replaced with the complex permittivity of the cell in Eq. 7.

In addition to single shell modeling, double or triple shell modeling are possible (Fig. 2.4). For this purpose, the Eq. 18 should be consecutively applied to the

internal layers of a cell aiming to obtain the equivalent dielectric properties of each cell layer. Generally, this method is applied to the cells with more complex interior structure or for the cells with larger nucleus that can influence the dielectric properties of the whole cell. For this purpose, the Eq.18 should be applied to the most inner layers of the cell. For a double shell modeling, below procedure should be followed:

1. $\epsilon_{mem}^* \rightarrow \epsilon_2^*$ and $\epsilon_i^* \rightarrow \epsilon_1^*$ \rightarrow 1 effective
2. $\epsilon_{mem}^* \rightarrow \epsilon_3^*$ and $\epsilon_i^* \rightarrow \epsilon_{1eff}^*$ \rightarrow 2 effective

Above method can be applied for extracting the higher order shell models of the particles.

An example of application of the double-shell model is used in modeling of the yeast cells [4] and neutrophils [5]. In the below section, use of double shell modeling will be presented for the neutrophil.

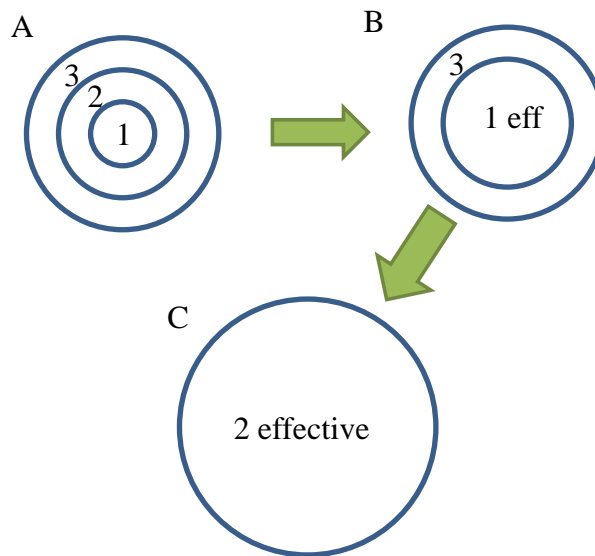


Figure 2. 4: Multilayer shell approach for determining the effective permittivity of the double-shell model. (A) A cell with 3 layers. (B) Determination of effective permittivity of the layers 1 and 2. (C) Determination of effective permittivity of the layers 1-effective and 3.

2.4.2 DEP and ER Spectra of Neutrophils

Neutrophils are the most abundant subpopulation of the human leukocytes, constituting up to 60% of the total leukocyte population. These cells have a segmented nucleus which is divided into several parts (Fig. 2. 5). Because of the large nucleus size, use of single-shell model can lead to misinterpretation of dielectric properties of the cell. Therefore, the double-shell cell model is used in study of the dielectric response of neutrophils.

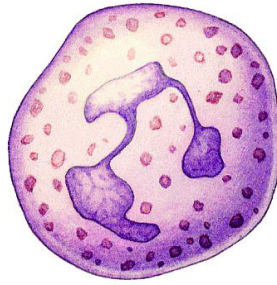


Figure 2. 5: A single neutrophil with segmented cell nucleus.

The dielectric properties of each layer of the neutrophils are presented below in Table 3.1 [74].

Table 2. 1: Dielectric properties of neutrophils.

cell radius (μm)	6
cell membrane thickness (nm)	8
nucleus radius (μm)	3.5
nuclear membrane thickness (nm)	20
medium conductivity (mS/cm)	0.4
medium permittivity	$79\epsilon_0$
cell membrane conductivity (mS/cm)	$10\text{e-}11$
cell membrane permittivity	$6.2 \epsilon_0$
cytoplasm conductivity (mS/cm)	3
cytoplasm permittivity	$60 \epsilon_0$
nucleoplasm conductivity (mS/cm)	13.5
nucleoplasm permittivity	$52 \epsilon_0$

For the double-shell modeling of the neutrophils, an automated MATLAB program with implemented double-shell equations is utilized. This program uses the dielectric properties of each layer of the neutrophils as the inputs and plots the imaginary and real part of the Clausius-Mossotti factor as the output. In addition to the dielectric properties of the cells, the dielectric properties of the medium can be adjusted. The plotted output shows the frequency response of the cell in the frequency band of 1 Hz to 1 GHz. The MATLAB code is presented in Appendix A.

The designed graphical user interface (GUI) of the MATLAB algorithm is shown in Fig. 2.6. For determination of the imaginary and real part of the F_{CM} the dielectric properties of the neutrophils are inserted as the inputs of the program. The conductivity and relative permittivity of the medium is assumed as 1 mS/m and 78, respectively. The plotted F_{CM} for the neutrophils is shown in Fig. 2.7. The imaginary and real part of the F_{CM} is plotted using green and red lines, respectively. Because of using the double-shell layer, two peak rotation frequencies are obtained for the cell, representing the relaxation constant of the cell membrane and the cell interior.

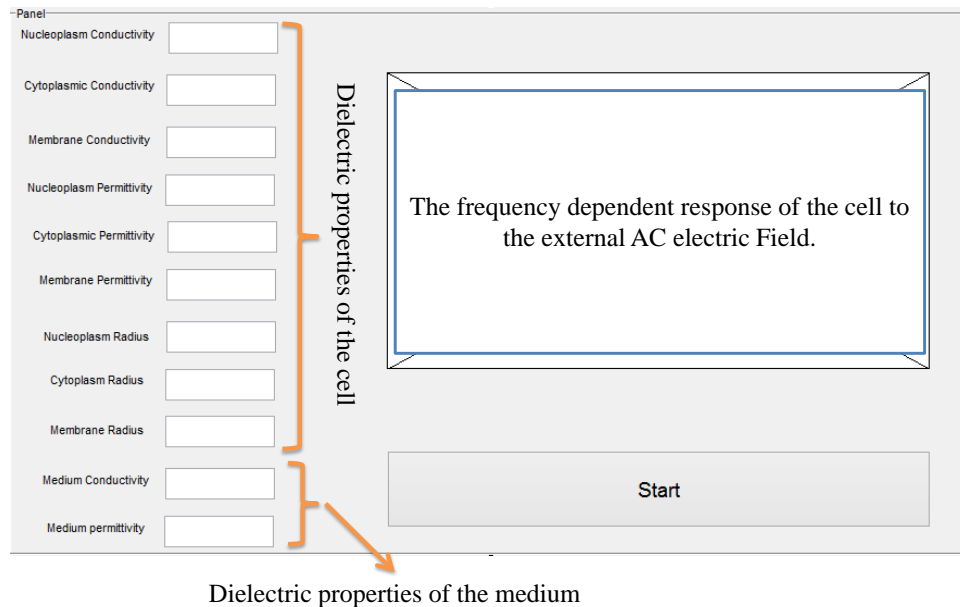


Figure 2. 6: The graphical user interface of the implemented MATLAB algorithm for calculating the frequency dependent response of cells inside an AC electric field.

Accordingly, two crossover frequencies are obtained for the real part of F_{CM} . The real part of the F_{CM} represents the DEP response of a cell under a non-uniform AC electric field. However, the imaginary part of the F_{CM} shows the rotational response (ER) of a cell under application of a uniformly rotating AC electric field. As shown in Eq. 9, in addition to the dielectric properties of the cell, the F_{CM} depends on the dielectric properties of the medium. In order to better show this fact, the F_{CM} is depicted for the neutrophils in three media with varying conductivities.

Figure 2.8 shows the F_{CM} factor in media with conductivities of 1, 5, and 10 mS/m. It can be inferred that, with the increase of the conductivity of the medium, the peak rotation and DEP crossover frequencies of the cell shift to higher frequencies. In addition, with increase in the conductivity of the medium, the magnitude of the peak rotation frequencies decreases. The same trend can be seen for the maximum values of the real part of the Clausius-Mossotti factor (DEP response).

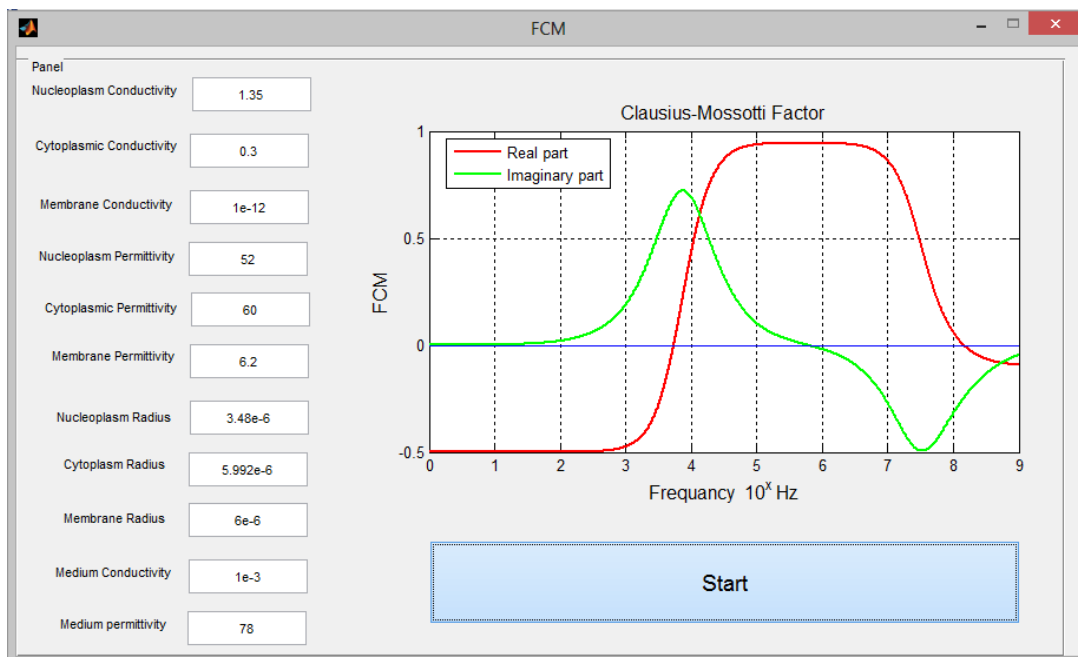


Figure 2. 7: Double-shell modeling of imaginary and real part of F_{CM} for the neutrophils.

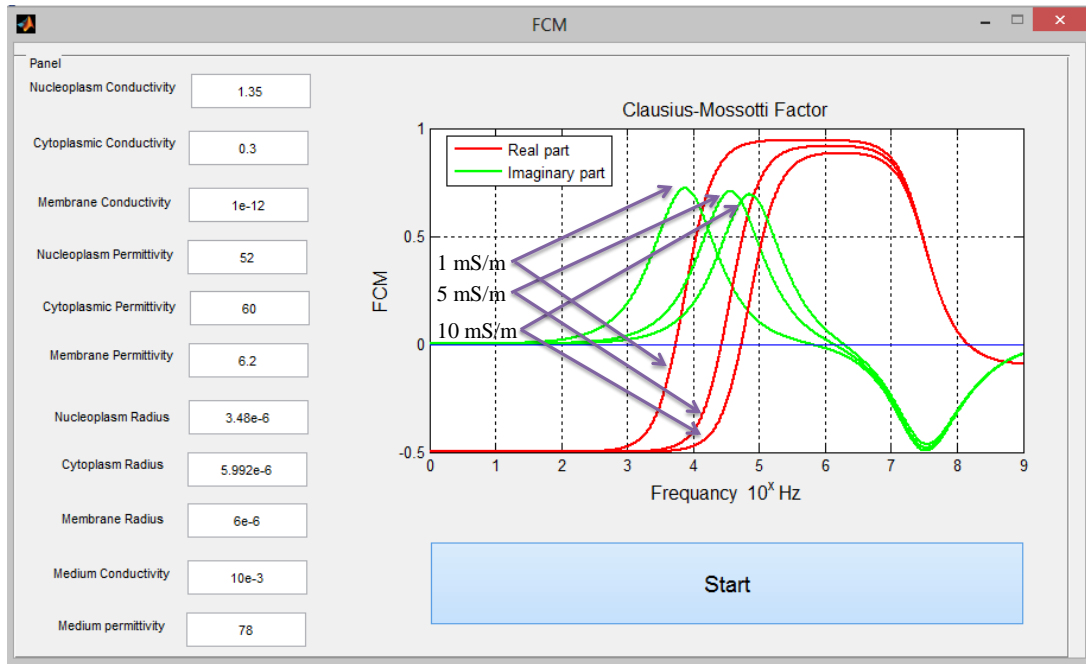


Figure 2. 8: Imaginary and real part of F_{CM} inside three media with different conductivities.

CHAPTER 3

DIELECTRIC CHARACTERIZATION

This section describes the use of the ER method in determination of the dielectric properties of the biological cells. The current ER theory is based on the use of low-frequency peak rotational frequency for the dielectric characterization of the biological cells. The method uses the equation of the effective complex permittivity of the cells, and applies different approximations to estimate the dielectric properties of the cells. Lei et al [6] has investigated the previously used theory and methods of ER dielectric characterization and has categorized the equations by applying limitation on the applied frequency range and the medium conductivities. Due to nonlinearity of the Eq. 18, the conventional analytical methods are not applicable to extract the dielectric properties of the cells. Therefore, different methods were used to simplify the equation by applying different limitations on the measured peak rotation frequency or the conductivity of the medium. Therefore, simplified equations can realize the determination of the dielectric properties of the cells by studying the frequency dependent ER response of the biological cells.

For a specific cell line, with known dielectric properties, the frequency dependent ER response of a cell can be obtained by plotting the imaginary part of the Clausius-Mossotti factor (Eq. 19). This plot shows the peak rotation frequencies of the cell, which are the maxima points of the $F_{CMimag}(\omega)$.

$$F_{CM}(\omega) = F_{CMreal}(\omega) + jF_{CMimag}(\omega) = \frac{\varepsilon_p^* - \varepsilon_{med}^*}{\varepsilon_p^* + 2\varepsilon_{med}^*} \quad (19)$$

At coming sections, four different levels of approximation, applied to the equation of the effective complex permittivity of the cell, will be presented. Then the proposed methods of extracting the dielectric properties of the cells will be discussed. In all of these methods, the dielectric properties of the cell membrane are determined using the slope and intercept method. Therefore, as the starting step, the slope and intercept method is introduced in Section 3.1. Then, in Sections 3.2 through 3.5, different levels of approximations are investigated. In Section 3.6, an automated MATLAB program for extracting the dielectric properties of the cells will be introduced. Introduced methods in Sections 3.1 through 3.5 are implemented in this MATLAB program. Finally, an example of utilization of this program in the calculation of the dielectric properties of K562 human leukemia cells is presented.

3.1 The Slope and Intercept Method

This method is used in the determination of the effective membrane capacitance (C_{mem}) and effective membrane conductance (G_{mem}^*) of cells. In this method, the peak rotation frequencies of the cells are studied in the media with varying conductivities. Subsequent to the determination of the peak rotation frequency, a straight line is fitted to the data points of the peak rotation frequencies multiplied by the cell radius ($f_{pk} \times R$) versus the conductivity of the media (σ_m) in which the cells are suspended.

According to the low frequency approximations, the slope and the intercept of the fitted line are proportional to the effective membrane capacitance and the effective membrane conductance, respectively.

According to the presented discussion in Section 2.2, the characteristic relaxation time constant (τ_{MW}) provides the positions of the peak rotation frequencies. Equation 20 shows the relation between the τ_{MW} and the peak rotation frequency (f_{pk}).

$$1/\tau_{MW} = 2\pi f_{pk} = \frac{\tilde{\sigma}_p + 2\sigma_m}{\tilde{\epsilon}_p + 2\epsilon_m} \quad (20)$$

Above equation relates the peak rotation frequency to the dielectric properties of the cells. Rewriting the equation for conductivity of the medium results in below equation:

$$\sigma_m = \frac{1}{2} \{2\pi f_{pk}(\tilde{\epsilon}_p + 2\epsilon_m) - \tilde{\sigma}_p\} \quad (21)$$

For the low frequency (DC limit), the effective permittivity and conductivity of the cells are approximated using below equation [102,103]:

$$\tilde{\epsilon}_p = \widetilde{\epsilon_{pDC}} = \epsilon_{mem} \left(\frac{R}{\delta} \right) = RC_{mem} \quad (22a)$$

$$\tilde{\sigma}_p = \widetilde{\sigma_{pDC}} = \sigma_{mem} \left(\frac{R}{\delta} \right) = RG_{mem} \quad (22b)$$

where, C_{mem} and G_{mem} represents the effective membrane capacitance and the membrane conductance of the cell, respectively. ϵ_{mem} and σ_{mem} are the permittivity and conductivity of the cell membrane, respectively. By substituting Eq. 22a and 22b in Eq. 21 and performing some mathematical operations, below equation is obtained:

$$Rf_{PK} = \frac{\sigma_m}{\pi C_{mem}} + \frac{G_{mem}R}{2\pi C_{mem}}. \quad (23)$$

This equation interprets the relation between the dielectric properties of the cell membrane and the parameters related to the ER measurements. Equation 23 is an expression of a straight line ($y = mx + c$) with the slope (m) and the intercept (c) as defined in Eq. 24. It is important to note that the permittivity of the medium is assumed to be negligible compared to the effective permittivity of the cell ($\tilde{\epsilon}_p \gg \epsilon_m$).

$$m = \frac{1}{\pi C_{mem}} \quad (24a)$$

$$c = \frac{G_{mem}R}{2\pi C_{mem}}. \quad (24b)$$

By fitting the obtained data from the ER experiment to the expression of the straight line, the slope of the line relates the conductivity of the medium to the effective membrane capacitance of the cell. In addition, the intercept point of the fitted line reveals the conductance of the cell membrane (Eq. 24). In the above equation, G_{mem} is replaced with total effective conductance, which includes both transmembrane conductance and the surface conductance of the cell (K_{ms}) (Eq. 25a & 25b). [51]

$$c = \frac{G_{mem}^* R}{2\pi C_{mem}} = \frac{1}{\pi C_{mem}} \left(\frac{G_{mem} R}{2} + \frac{K_{ms}}{R} \right) = \frac{R}{2\pi C_{mem}} \left(G_{mem} + \frac{2K_{ms}}{R^2} \right) \quad (25a)$$

$$G_{mem}^* = G_{mem} + \frac{2K_{ms}}{R^2} \quad (25b)$$

3.2 First Level Approximations

This method uses the slope and intercept method for determining the dielectric properties of the cell membrane, including the effective transmembrane capacitance (C_{mem}) and the effective membrane conductance (G_{mem}^*).

In order to calculate the interior conductivity of the cell, a group of approximations should be applied to the expression of the effective complex permittivity of the cells. These approximations are listed as below:

- The first peak rotation frequency of the cell should be below 0.1 MHz ($\omega_{pk} \leq 0.1 \text{ MHz}$).
- The conductivity of the test media should be below 1 mS/m ($\sigma_m \leq 1 \text{ mS/m}$).
- The permittivity of the medium should be negligible compared to the effective permittivity of the cell ($\tilde{\epsilon}_p \gg \epsilon_m$).
- The cell radius is three orders of magnitude larger than the membrane thickness ($R/\delta \approx 10^3$).
- $\epsilon_{mem}/\epsilon_0 \approx 10$, $\sigma_{mem} \approx 10^{-6} \text{ S/m}$, and $\epsilon_{int}/\epsilon_0 \approx 100$.

If all above mentioned conditions are satisfied by the cell structure and the test conditions, the effective complex permittivity of the cell can be simplified and the effective permittivity and conductivity of the cell can be approximated as below:

$$\tilde{\epsilon}_p = \frac{\frac{\sigma_{int}^2}{\omega^2 \epsilon_0^2} \left(\frac{\epsilon_{mem}}{\epsilon_0} \right) \left(\frac{\delta}{R} \right)}{\frac{\sigma_{int}^2}{\omega^2 \epsilon_0^2} \left(\frac{\delta}{R} \right)^2} \approx \epsilon_m \left(\frac{R}{\delta} \right) \quad (26a)$$

$$\tilde{\sigma}_p = \sigma_{mem} \left(\frac{R}{\delta} \right). \quad (26b)$$

By substituting Eq. 26 in Eq. 20, below equation is obtained for the membrane and the interior properties of the cell, based on the properties of the suspension medium and the peak rotation frequency:

$$y_{pk} = G_{mem}^* R + \frac{y_{pk}^2}{\sigma_{int}} + 2\sigma_m \quad (27a)$$

where,

$$y_{pk} = \omega_{pk} \epsilon_{mem} \frac{R}{\delta} = 2\pi C_m R f_{pk}. \quad (27b)$$

Equation 27b is a quadratic equation, which naturally has two roots. The acceptable answer for the interior conductivity of the biological cells, are as below:

$$y_{pk} = 2\pi C_{mem} R f_{pk} = \frac{\sigma_{int}}{2} \left\{ 1 - \sqrt{1 - \frac{4}{\sigma_{int}} (2\sigma_m + G_{mem}^* R)} \right\} \quad (28)$$

In the above equation, f_{pk} and σ_m are the known parameters from the ER measurements, C_{mem} and G_{mem}^* are calculated using the slope and intercept method, therefore the only unknown parameter is the cell interior conductivity (σ_{int}). The cell interior conductivity can be obtained by solving Eq. 28 using hand calculations or in MATLAB.

3.3 Second Level Approximations

In the second level of the approximations, the slope and intercept method is utilized for determining the dielectric properties of the cell membrane. In order to reduce

the applied limitations on Eq. 18, Eq. 20 and 21 are used as the beginning step. In the first level approximations, we have assumed that the permittivity of the medium is negligible compared to the effective permittivity of the cell. However, depending on the cell type, this assumption can lead to errors in the calculated properties of the cell. Therefore, in the second level approximations, we will include the effect of permittivity of the medium in the calculations.

Below is a list of assumptions made in second level approximations:

- The first peak rotation frequency of the cell should be below 0.3 MHz ($\omega_{pk} \leq 0.3 \text{ MHz}$).
- The conductivity of the media should be below 10 mS/m ($\sigma_m \leq 10 \text{ mS/m}$).
- The cell radius is three orders of magnitude larger than the membrane thickness ($R/\delta \approx 10^3$).
- $\epsilon_{mem}/\epsilon_0 \approx 10$, $\sigma_{mem} \approx 10^{-6} \text{ S/m}$, and $\epsilon_{int}/\epsilon_0 \approx 100$.

By applying these assumptions to the Eq. 18, the effective conductivity and permittivity of the cell is obtained as below:

$$\tilde{\sigma}_2 = \frac{\left(\frac{\epsilon_{mem}}{\epsilon_0}\right)^2 \sigma_{int} + \frac{\sigma_{mem} \sigma_{int}^2}{\omega^2 \epsilon_0^2} \left(\frac{\delta}{R}\right)}{\frac{\sigma_{int}^2}{\omega^2 \epsilon_0^2} \left(\frac{\delta}{R}\right)^2} = \frac{\epsilon_{mem}^2 \omega^2}{\sigma_{int}} \left(\frac{R}{\delta}\right) + \sigma_{mem} \left(\frac{R}{\delta}\right) \quad (29a)$$

$$\tilde{\epsilon}_p = \frac{\frac{\sigma_{int}^2}{\omega^2 \epsilon_0^2} \left(\frac{\epsilon_{mem}}{\epsilon_0}\right) \left(\frac{\delta}{R}\right)}{\frac{\sigma_{int}^2}{\omega^2 \epsilon_0^2} \left(\frac{\delta}{R}\right)^2} \approx \epsilon_{mem} \left(\frac{R}{\delta}\right). \quad (29b)$$

It is important to note that, in this level, the maximum acceptable frequency for the peak rotation frequency is increased to 0.3 MHz. By substituting Eq. 29 into Eq. 21 below equation is obtained:

$$y_{pk} + 4\pi f_{pk} \epsilon_m = \frac{y_{pk}^2}{\sigma_{int}} + G_{mem}^* R + 2\sigma_m. \quad (30)$$

This equation relates the dielectric properties of the cell membrane and the interior to the measured peak rotation frequency and the conductivity of the medium. By

substituting Eq. 27b in the above equation, a quadratic equation is obtained. The parameters of this equation are as below:

- G_{mem}^* is calculated using the slope and intercept method.
- C_m is calculated using the slope and intercept method.
- f_{pk} is measured using the ER experiments, in media with varying conductivities.
- R and δ are known for the tested particle.
- σ_m is known from each ER experiment.

Therefore, the only unknown parameter is the interior conductivity of the cell (σ_{int}). By solving this quadratic equation, below answer is obtained for the interior conductivity of the cell.

$$\sigma_i = \frac{(2\pi f_{pk} C_m R)^2}{2\pi f_{pk} C_m R + 4\pi f_{pk} \varepsilon_m - G_{mem}^* R - 2\sigma_m}. \quad (31)$$

In this level, the accuracy of the calculations is increased by widening the acceptable conductivity of the medium (from 1mS/m to 10 mS/m), obtained peak rotation frequency (from 0.1 MHz to 0.3 MHz), and by entering the permittivity of the medium to the calculations. Increasing the applicable range for the conductivity of the test medium can increase the accuracy of the measurement by eliminating the probability of the ion transfer between the cell and the medium.

3.4 Third Level Approximations

In the third level approximations, the dielectric properties of the cell membrane is calculated using the slope and intercept method. Same as the second level, Eq. 20 and 21 are used as the starting steps. In addition, the applied limitations on the conductivity of the medium and the peak rotation frequency are reduced. Although this method increases the accuracy of the calculated dielectric properties of the cell interior, it adds to the complexity of the equations. In this level, the applicable range for the conductivity of the test media is increased to 100 mS/m, and obtained peak rotation frequencies up to 1 MHz are acceptable. A list of applied assumptions is presented in below:

- The first peak rotation frequency of the cell should be below 1 MHz ($\omega_{pk} \leq 1 \text{ MHz}$).
- The conductivity of the media should be below 100 mS/m ($\sigma_m \leq 100 \text{ mS/m}$).
- The cell radius is three orders of magnitude larger than the membrane thickness ($R/\delta \approx 10^3$).
- $\epsilon_{mem}/\epsilon_0 \approx 10$, $\sigma_{mem} \approx 10^{-6} \text{ S/m}$, and $\epsilon_{int}/\epsilon_0 \approx 100$.

By applying above assumptions to the expression of effective complex permittivity of the cell, below expressions are obtained for the effective conductivity and permittivity of the cell.

$$\tilde{\sigma}_p = \frac{\left(\frac{\epsilon_{mem}}{\epsilon_0}\right)^2 \sigma_{int} + \frac{\sigma_{mem} \sigma_{int}^2}{\omega^2 \epsilon_0^2} \left(\frac{\delta}{R}\right)}{\left(\frac{\epsilon_{mem}}{\epsilon_0}\right)^2 + \frac{\sigma_{int}^2}{\omega^2 \epsilon_0^2} \left(\frac{\delta}{R}\right)^2} \quad (32a)$$

$$\frac{\tilde{\epsilon}_p}{\epsilon_0} = \frac{\frac{\sigma_{int}^2}{\omega^2 \epsilon_0^2} \left(\frac{\epsilon_{mem}}{\epsilon_0}\right) \left(\frac{\delta}{R}\right)}{\left(\frac{\epsilon_{mem}}{\epsilon_0}\right)^2 + \frac{\sigma_{int}^2}{\omega^2 \epsilon_0^2} \left(\frac{\delta}{R}\right)^2} \quad (32b)$$

By substituting the Eq. 32 into Eq. 21, one will obtain below expression for the dielectric properties of the cell.

$$\begin{aligned} \sigma_{int}^2 \left[\frac{C_m \delta^2}{\omega_{pk} \epsilon_0^2 R} + \frac{2m}{\omega_{pk} \epsilon_0^2} \left(\frac{\delta}{R}\right)^2 - \frac{G_{mem}^* \delta^2}{\omega_{pk}^2 \epsilon_0^2 R} - \frac{2\sigma_m}{\omega_{pk}^2 \epsilon_0^2} \left(\frac{\delta}{R}\right)^2 \right] \\ - \sigma_i \left[\left(\frac{C_m \delta}{\epsilon_0}\right)^2 \right] = \frac{2\sigma_m C_m^2 \delta^2}{\epsilon_0^2} - 2\epsilon_m \omega_{pk} \frac{C_m^2 \delta^2}{\epsilon_0^2}. \end{aligned} \quad (33)$$

This provides a quadratic equation for the interior conductivity of the cell. Six different parameters are available in this equation; however the only unknown parameter is the interior conductivity of cell. The known parameters are listed as below:

- G_{mem}^* is calculated using the slope and intercept method.
- C_m is calculated using the slope and intercept method.

- f_{pk} is measured using the ER experiments, in media with varying conductivities.
- R and δ are known for the tested particle.
- σ_m is known from each ER experiment.

For solving Eq. 33 MATLAB software is used. Because of the quadratic nature of this equation, two answers are available for Eq. 33. However, only one of them is acceptable for the biological cells (positive and real answer).

Although there is a defined boundary for the conductivity of the medium and the peak rotation frequencies in the third level approximations, it provides a wider acceptable range for these parameters. In addition, by utilizing more complex form of the expression of the effective complex permittivity of the cell, more accurate result is obtained for the conductivity of the cell interior.

3.5 Fourth Level Approximations

In the fourth level approximations, same as the previous methods, the dielectric properties of the cell membrane are calculated using the slope and intercept method. In addition, by eliminating all limitation on the test conditions, this level is applicable to all medium conductivities and all the peak rotation frequencies. The starting point for obtaining the interior conductivity of the cell is use of full expression of the characteristic time constant (τ_{MW}). This level uses a complex form of the expression of the effective complex permittivity of the cell. A list of applied assumptions on the Eq. 18, for obtaining the effective permittivity and conductivity of the cell is listed below:

- The cell radius is three orders of magnitude larger than the membrane thickness ($R/\delta \approx 10^3$).
- $\epsilon_{mem}/\epsilon_0 \approx 10$, $\sigma_{mem} \approx 10^{-6} S/m$, and $\epsilon_{int}/\epsilon_0 \approx 100$.

Using the above assumptions, the expressions of the effective conductivity and permittivity of the cell are obtained as below:

$$\tilde{\delta}_p = \frac{\left(\frac{\varepsilon_{mem}}{\varepsilon_0}\right)^2 \sigma_{int} + \frac{\sigma_{mem} \sigma_{int}^2}{\omega^2 \varepsilon_0^2} \left(\frac{\delta}{R}\right)}{\left(\frac{\varepsilon_m}{\varepsilon_0}\right)^2 + \frac{\sigma_{int}^2}{\omega^2 \varepsilon_0^2} \left(\frac{\delta}{R}\right)^2} \quad (34a)$$

$$\frac{\tilde{\varepsilon}_p}{\varepsilon_0} = \frac{\left(\frac{\varepsilon_{mem}}{\varepsilon_0}\right)^2 \left(\frac{\varepsilon_{int}}{\varepsilon_0}\right) + \frac{\sigma_{int}^2}{\omega^2 \varepsilon_0^2} \left(\frac{\varepsilon_{mem}}{\varepsilon_0}\right) \left(\frac{\delta}{R}\right)}{\left(\frac{\varepsilon_{mem}}{\varepsilon_0}\right)^2 + \frac{\sigma_{int}^2}{\omega^2 \varepsilon_0^2} \left(\frac{\delta}{R}\right)^2} \quad (34b)$$

By substituting the Eq. 34 in Eq. 21, below equation is obtained for the interior conductivity of the cell.

$$\begin{aligned} & \omega_{pk} \left(\frac{C_{mem} \delta}{\varepsilon_0}\right)^2 \varepsilon_{int} \\ & + \sigma_{int}^2 \left[\frac{C_{mem} \delta + 2\varepsilon_m \left(\frac{\delta}{R}\right)}{\omega_{pk} \varepsilon_0^2} \left(\frac{\delta}{R}\right) - \frac{G_{mem}^* \delta + 2\sigma_m \left(\frac{\delta}{R}\right)}{\omega_{pk}^2 \varepsilon_0^2} \left(\frac{\delta}{R}\right) \right] \\ & - \sigma_{int} \left(\frac{C_{mem} \delta}{\varepsilon_0}\right)^2 = \left(\frac{C_{mem} \delta}{\varepsilon_0}\right)^2 (2\sigma_m - 2\omega_{pk} \varepsilon_m) \end{aligned} \quad (34c)$$

In the above equation, there are two unknown parameters, the effective permittivity and conductivity of the cell interior. Therefore, it needs an initial assumption on the interior permittivity of the cell, and then the interior conductivity of the cell can be determined by solving the quadratic equation. List of known parameters in Eq. 34c are given in below:

- G_{mem}^* is calculated using the slope and intercept method.
- C_m is calculated using the slope and intercept method.
- f_{pk} is measured using the ER experiments, in media with varying conductivities.
- R and δ are known for the tested particle.
- σ_m is known from each ER experiment.

Same as the third level approximations, two answers are available for the above equation, however only the real and positive answer is acceptable for the biological cells. As seen, the utilized equations for extracting the dielectric properties of the cells from the measured peak rotation frequencies are complex. In addition, use of

hand calculations is not possible. Therefore, an automated MATLAB algorithm is developed for the calculation of dielectric properties of the cell. This program includes all levels of approximations. The details of this program are given in below section.

3.6 An Automated MATLAB Algorithm for Cell Characterization

As discussed in sections 3.5, determination of the dielectric properties of the cells needs complex mathematical operations, which includes data fitting, solving quadratic equations, and calculation of the average and the standard deviation of the results. Therefore, use of hand calculation is time consuming and can lead to errors in the results. To overcome these difficulties, an automated MATLAB algorithm with graphical user interface (GUI) is designed and implemented for the calculation of the membrane and the interior dielectric properties of the cells. This program uses the obtained peak rotation frequencies and the experimental conditions, like the conductivity of the test media as the input and calculates the dielectric properties of the cells as the output. The written algorithm is presented in Appendix B. In the following sections, inputs, outputs, and operating principles of this program will be introduced.

3.6.1 Inputs for the MATLAB program

There are six groups of inputs implemented in the program, which are listed as below:

1. *The conductivity of the test medium:* The program has five inputs for the conductivity of the test media in mS/m.
2. *Peak rotation frequencies:* There are five inputs for the measured peak rotation frequencies in each medium. The frequency values should be inserted in Hertz.
3. *Frequency variations:* The measured peak rotation frequencies from the ER tests are the average values and include a variation range. There are five inputs for the inserting the variations in the measured peak rotation frequencies. The values should be inserted in Hertz.

4. *Average cell radius*: This input is used for inserting the average cell radius in μm .
5. *Radius Variances*: The radius of a specific cell population shows variations from the average value. This input is used to insert the variances of the measured cell radius in μm .
6. *Method number*: Four different levels of approximations are used in the determination of dielectric properties of the cells. This input is used to specify the utilized method.

Figure 3. 1 shows the input section of the MATLAB program. As indicated above, there are two input sections for deviations from the peak rotation frequency and variances in the radius of the cells. Therefore, it is assumed that the radius of each cell can vary in the range of $[R - \delta R, R + \delta R]$, where δR is the variances in the cell radius.

The input panel consists of a table for five media and several individual input fields. Green callout boxes point to specific fields:

- Peak rotation frequency in each medium**: Points to the 'Peak Rotation Frequency (Hz)' row in the table.
- Conductivity of the medium**: Points to the 'Medium Conductivities (mS/m)' row in the table.
- Average cell radius**: Points to the 'Cell Radius (um)' input field.
- Select one of the 4 methods**: Points to the 'Enter the Method Number' input field.
- Deviations from average cell radius**: Points to the 'Radius Variances (um)' input field.
- Deviations from the Peak rotation frequency**: Points to the 'Frequency Variances (Hz)' row in the table.

	Medium 1	Medium 2	Medium 3	Medium 4	Medium 5
Medium Conductivities (mS/m)	<input type="text"/>	<input type="text"/>	<input type="text"/>	<input type="text"/>	<input type="text"/>
Peak Rotation Frequency (Hz)	<input type="text"/>	<input type="text"/>	<input type="text"/>	<input type="text"/>	<input type="text"/>
Frequency Variances (Hz)	<input type="text"/>	<input type="text"/>	<input type="text"/>	<input type="text"/>	<input type="text"/>

Cell Radius (um)

Radius Variances (um)

Enter the Method Number

Figure 3. 1: Input Panel for the MATLAB program.

The same assumption is made on each peak rotation frequency, therefore the peak rotation frequency of the cells in each medium is in the range of $[f_{pk} - \delta f_{pk}, f_{pk} + \delta f_{pk}]$, where δf_{pk} is the deviation from the average peak rotation frequency. As stated in section 3.1, to extract the membrane properties of the cell, the slope and intercept of the straight line fitted to the data points of the peak rotation frequency and the cell radius versus the medium conductivity is utilized. The test medium is replaced with the fresh medium several times during each ER measurement; therefore, the changes in the conductivity of the medium due to resistive heating can be neglected. In order to consider the changes of the average cell radius and variances in the peak rotation frequency, three fitting processes are followed. For

this purpose, three data points are formed for the peak rotation frequency and the cell radius, which are $[(f_{pk} - \delta f_{pk}) \times (R - \delta R)]$, $[(f_{pk}) \times (R)]$, and $[(f_{pk} + \delta f_{pk}) \times (R + \delta R)]$. The fitting process is applied for each data set and the average membrane properties and the standard deviation from the average data are calculated based on the obtained results. The details are discussed in section 3.6.2.

3.6.2 Outputs of the MATLAB Program

The output section of the MATLAB program is divided into six sections. The list of the output sections is presented in below:

1. *Slope and intercept*: This section presents the calculated results for the slope and the intercept from the three fitting processes. Following the discussion in section 3.6.1, the fitting is applied on three data sets, which are $[(f_{pk} - \delta f_{pk}) \times (R - \delta R)]$, $[(f_{pk}) \times (R)]$, and $[(f_{pk} + \delta f_{pk}) \times (R + \delta R)]$. The slope and intercept section is shown in Fig. 3.2.

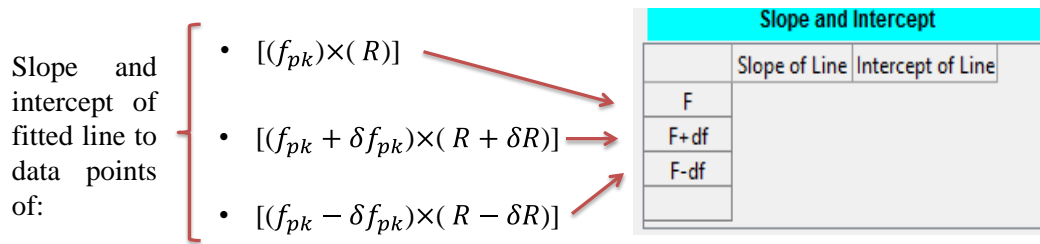


Figure 3. 2: The slope and the intercept of the fitted data.

2. *Dielectric properties of the cell membrane*: This section provides the calculated results for the dielectric properties of the cell membrane (Fig. 3.3). It uses the slope and the intercept data for each fitted line and performs the calculations using Eq.23 and 24. The average and the standard deviation results for the membrane capacitance, conductance, and permittivity are calculated based on the calculated data from the three fittings.

Dielectric properties of cell membrane			
	Membrane Capacitance (mF/m2)	Membrane Conductance (S/m2)	Membrane Permittivity
F	0	0	0
F+df	0	0	0
F-df			
Average			
Deviation			

Figure 3. 3: The output section for dielectric properties of the cell membrane.

The membrane permittivity is calculated based on the cell radius and membrane thickness. Obtained results from this section are used as the inputs for the calculation of the interior conductivity of the cell.

3. *Conductivity of the cell interior*: This section calculates the interior conductivity of the cell. For this purpose, the program uses the slope and the intercept data and implements it into one of the discussed levels of approximations. Two distinct averages and standard deviations are calculated for the interior conductivity (Fig. 3.4), which are:

- Performing the averaging on the calculated results for one of the fitting data sets, in different medium conductivities (colored with blue in Fig. 3.4). For example, for the data set of $[(f_{pk} - \delta f_{pk}) \times (R - \delta R)]$ in all of the test media.
- Performing the averaging on the obtained results from three data sets for each of the test media (colored with green in Fig. 3.4). For example, averaging the calculated results for $[(f_{pk} - \delta f_{pk}) \times (R - \delta R)]$, $[(f_{pk}) \times (R)]$, and $[(f_{pk} + \delta f_{pk}) \times (R + \delta R)]$ data sets in the first test medium.

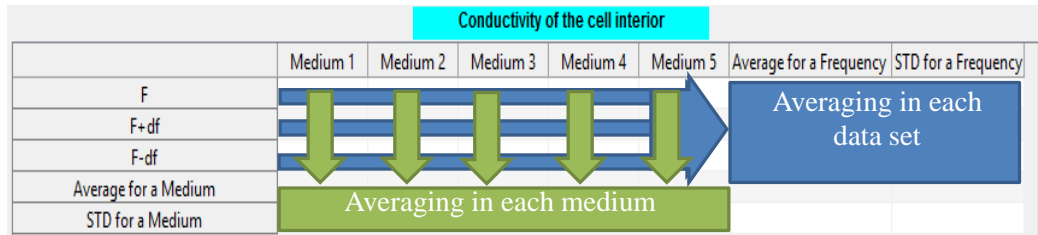


Figure 3. 4: Determining the interior conductivity of the cell by two distinct averaging methods. Blue colored section indicates averaging based on three data sets. Green colored section indicated the averaging based on the calculated data in each medium.

4. *Average for the interior conductivity*: Following the discussion in the previous section, two distinct groups of averages are calculated for the interior conductivity of the cell. In the first averaging, the conductivity of the medium is the changing factor. In the second averaging the variation in the membrane properties of the cell is the changing factor. However, the calculated cell interior conductivity is negligibly dependent on the medium conductivity. Therefore, a more accurate and reliable method is applying the averaging on each data set. Following this method, three results are obtained for the interior conductivity of the cell. The finalized interior conductivity of the cell is calculated by averaging between these three data (colored blue in Fig. 3.4).
5. *Curve fitting graph*: This graph shows the fitted straight line to the three data sets of the cell radius and peak rotation frequency, which are $[(f_{pk} - \delta f_{pk}) \times (R - \delta R)]$, $[(f_{pk}) \times (R)]$, and $[(f_{pk} + \delta f_{pk}) \times (R + \delta R)]$. Figure 3.5 shows an example of presented data in this graph for the dielectric properties of a cell.
6. *Cell interior conductivity versus medium conductivity*: Following the discussion on the different levels of approximations, the calculated interior conductivity of the cell depends on the number of parameters including the conductivity of the medium and the measured peak rotation frequency in that medium. This graph shows the changes in the calculated interior conductivity based on the conductivity of the utilized medium.

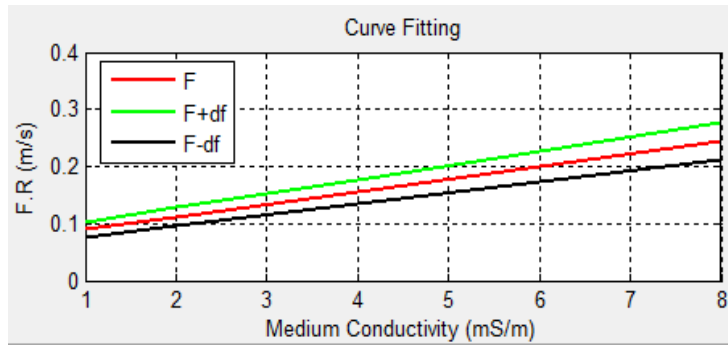


Figure 3. 5: Fitted lines for peak rotation frequencies of an unreal cell.

Below figure summarizes the used steps in calculation of the dielectric properties of the cell.

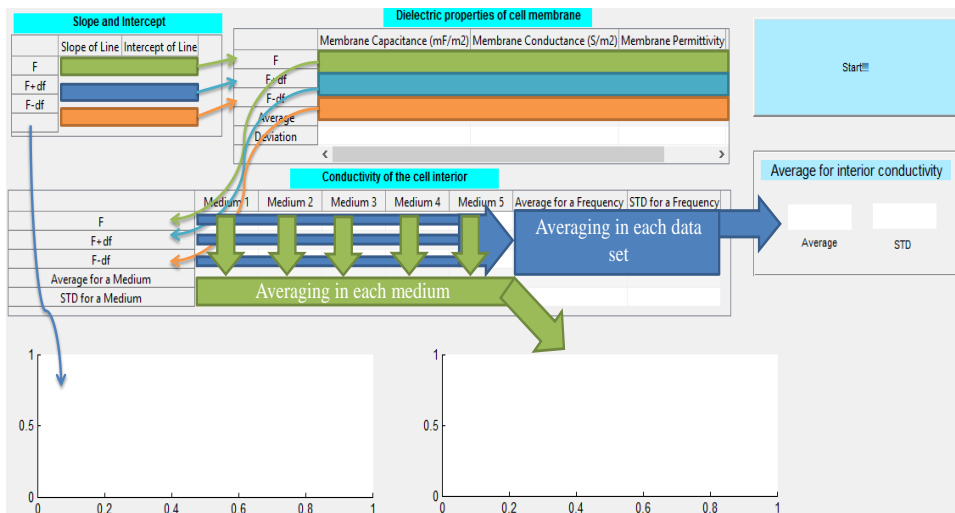


Figure 3. 6: Summary of calculation steps, in the MATLAB program.

3.7 Dielectric properties of K562 human leukemia cells

This section provides an example for calculation of the dielectric properties of a cell, using the automated MATLAB program. K562 human leukemia cells are chosen as the intended cell line. Labeed et al. has measured the dielectric properties of the K562 cells using the DEP collection rate method [50]. We will use their data as a reference for calculation of the peak rotation frequencies in media with varying conductivities. Below table shows the presented dielectric properties of K562 cells, by Labeed et al.

Table 3. 1: Dielectric properties of K562 cells (Labeed et al. [5]).

Membrane Capacitance (mF/m ²)	8.2
Interior Permittivity	60 ϵ_0
Interior Conductivity (S/m)	0.23 (0.21 – 0.24)

In order to obtain the peak rotation frequencies of the K562 cells inside the media with varying conductivities, the imaginary part of Clausius-Mossotti factor should be simulated. For this purpose, the graphs of the imaginary part of the Clausius-Mossotti factor are depicted for the K562, inside the media with conductivities of 2, 4, 6, and 8 mS/m. Figure 3.7 shows the peak rotation frequencies of the K562 cells.

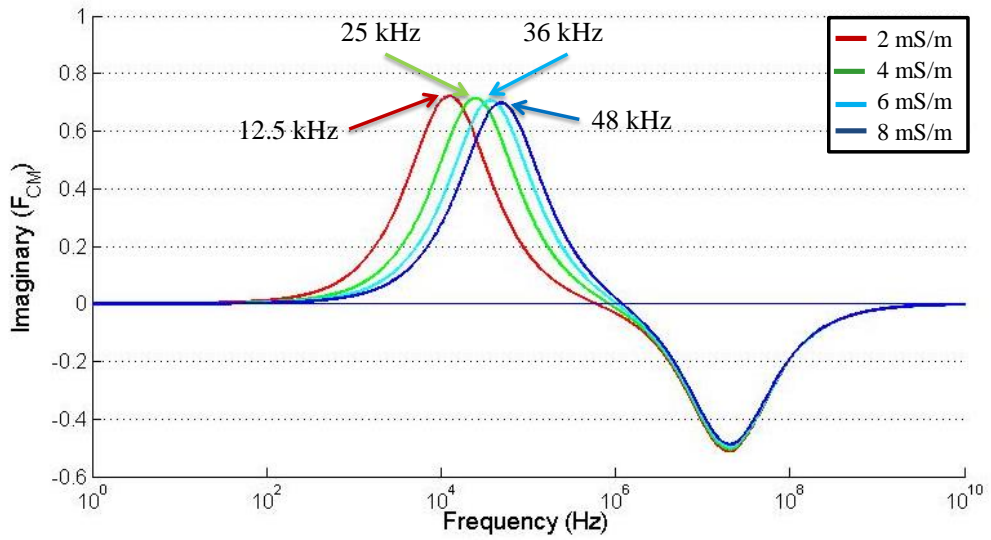


Figure 3. 7: Graph of imaginary part of the F_{CM} , inside media with varying conductivities.

In order to calculate the dielectric properties of the K562 cell using the automated MATLAB program, calculated peak rotation frequencies in each media are inserted to the program. Fig. 3.8 presents the dielectric properties of the K562 cell.

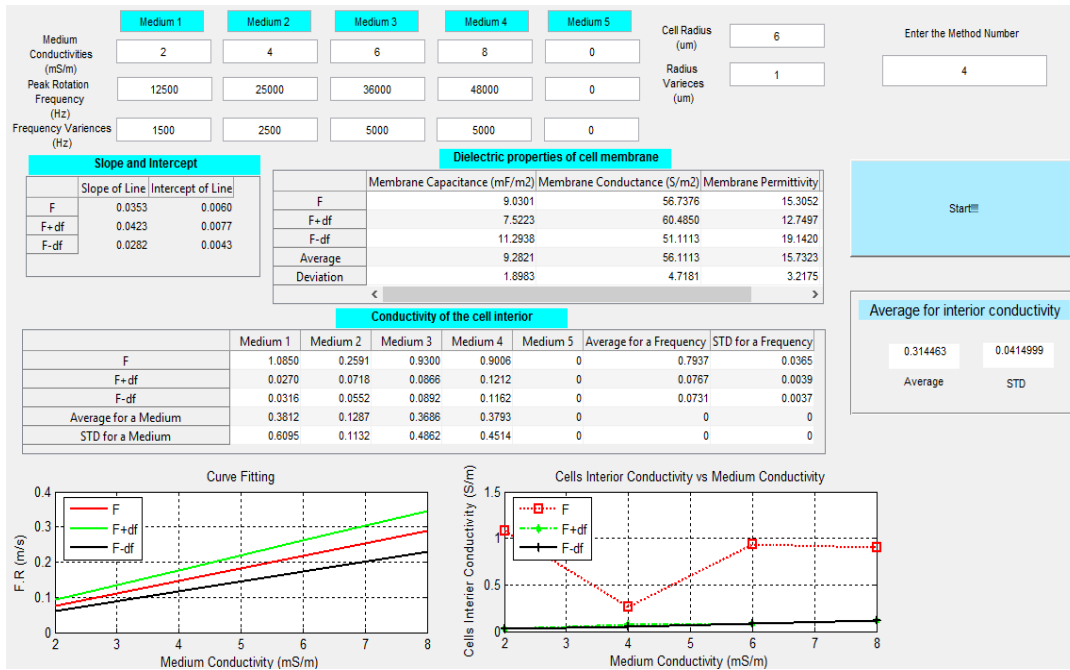


Figure 3. 8: Calculated dielectric properties of the K562 cell.

Below table provides a comparison between calculated dielectric properties of the K562 cells and presented data by Labeed et al.

Table 3. 2 : Dielectric properties of K562 cells.

	Labeed et al [5]	Automated program
Membrane Capacitance (mF/m ²)	8.2	9.28 ± 1.89
Membrane Conductance (mS/m ²)	-	56.1 ± 4.7
Membrane Permittivity (ε ₀)	-	15.7 ± 3.2
Interior Permittivity	40-80 ε ₀	60 ε ₀
Interior Conductivity (S/m)	0.23 (0.21 – 0.24)	0.31 ± 0.04

A comparison between the obtained results shows that there is a good agreement between the calculated results and the proposed values by Labeed et al. However, the variations should be due the differences between the DEP and ER method.

CHAPTER4

DESIGN AND SIMULATIONS

In this chapter, the design and simulation of the ER devices are presented. First, the simulations and analyses of the 1st generation of the ER devices with the planar pyramidal (2D) electrodes are presented and followed by a discussion on the performance of the 2D electrodes. Next, the simulations and the design of the 2nd generation of the ER devices with 3D pyramidal electrodes are presented. Finally, the simulations and design of the 3rd generation of the ER devices, with six different electrode geometries are presented. For the 3rd generation of the ER devices, in addition to the FEM analyses of the effective electric field (EEF) distribution, the experimental study of the rotational torque (ROT-T) distribution is presented as a verification of the simulation results. For this purpose, the rotation rates of the K562/IMA-0.3 cells were measured in the inter-electrode region of the ER devices with different electrode geometries. Then, the distribution map of the ROT-T is extracted for each ER device.

4.1 Design Criteria for the ER devices

There are a number of criteria in the design of ER devices; the most important points that should be taken care of are as below:

1. Electrodes shape and material

As discussed in the Introduction section, different electrode geometries are used in ER studies, including pyramidal, polynomial, circular, and elliptical. The electrode geometry is a determinant factor in the uniformity and the magnitude of the EEF and therefore the ROT-T. Another important factor is the material used in the fabrication of the electrodes. Electrodes should have persistent structure and be inert to the utilized chemicals in the test media.

2. Gap between the opposing electrodes

The distance between the opposing electrodes is a determinant factor in the magnitude of the generated ROT-T and its uniformity. Moreover, due to non-uniform nature of the generated rotating electric field in the ER devices, the gap between the electrodes determines the effective DEP force on the particles. Beside these, the maximum number of cells inside the measurement area depends on the size of the measurement area. This area should be wide enough to insure the independency of the rotation rate of a cell from the imposed dipole potential of its surrounding cells.

3. Electrode height

Height of the electrodes is another important factor, playing a crucial role in increasing the accuracy of the ER measurements. In the previous studies reported in literature, extensively 2D planar electrodes were utilized for the characterization purpose. Non-uniformity of the EEF along the z-direction is considered as a significant drawback of planar electrodes, as the height of the electrodes (~300 nm) becomes negligible compared to that of the biological cells (5-20 μm). In addition, the 3D electrodes increase the stability of the position of the cells along the z-direction, which results in consistency of the induced ROT-T on the biological cells.

4.2 The 1st Generation of the ER Devices

The aim of the 1st generation of the ER devices was to investigate the possibility of performing ER measurements for dielectric characterization of the biological cells. These devices with planar (2D) pyramidal electrodes were fabricated using Ti/Au sputtering on the Si wafer. The height of the sputtered electrode structures was

about 300 nm. The designed layout of the fabrication of the ER device is shown in Fig. 4.1. The distance between the opposing electrode tips was 280 μm . A PDMS reservoir was mounted on the fabricated ER devices for holding the cells in the measurement area. Epoxy bonding was used in mounting the PDMS reservoir on the measurement area. Figure 4.2 presents a fabricated prototype of the 1st generation of the ER devices. For the initial tests, yeast cells were utilized. After successfully accomplished experimental analysis of the rotation of the yeast cells, the ER measurement was performed using the imatinib resistant human leukemia cells, K562/IMA-0.2 μM . However, some difficulties were encountered in obtaining reproducible ER spectrum with planar electrodes.

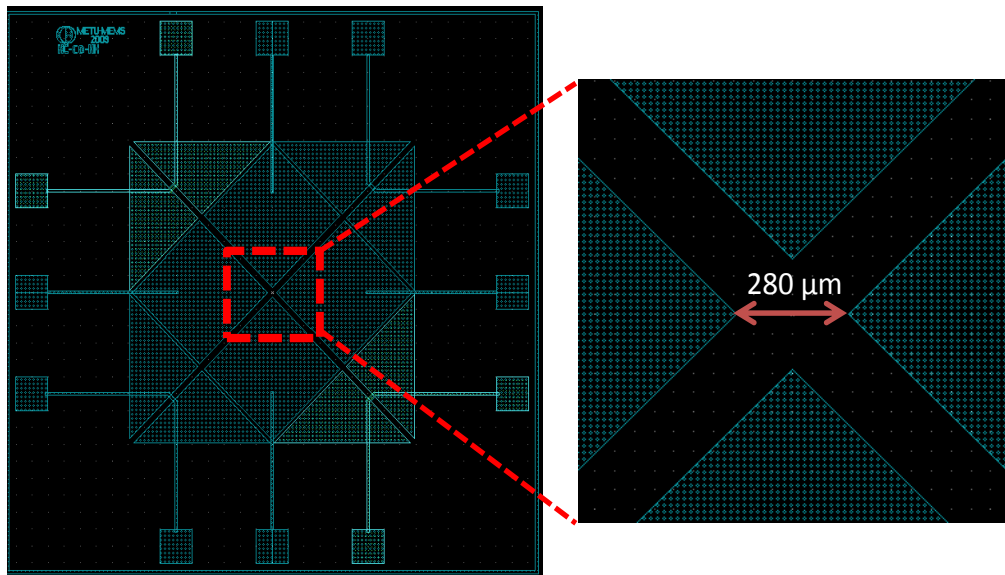


Figure 4. 1: Layout of the 1st generation of the ER devices, with magnified electrode region.

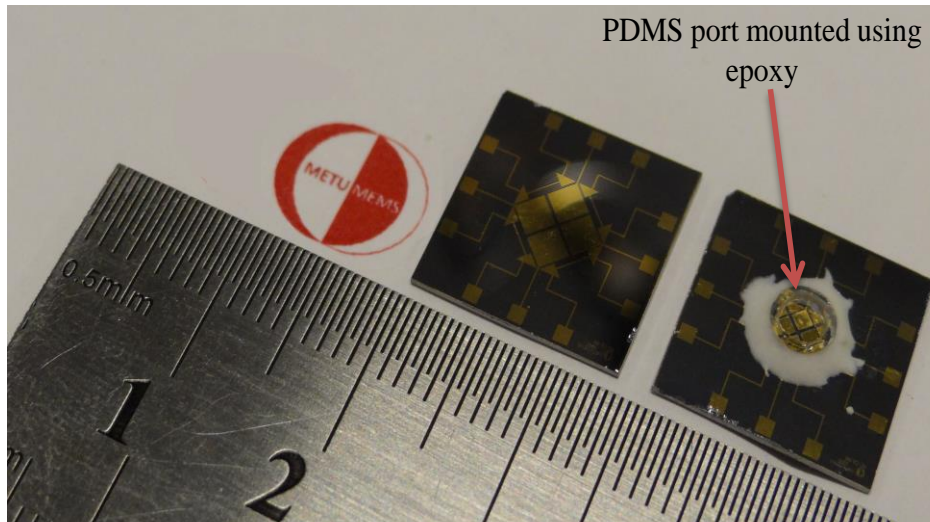


Figure 4. 2: Fabricated prototype of the ER device with planar pyramidal electrodes.

First, the vertical position of the cells was changing continuously, which results in the alternation of the induced ROT-T on the cells. This leads to a significant error in the calculations of the dielectric properties of the cells. Second, there was an inconsistency in the measured peak rotation frequencies. With further studies of the planar electrodes using FEM simulations, it was concluded that, because of the negligible volume to surface ratio in the planar electrode, the current density passing through the electrodes was significant. This results in a high resistive thermal heating in the test medium. Therefore, the conductivity of the medium was rapidly changing during the ER measurements. According to the presented discussion on Section 3.7, the measured peak rotation frequencies are highly dependent on the conductivity of the test medium. Therefore, variations in the conductivity of the test medium can shift the measured peak rotation frequencies. Figure 4.3 shows the FEM analyses (COMSOL) of the generated resistive heating of the 2D electrodes. The maximum generated resistive heating in the planar electrodes is about $3E9 \text{ W/m}^3$, which is at least an order of magnitude higher than that for the devices with 3D electrodes. In addition, FEM analyses are utilized to calculate the current density passing through the 2D electrodes. Figure 4.4 shows the FEM simulation results for the current density passing through the planar electrodes.

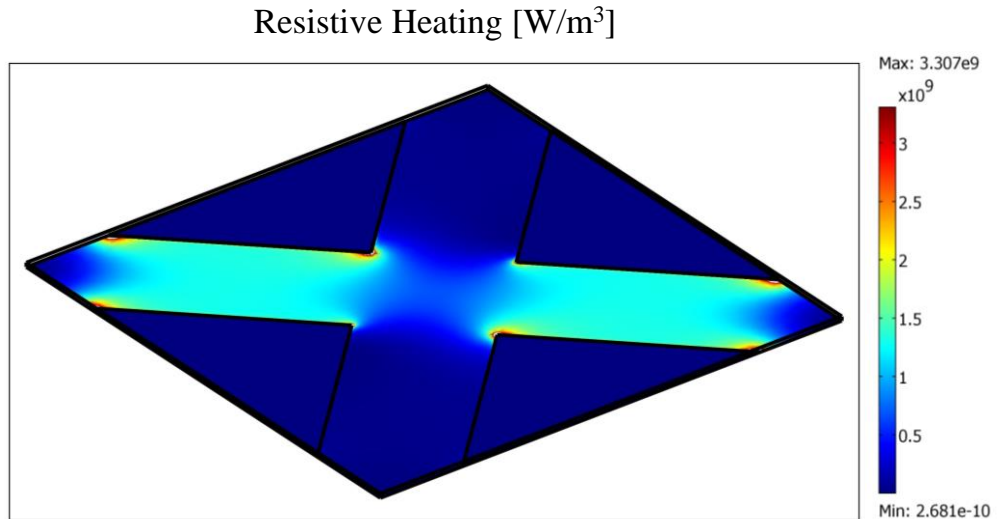


Figure 4. 3: FEM simulation of the generated resistive heating in the ER devices with planar electrodes.

The maximum value of the current density is about $5250 \text{ A}/\text{m}^2$, which is about three fold of that in the 3D electrodes. It is important to note that, the height of the electrodes is simulated as 300 nm and the simulation results are shown for a plane passing through the middle of the electrodes ($z = 150 \text{ nm}$). Moreover, the thermal heating in the electrode tip can damage the cells, which was seen during the experimental analyses of the K562/IMA-0.2 cell.

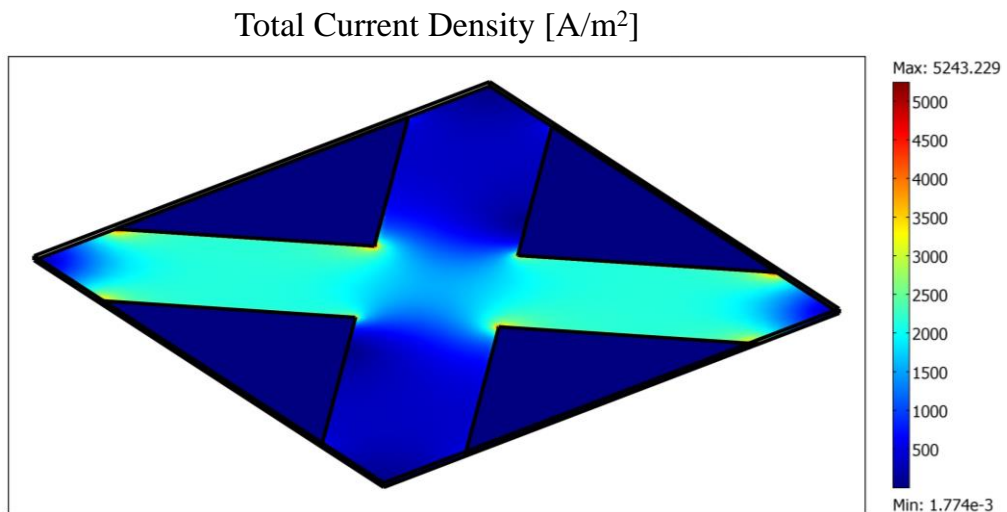


Figure 4. 4: The FEM analyses of the total current density passing through the planar electrodes.

To overcome the problems related to the planar electrodes, the 2nd generation devices with 3D electrodes were designed and fabricated.

4.3 The 2nd Generation of the ER Devices

The aim of the 2nd generation of the ER device was to achieve a higher accuracy and reproducibility in the ER measurements. For this purpose, the ER devices with 3D pyramidal electrodes were designed and fabricated. The height of the 3D electrodes was designed as 30 μm , to encompass the whole cell body. By this, the fringing electric field effect on the rotation of the cells due to negligible height of the planar electrodes (~ 300 nm) compared to the biological cells (5-20 μm), was eliminated. In addition, the 3D electrodes provide a uniform distribution of the electric potential along the z-direction, which results in a negligible magnitude of the z-component of the electric field. Therefore, the out of focal movements of the cells due to the presence of a DEP force was eliminated. This insures the consistency of the generated EEF along the z-direction. The time-variant FEM simulation of the EEF distribution is shown in Fig. 4.5. Another important criterion in design of the ER devices is limiting the generated DEP force due to non-uniformities of the electric field. The magnitude of the DEP force is directly proportional to the distribution of the electric field gradient intensity ($\nabla|E|^2$). 3D FEM analysis was utilized to study the distribution of the $\nabla|E|^2$. As it is shown in Fig. 4.6, the electrode tips has the maximum value of the $\nabla|E|^2$ (p-DEP region), which reduces gradually toward the center of the device (n-DEP region).

The 3D electrodes were fabricated using the Cu electroplating technique on the sputtered Ti/Au seed layer. Then, a thin layer of parylene (~ 300 nm) was deposited on the Cu electrodes to eliminate the risk of interaction of the Cu electrodes with the PBS containing test medium. In addition, this insulator layer reduces the flow of the generated resistive heat to the test medium. A parylene reservoir with 580 μm diameter and 30 μm height was formed on the electrode region to hold the cells in the measurement area. The layout of the 2nd generation of the ER devices is presented in Fig. 4.7.

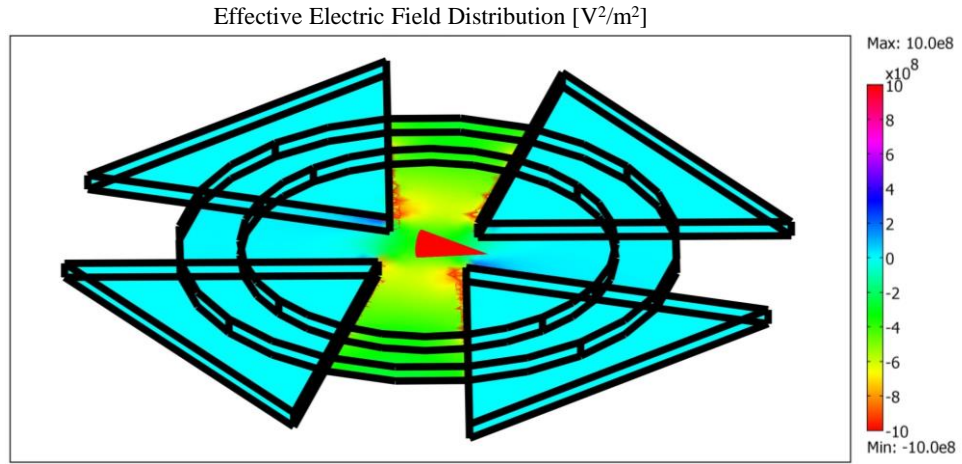


Figure 4. 5: FEM simulation of the EEF in the inter-electrode region of the 2nd generation of the ER devices. The red arrow shows the direction of the electric field at an arbitrary time instant.

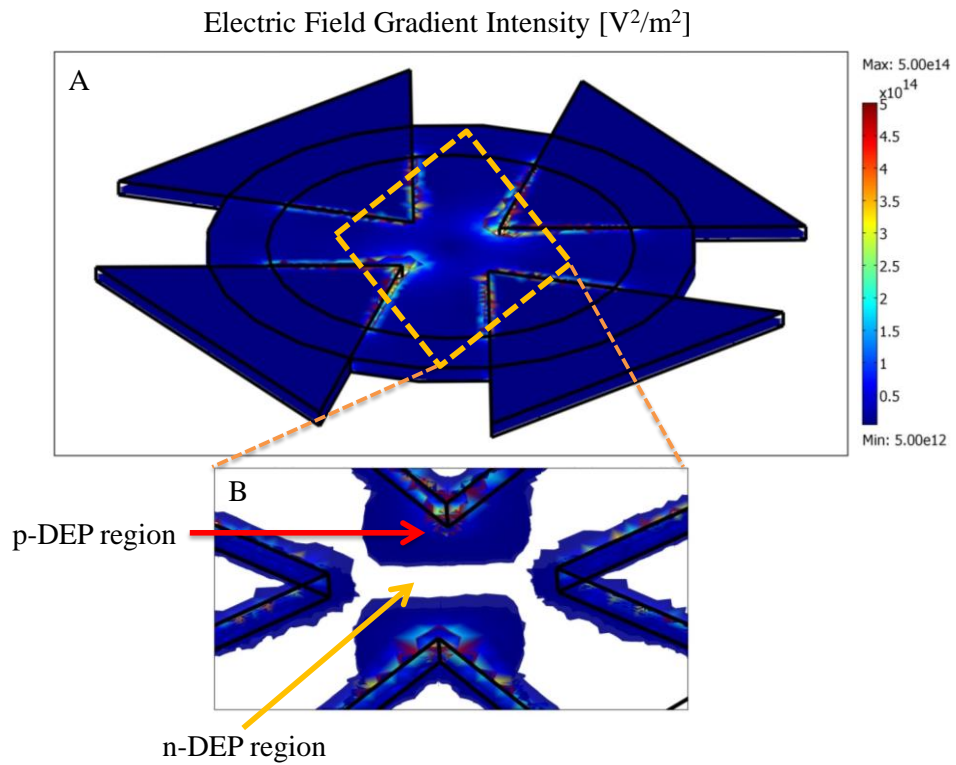


Figure 4. 6: FEM simulation of the electric field gradient intensity on the 2nd generation of the ER devices. (A) Distribution of $(\nabla|E|^2)$ on the ER chip. (B) The region in the vicinity of the electrode tips has the maximum value of the $(\nabla|E|^2)$ which reduces toward the electrodes center.

There were a number of problems evoked during the practical use of the 2nd generation ER devices. First, on the glass substrate of the ER chips, it was difficult to observe cells under microscope, as the cells are transparent. Utilized Si substrate in the 1st generation of the ER chip was more appropriate for the observation of the rotation rate of the cells. The fabricated prototypes of the 1st and 2nd generation of the ER devices are presented in Fig. 4.8. Second, parylene is a hydrophobic material; therefore there were a number of problems related to the entrance of the cells into the measurement area, due to use of parylene reservoir with very small dimensions (~ 600 μm).

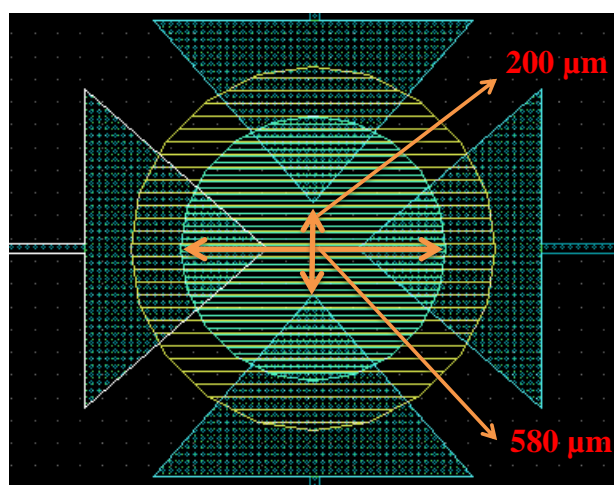


Figure 4. 7: Designed layout for the 2nd generation of the ER chips.

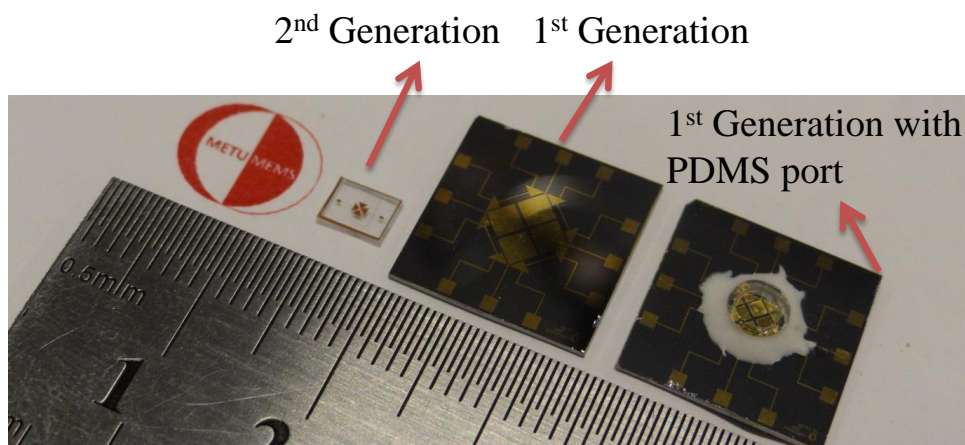


Figure 4. 8: Fabricated prototypes from 1st and 2nd generation of the ER devices.

In addition, the fabrication process of these devices consist of four masks, which was complex and time consuming, and there were six ER chips on each fabricated wafer. Considering all these problems, a new fabrication process was developed for the fabrication of the ER chips which utilizes a single mask.

4.4 The 3rd Generation of the ER Devices

The aim of the 3rd generation of the ER devices was to surmount the problems faced in the previous generations. In the fabrication of these devices, a single mask fabrication process was used. 88 ER chips with six different electrode geometries were fabricated on each Si wafer (Fig. 4.9). To overcome the problems regarding the planar electrodes (1st generation), quadrupole electrodes with 3D structures (extruded 30 μm in z-direction) were designed and fabricated. The electrodes were fabricated using the Cu electroplating technique on the patterned Ti/Au seed layer. In the 2nd generation of the ER devices, a thin parylene layer was deposited on the Cu electrodes, to eliminate the risk of reaction of the Cu electrodes with PBS containing medium. Although the parylene layer acts as a protective layer against the chemical reactions of the Cu electrodes, it is an electric insulator. Therefore, it reduces the magnitude of the generated electric field. In addition, the parylene deposition is a uniform deposition process, which covers the whole device surface, including the measurement area and the contact pads. Therefore, an additional mask is required for the RIE opening of the contact pads. To overcome these problems, in the 3rd generation of the ER chips, electroless Au deposition was utilized. Deposited gold layer, acts as an inert material, protecting the Cu electrodes against the chemical reaction and the risk of electrolysis. In addition, the magnitude of the generated electric field was not affected by the deposited gold layer. Moreover, in the electroless gold deposition, only the metal structures and lines were subjected to the Au deposition. This eliminates the need for an extra mask for the opening of the contact pads or the measurement area. Same as the parylene deposition, electroless deposition provides a uniform deposition thickness. In order to come up with more appropriate electrode geometry for the ER characterization tests, 3D distributions of the EEF and the ROT-T were studied on five commonly used electrodes geometries. In the following sections a brief introduction and

essential background about the ROT-T and the EEF characterization procedures are given. Then, the FEM analyses of the EEF distribution, followed by the experimental analyses of the ROT-T is presented for each of the ER devices.

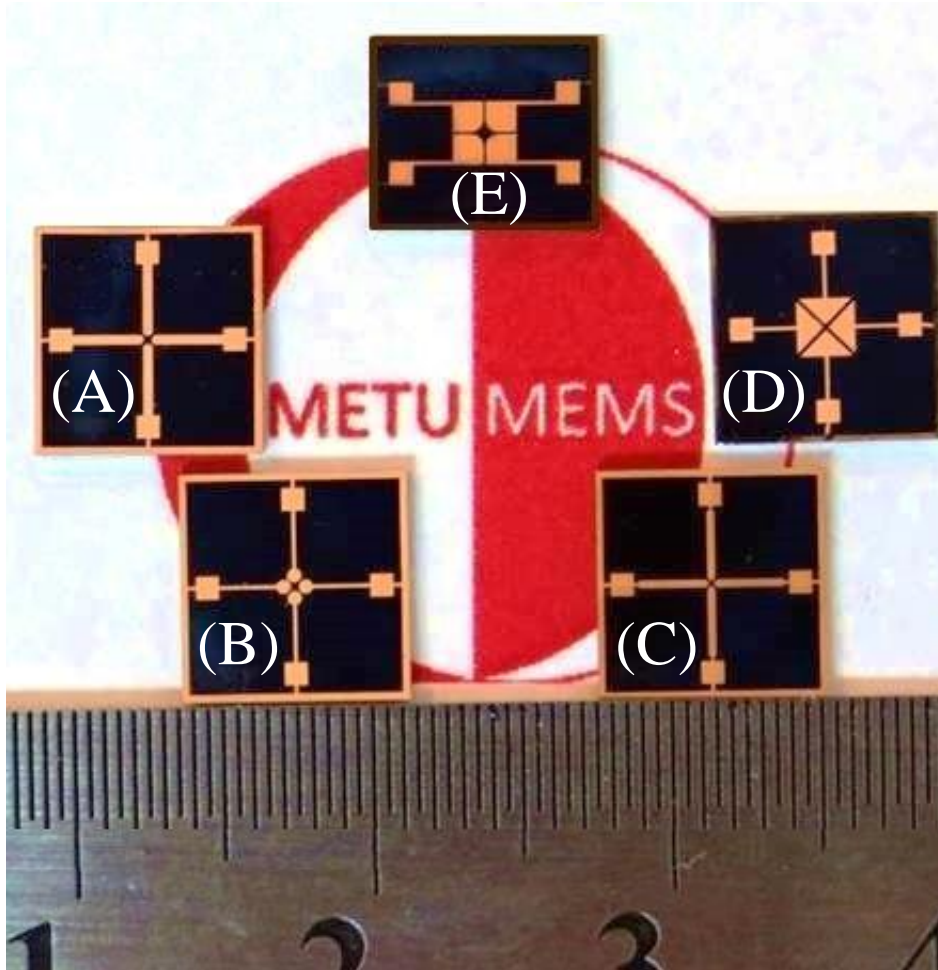


Figure 4. 9: Photograph of the fabricated prototypes of the ER device with different electrode shapes. (A) oblate elliptical, (B) circular, (C) prolate elliptical, (D) pyramidal, and (E) polynomial.

4.4.1 Introduction

The rotation of the particles is a result of the interaction of the induced dipole on the particles with the rotating electric field. Therefore, the rotational torque is proportional to the effective electric field (EEF) distribution. The rotating electric field is generated by application of electric signals (generally sinusoidal) with equal amplitudes with 90° phase shifted apart to the quadrupole electrodes. The

reproducibility and reliability of the measured rotation rates depend on a number of experimental and physical conditions including consistency of the ionic concentration and temperature of the medium and uniformity and sustainability of the induced rotational torque (ROT-T) on the particles [62]. It is known that the induced rotational torque on the particles under a rotating electric field is spatial-dependent. Therefore, to achieve high accuracy in the measurements and assure reproducibility of the collected ER data, a highly uniform EEF distribution with a constant magnitude is desirable over the measurement area. To characterize the EEF and the ROT-T distribution of the ER device, FEM and experimental analyses are utilized, respectively.

4.4.2 Finite Element Modeling

Time variant electrostatic analyses were used to study the EEF distribution on the ER devices. For this purpose, generalized electrostatic module of the COMSOL Multiphysics® software was used. The modeled electrode geometries were the replicates of the fabricated devices. In addition, subdomain and boundary conditions were introduced to reflect the actual test conditions. The electrodes were modeled as being 30 μm thick inside a suspending medium of 100 μm height. The conductivity and the relative permittivity of the suspension medium were defined as 8.5 mS/m and 78, respectively. To generate the rotating electric field, sinusoidal signals with constant frequency of 50 kHz in phase quadrature were applied to each electrode. The maximum mesh size of the inter-electrode region was under 500 nm, which facilitates the accurate sensing of the changes in the EEF distribution. For 3D analyses of changes in the EEF along the z-axis, a constant position was defined on the x-y plane for each device. This point was placed on the line passing from the device center with 45° apart from the x-axis. The x and y coordinates of this point were equal to half of the distance between the center and the electrode tip. The simulations along the z-axis were performed at $z = 5, 15, 25, 50, 75,$ and 100 μm . The changes of EEF in each vertical position were compared to that of $z = 5\mu\text{m}$ on each device.

Assuming the radii of 3-8 μm for the biological cells and considering the levitation forces inside the suspension medium, a plane that is 15 μm above the device surface

was selected for studying the EEF distribution on the x-y plane. For each device, circular areas around the device center were defined, in which the maximum deviation from the central EEF do not exceed the 5%, 10%, and 20% margins. The obtained COMSOL simulation results were studied by sampling the magnitude of the EEF from center of the device toward the boundaries of the measurement region, with 1 μm step size. For this purpose the FEM results (COMSOL) were transferred to MATLAB and further numerical analyses were performed on the FEM data.

4.4.3 Cell Preparation

Imatinib resistant K562 human leukemia cells were used in experimental investigation of the ROT-T on ER devices. For this purpose, initially the sample solution of the K562 cells, resistant to 0.3 μM imatinib (K562/IMA-0.3), was prepared. K562/IMA-0.3 cells were first washed by centrifuging the cell suspension at 1000 RPM for 5 minutes at room temperature. Centrifugation was followed by discarding the supernatant and adding fresh solution on the pellet. This washing step was performed two times. Finally, the pellets were suspended in an isotonic solution, consisting of 8.5% (w/v) sucrose plus 0.3% (w/v) dextrose, having a conductivity of 8.5 mS/m at room temperature. The conductivities were adjusted by using 0.1X PBS (Santa Cruz Biotechnology).

4.4.4 Experimental

Experimental analyses were utilized for verification of the FE models. This was achieved by measuring the rotation rate of the cells in the measurement area of the devices. The rotation rate of the cells is used to estimate the rotational torque, which depends on the EEF acting on the cells. For this purpose, the inter-electrode area on each device was divided into square segments. The number of segmentations varied between 64 and 88, depending on the area of the inter-electrode region and the distance between opposing electrodes on each ER device. In addition, the minimum segment size was defined to encompass a whole cell body, with reference to the radius of the K562/IMA-0.3 cells. A four-channel signal generator (Agilent-81150A) was used to energize the electrodes by 50 Ω coaxial cables with BNC connections. Sinusoidal signals in phase quadrature with

constant frequency of 50 kHz were applied to the electrodes. The amplitude of the signals was optimized for each device to keep the rotation rate of the cells in a manually measurable range of 180-240 RPM.

In order to study the dependency of the ROT-T on the vertical position of the cells, the measurements were performed along the electrode height ($z < 30 \mu\text{m}$) and above the electrode ceiling ($z \cong 100 \mu\text{m}$). The rotation of the cells was recorded using a video microscope (Karl Suss, PM5). Rotation rates were manually measured using a stopwatch for two complete revolutions for each cell. The vertical position of the cells was determined by either focusing the microscope to the device surface ($z < 30 \mu\text{m}$) or focusing above the electrodes ceiling ($z \cong 100 \mu\text{m}$), to the surface of the medium. The height of the medium was determined by using a PDMS reservoir with a radius of 2.5 mm and controlling the volume of the injected sample ($\cong 2 \mu\text{L}$). The focus of the microscope was kept constant during each experiment. In order to increase the reliability of the recorded data, at least two measurements were performed on each segment. The congestion of studied cells was higher in the center of the device, compared to the electrode tips. During the measurements, cells were not located exactly in the center of the segments, in most of the cases. Therefore, cells were affected from the EEF of neighboring segments. To eliminate misinterpretations in the recorded data and to increase the accuracy of extracted ROT-T maps, a neighboring average algorithm was utilized. In this method, the value of each segment was determined by averaging the measured rotation rate for that segment with its surrounding segments. Besides increasing the accuracy, this method acts as a low pass filter mechanism, which eliminates the sharp changes and smooth the extracted ROT-T map. Recorded rotations of the cells were then mapped to the corresponding segments on the device surface using MATLAB (The MathWorks, Natick, MA) surface fitting toolbox.

In the following sections the experimental and FEM results are provided for the ER devices with different electrode geometries.

4.4.5 ER Devices with Pyramidal Electrodes

The distance between the opposing electrodes in the pyramidal designs is $200\ \mu\text{m}$. The designed layout of the pyramidal electrodes is shown in Fig. 4.10. The inter-electrode region of the ER device with pyramidal electrodes was divided into 64 segments and rotation of 232 cells was studied on these devices. Figure 4.11 shows the segmented measurement area on the pyramidal electrodes.

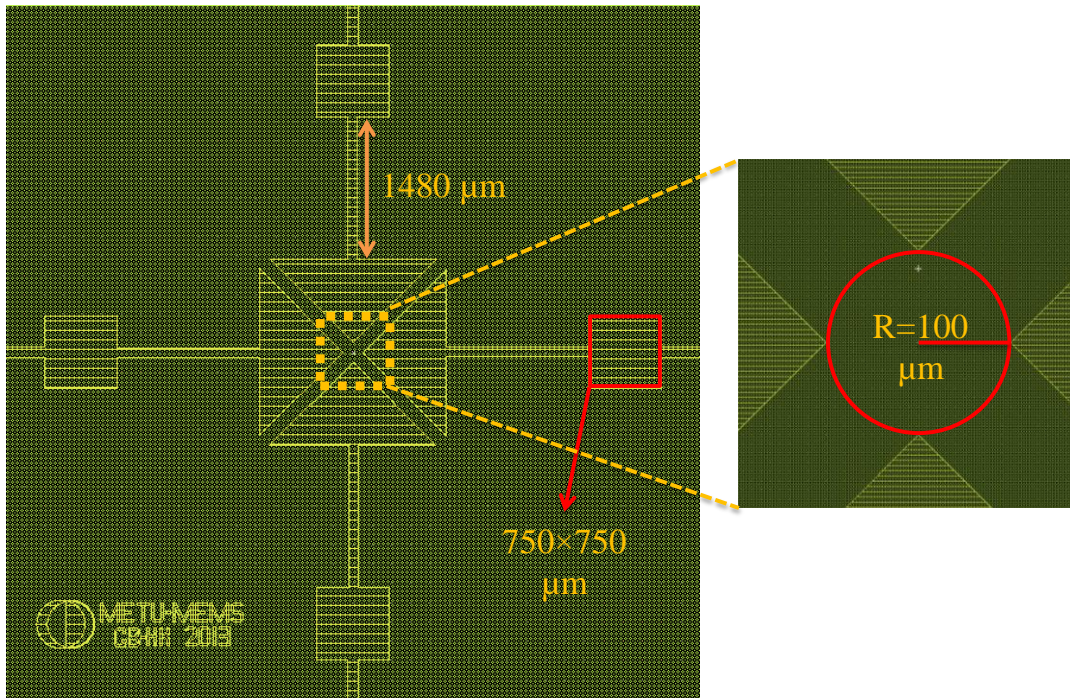


Figure 4. 10: Designed layout of the devices with pyramidal electrodes, together with the magnified inter-electrode region.

In order to extract the experimental ROT-T map on the pyramidal electrodes, the calculated average rotation rate of each cell is mapped to the corresponding segment on the device surface. For this purpose the MATLAB surface fitting software is used. Figure 4.12 and 13 show the calculated ROT-T map of the ER devices with pyramidal electrodes. The SEM photographs of the electrodes (Fig. 4.12(A) and 4.13(A)) represent the orientation of the electrodes in the mapped data. Figure 4.12 (B) and (C) show the surface map and the counter-plot of the extracted ROT-T for the cells positioned along the electrode wall ($z < 30\ \mu\text{m}$), respectively. Figure 4.13

(B) and (C) represent the surface map and the counter-plot of the extracted ROT-T map for the cells positioned at $z \cong 100 \mu\text{m}$, respectively.

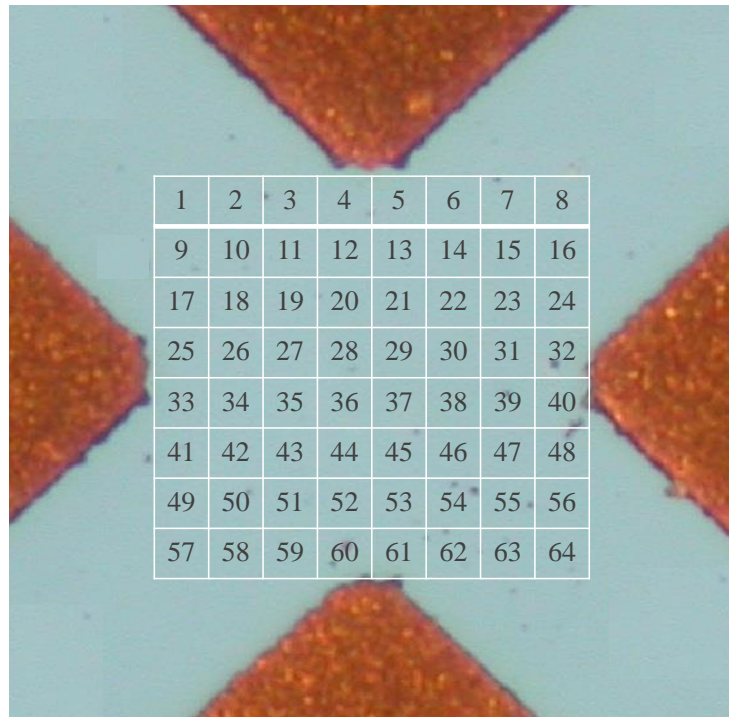


Figure 4. 11: Segmented inter-electrode region in the ER devices with pyramidal electrodes.

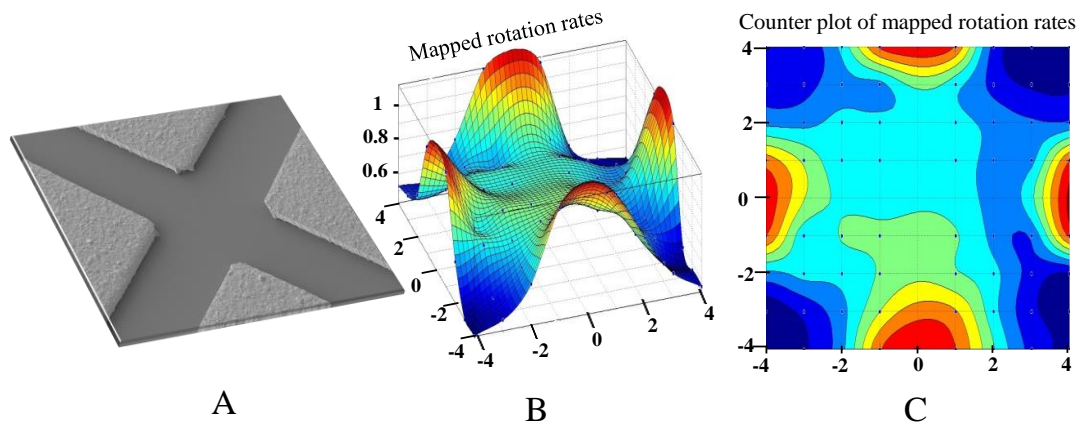


Figure 4. 12: Experimentally measured rotation rates mapped to the ER devices with pyramidal electrodes. (A) SEM photographs of the measurement region. The orientations of the electrodes show the position of the electrodes in the mapped data. (B) Surface plot and (C) Counter-plot of the rotation of the cells at $z < 30 \mu\text{m}$.

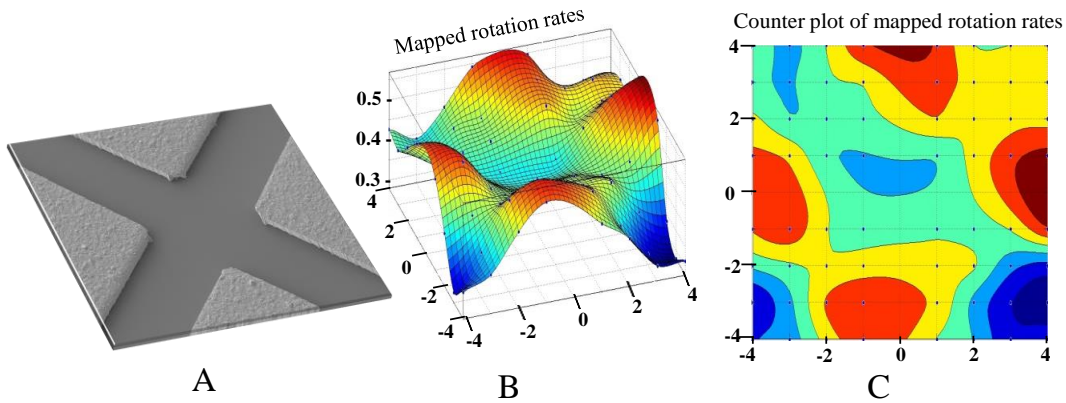


Figure 4. 13 : Experimentally measured rotation rates mapped on the devices pyramidal electrodes. (A) SEM photographs of the measurement region. The orientations of the electrodes show the position of the electrodes in mapped data. (B) Surface plot and (C) Counter-plot of the rotation of the cells at $z \cong 100 \mu\text{m}$.

FEM simulations were utilized to study the distribution of the EEF on the devices. Figure 4.14 presents the height presentation of EEF distribution on the surface of the pyramidal electrodes.

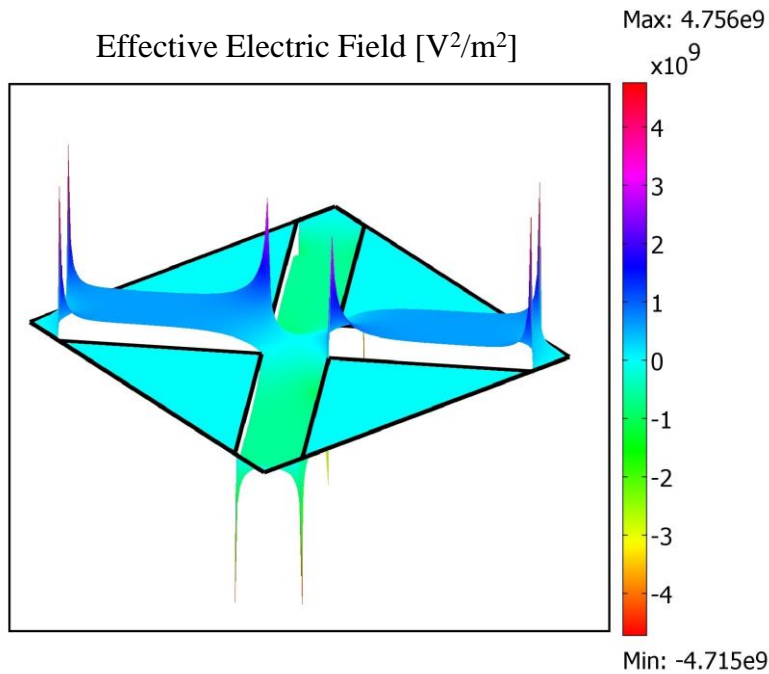


Figure 4. 14 : Height presentation of the effective electric field distribution on the devices with pyramidal electrodes.

3D FEM analysis was utilized to specify the circular regions on the inter-electrode region of the pyramidal electrodes. In these areas the maximum deviations from the central EEF do not exceed the 5%, 10%, and 20%. For this purpose, first the distribution of the EEF on the plane $15\ \mu\text{m}$ above the device surface was simulated in the COMSOL. Then, the simulation results were transferred to the MATLAB program for the further numerical analyses. To determine the boundaries of the circular area, the magnitude of the simulated EEF in the inter-electrode region was sampled with $1\ \mu\text{m}$ step size. The sampled results were then transferred to the Excel program, and the percentages of variances were calculated compared to the central magnitude of the EEF. Figure 4.15 shows the 3D simulation of the EEF on $z=15\ \mu\text{m}$.

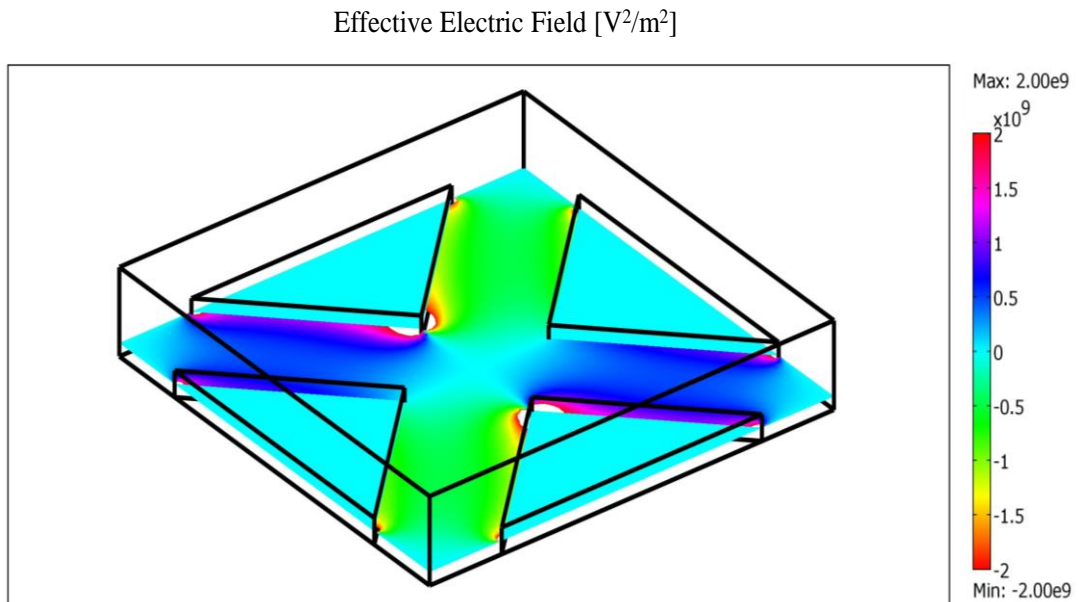


Figure 4. 15: 3D simulation of distribution of the EEF on the $z = 15\ \mu\text{m}$ plane.

Extracted ROT-T map shows the highest uniformity and sustainability of the ROT-T compared to other ER electrodes. In the pyramidal electrodes, the maximum rotation rate was measured at the electrode tips, which reduces gradually toward the center. However, in the FEM simulations the maximum EEF was obtained in the region between the adjacent electrodes. This difference between the experimental and FEM results can be interpreted based on the electrode geometry effects. In the sharp-ended pyramidal electrode, unlike the curved electrodes, the transition from

the electrode tips to the region between the adjacent electrodes is much rapid. This sudden change in magnitude of the EEF cannot be distinguished by the experimental analyses and resulted in the divergence between FEM and experimental results. The average of recorded rotation rates of the pyramidal devices, drops from $1.4 \text{ rev. sec}^{-1}$ to $0.88 \text{ rev. sec}^{-1}$ for $z < 30 \text{ }\mu\text{m}$ and $z \cong 100 \text{ }\mu\text{m}$, respectively. This shows a 37% decrease, which is calculated as 29% using FE simulations. The pyramidal electrodes show the highest sustainability of the EEF and ROT-T. The area with maximum 5% and 10% variations from central EEF encompasses the 16.81% and 49% of the circular measurement area. However the changes of the EEF in the inter-electrode region do not exceed 20% margin.

4.4.6 ER Devices with Polynomial Electrodes

The distance between the opposing electrodes is $500 \text{ }\mu\text{m}$ in the ER devices with polynomial electrodes. The designed layout of the polynomial electrodes and the critical dimensions of the device are shown in Fig. 4.16. The inter-electrode area was divided into 88 segments (Fig. 4.17) and rotations of 395 cells were studied in the segmented area.

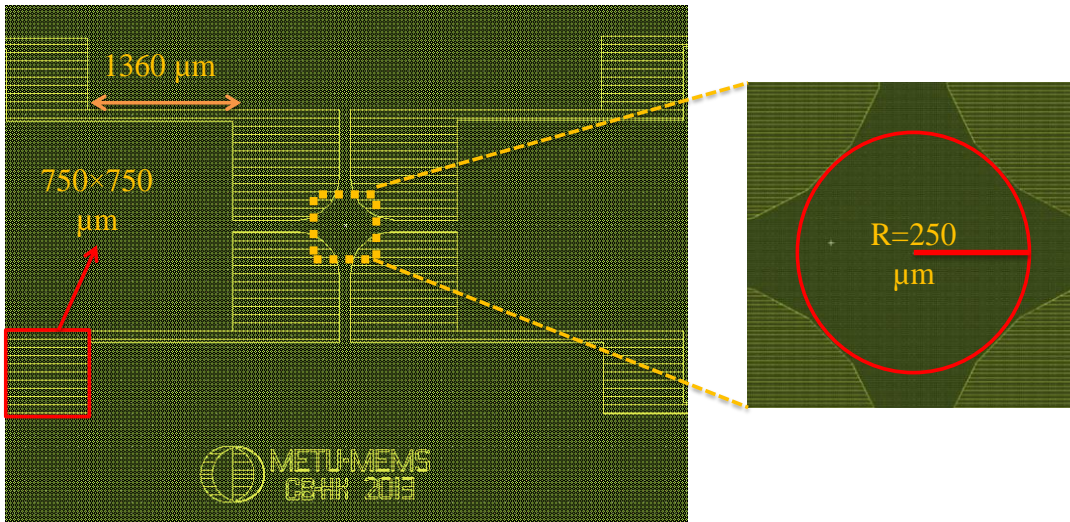


Figure 4. 16: Designed layout of the devices with polynomial electrodes, together with the magnified inter-electrode region.

In order to extract the experimental ROT-T map of the ER devices with polynomial electrodes, the calculated average rotation rate of each cell was mapped to the

corresponding segment on the device surface. The Excel software was utilized for the averaging purpose. For the mapping purpose, the MATLAB surface fitting software was used. Figures 4.18 and 19 show the extracted ROT-T map of the ER devices with polynomial electrodes. The SEM photographs of the electrodes (Fig. 4.18(A) and 4.19(A)) represent the orientation of the electrodes in the extracted maps. Figure 4.18 (B) and (C) show the surface map and the counter-plot of the extracted ROT-T for the cells positioned along the electrode wall ($z < 30\mu\text{m}$), respectively. Figure 4.19 (B) and (C) represent the surface map and the counter-plot of the extracted ROT-T map for the cells positioned at $z \cong 100 \mu\text{m}$, respectively.

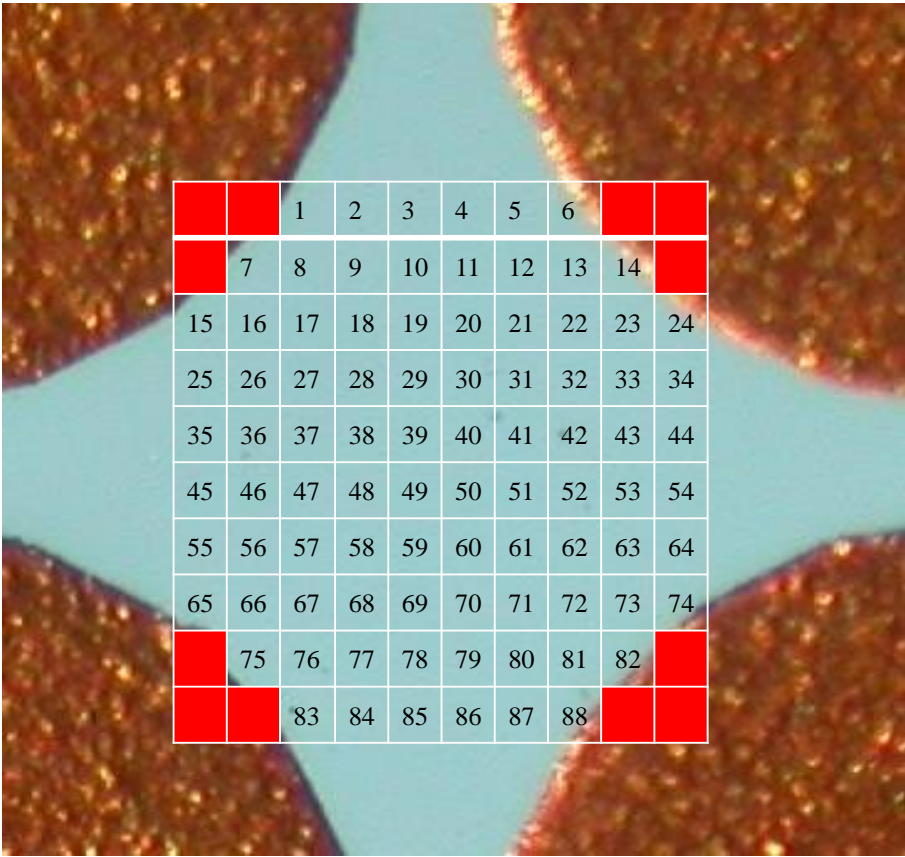


Figure 4. 17: Segmented inter-electrode region in the ER devices with polynomial electrodes.

In order to verify the experimentally extracted ROT-T maps, FEM simulations were utilized to study the distribution of the EEF in the devices with polynomial

electrodes. Figure 4.20 presents the height presentation of EEF distribution of the surface of the polynomial electrodes.

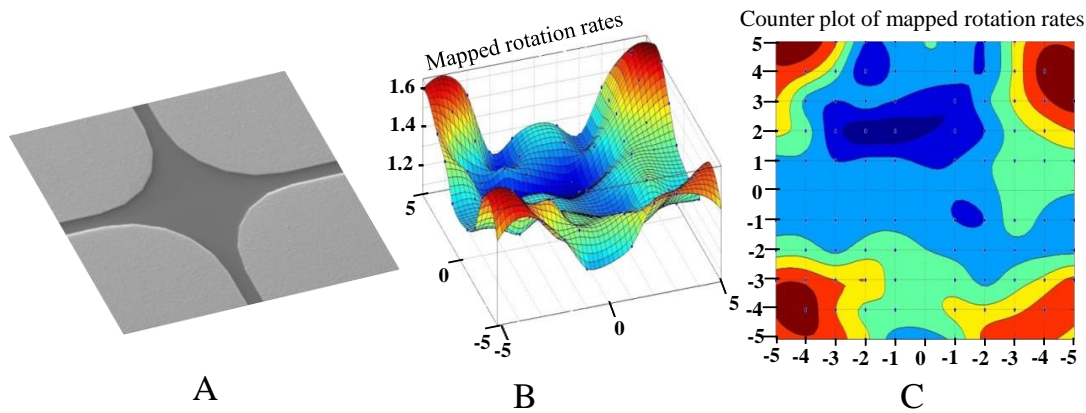


Figure 4. 18: Experimentally measured rotation rates mapped to the devices with polynomial electrodes. (A) SEM photographs of the measurement region. The orientations of the electrodes show the position of the electrodes in the mapped data. (B) Surface plot and (C) Counter-plot of the rotation of the cells at $z < 30 \mu\text{m}$.

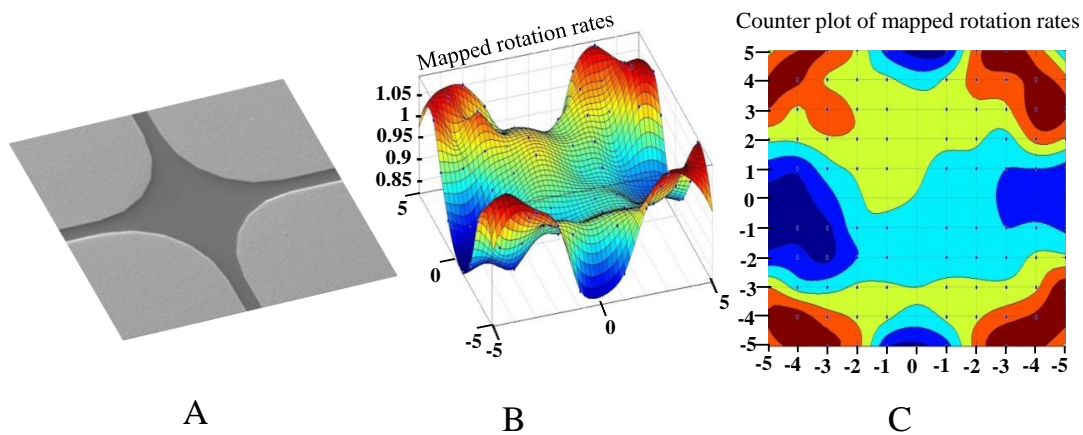


Figure 4. 19: Experimentally measured rotation rates mapped to the devices with polynomial electrodes. (A) SEM photographs of the measurement region. The orientations of the electrodes show the position of the electrodes in the mapped data. (B) Surface plot and (C) Counter-plot of the rotation of the cells at $z \cong 100 \mu\text{m}$.

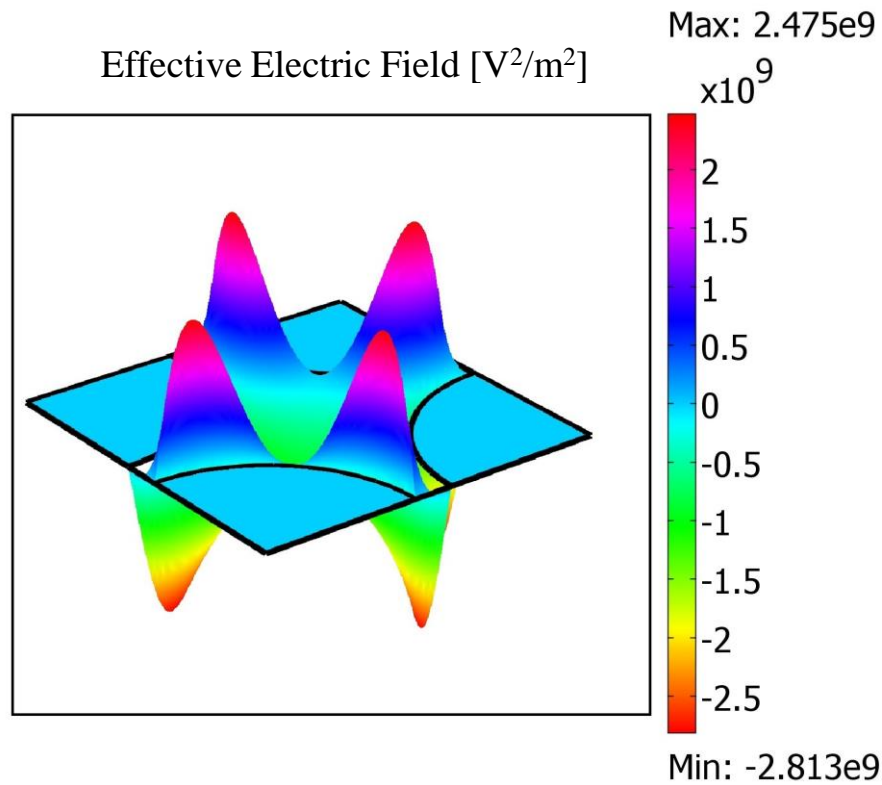


Figure 4. 20: Height presentation of the effective electric field distribution of the devices with polynomial electrodes.

3D FEM analyses were utilized to specify the circular regions on the inter-electrode area of the ER devices with polynomial electrodes. In the boundaries of these areas the maximum deviations from the central EEF do not exceed the 5%, 10%, and 20% margins. For this purpose first, the distribution of the EEF on the plane $15 \mu\text{m}$ above the device surface was simulated in the COMSOL software. Then, the simulation results were transferred to the MATLAB software for the further numerical analyses. To determine the boundaries of the circular areas, the magnitude of the simulated EEF in the inter-electrode region of the polynomial electrodes is sampled with $1 \mu\text{m}$ step size. The sampled results were then transferred to the Excel program, and the ratio of the variances was compared to the magnitude of the central EEF. By this method the boundaries of the circular areas with 5%, 10%, and 20% variations were defined. Figure 4.21 shows the 3D simulation of the EEF on the $z=15 \mu\text{m}$ plane of the polynomial electrodes.

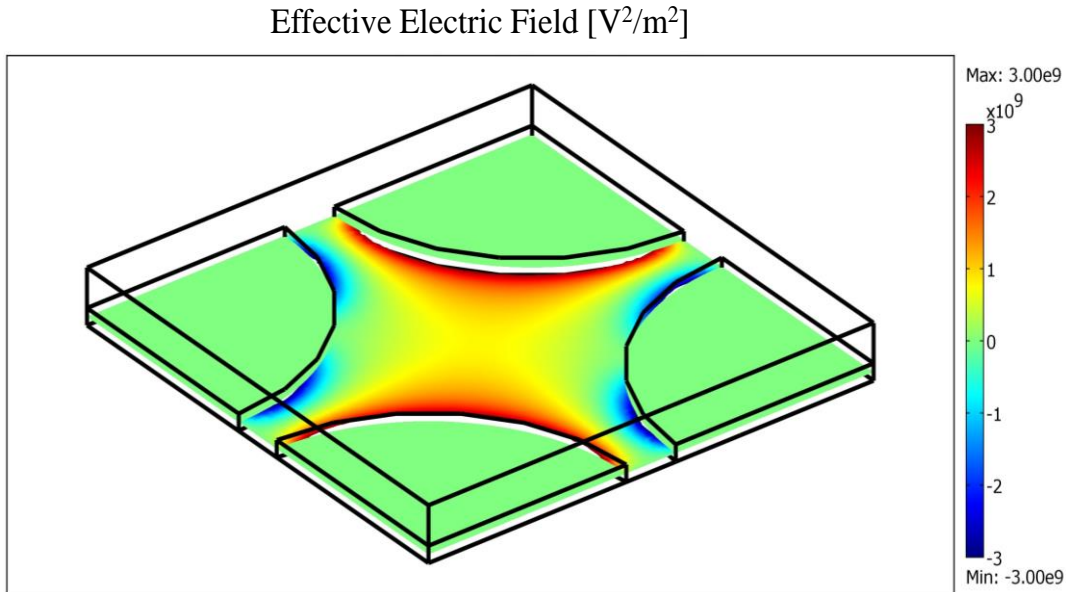


Figure 4. 21: 3D simulation of distribution of the EEF on the $z = 15 \mu\text{m}$ plane of the polynomial electrodes.

In the polynomial electrodes, the maximum rotation rates were measured at the curved electrodes tips, which reduce gradually toward the center of the electrodes. However, in the FEM simulations the maximum EEF was obtained in the vicinity of the region between the adjacent electrodes. This difference between the experimental and FEM results can be interpreted based on the geometry of the polynomial electrodes. In the polynomial design, the electrode tips were widespread from the region between the adjacent electrodes, compared to other geometries. Therefore, due to increased gap between the electrode tips and adjacent electrode, the EEF drops at electrode tip. The average of the recorded rotation rates of the cells positioned above the electrode ceiling ($1.92 \text{ rev}\cdot\text{sec}^{-1}$) shows a 28% decrease compared to the cells below the electrode ceiling ($2.68 \text{ rev}\cdot\text{sec}^{-1}$). This rate is calculated as 28% using the FE simulations, as well. The area with maximum 5%, 10%, and 20% variations from central EEF encompasses the 12.96%, 17.64%, and 23.04% of the circular measurement area. Comparing the obtained results for the uniformities of the EEF areas with other curved electrode geometries show that the polynomial electrodes have the highest uniformity of the EEF among others.

4.4.7 ER Devices with Prolate Elliptical Electrodes

The distance between the opposing electrodes in the prolate elliptical structures was $200\ \mu\text{m}$. The designed layout of the ER devices with prolate elliptical electrodes and the critical dimensions of the device are shown in Fig. 4.22. For the experimental analyses, the inter-electrode region was divided into 64 square segments (Fig. 4.23). In order to extract the ROT-T map, rotations of 421 cells were studied on these devices.

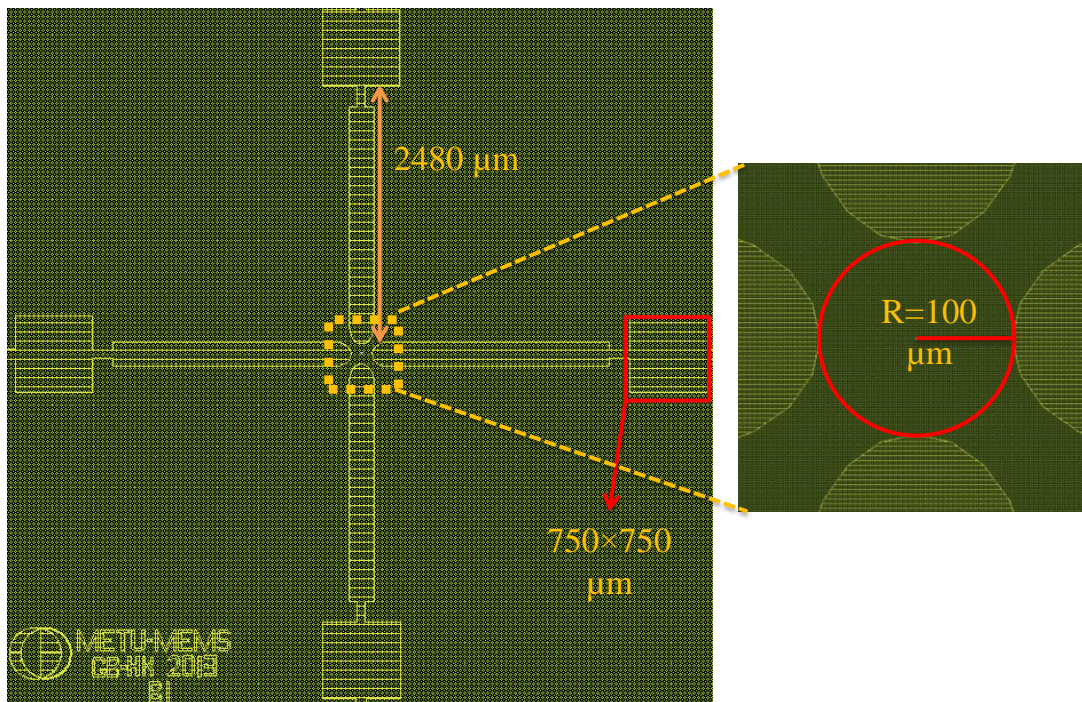


Figure 4. 22: Designed layout for the devices with the prolate elliptical electrodes, together with the magnified inter-electrode region.

In order to extract the experimental ROT-T map of the ER devices with the prolate elliptical electrodes, the measured rotation rate of each cell was mapped to the corresponding segment on the device surface. Then averaging algorithms were utilized to calculate the average rotation rate for each segment. The Excel software was utilized for the calculation of the average values. To fit the averaged data on the surface of the device, MATLAB surface fitting software was used. Figure 4.24 and 25 show the extracted ROT-T map of the ER devices with the prolate elliptical electrodes. The SEM photographs of the electrodes (Fig. 4.24(A) and 4.25(B))

represent the orientation of the electrodes in the extracted maps. Figure 4.24(B) and (C) show the surface map and the counter-plot of the extracted ROT-T for the cells positioned along the electrode wall ($z < 30\mu\text{m}$), respectively. Figure 4.25(B) and (C) represent the surface map and the counter-plot of the extracted ROT-T map for the cells positioned at $z=100\mu\text{m}$, respectively.

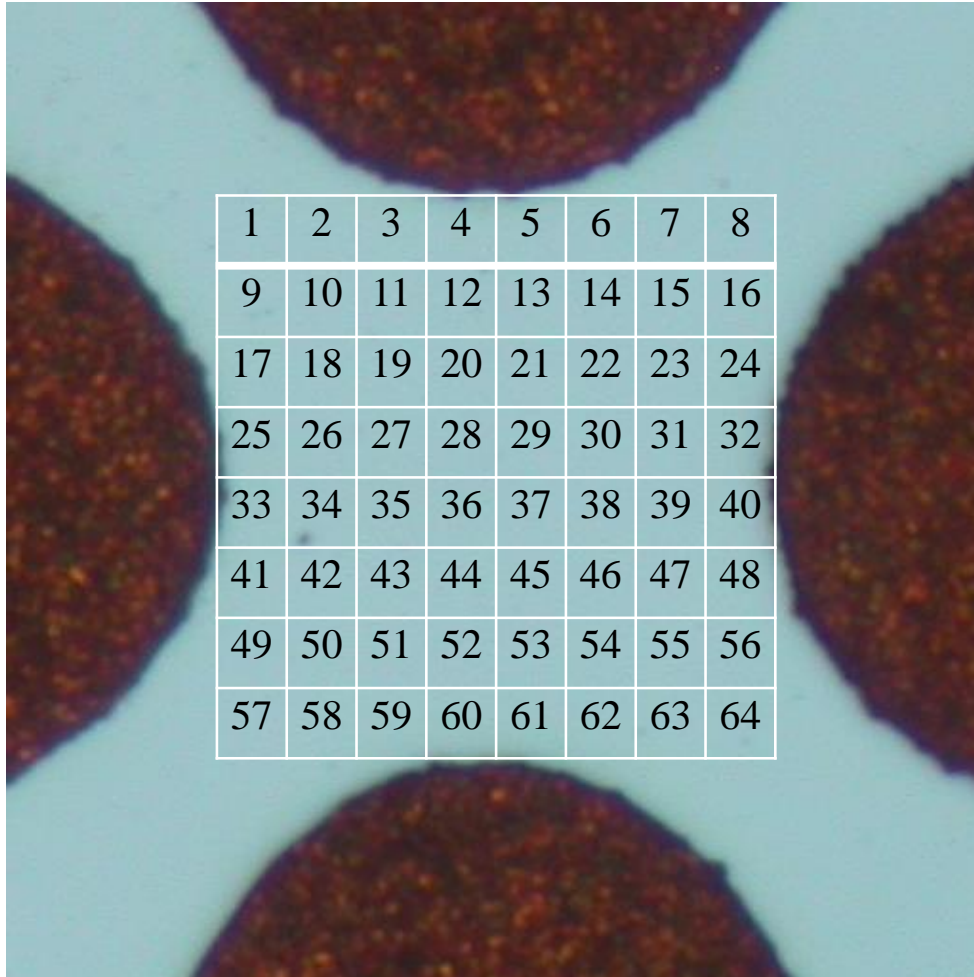


Figure 4. 23: Segmented inter-electrode region of the ER devices with prolate elliptical electrodes.

In order to verify the experimentally extracted ROT-T maps, FEM simulations (COMSOL) were utilized to study the distribution of the EEF on the devices with prolate elliptical electrodes. Figure 4.26 presents the height presentation of EEF distribution on the surface of the prolate elliptical electrodes.

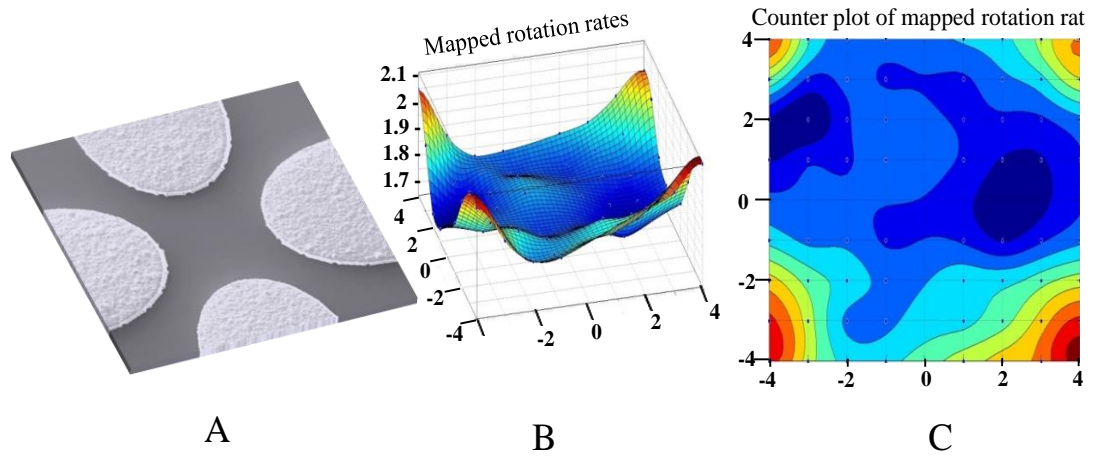


Figure 4. 24: Experimentally measured rotation rates mapped to the devices with prolate elliptical electrodes. (A) SEM photographs of the measurement region. The orientations of the electrodes show the position of the electrodes in the mapped data. (B) Surface plot and (C) Counter-plot of the rotation of the cells at $z < 30 \mu\text{m}$.

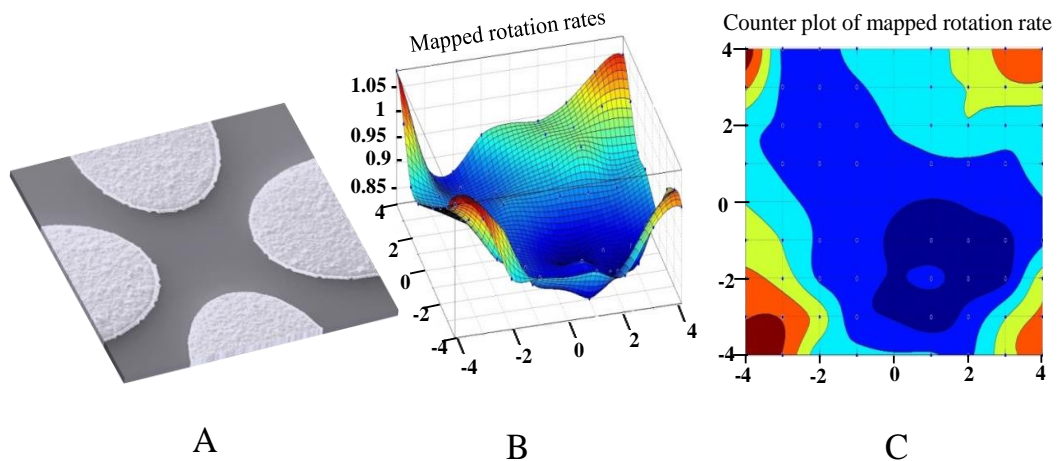


Figure 4. 25: Experimentally measured rotation rates mapped to the devices with prolate elliptical electrodes. (A) SEM photographs of the measurement region. The orientations of the electrodes show the position of the electrodes in the mapped data. (B) Surface plot and (C) Counter-plot of the rotation of the cells at $z = 100 \mu\text{m}$.

3D FEM analyses were utilized to specify the circular regions on the inter-electrode region of the ER device with prolate elliptical electrodes. In these circular regions

the maximum deviations from the central EEF do not exceed the 5%, 10%, and 20% margins.

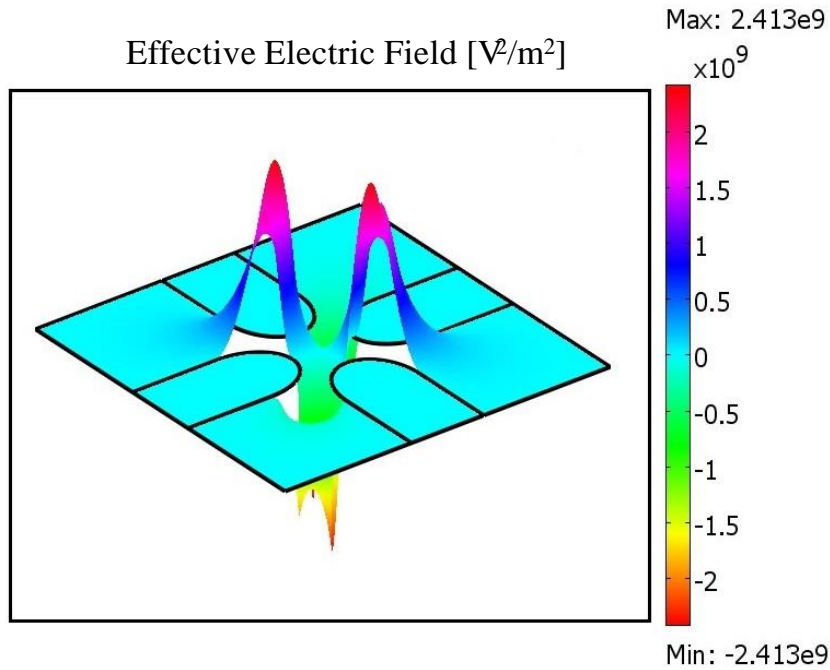


Figure 4. 26: Height presentation of the effective electric field distribution on the devices with prolate elliptical electrodes.

For this purpose first, the distribution of the EEF on the plane 15 μm above the device surface was simulated in the COMSOL. Then, the simulation results were transferred to the MATLAB software for the further numerical analyses. To determine the boundaries of the circular areas, the magnitude of the simulated EEF in the inter-electrode region was sampled with 1 μm step size, from the center of the device toward the edges of the inter-electrode region. The sampled results are then transferred to the Excel program and the percentages of variances were calculated compared to the magnitude of the central EEF. Figure 4.27 shows the 3D simulation of the EEF on the $z=15 \mu\text{m}$ plane of the prolate elliptical electrodes. In the ER devices with prolate elliptical electrodes, the experimental data shows a uniform distribution of the ROT-T in the vicinity of the electrodes center, which increases gradually toward the region between the adjacent electrodes tips. The average recorded rotation rate of the cells positioned below the electrode ceiling compared to that of $z \cong 100 \mu\text{m}$ drops from $1.83 \text{ rev.}\text{sec}^{-1}$ to $0.92 \text{ rev.}\text{sec}^{-1}$,

respectively. It shows 49% variance according to experimental data, which is calculated as 42% using FEM.

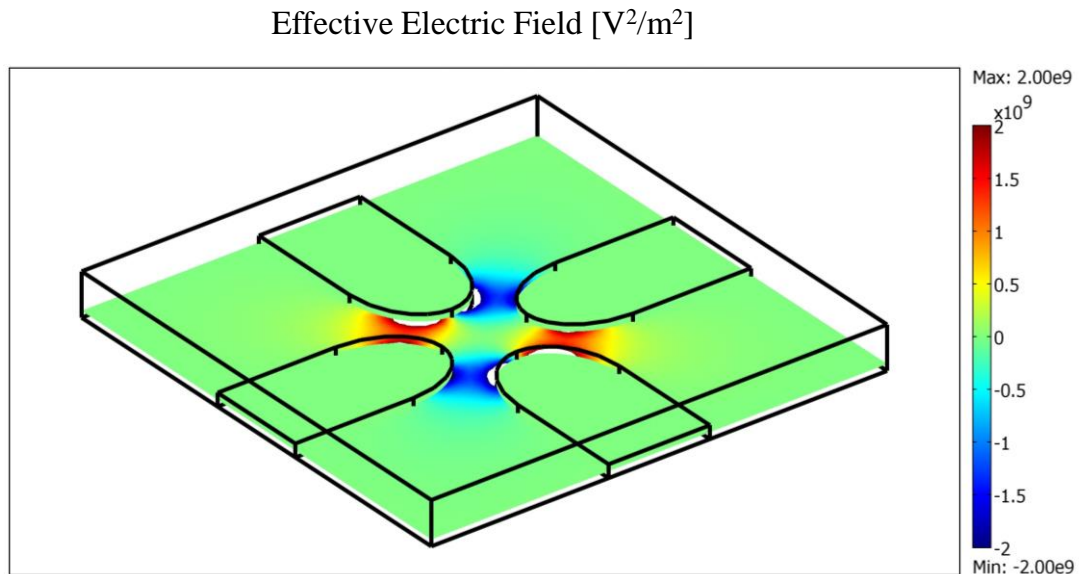


Figure 4. 27: 3D simulation of distribution of the EEF on the $z=15 \mu\text{m}$ plane of the prolate elliptical electrodes.

The circular areas with the maximum variation of 5%, 10%, and 20% variations from the central EEF were calculated to encompass the 7.84%, 12.96%, and 21.16% of the measurement area, respectively. Because of an extreme decrease in one of the x or y components of the electric field in the electrode tips, the ROT-T drops considerably in these regions. However, the maximum ROT-T was recorded in the region between the adjacent electrodes. The simulation results follow the same trend for the EEF distribution, having a uniform distribution at central region and increasing toward the region between the neighboring electrodes. Obtained results show that the ER devices with prolate elliptical electrodes have the highest instability of the EEF along the z-direction.

4.4.8 ER Devices with Oblate Elliptical Electrodes

The distance between the opposing electrodes in the oblate elliptical structures is $300 \mu\text{m}$. The designed layout of the ER devices with oblate elliptical electrodes and the critical dimensions of the device are shown in Fig. 4.28. For the experimental analyses, the measurement area was divided into 81 square segments (Fig. 4.29). In

order to extract the ROT-T map, rotations of 652 cells were studied on these devices.

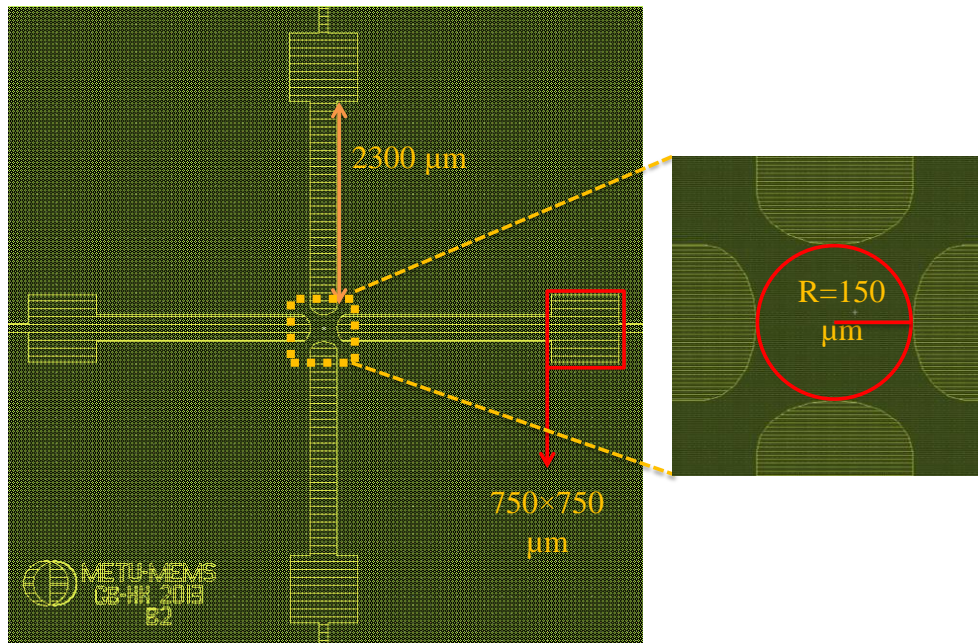


Figure 4. 28: The designed layout of the ER devices with the oblate elliptical electrode geometry.

In order to extract the experimental ROT-T map of the ER devices with the oblate elliptical electrodes, the measured average rotation rate of each cell was mapped to the corresponding segment on the device surface. The Excel software was utilized for the calculation of the average rotation rates. To fit the averaged data on the surface of the device, MATLAB surface fitting software was used. Figure 4.30 and 31 show the extracted ROT-T map of the ER devices with the oblate elliptical electrodes. The SEM photographs of the electrodes (Fig. 4.30(A) and 4.31(A)) represent the orientation of the electrodes in the extracted maps. Figure 4.30(B) and (C) show the surface map and the counter-plot of the extracted ROT-T for the cells positioned along the electrode wall ($z < 30\mu\text{m}$), respectively. Figure 4.31(B) and (C) represent the surface map and the counter-plot of the extracted ROT-T map for the cells positioned at $z \cong 100\mu\text{m}$, respectively. To verify the experimentally extracted ROT-T maps, FEM simulations were utilized. In addition, simulations were used to study the distribution of the EEF on the devices with oblate elliptical

electrodes. Figure 4.32 presents the height presentation of the EEF distribution on the surface of the oblate electrodes.

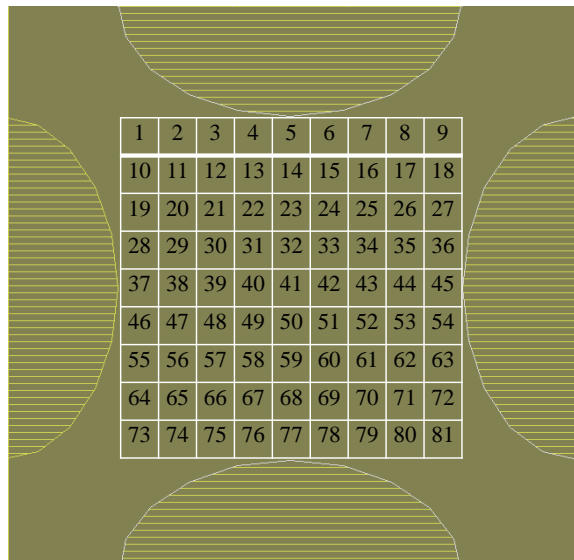


Figure 4. 29: Segmented inter-electrode region of the ER devices with the oblate elliptical electrodes.

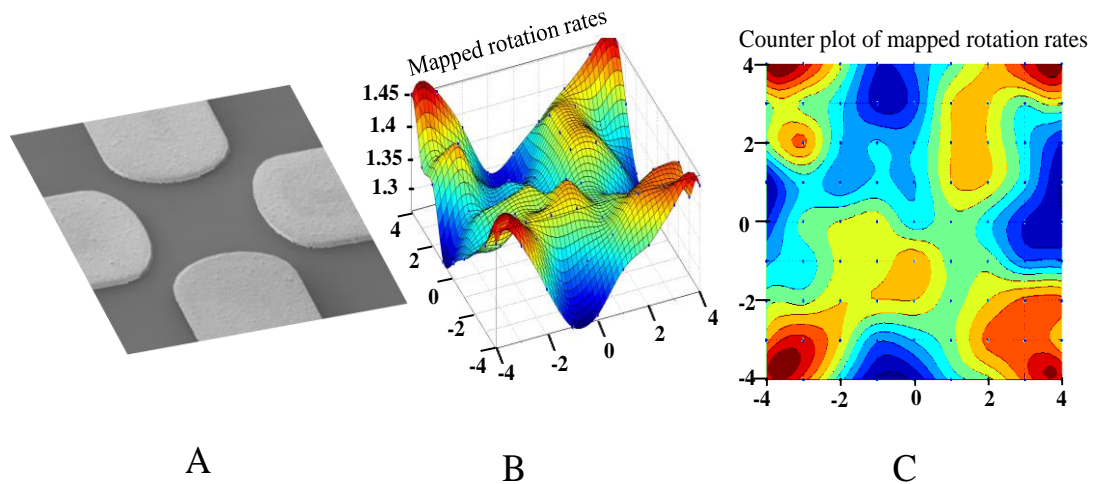


Figure 4. 30: Experimentally measured rotation rates mapped on the devices with oblate elliptical electrodes. (A) SEM photographs of the measurement region. The orientations of the electrodes show the position of the electrodes in the mapped data. (B) Surface plot and (C) Counter-plot of the rotation of the cells at $z < 30 \mu\text{m}$.

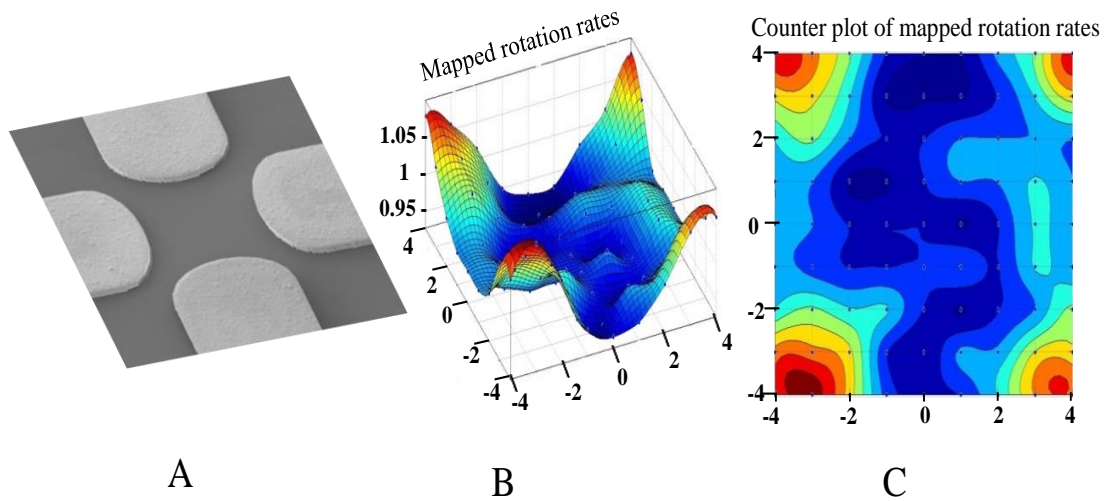


Figure 4. 31: Experimentally measured rotation rates mapped on the devices with oblate elliptical electrodes. (A) SEM photographs of the measurement region. The orientations of the electrodes show the position of the electrodes in the mapped data. (B) Surface plot and (C) Counter-plot of the rotation of the cells at $z \cong 100 \mu\text{m}$.

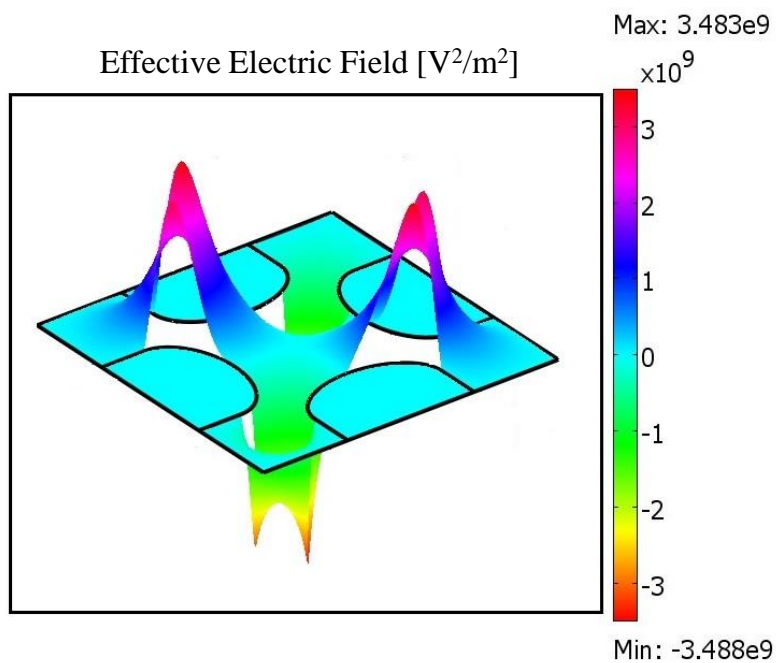


Figure 4. 32: Height presentation of the effective electric field distribution of the devices with oblate elliptical electrodes.

3D FEM analyses were utilized to specify the circular regions on the inter-electrode area of the device with oblate elliptical electrodes. In these areas the maximum deviations from the central EEF do not exceed the 5%, 10%, and 20% margins. For this purpose first, the distribution of the EEF on the plane $15\ \mu\text{m}$ above the device surface is simulated in the COMSOL. Then, the simulation results were transferred to the MATLAB software for the further numerical analyses. To determine the boundaries of the circular areas, the magnitude of the simulated EEF in the inter-electrode region is sampled with $1\ \mu\text{m}$ step size. The sampled results are then transferred to the Excel program, and the percentages of variances are calculated compared to the central magnitude of the EEF. Figure 4.33 shows the 3D simulation of the EEF on the $z=15\ \mu\text{m}$ plane of the oblate elliptical electrodes.

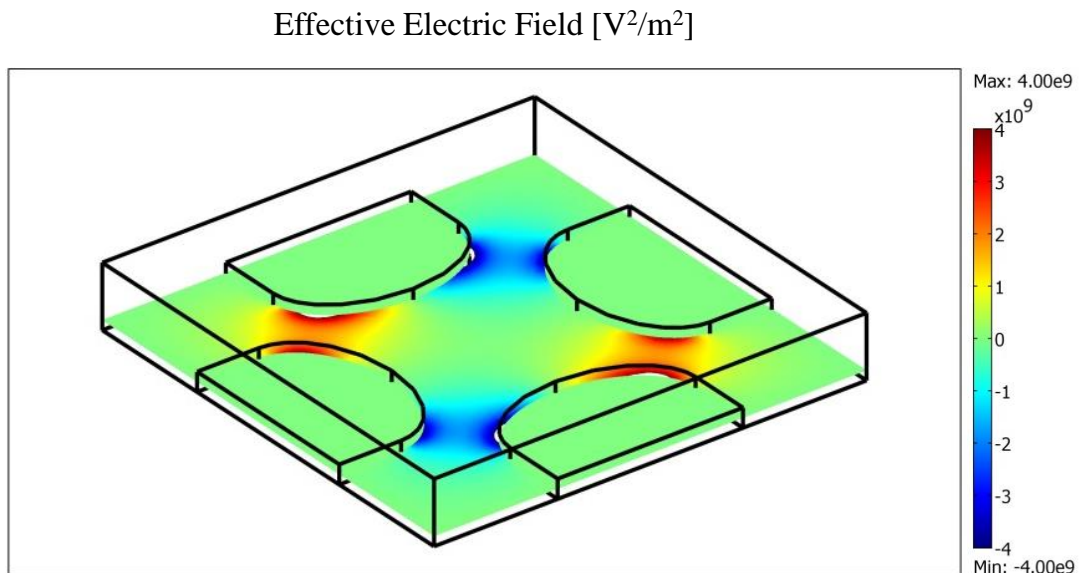


Figure 4. 33: 3D simulation of distribution of the EEF on the $z = 15\ \mu\text{m}$ plane of the oblate elliptical electrodes.

The experimental results show that the rotation rates of the cells were lower in the electrode tips, which increased toward the center of the devices. This increase was markedly toward the region between the neighboring electrode tips. Because of the weaker magnitude of rotating electric field at the vicinity of the electrode tips, the rotation rates of the cells were decreased significantly in these regions. The presented simulation results for the electric field distribution in the Fig. 4.32 present a uniform distribution of the EEF in the center of the electrodes. The magnitude of

the EEF reaches to its maximum value at the region between the neighboring electrodes. The average of recorded rotation rates, shows a 31% decrease for cells at $z \cong 100 \mu\text{m}$, compared to the cells below the electrode ceiling (from $2.78 \text{ rev. sec}^{-1}$ to $1.92 \text{ rev. sec}^{-1}$). However, this rate was calculated as 23% using FEM. The area with maximum of 5%, 10%, and 20% deviation from central EEF is calculated to cover 9.4%, 14.44%, and 21.78% of the total circular measurement area (bounded by the electrode), respectively.

4.4.9 ER Devices with Circular Electrodes

The distance between the opposing electrodes in the circular structures was $300 \mu\text{m}$. The designed layout of the ER devices with circular electrodes and the critical dimensions of the device are shown in Fig. 4.34. For the experimental analyses, the measurement area was divided into 81 square segments (Fig. 4.35). In order to extract the ROT-T map, rotations of 551 cells were studied on these devices.

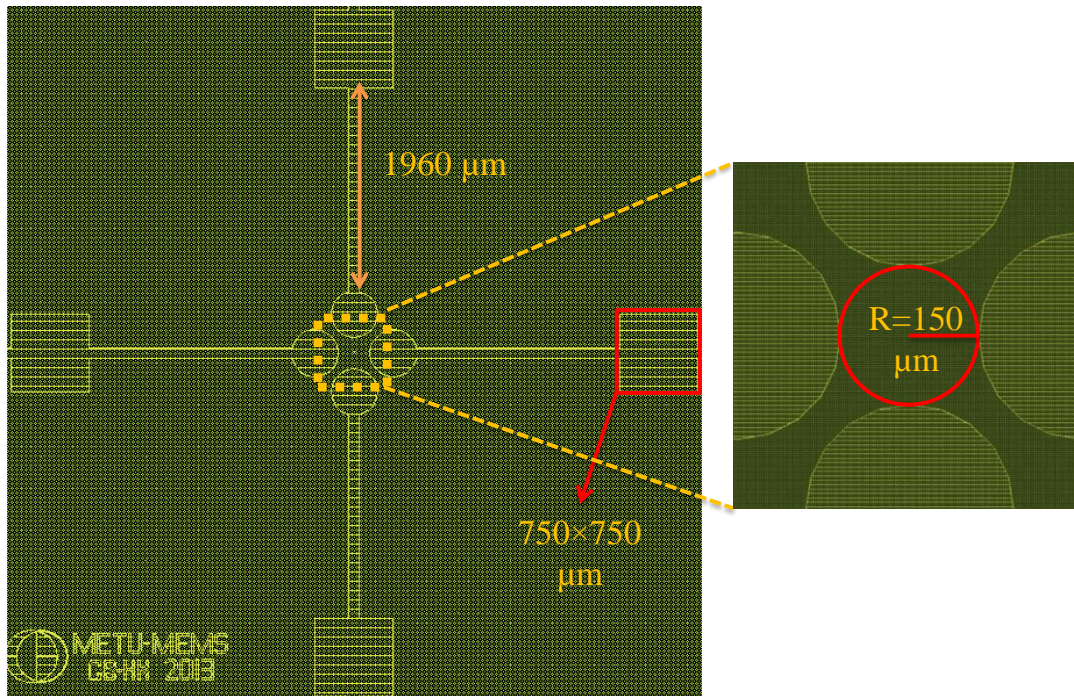


Figure 4. 34: The designed layout of the ER devices with the circular electrode geometry.

In order to extract the experimental ROT-T map of the ER devices with the circular electrodes, the measured average rotation rate of each cell was mapped to the

corresponding segment on the device surface. The Excel software was utilized for the calculation of the average rotation rates. To fit the averaged data on the surface of the device, MATLAB surface fitting software was used. Figure 4.36 and 37 show the extracted ROT-T map of the ER devices with the circular electrodes. The SEM photographs of the electrodes (Fig. 4.36(A) and 4.37(A)) represent the orientation of the electrodes in the extracted maps. Figure 4.36(B) and (C) show the surface map and the counter-plot of the extracted ROT-T for the cells positioned along the electrode wall ($z < 30\mu\text{m}$), respectively. Figure 4.37(B) and (C) represent the surface map and the counter-plot of the extracted ROT-T map for the cells positioned at $z \cong 100\mu\text{m}$, respectively.

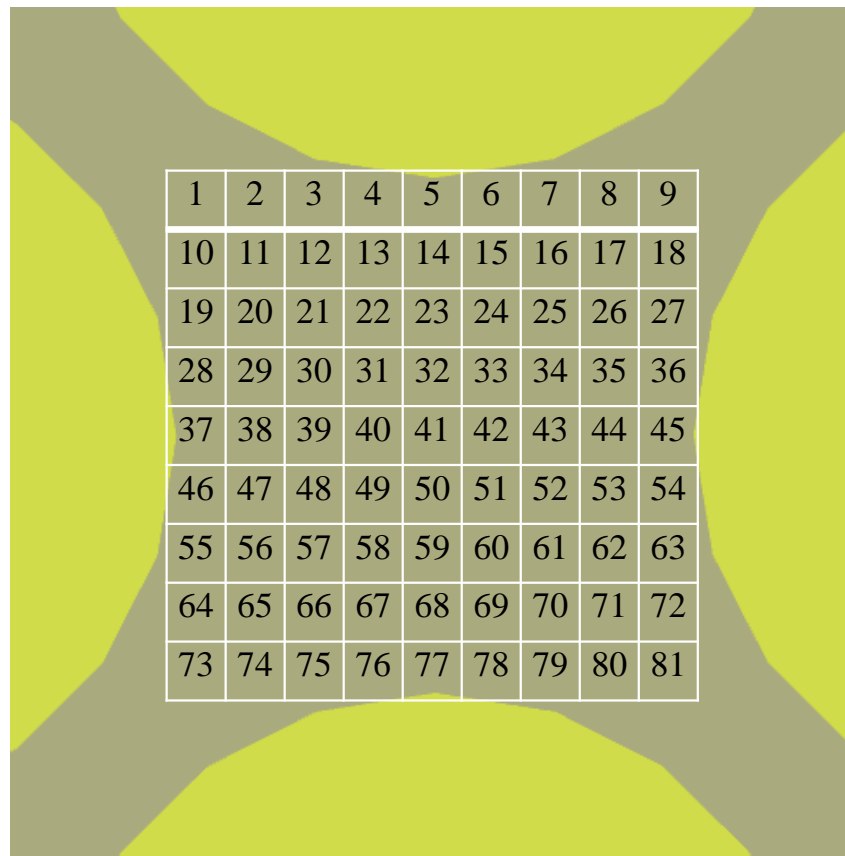


Figure 4. 35: Segmented inter-electrode region of the ER devices with circular electrodes.

FEM simulations were utilized to study the distribution of the EEF on the devices with circular electrodes. Figure 4.38 presents the height presentation of the EEF distribution on the surface of the oblate electrodes.

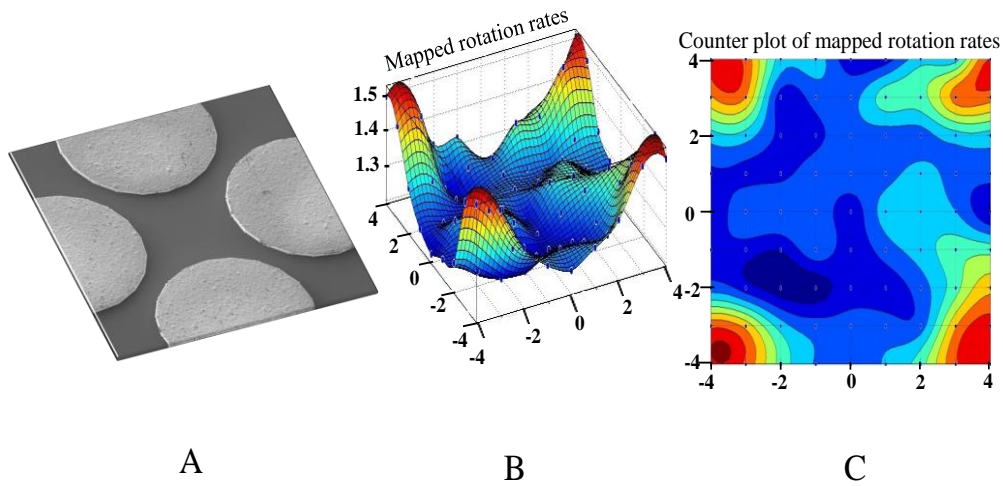


Figure 4. 36: Experimentally measured rotation rates mapped on the devices with circular electrodes. (A) SEM photographs of the measurement region. The orientations of the electrodes show the position of the electrodes in the mapped data. (B) Surface plot and (C) Counter-plot of the rotation of the cells at $z < 30 \mu\text{m}$.

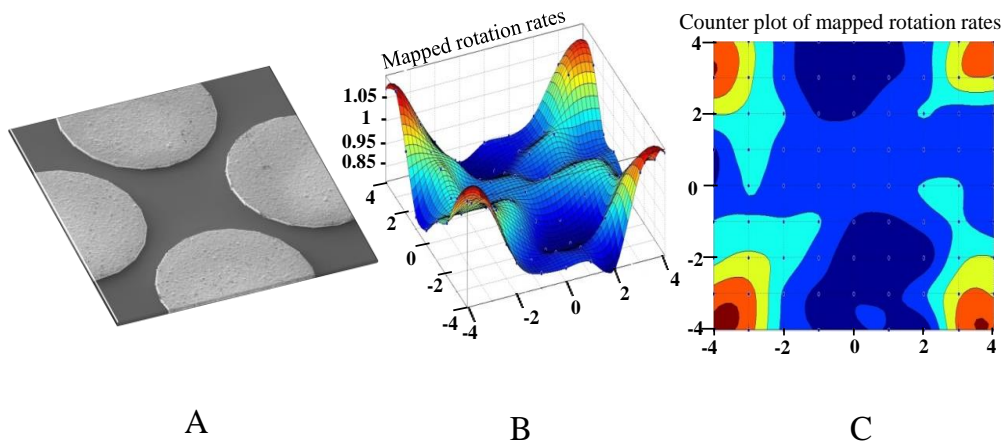


Figure 4. 37: Experimentally measured rotation rates mapped on the devices with circular electrodes. (A) SEM photographs of the measurement region. The orientations of the electrodes show the position of the electrodes in the mapped data. (B) Surface plot and (C) Counter-plot of the rotation of the cells at $z = 100 \mu\text{m}$.

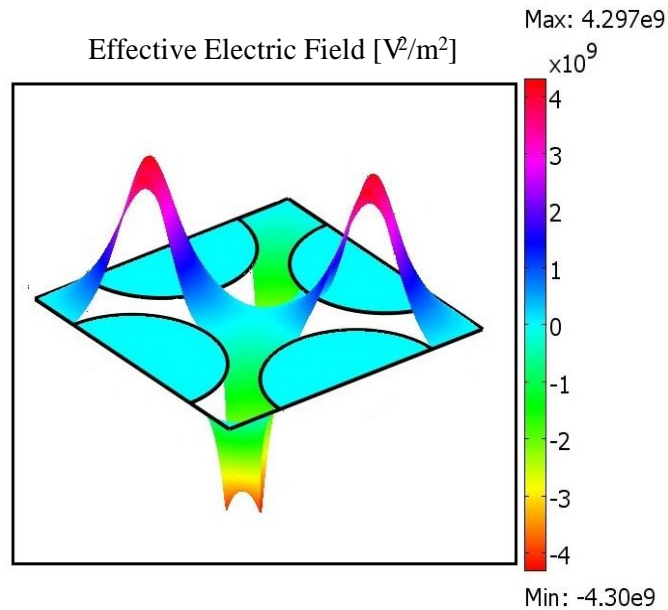


Figure 4. 38: Height presentation of the effective electric field distribution on the devices with circular electrodes.

3D FEM analyses were utilized to specify the circular regions on the inter-electrode area of the device with circular electrodes. In these areas the maximum deviations from the central EEF do not exceed the 5%, 10%, and 20% margins. For this purpose first, the distribution of the EEF on the plane $15\ \mu\text{m}$ above the device surface was simulated in the COMSOL. Then, the simulation results were transferred to the MATLAB software for the further numerical analyses. To determine the boundaries of the circular areas, the magnitude of the simulated EEF in the inter-electrode region was sampled with $1\ \mu\text{m}$ step size. The sampled results were then transferred to the Excel program, and the percentages of variances were calculated compared to the central magnitude of the EEF. Figure 4.39 shows the 3D simulation results of the EEF distribution on the $z = 15\ \mu\text{m}$ plane of the circular electrodes. The average of recorded rotation rates of the cells below the electrode ceiling compared to the cells located at $z \cong 100\ \mu\text{m}$ plane, drops from $2.64\ \text{rev. sec}^{-1}$ to $1.8\ \text{rev. sec}^{-1}$, respectively. The rate of changes in the experimental data is 32%, which is calculated as 23% using FE simulations. The circular area with maximum variations of 5%, 10%, and 20% for the EEF is calculated as the 9.4%, 14.44%, and 21.78%, respectively. The ROT-T map shows a uniform distribution of the ROT-T

in the central region of the devices, which increases toward the region between neighboring electrodes tips.

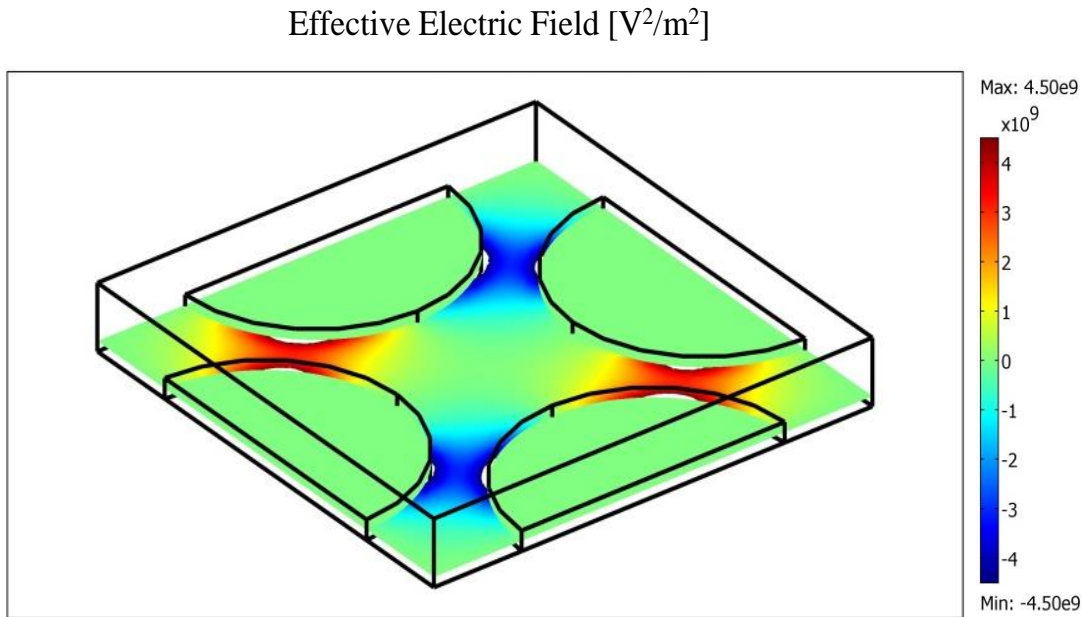


Figure 4. 39: 3D simulation of distribution of the EEF on the $z = 15 \mu\text{m}$ plane of the circular electrodes.

In ER experiments the rotation speed of the cells decreases significantly in the electrode tips because of weak rotating electric field due to negligible magnitude of one of the x or y component of the electric field. This can be inferred from the EEF simulation results.

4.4.10 ER Devices with Bone Electrodes

The distance between the opposing electrodes in the ER devices with bone electrodes is varying between $350 \mu\text{m}$ and $500 \mu\text{m}$. The designed layout of the bone electrodes and critical dimensions of the device are shown in Fig. 4.40. In the ER device with the bone shape electrodes, due to the non-uniformities of the generated EEF performing the experimental analyses for studying the distribution of the ROT-T was not possible. FEM simulations were utilized in the study of the distribution of the EEF on the ER devices with bone electrodes. Figure 4.41 presents the simulation result of distribution of the EEF. The non-uniformities of the generated EEF are obvious in Fig.4.41.

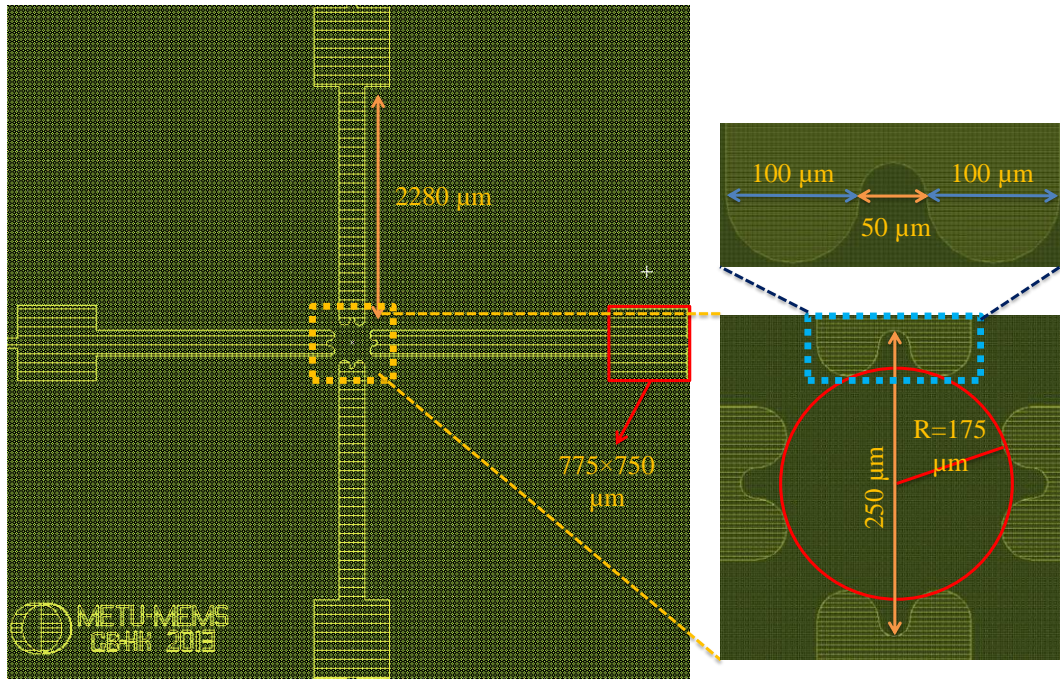


Figure 4. 40: The designed layout of the ER devices with the bone electrode geometry.

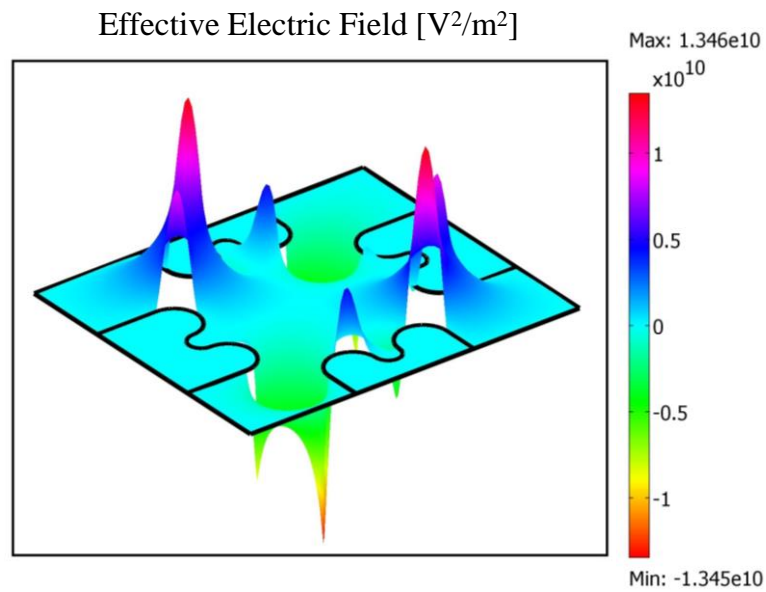


Figure 4. 41: Height presentation of the effective electric field distribution on the devices with bone electrodes.

These are originated from the inward and outward curvature of the bone electrodes, which lead to simultaneous presence of maximum regions for the EEF in the inter-electrode region of the devices. This leads to instabilities in the rotation of cells on

the surface of the device. In addition, significant non-uniformities in the distribution of the electric field lead to the presence of a strong DEP force regions on the device surface. Therefore, cells were attracted to the electrode tips, due to p-DEP force. Therefore, measuring the rotation rate of the cells in the central region of the devices was not possible. Due to above mentioned reasons the ER devices with bone shape electrodes were found to be unsuitable for ER measurements. Therefore, these devices are not included in the Table 1 and Table 2 that presents the device characterization results.

4.5 Discussion

The aim of this study was to investigate the 3D distribution of the EEF over the measurement area of the ER devices with 3D electrode structures. For this purpose, 3D FEM simulations of the EEF distributions and experimental extraction of ROT-T maps were carried out. By this, the precise boundaries of the circular areas with maximum variation margins of 5%, 10%, and 20% from the central EEF were specified (Table 4.1). To study the dependence of the EEF on vertical positions of the suspending cells inside the test medium, 3D simulations were performed for different positions along the z-axis using the COMSOL software. In order to verify the simulation results, the ROT-T distribution of the ER devices was extracted experimentally by measuring the rotation rates of the K562/IMA-0.3 cells in the inter-electrode region. For each device, the surface map and the counter-plot of the ROT-T is presented for the cells below ($z < 30 \mu\text{m}$) and above the electrodes ceiling ($z \cong 100 \mu\text{m}$). Since the precise determination of the cells position along the electrode height was not possible, the rotation of the cells along the electrode height and above the electrode ceiling was categorized as a single group.

The results of the FEM analysis together with experimental verifications are given in Table 4.2. The EEF simulations were performed on different planes along the z-axis. For each plane a comparison was made based on the variations of the magnitude of the EEF compared to that of at $z = 5 \mu\text{m}$.

Table 4. 1: Comparison of the sustainability of the effective electric field for different electrode geometries. Results present percentage of the circular area compared to the total measurement area with maximum of 5%, 10%, and 20% variations in the effective electric field compared to device center.

Electrode Shape	Tip-Device Gap (μm)	5% Deviation from central EEF		10% Deviation from central EEF		%20 Deviation from central EEF	
		Radial Distance from Device Centre (μm)	% Circular Area to Total Measurement	Radial Distance from Device Centre (μm)	% Circular Area to Total Measurement	Radial Distance from Device Centre (μm)	% Circular Area to Total Measurement
Prolate elliptical	200	28	7.84 %	36	12.96%	46	21.16%
	300	46	9.40%	57	14.44%	70	21.78%
Circular elliptical	300	46	9.40%	57	14.44%	70	21.78%
	500	90	12.96%	105	17.64%	120	23.04%
Pyramidal	200	41	16.81%	70	49%	100	100%
	500	90	12.96%	105	17.64%	120	23.04%

Simulations for the EEF variation in z-direction show that EEF remains almost constant along the height of the 3D electrodes, with a maximum variation of 7% in prolate elliptical ER devices (less than 4% for other devices). Therefore, 3D electrodes eliminate the variations of ROT-T due to the changes in vertical positions of the cells as long as the data were collected along the electrode heights. However, the FEM results show significant changes in the EEF magnitude above the electrodes ceiling. The oblate elliptical and circular electrodes have the lowest variance rate (23%) and the prolate electrodes have a significant rate of changes (42%). It can be inferred that the circular and extended elliptical electrodes provide better sustainability in EEF distribution along the z-axis. Table 4.2 also shows the results of the experimental analyses for studying the dependency of the ROT-T on the vertical position of the cells. A good agreement between the experimental measurements and simulation results can be seen, by comparing the variance of the ROT-T on $z \cong 100 \mu\text{m}$ versus $z < 30 \mu\text{m}$ and the variances of the EEF on $z = 100 \mu\text{m}$ and $z = 5 \mu\text{m}$.

Table 4. 2: Comparison between the FEM modeling and experimentally obtained characteristics of the various electrode geometries. The variance of the simulation data is compared based on the magnitude of the effective electric field at $z=5\mu\text{m}$. For the experimental data the variance is calculated based on the average rotation rates for the cell positioned at $z < 30\mu\text{m}$.

z [μm]	EEF simulation results [$\text{V}^2 \text{m}^{-2}$]					Experimental results		
	$Z < 30\mu\text{m}$			$Z > 30\mu\text{m}$		Rotation rate (rev s $^{-1}$)		
	5	15	25	50	75	100	< 30	~ 100
Prolate elliptical electrodes	1.55E+09	1.52E+09	1.44E+09	1.18E+09	9.60E+08	8.98E+08	3.66	0.92
Variance	-	2%	7%	24%	38%	42%	-	49%
Oblate elliptical electrodes	1.43E+09	1.41E+09	1.38E+09	1.25E+09	1.15E+09	1.10E+09	2.78	1.92
Variance	-	1%	4%	12%	20%	23%	-	31%
Circular electrodes	1.45E+09	1.43E+09	1.40E+09	1.28E+09	1.16E+09	1.12E+09	2.64	1.80
Variance	-	1%	4%	12%	20%	23%	-	32%
Polynomial electrodes	2.01E+09	1.98E+09	1.92E+09	1.70E+09	1.52E+09	1.44E+09	2.68	1.92
Variance	-	2%	4%	16%	25%	28%	-	28%
Pyramidal electrodes	1.02E+09	1.00E+09	9.71E+08	8.57E+08	7.57E+08	7.21E+08	1.40	0.88
Variance	-	2%	5%	16%	26%	29%	-	37%

For studying the sustainability of the EEF on the x-y plane, the distribution of the EEF was investigated on a plane 15 μm above the device surface. The results show that the devices with sharp tip electrodes have better uniformity in the EEF distribution (Table 3). The area with 5% variance margin in pyramidal devices, cover about 16.8% of the total measurement area. This rate is about 7.8%, 9.4 % and 12.96% for elliptical, circular, and polynomial electrodes, respectively. In the literature, most of ER experiments are performed in the region with maximum of 10% variances from the central EEF. This region is calculated to cover about 49% of the measurement area in devices with pyramidal electrodes. However, this ratio is less than 18% for the devices with curved electrodes. Although the pyramidal electrodes (sharp-ended) have the most uniform distribution of the EEF, the magnitude of the generated ROT-T is lower compared to curved electrodes. ER devices with extended and curved electrode tips generate a higher ROT-T in the central region. For the elliptical and circular electrodes, the ROT-T shows a uniform distribution in the central region of the devices, which increases toward the region between neighboring electrodes. In the ER experiments, the rotation rate of the cells decreases significantly in the electrode tips due to the lowered magnitude of the rotating electric field. This is related to the negligible magnitude of one of the x or y component of the electric field in the electrodes tips [63]. The FEM analyses of the EEF support the experimental measurements by showing a decreased magnitude of the rotating electric field in the vicinity of the electrode tips. In addition, due to intense DEP force in the electrode tips, the cells made rapid movements toward or away from the electrode tips, which results in the alternation of sensed torque by the cells. This resulted in non-uniform semi-circular movements of the cells, which lead to non-reproducible measurements.

In the pyramidal electrodes, the maximum rotation rate was measured at the electrode tips, which reduces gradually toward the center. However, in the FEM simulations the maximum EEF was obtained in the region between the adjacent electrodes. This difference between the experimental and FEM results can be interpreted based on the electrode geometry effects. In the sharp-ended pyramidal electrode, unlike the curved electrodes, the transition from the electrode tips to the region between the adjacent electrodes is much rapid. This sudden change in

magnitude of the EEF cannot be distinguished by the experimental analyses and resulted in the divergence between FEM and experimental results. The same trend was seen in the polynomial electrodes, where the electrode tips were widespread from the region between the adjacent electrodes, compared to other geometries. Therefore, due to increased gap between the electrode tips and adjacent electrode, the EEF drops at electrode tip.

4.6 Conclusion

With increasing interest toward the DEP based separation and manipulation of biological cells, especially the circulating tumor cells (CTCs), accurate determination of dielectric properties of cells gains further significance. Therefore, reliability in the methods of characterization becomes increasingly important. For decades, the ER method had been utilized as the most accurate and practical method for dielectric characterization of the biological cells. It has the capability of determining cells' membrane and interior dielectric properties with high accuracy. Thereby, there is a wealth of the literatures on the ER based characterization methods and reliability of the obtained data. Part of these researches has been focused on studying the uniformity of the EEF on the measurement area. These studies aim to provide a large area over the surface of the devices, where the magnitude of the generated electric field remains relatively constant. Along with the optimizations on the geometry of the electrodes to increase the uniformity of the electric field, many researchers have introduced arbitrary regions around the device center, where the variations in the EEF do not exceed a specified error margin [104]. These regions are defined based on the electrode geometry, the gap between the opposing electrodes, and the tolerable variation margin from the central EEF. Therefore, during the ER experiments, the measurements are confined to the defined area, assuming constant magnitude of the EEF and thus the ROT-T. Although the uniformities of the EEF or ROT-T over the ER devices are studied utilizing analytical and simulation models in the literature, out of plane variations in the ROT-T are neglected.

To this end, the characterization of 3D rotational torque and effective electric field distribution on ER with different electrodes geometries, both by FEM and

experimental analyses, was presented. The optimal region, with the minimum variances of the ROT-T was determined for the various ER electrode geometries and a comparison has been made on the sustainability of the EEF distribution over the measurement area of each device. When the space-dependent variations of EEF are limited to 10% of the maximum, a circular area around the center of the device with a diameter of 20% of the tip-tip electrode distance in curved electrode geometries is found. However, this ratio is calculated as 35% for the pyramidal electrodes. The pyramidal electrodes, provides the highest uniformity and sustainability in EEF and ROT-T distribution. Moreover, the variances of the EEF magnitude do not exceed 20% of central EEF on these devices. Comparison of the magnitude of the generated EEF for different electrode geometries shows that the electrodes with curved tips (circular and polynomial) provide the higher EEF magnitude.

It has been shown that the 3D electrodes have further advantages to traditional 2D structures. 3D electrodes encompass the whole cell body and eliminate the fringing field effect on the rotating cells. In addition, utilization of 3D electrodes decreases the z-component of the electric field by providing a uniform distribution of the potential along the electrodes walls. This minimizes the out of plane movements of the cells during the ER measurements, by generating a steady electric field magnitude along the z-direction. Moreover, due to increased volume in 3D structures the current density passing through the electrodes drops significantly. This results in lower resistive heating at electrodes. It is verified using FEM analyses that the thermal heating of the 3D structures was decreased by more than an order of magnitude compared to planar structures. Thermal heating on the planar electrode leads to an increase in the medium temperature and causes instability of the suspending medium conductivity, which introduces an error to the ER measurements [62].

Presented data can be utilized in the design and implementation of the ER devices, with higher stability in the measurement conditions. In addition, by exact determination of the boundaries of the regions with specific variations in EEF, space-dependent errors can be eliminated by confining the measurement into

introduced regions. In addition, presented experimental and simulation results correlate with the rotation rates to the cells' position in the 3D. Moreover, the results provide a data base for the automated ER mechanism that is based on imaging techniques.

CHAPTER 5

FABRICATION

This section presents the utilized microfabrication techniques in the fabrication of the different generation of the ER devices. In the 1st generation of the ER device Ti/Au sputtering and lithography techniques were used for the fabrication of the planar pyramidal electrodes on the Si wafer. In the fabrication of the 2nd generation of the ER devices parylene microchannel fabrication technique, which is optimized in the BioMEMS group, was utilized in the fabrication of the pyramidal electrodes with 3D structures on the glass wafer. In the fabrication of the 3rd generation of the ER devices, a single mask fabrication process was used for the fabrication of 3D electrodes with different electrode geometries. In the following sections the details of the fabrication steps of the ER device are presented.

5.1 Fabrication of the 1st Generation of the ER Devices

Figure 5.1 presents the fabrication flow of the 1st generation of the ER devices. A single mask was utilized in the fabrication of the first generation of the ER devices. The fabrication process includes metal sputtering (Ti/Au), wet etching, and photolithography. In the first step, a thin oxide layer was grown on the Si wafer as an insulator layer. Then, the Ti and Au were sputtered on the wafer to form the metal layer. Then the S1813 photoresist was spun on the metal layer and patterned using lithography technique. Then the metal layer was patterned using the designed mask (Fig. 5.2).

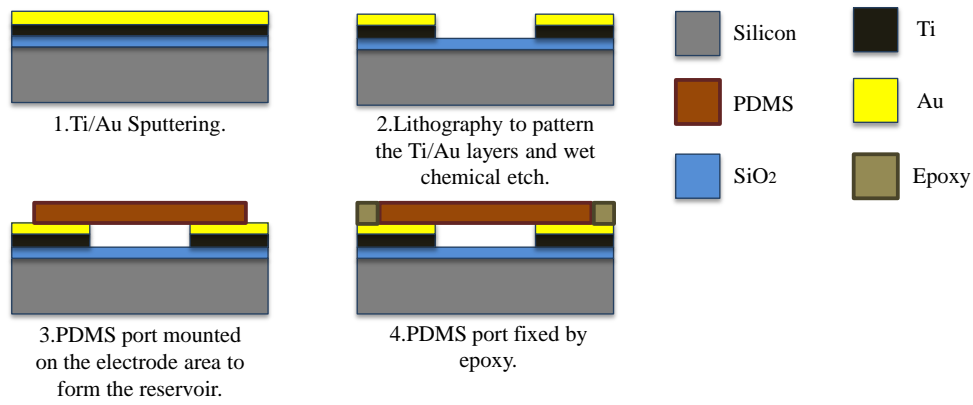


Figure 5. 1: Fabrication flow of the 1st generation of the ER devices using a single mask.

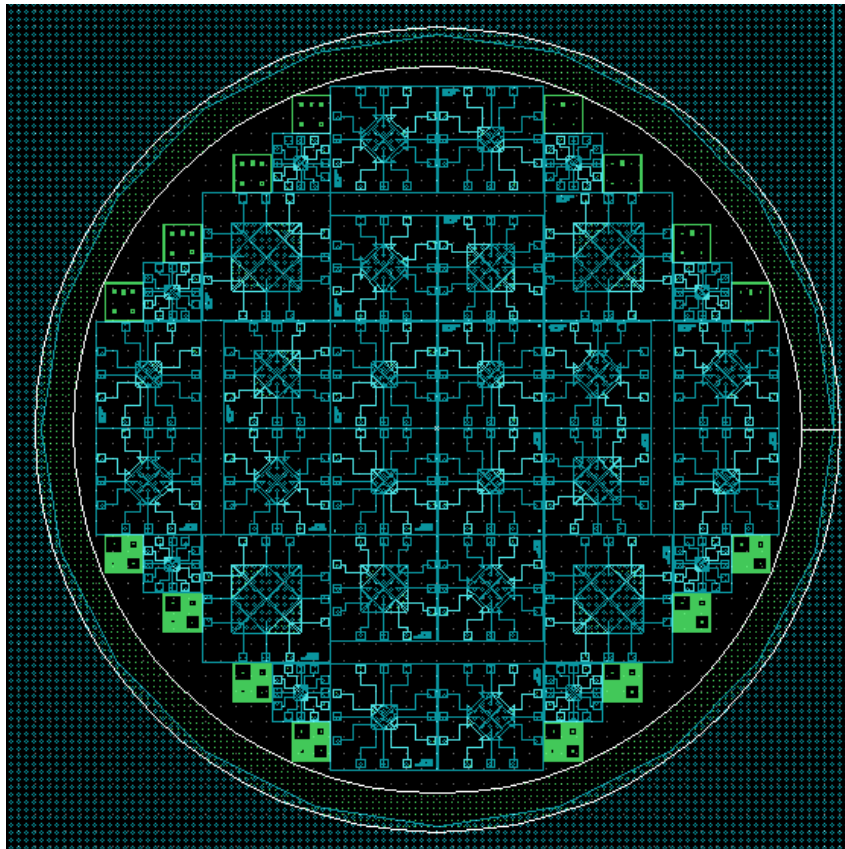


Figure 5. 2: Utilized mask for the fabrication of the 1st generation of the ER devices.

After patterning the photoresist layer, wet etching of Ti and Au layers were carried out with commercial Au etchant and freshly prepared Ti etchant. After etching the Au and Ti layers, the photoresist was stripped using acetone. Finally, the wafer was diced and 32 ER devices with varying dimensions were obtained from each wafer.

The distance between the opposing electrodes was 285 μm in all of the devices. After the fabrication of the devices, a PDMS port was mounted on the measurement area of the ER devices, to form a reservoir for holding the cells. The photograph of the fabricated ER devices with planar pyramidal electrodes is presented in Fig. 5.3. (See Appendix E for fabrication process flow)

PDMS port mounted on the 1st generation of the ER devices

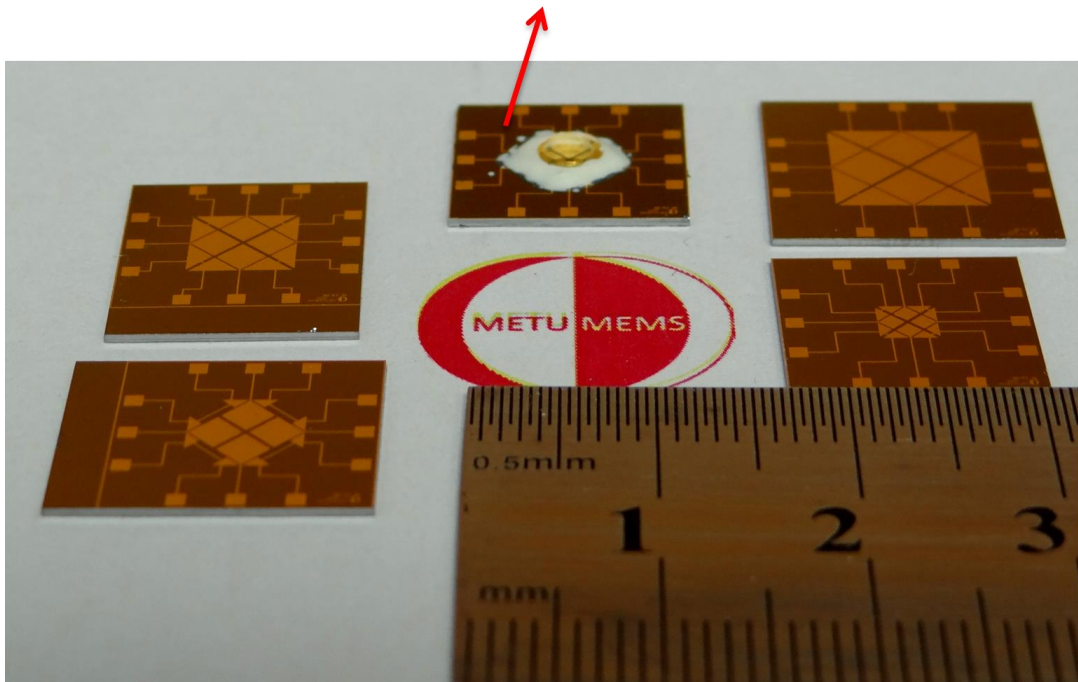


Figure 5. 3: Fabricated prototypes of the 1st generation of the ER devices.

5.2 Fabrication of the 2nd Generation of the ER Devices

In the fabrication of the 2nd generation of the ER devices four masks were utilized. These ER devices were fabricated on a common wafer, which was used for the fabrication of the DEP devices. Therefore, the microchannel fabrication process was applied to the fabrication of the ER devices. The fabrication process includes metal sputtering, wet and dry etching, photolithography, electroplating and polymer (parylene) coating steps. The fabrication process of the 2nd generation of the ER devices is presented in Fig. 5.4.

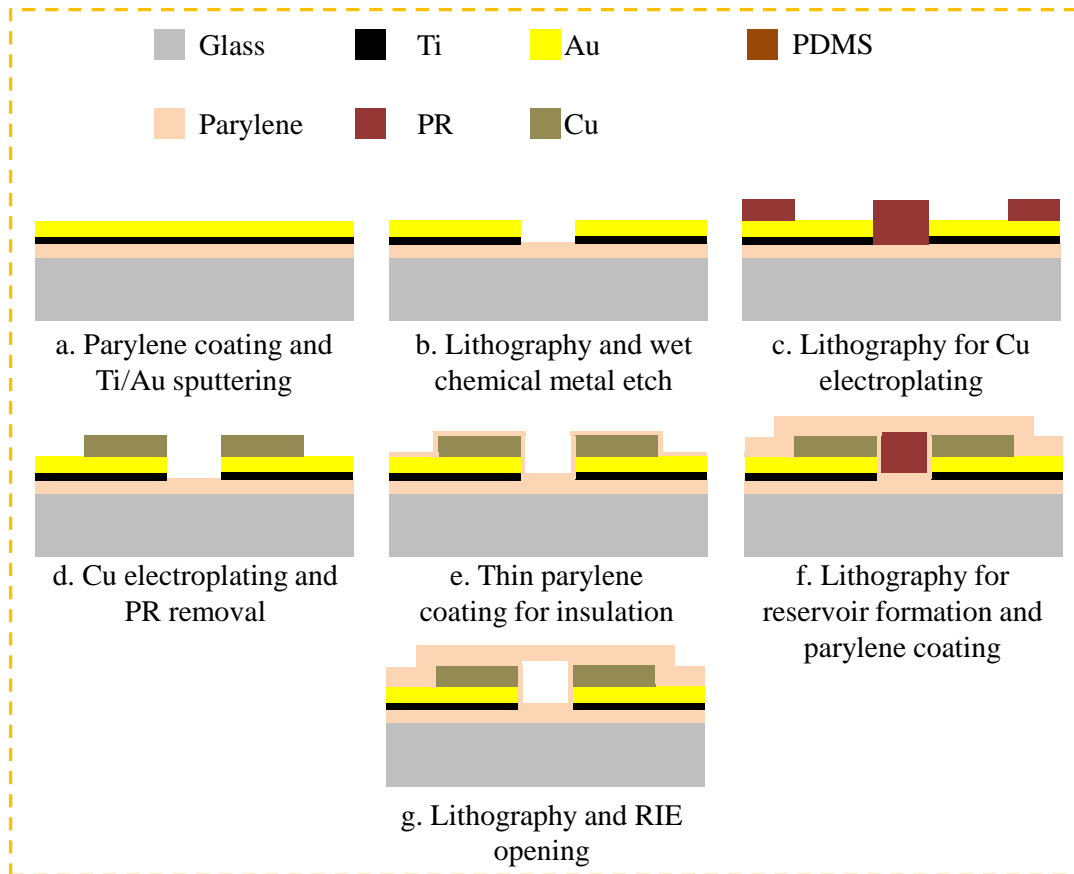


Figure 5. 4: Fabrication flow of the 2nd generation of the ER devices.

As the initial step, piranha cleaning of the glass wafers was performed to obtain a polished and rugged surface, which increases the adhesion capabilities of the surface of the glass wafers. For this purpose, buffered hydrofluoric (BHF) etchant was used. After cleaning the glass wafer, a thin parylene was coated on the wafer. The parylene coating can be realized by simultaneous use of silane. Silane increases the adhesion of the coated parylene to the glass wafer. The coating parameters of the parylene were optimized in our group. A ratio of 1:2 (thickness in micrometers: parylene weight in grams) was used for the coating purpose. Following the initial parylene coating, Ti and Au were sputtered on the wafer to form a seed layer for the Cu electroplating. Then, mask 1 was utilized for patterning of the Ti/Au seed layer (Fig. 5.5). For this purpose, S1813 photoresist was utilized. S1813 photoresist is generally used for the thin coatings. After this step, the Au layer was etched using commercial Au etchants. For Ti etching an

etchant solution was prepared, consisting of 10 ml HF, 10 ml H₂O₂ and 80 ml DI water.

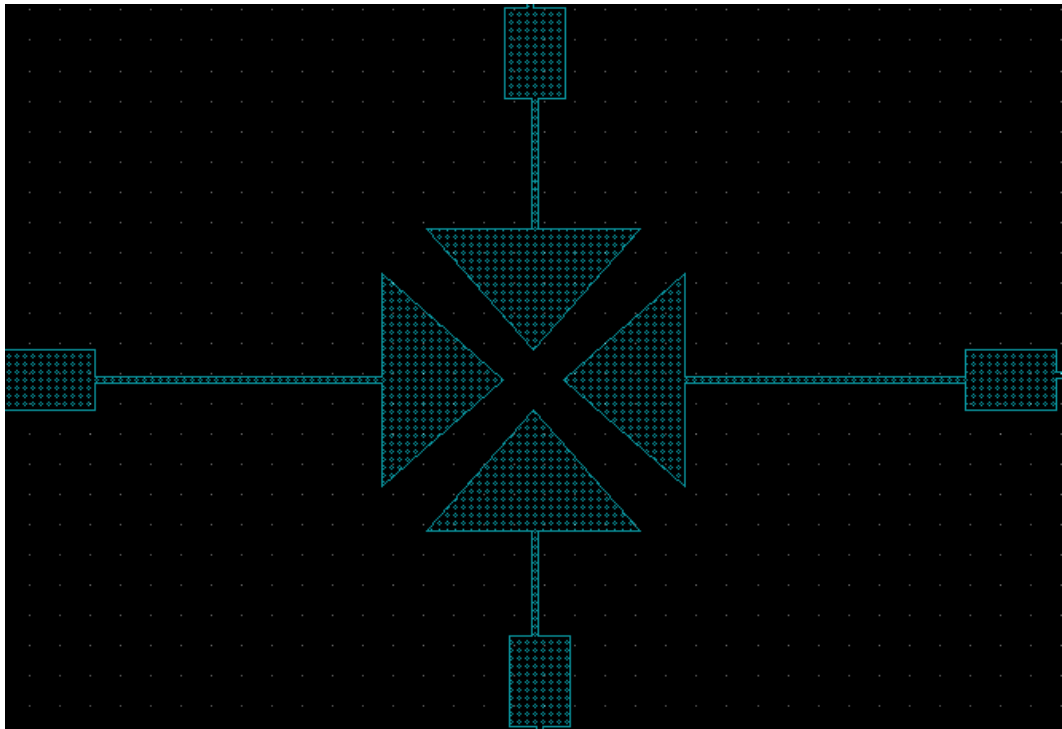


Figure 5. 5: Mask 1 used for patterning of the Ti/Au layer.

After patterning the seed layer, the S1813 photoresist was stripped using acetone. For determining the Cu electroplating area, lithography technique was utilized using the mask 2 (Fig. 5.6). The height of the electroplated electrodes was aimed to be 30 μm . Therefore, AZ9260 photoresist was used which is proper for thick coatings. Then, the 3D electrodes were electroplated using the Cu electroplating technique. The process parameters were optimized as 50 mA current for 90 minutes. The aim of the 3D electrodes is to provide a uniform distribution of the electric field by covering the whole cell body. Therefore, the height of the electrodes should be at least 20 μm . The mask 3 was used for forming the reservoir in the inter-electrode region of the 3D pyramidal electrodes (Fig. 5.7). For this purpose, AZ9260 photoresist was spun and patterned. Then a parylene layer was coated on the wafer to form the reservoir walls. As the final step, RIE was used to open the reservoirs capping and the contact pads (Mask 4). Then the wafer was diced and six ER

devices were obtained from each wafer. (See Appendix E for fabrication process flow)

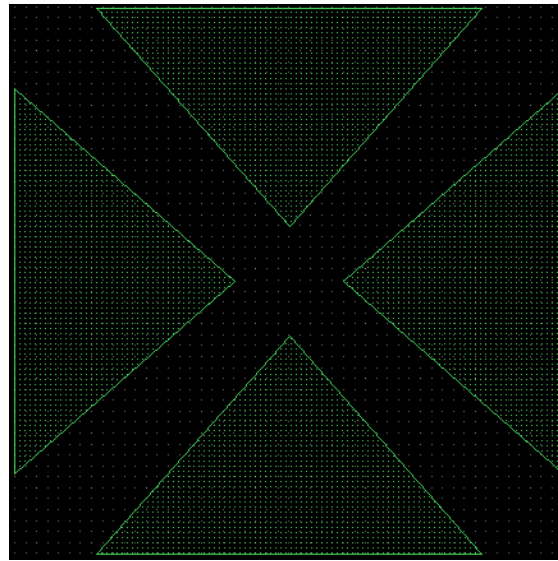


Figure 5. 6: Mask 2 for determining the Cu electroplating areas.

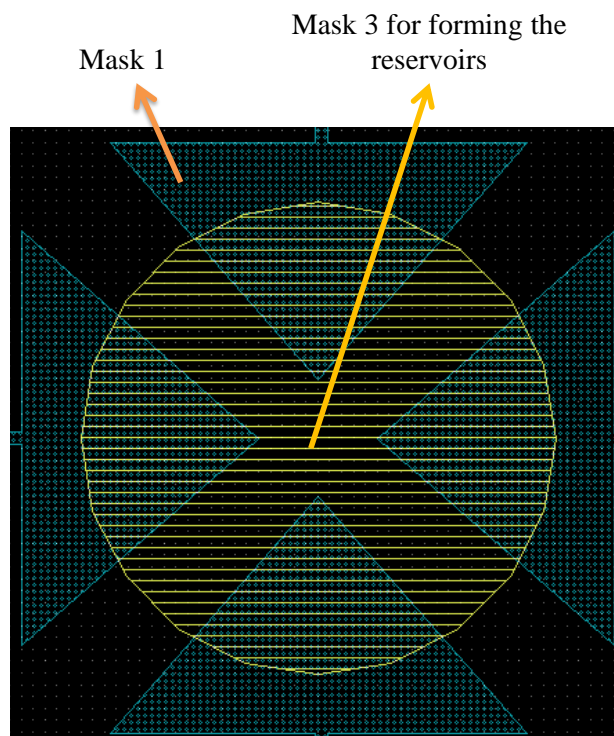


Figure 5. 7 : Mask 3 for determining the reservoir area in the inter-electrode region of the pyramidal electrodes.

In addition to the ER devices, this wafer was used as a common platform for the fabrication of the DEP separation and DEP dielectric characterization devices. Figure 5.8 presents the full view of the designed layout.

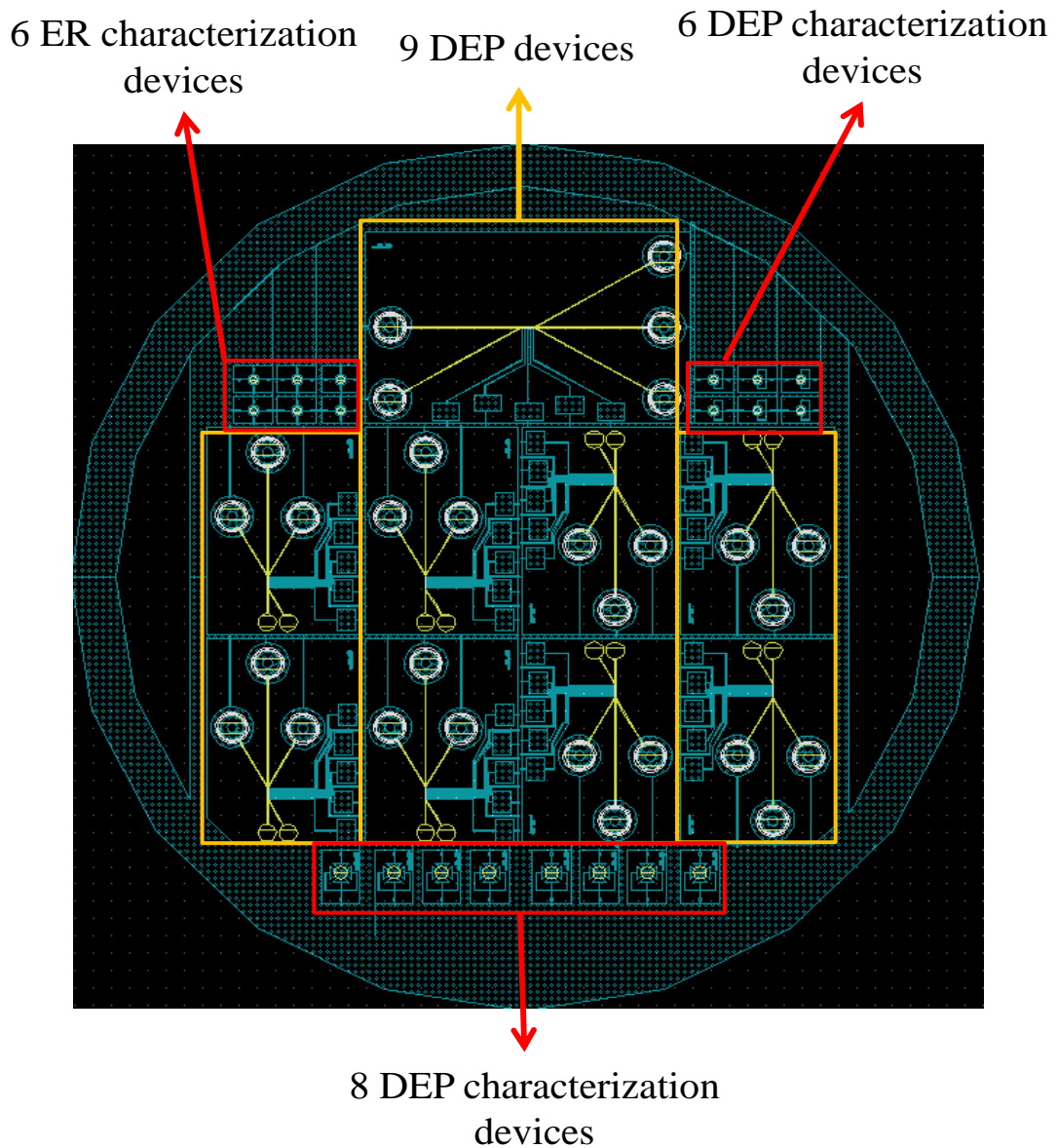


Figure 5. 8: Designed layout for the fabrication of the ER devices on a common wafer with the DEP devices.

After opening the reservoir region using the RIE (mask 4), the photoresist was released in the acetone. The fabricated prototypes of the 2nd generation of the ER devices are shown in Fig. 5.9.

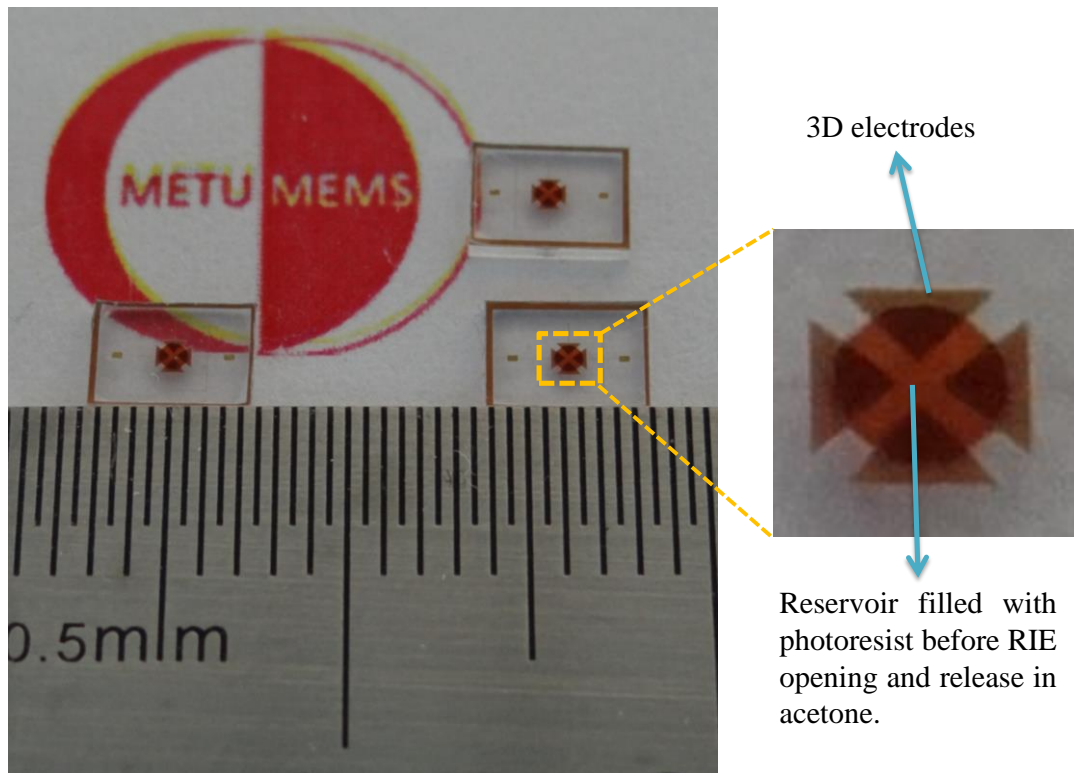


Figure 5. 9: Fabricated prototypes of the 2nd generation of the ER devices with magnified electrode and reservoir region.

5.3 Fabrication of the 3rd Generation of the ER Devices

A single mask fabrication process was used for the fabrication of the 3rd generation of the ER devices. The fabrication process includes metal sputtering, wet etching, lithography, electroplating, and electroless metal deposition. The fabrication process flow of the 3rd generation of the ER devices is shown in Fig. 5.10. (See Appendix E for fabrication process flow)

In the first step a nitride (Si_3N_4) layer was grown on the Si wafer for the insulation purpose. Then the Ti and Au were sputtered on the surface of the wafer to form the seed layer for the Cu electroplating. Then, using the designed dark field mask (Fig. 5.11) the Ti and Au layers were patterned. For this purpose, commercial Au etchant and freshly prepared Ti etchant were utilized. After patterning the metal layers, Cu electroplating was employed for the fabrication of the 3D electrodes. For this, AZ9260 photoresist was spun and patterned. The electroplating parameters were

optimized as 200 mA and 120 minutes. After the electroplating step the photoresist was stripped from the surface of the device using acetone.

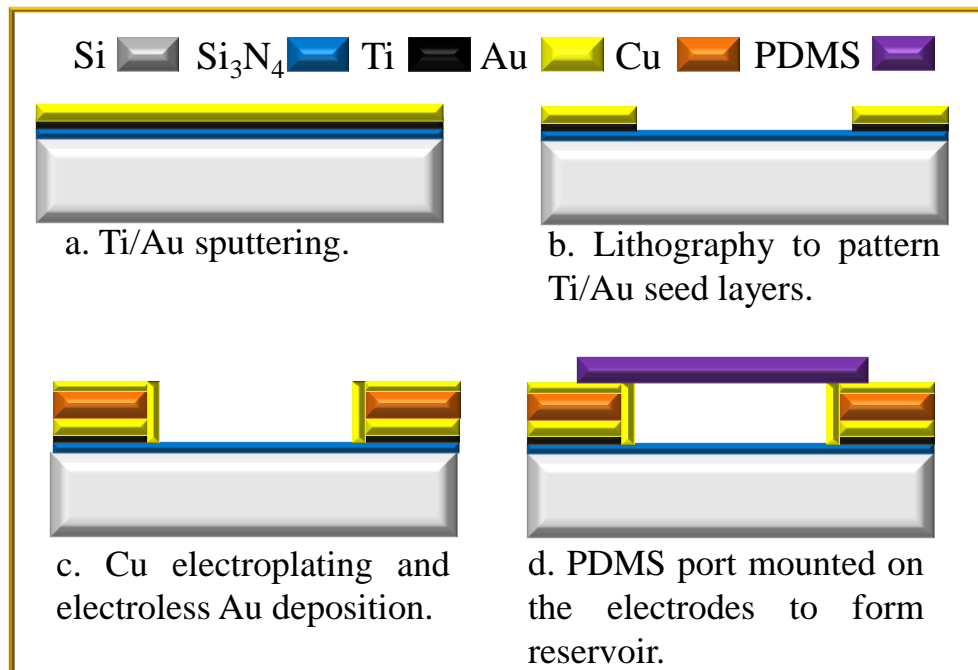
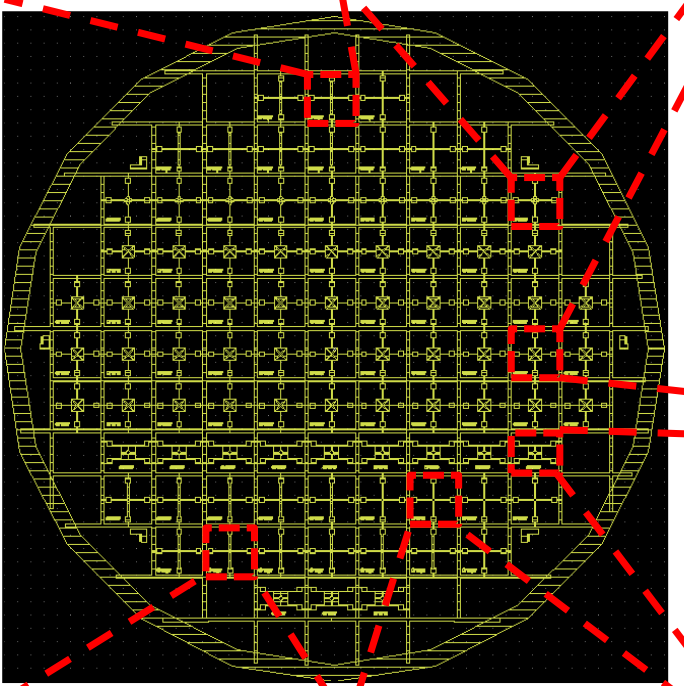
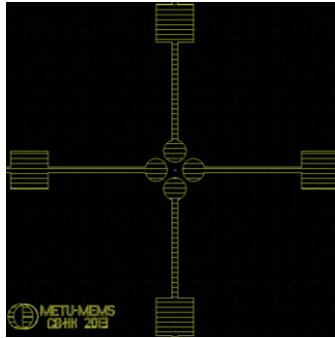
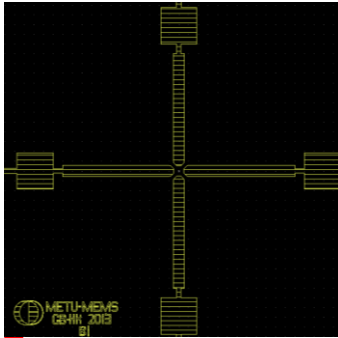


Figure 5.10 : Fabrication flow of the 3rd generation of the ER devices with 3D electrodes, using a single mask.

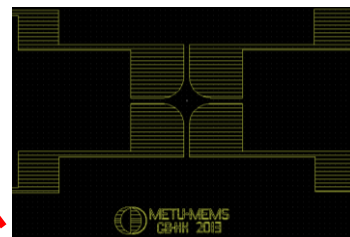
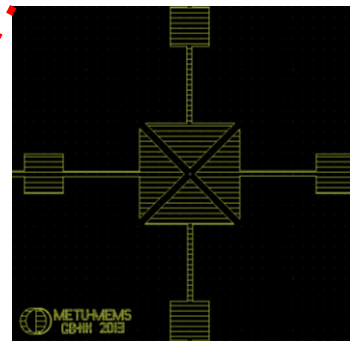
For eliminating the risk of reaction of the Cu electrodes with the PBS containing medium (used during the ER experiments), a thin Au layer (400 nm) was deposited on the electrode regions. To accomplish this, electroless Au deposition technique was utilized, which is a selective deposition technique. Therefore, only the Cu electrodes were coated with the Au layer. Before dicing of the fabricated wafer, an AZ9260 layer was spun on the wafer to eliminate the risk of peeling off of the electroplated electrodes during the dicing process. 88 ER chips with six different electrode geometries were obtained from each wafer. To release the photoresist layer, the devices were kept in acetone for 24 hours. The SEM photographs of the fabricated ER devices with 3D electrodes are shown in Fig. 5.12. The uniformity of the height of the electroplated electrodes is obvious in this figure.

Prolate elliptical

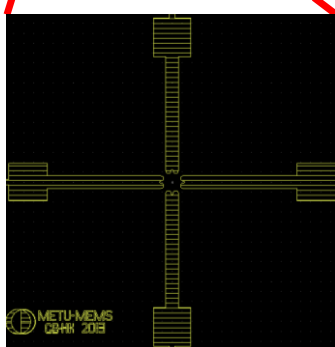
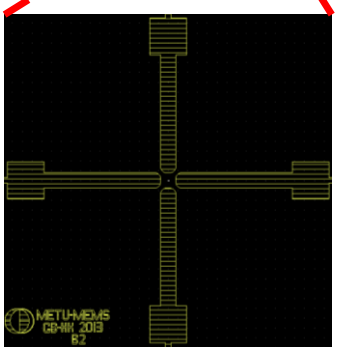
Circular



Pyramidal



Polynomial



Oblate elliptical

Bone

Figure 5. 11: Layout of the designed mask for the fabrication of the 3rd generation of the ER devices.

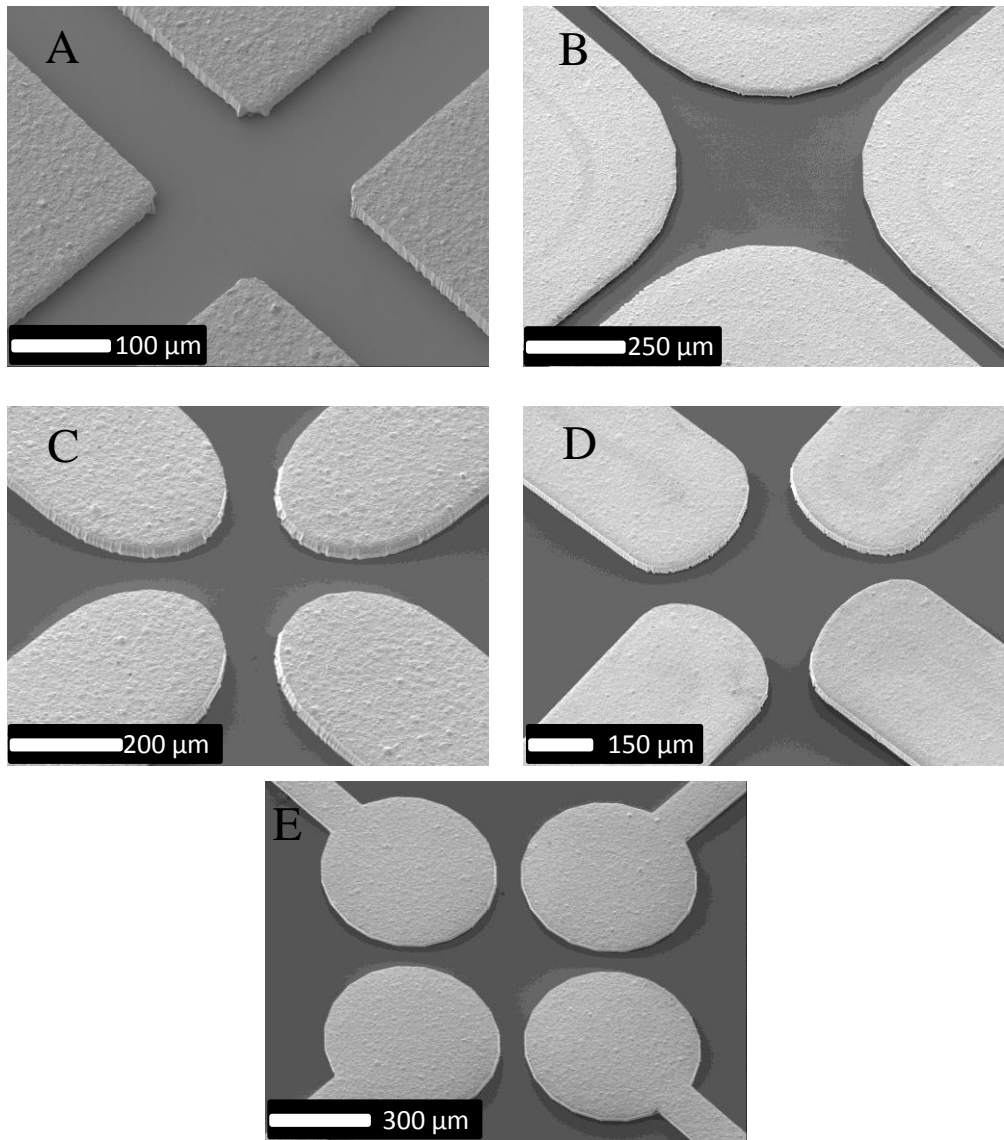


Figure 5. 12 : SEM photograph of the ER devices with 3D electrodes. (A) Pyramidal, (B) Polynomial, (C) Prolate elliptical, (D) Oblate elliptical, and (E) Circular electrodes

CHAPTER 6

RESULTS AND DISCUSSION

This chapter presents the dielectric characterization of the cancer cells using the 3rd generation of the ER devices. In this study the dielectric properties of 9 cell lines were determined using the ER technique. These cells are K562 human leukemia cells and its multidrug resistance (MDR) counterparts, including the imatinib resistant (K562/IMA-0.2, 0.3, 0.5 μM) and doxorubicin resistant cells (K562/DOX-0.1, 0.3, and 0.5 μM). In addition, the dielectric properties of the human breast cancer cells (MCF7) and its doxorubicin resistant (MCF7/DOX-1000 nM) derivation were measured using this technique. Considering the presented results in the Chapter 4 for the characterization of ROT-T and EEF for the ER devices, devices with polynomial electrodes were chosen for analyzing of the dielectric properties of the cells. In this chapter, first the designed and installed test setup for the ER measurements is introduced. Then, the procedures related to the preparation of the biological cells for the ER experiment is presented. Finally the obtained results from the ER dielectric characterization tests will be presented.

6.1 Experimental Test Setup for the ER Measurements

This section introduces the designed and utilized test setup for performing the ER measurements. Figure 6.1 shows the schematic presentation of the installed test setup. A four channel function generator (Agilent-81150A) capable of producing four sinusoidal signals with 90° phase shifted apart was used for

the energizing the quadrupole electrodes (Fig. 6.2). Before energizing the electrodes, 3 μL of the cell suspension (in the room temperature) were loaded into the PDMS reservoir of the ER device. Sinusoidal voltages in the range of 10 - 12.5 V_{PP} depending on the cell type, in frequencies between 1 kHz to 100 kHz (with 5 kHz intervals), were applied to each electrode. For this purpose, 50 Ω coaxial cables with BNC connections were used. The applied voltages were optimized by FEM studies of the effective electric field (EEF) and the magnitude of the DEP force. Then, the applied voltages were tested experimentally to adjust the rotation rate at a measurable range for manual counting of the cell revolution (180-240 rpm). A stopwatch was used to measure the rotation rate of the cells. During the measurements, the cells inside the PDMS reservoir were replaced with fresh cells several times, in order to reduce the possibility of change in cells' dielectric properties due to application of an external electric field. Rotation of cells was recorded using a video microscope (Karl Suss, PM5). The photograph of the experimental setup is shown in Fig. 6.3. The boundaries of the measurement area (in the inter-electrode region) was optimized using FEM analysis to minimize the variation of the rotational torque. The details about the determination of the boundaries of the circular area, where the maximum deviations from the central EEF is limited to 5%, 10%, and 20% is presented in Chapter 4. A circular area with a radial length of approximately 100 μm centered in the center of the electrodes was chosen for the ER measurements. According to the Table 4.1, in this area, the maximum variation of the rotational torque induced on the cells is less than 10% compared to the central torque, which guaranties reproducible test results.

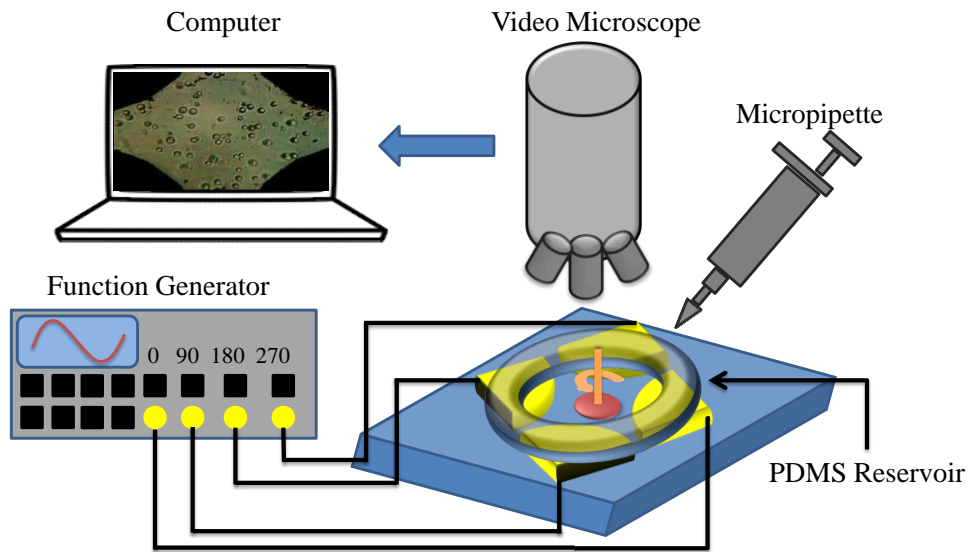
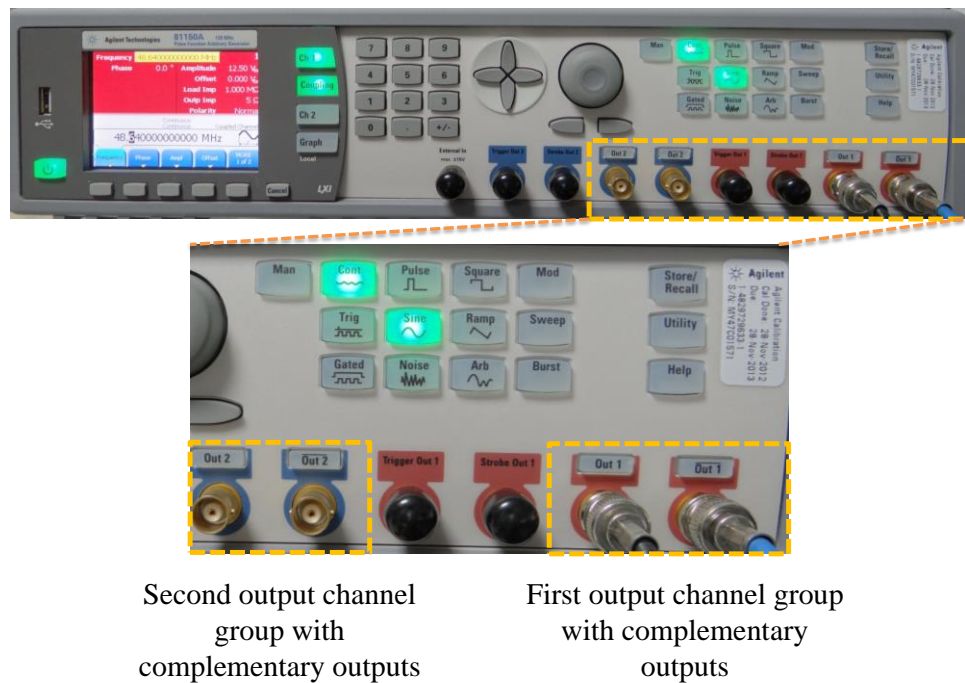


Figure 6. 1: ER test setup. Micropipette is used for loading $3\mu\text{l}$ of cell suspension into the PDMS reservoir. Rotational torque is generated on the cells by energizing the polynomial electrodes with sinusoidal signals in phase quadrature. The rotations of the cells are recorded using a video microscope for further analyses.

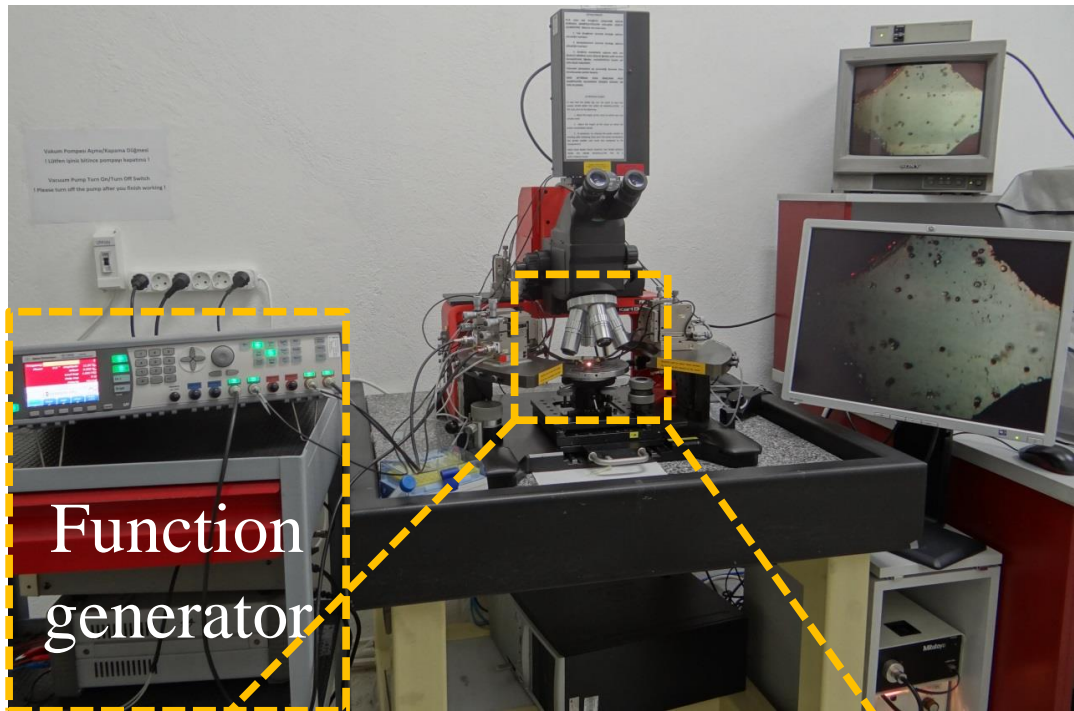


Second output channel group with complementary outputs

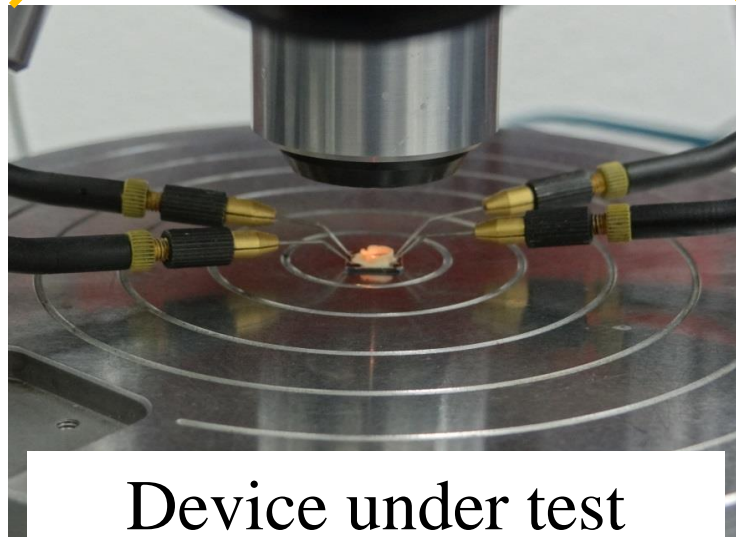
First output channel group with complementary outputs

Figure 6. 2: Utilized four channel function generator for generating four sinusoidal signals in phase quadrature.

One of the challenging issues in the ER tests is the immobilization of cells in their position while a rotating electric field is applied. Therefore, the amplitude of the rotational torque remains constant, which increases the reliability of the collected data. Different methodologies are suggested and developed for immobilizing cells, including use of laser tweezers [73,92–96] and DEP-cages [93,96,97]. In this study, cells were kept in the center of the electrode tips by utilizing the repulsive negative DEP (n-DEP) force. In the low ionic strength media (around 10^{-3} S/m), K562 and MCF7 cells observe n-DEP force at the applied frequency range. Under n-DEP force, cells experience a repulsive force from the electrode tips and are gathered in the center of the inter-electrode region, where the electric field gradient intensity is lower (n-DEP region). Moreover, the use of the low ionic medium conductivities reduces the joule heating and electrolysis effects [3,70]. At each frequency step, rotation rates were measured for 12 different cells placed within the defined circular boundaries. To minimize the influence of the cells from the dipole moment of nearby rotating cells, measurements were limited to the cells separated by at least three cell diameters from the nearby cells [74]. Each test was repeated twice, ascending from 1 kHz to 100 kHz and descending to 1 kHz with 5 kHz intervals. Peak rotation frequency in each medium with specific conductivity was calculated based on the average of collected rotation rates. Instead of selecting a specific peak frequency, a peak frequency with a deviation range was chosen. This method was used in the calculation of the average cells dielectric properties and their standard deviations.



Function
generator



Device under test

Figure 6. 3 : Photograph of the experimental test setup with magnified view of the device under test.

6.2 Cell Preparation

The MDR cancer cells used in this study were raised and cultured in METU Biology Department, in collaboration with Prof. Dr. Ufuk Gündüz. The Philadelphia chromosome positive K562 cell lines were obtained from the German Collection of Microorganisms and Cell Cultures, Germany, and cultured in RPMI

1640 medium (Invitrogen) with fetal bovine serum and penicillin-streptomycin. Imatinib (Novartis) or doxorubicin (Adriamycin, SABA) was added to the culture medium with gradual dose increments until the cells become resistant to desired level of drug concentrations (DOX: 100, 300, 500 nM; IMA: 200, 300, 500 nM) [105]. The human chronic myeloid leukemia cells (K562) and its drug resistant counterparts with different levels of resistance to imatinib (K562/IMA) and doxorubicin (K562/DOX) drugs were grown in RPMI-1640 medium, at 37°C, under 5% CO₂. Before analyzing each population, cells were washed twice by centrifuging at 1000 rpm for 5 minutes at room temperature. Finally, the pellets were re-suspended in isotonic medium, consisting of 8.5% (w/v) sucrose plus 0.3% (w/v) dextrose. Cell concentration was adjusted to 5x10⁵ cells/ml. Phosphate buffered saline (PBS, Santa Cruz Biotechnology, 10X) was used to adjust the medium conductivities (1-8 mS/m).

The same cell preparation procedure was followed for the MCF7 and MCF7-DOX-1000 nM cells. The only difference was in the use of trypsin before the centrifuging step. The MCF7 cells are adherent cells, and adhesion to a surface is essential for their growth (in our case surface of the flask). Therefore, trypsin is used for ease of lift up of the adhered cells from the surface of the growth environment. For this purpose the growth medium (RPMI-1640) was first removed and trypsin was added to cell flask. Generally a short time, about 10 minutes is needed to complete lift up of the cells from the flaks surface. Then the cells were washed by centrifuging the cell suspension at 1000 rpm for 5 minutes and at room temperature.

6.3 Dielectric Characterization of K562 and K562 MDR Cells

Subsequent to measurement of the peak rotation frequencies of each cell population in medium conductivities ranging from 1 to 8 mS/m, a linear formulation was fitted to the data points of the peak rotation frequency multiplied by the cell radius versus the medium conductivity. The slope and the intercept of the fitted line were used in the determination of the effective membrane capacitance and conductance of the cells, respectively. Then, using the low frequency (DC limit) approximation the interior conductivity of the cells was calculated. The details regarding the calculation of dielectric properties of the cell are presented in the Chapter 3.

6.3.1 Dielectric Characterization of K562 Cells

Figure 6.4 shows a photograph of the K562 cells during the ER measurement with polynomial quadrupole electrodes. The peak rotation frequencies of the K562 cells were measured in four media with conductivities of 1.91, 3.97, 5.91, and 8.06 mS/m. Figure 6.5 shows the measured rotation rates for the K562 cells in four media. The measurements were performed in the frequency range of 1-100 kHz. Each data point is the average value, which is obtained from double repeated ER measurements. Presented fitting parameters (slope and intercept point) in Fig. 6.6 were used to calculate the effective membrane capacitance and conductance of the K562 cells. Then, using the calculated membrane properties of the cells, the conductivity of the cell interior was calculated. The dielectric properties of the K562 cells are presented in Table 6.1.

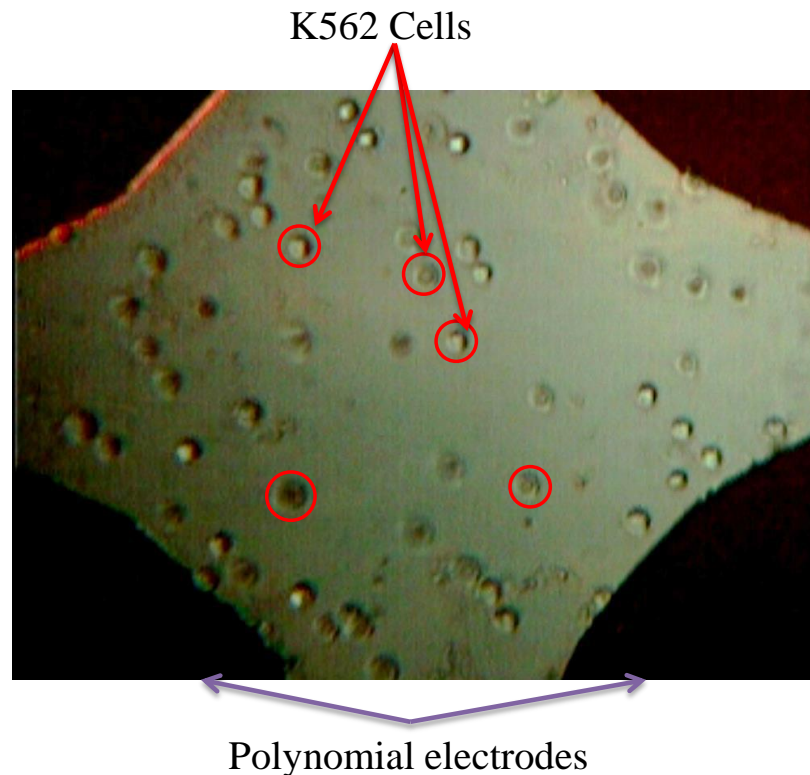


Figure 6. 4: K562 cells under the ER characterization tests.

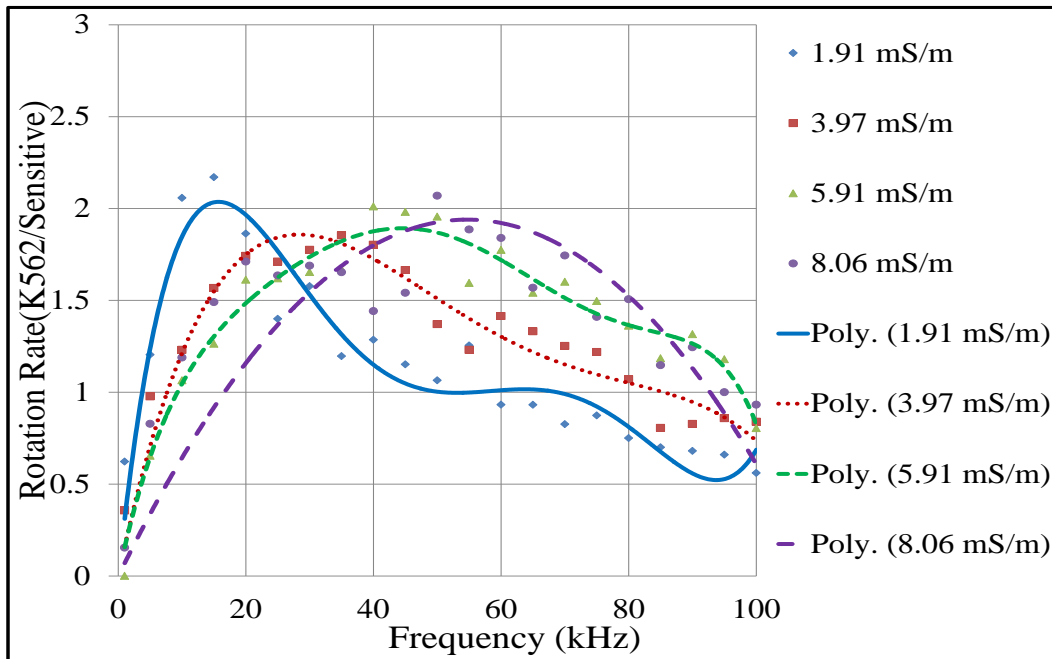


Figure 6. 5: Rotation rates of K562 sensitive cells in the frequency range of 1 kHz to 0.1 MHz, inside four media with different conductivities.

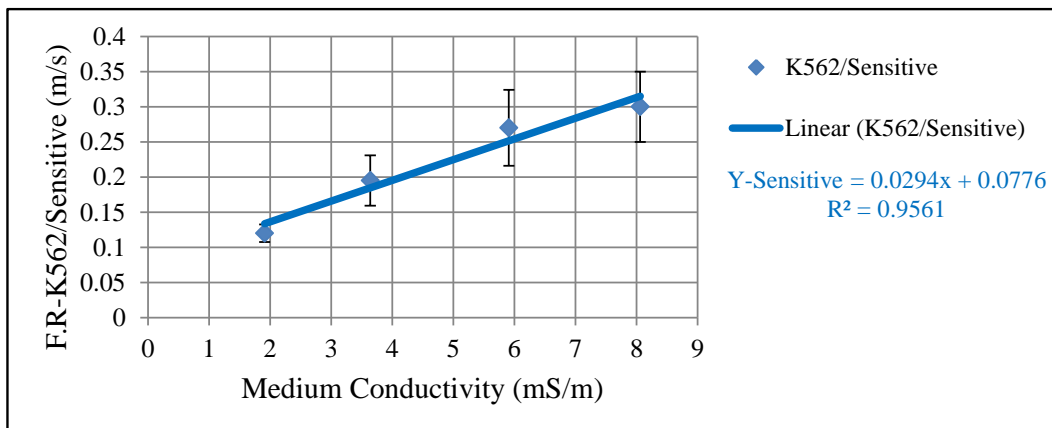


Figure 6. 6: Straight line fitted to the data points of peak rotation frequency and cell radius versus medium conductivity. The membrane capacitance and effective conductance are calculated using the slope and intercept of the fitted line.

Table 6. 1 : Extracted dielectric properties of drug sensitive K562 human leukemia cells, using ER method.

Dielectric Parameters	Dielectric properties
Membrane capacitance [mFm^{-2}]	8.93 ± 1.43
Membrane effective conductance [Sm^{-2}]	336 ± 73
Membrane relative permittivity	10.09 ± 1.61
Cytoplasmic conductivity [Sm^{-1}]	0.32 ± 0.08
Cells radius [μm]	6 ± 1

The membrane and interior dielectric properties of the cells were calculated using the automated MATLAB algorithm, which was presented in the Chapter 3.

6.3.2 Dielectric Characterization of K562/IMA Cells

The peak rotation frequencies of the imatinib resistant human leukemia cells with varying resistance levels to the imatinib drug (K562/IMA-0.2, 0.3, and 0.5 μM) were measured in four media with varying conductivities. The conductivities of the test media were 1.16, 2.44, 5.2, and 8.1 mS/m for K562/IMA-0.2 μM and 1.91, 3.97, 5.91, and 8.3 mS/m for K562/IMA-0.3 μM and 1.91, 3.97, 5.91, and 8.06 mS/m for the K562/IMA-0.5 μM cells. Figure 6.7 shows a photograph of the K562/IMA-0.5 μM cells during the ER measurements with polynomial quadrupole electrodes. The calculated peak rotation frequencies for each cell population inside four media with distinct conductivities are shown in Fig. 6.8 - 10. It is necessary to mention that each polynomial line presents the averaged rotation rates obtained from the double repeated ER measurements. Obtained peak rotation frequencies from the Fig. 6.8 – 10 were used in the fitting of the expression of the straight line to the data points of the peak rotation frequency and average cell radius versus the medium conductivity (Fig. 6.11).

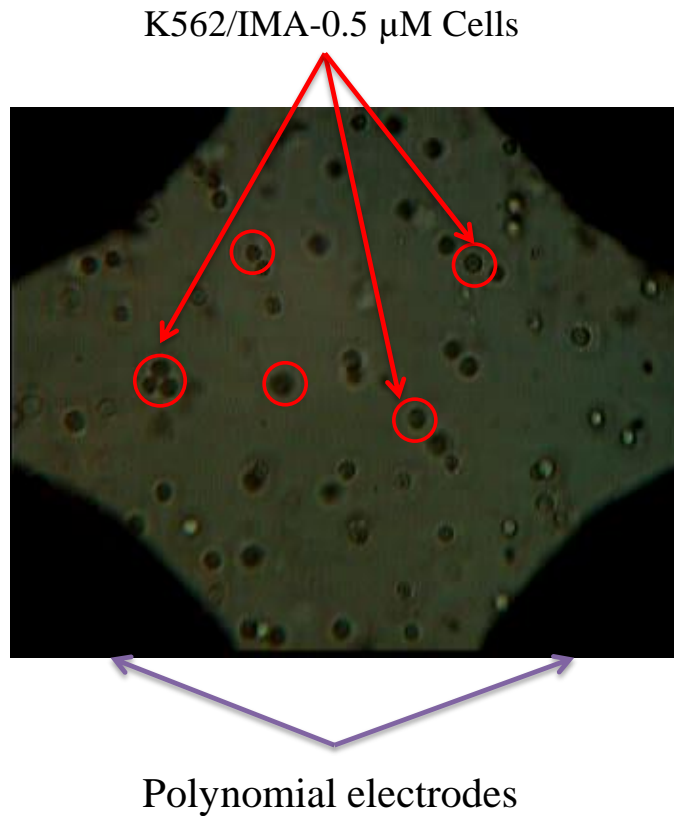


Figure 6. 7: K562/IMA-0.5 μM cells under the ER characterization tests with quadrupole polynomial electrodes.

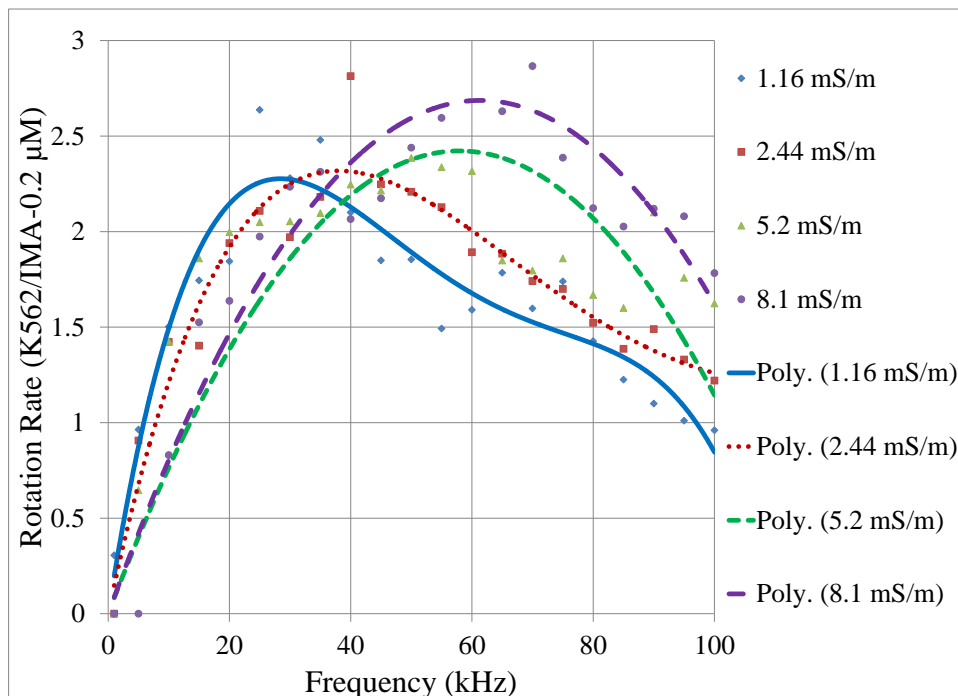


Figure 6. 8: Rotation rates of K562/IMA-0.2 μM cells in the frequency range of 1 kHz to 0.1 MHz, inside four media with different conductivities.

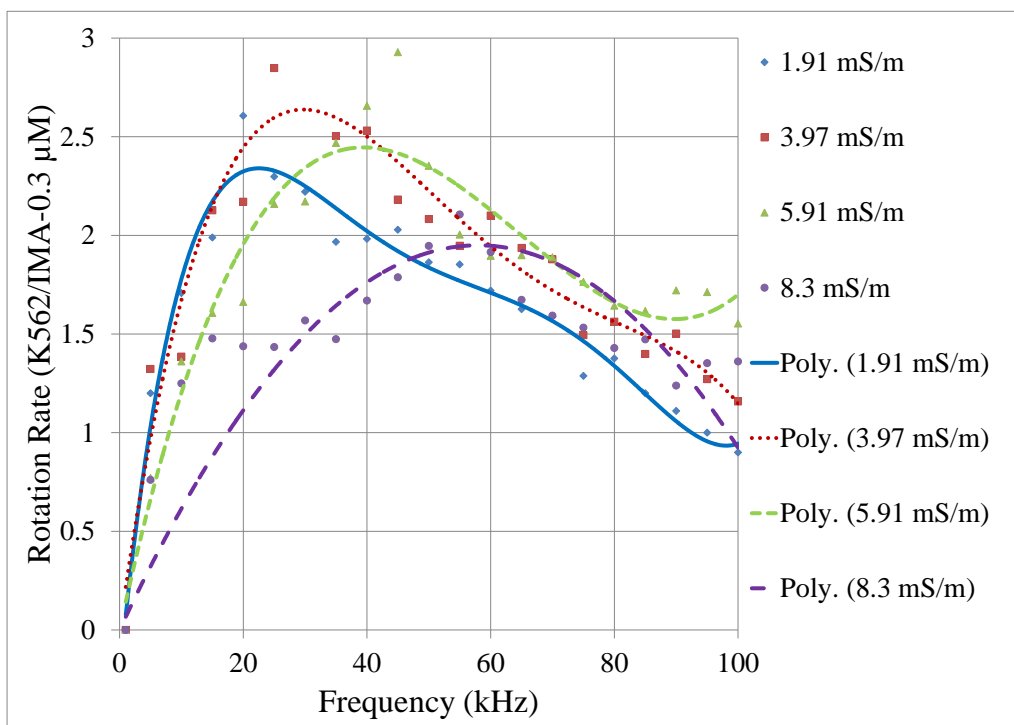


Figure 6. 9: Rotation rates of K562/IMA-0.3 μM cells in the frequency range of 1 kHz to 0.1 MHz, inside four media with different conductivities.

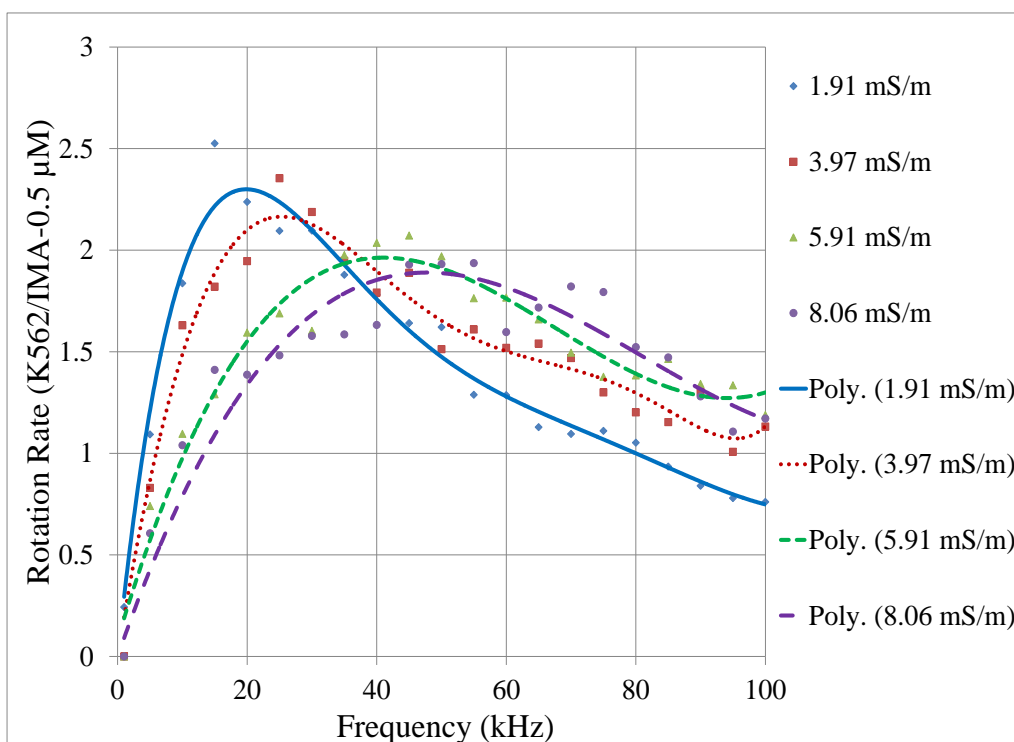


Figure 6. 10: Rotation rates of K562/IMA-0.5 μM cells in the frequency range of 1 kHz to 0.1 MHz, inside four media with different conductivities.

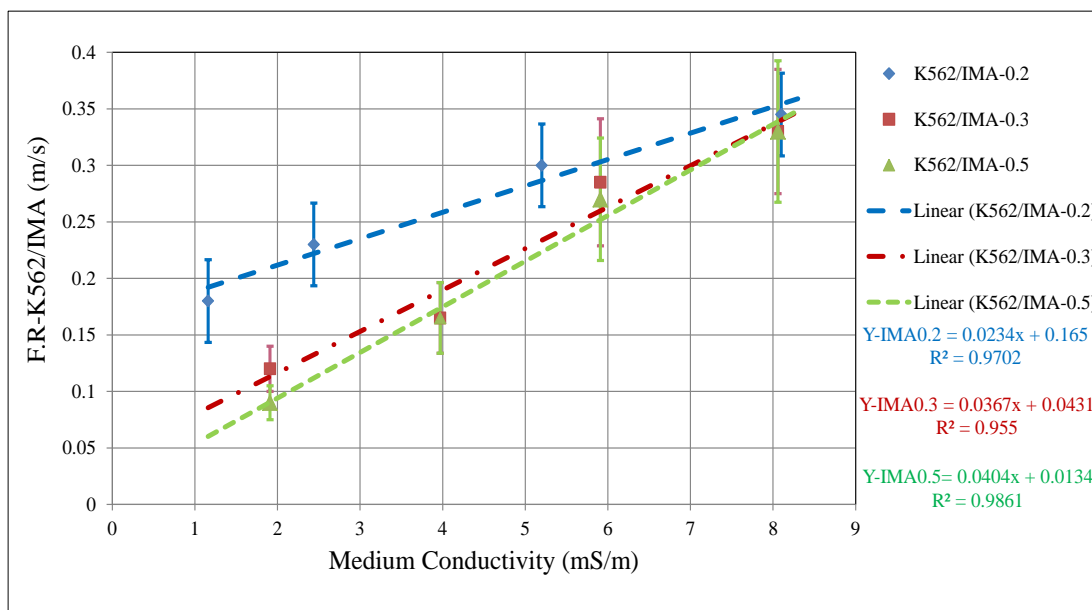


Figure 6. 11: Straight line fitted to the data points of peak rotation frequency and cell radius versus medium conductivity. For each cell population, the membrane capacitance and effective conductance are calculated using the slope and intercept of the fitted line, respectively.

Calculated dielectric properties of the K562/IMA-0.2, 0.3, and 0.5 μM cells are presented in Table 6.2.

Table 6. 2 : Extracted dielectric properties of K562/IMA human leukemia cells, using ER method.

Cell line	IMA-0.2 [μM]	IMA-0.3 [μM]	IMA-0.5 [μM]
Properties			
Membrane capacitance [mFm^{-2}]	15.63 ± 3.02	9.19 ± 1.52	8.10 ± 1.69
Membrane effective conductance [Sm^{-2}]	2953 ± 82	450 ± 20	113 ± 18
Membrane relative permittivity	17.66 ± 3.41	10.38 ± 2.59	9.15 ± 2.81
Cytoplasmic conductivity [Sm^{-1}]	0.60 ± 0.10	0.27 ± 0.10	0.78 ± 0.19
Cells radius [μm]	6 ± 1	6 ± 1	6 ± 1

The slope and the intercept of each line were used to calculate the effective conductance and the capacitance of the cell membrane. Then using the calculated dielectric properties of the cell membrane, the interior conductivity of the cell was determined. The dielectric properties of the cells were calculated using an automated MATLAB program.

6.3.3 Dielectric Characterization of K562/DOX Cells

The peak rotation frequencies of the doxorubicin resistant human leukemia cells, with varying levels of resistance to doxorubicin (K562/DOX- 0.1, 0.3, and 0.5 μM) were measured inside four media with varying conductivities. Figure 6.12 shows a photograph of the K562/DOX- 0.3 μM cells under the ER measurements with quadrupole polynomial electrodes.

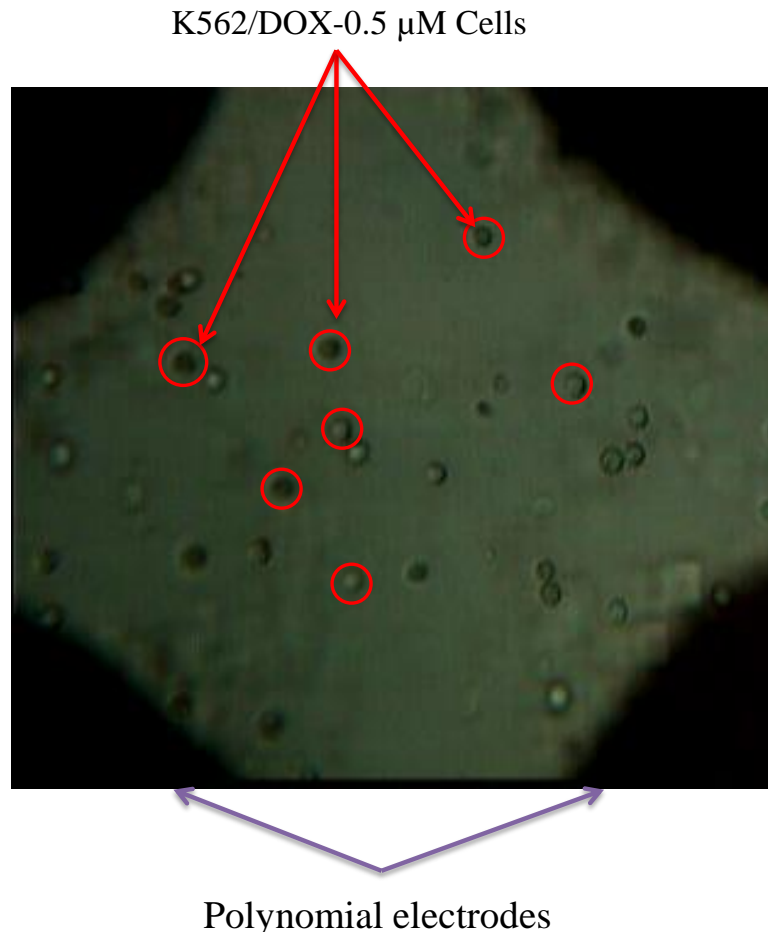


Figure 6. 12 : K562/DOX-0.5 μM cell under the ER measurements.

The conductivities of the test media were adjusted as 1.16, 2.44, 5.2, and 8.1 mS/m for K562/DOX 0.1 and 0.3 μM , and as 1.27, 2.44, 5.2, and 8.1 mS/m for the K562/DOX-0.5 μM . Calculated peak rotation frequencies of the doxorubicin resistant human leukemia cells inside four media with distinct conductivities in the frequency range of 1 kHz to 0.1 MHz are shown in the Fig. 6.13 -15. Calculated peak rotation frequencies based on the obtained results from the Fig. 6.13 – 15 were used in the fitting of the expression of the straight line to the data points of the peak rotation frequency and average cell radius versus the medium conductivity (Fig. 6.16). The slope and the intercept of each cell population were used to calculate the effective conductance and the capacitance of the cell membrane using the slope and intercept method which is discussed in the Chapter 3. Then using the calculated dielectric properties of the cell membrane the interior conductivity of the cell was determined. All of these calculation steps were embedded in the automated MATLAB program, which was introduced in the Chapter 3.

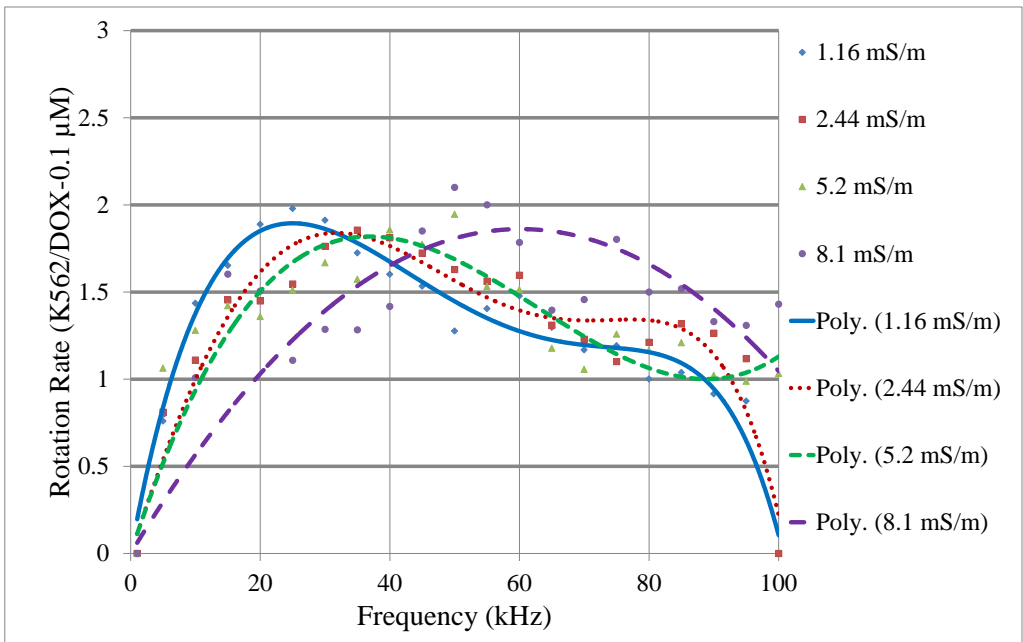


Figure 6. 13: Rotation rates of K562/DOX-0.1 μM cells in the frequency range of 1 kHz to 0.1 MHz, inside four media with different conductivities.

The calculated dielectric properties of the K562/DOX-0.1, 0.3, and 0.5 μM cells are presented in Table 6.3.

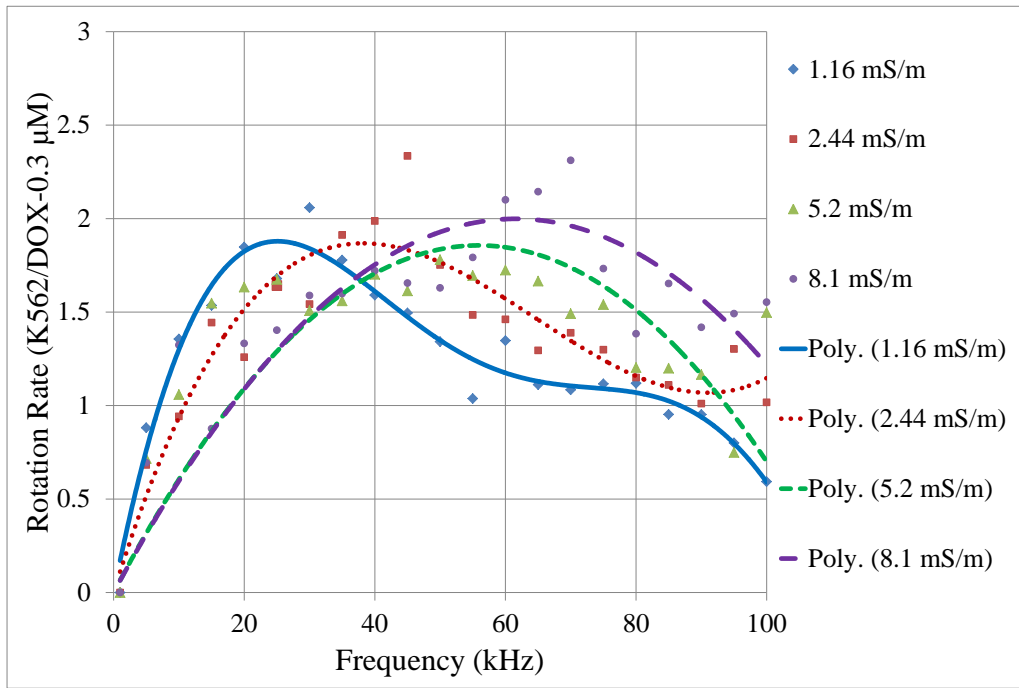


Figure 6. 14: Rotation rates of K562/DOX-0.3 μM cells in the frequency range of 1 kHz to 0.1 MHz, inside four media with different conductivities.

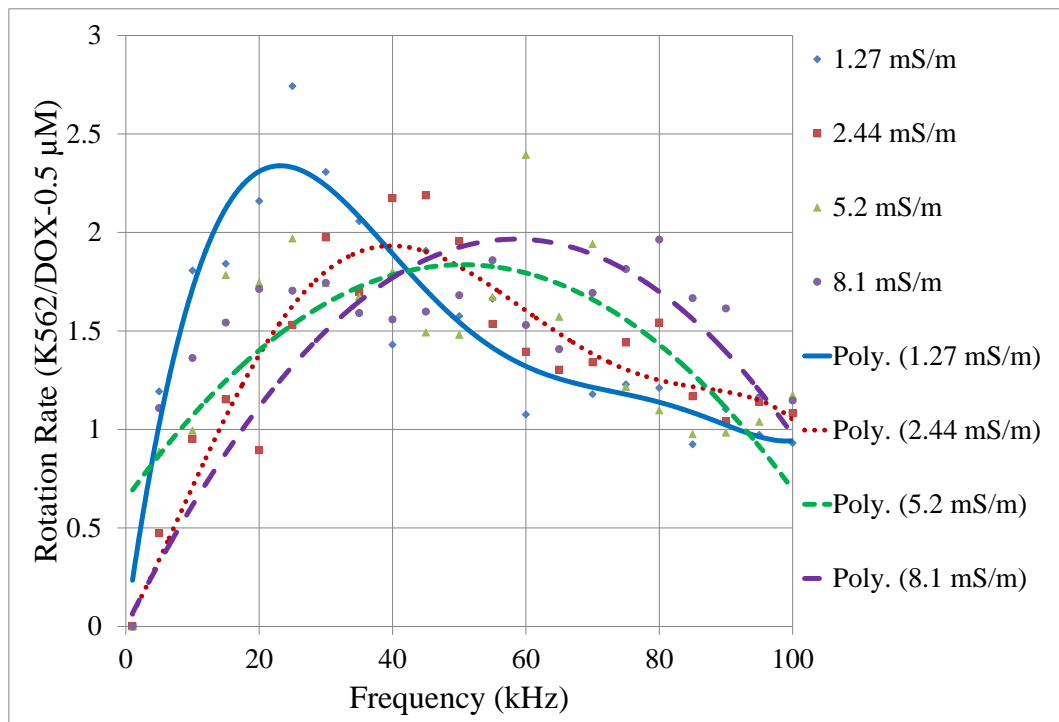


Figure 6. 15: Rotation rates of K562/DOX-0.5 μM cells in the frequency range of 1 kHz to 0.1 MHz, inside four media with different conductivities.

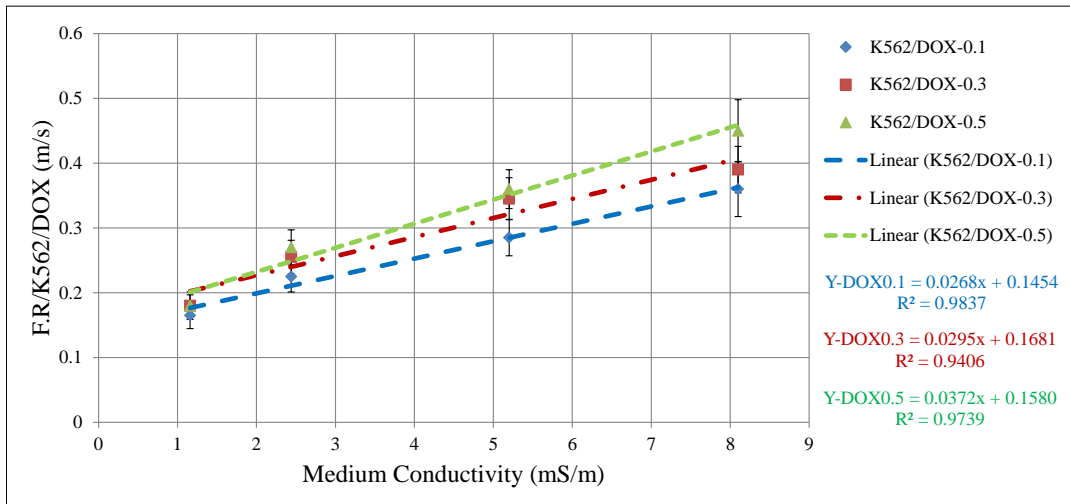


Figure 6. 16: Straight line fitted to the data points of peak rotation frequency and cell radius versus medium conductivity. For each cell population, the membrane capacitance and effective conductance are calculated using the slope and intercept of the fitted line, respectively.

Table 6. 3: Extracted dielectric properties of K562/IMA human leukemia cells, using ER method.

Cell line	DOX-0.1 [μM]	DOX-0.3 [μM]	DOX-0.5 [μM]
Properties			
Membrane capacitance [mFm^{-2}]	12.29 ± 2.15	11.02 ± 1.93	8.70 ± 1.71
Membrane effective conductance [Sm^{-2}]	1810 ± 14	1895 ± 59	1377 ± 22
Membrane relative permittivity	13.89 ± 3.21	12.45 ± 2.17	9.82 ± 1.93
Cytoplasmic conductivity [Sm^{-1}]	0.14 ± 0.01	0.41 ± 0.07	0.26 ± 0.04
Cells radius [μm]	6 ± 1	6 ± 1	6 ± 1

6.3.4 Conclusion

Dielectric characterizations of K562 human leukemia cells and its MDR counterparts were carried out using the ER technique with 3D electrodes. ER

characterization results prove variations in the membrane and the cytoplasmic dielectric properties as cells develop resistance to chemotherapeutic drugs. Development of resistance to the chemotherapeutic drugs in sensitive K562 cells is associated with an increase in the expression of membrane-bound drug efflux pumps (P-gp), which is known to modulate the activity of outward rectifying, volume-activated Cl^- channels [106,107]. This modulation seems to result in an increase in the effective membrane conductance and capacitance at low drug resistance levels (0.1-0.2 μM). With an increase in the surface conductance of the membrane, the capacitance and permittivity of the membrane also increase. However, our findings have shown that further increase in the drug resistance level in the MDR cells results in a gradual decrease in the dielectric properties of the cell membrane, and finally reaching to the levels of sensitive cells at 0.5 μM resistance level. This reversal in dielectric properties of the membrane may imply a different mechanism of rising resistance when cells are exposed to higher drug concentrations.

Our results also indicate that the response of K562 cells to IMA and DOX in terms of effective membrane conductance shows variations. K562/IMA cells exhibited a significant increase (around an order of magnitude) in membrane effective conductance at low drug resistance level (0.2 μM), followed by a rapid reversal to the levels of sensitive cells when drug resistance level increases. K562/DOX cell, on the other hand, exhibited an increased membrane effective conductance at low drug resistance level, and this was stored to a large extent by an increase in drug resistance.

Although there is a definite trend in membrane dielectric properties with varying levels of resistance, the interior conductivity values did not show such a trend, as shown in Tables 6.1-3. Although there is a change in the interior conductivity, no correlation could be driven in relation to the drug resistance level, for both IMA and DOX resistant cells.

The results of this study reveal significant variation in cell dielectric properties of sensitive and resistant cancer cells, which can be utilized as an effective tool to detect MDR through DEP based methods. With the obtained dielectric properties,

MATLAB simulations of the DEP spectrum have been carried out, showing that MDR cells can be differentiated from the sensitive ones through DEP (Fig. 6.17). Such a system can be used effectively in detection of MDR before and during chemotherapy.

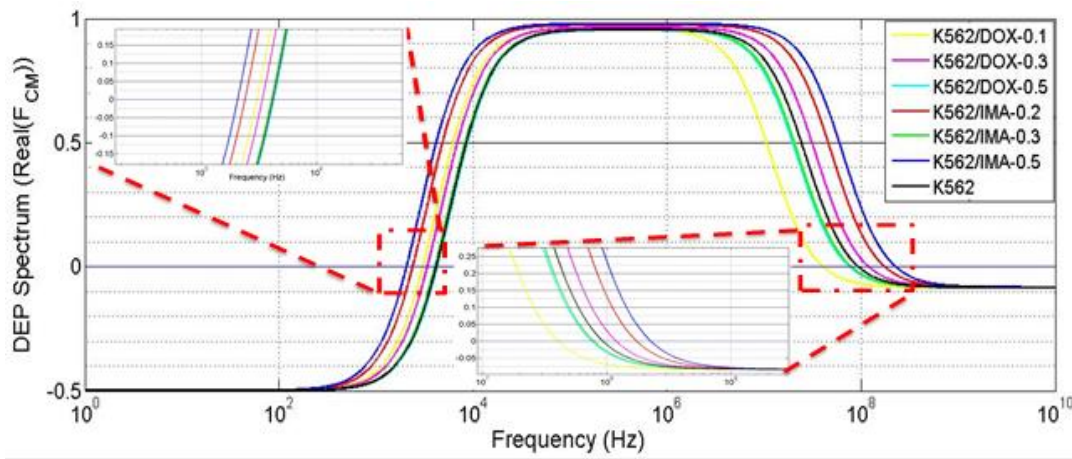


Figure 6. 17: MATLAB simulation of K562 sensitive and resistant cells for DEP spectrum analysis, in medium with conductivity of 1 mS/m and relative permittivity of 78.

6.4 Dielectric Characterization of MCF7 and MCF7/DOX-1 μ M Cells

The peak rotation frequencies of the human breast cancer cells (MCF7) and its doxorubicin resistant derivation (MCF7-DOX-1000 nM) were determined inside four media with varying conductivities. A photograph of the MCF7/DOX-1000 nm cells under the ER measurements with the polynomial quadrupole electrodes is shown in the Fig. 6.18.

The conductivities of the test media were 1.98, 4.2, 6.13, and 8.34 mS/m. By comparing the presented figures for the K562 and MCF7 cells, it can be inferred that the radii of the MCF7 cells are larger than the K562 cells. The average radius of the MCF7 cells was experimentally measured as 10 μ m. The measured average peak rotation frequencies of the MCF7 and MCF7/DOX-1000 nM cells inside four media with varying conductivities are presented in the Fig. 6.19 and 20. The measurements were performed in the frequency range of 1 kHz to 0.1 MHz.

Calculated peak rotation frequencies based on the obtained results from the Fig. 6.19 and 20 were used in the fitting of the expression of the straight line to the data points of the peak rotation frequency and average cell radius versus the medium conductivity (Fig. 6.21).

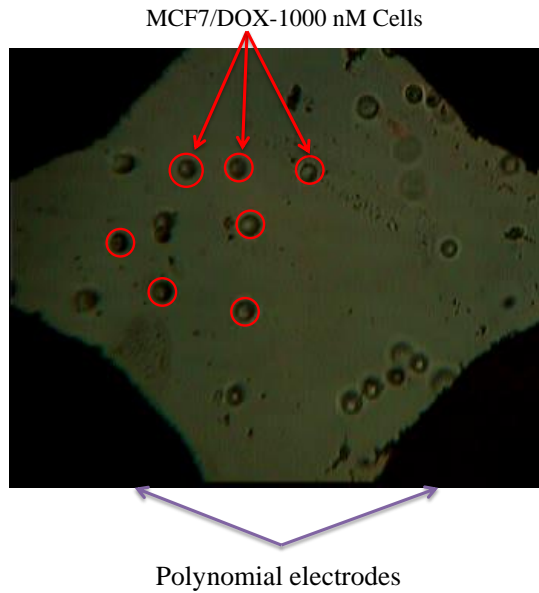


Figure 6. 18: MCF7/DOX-1000 nM cells under the ER measurements.

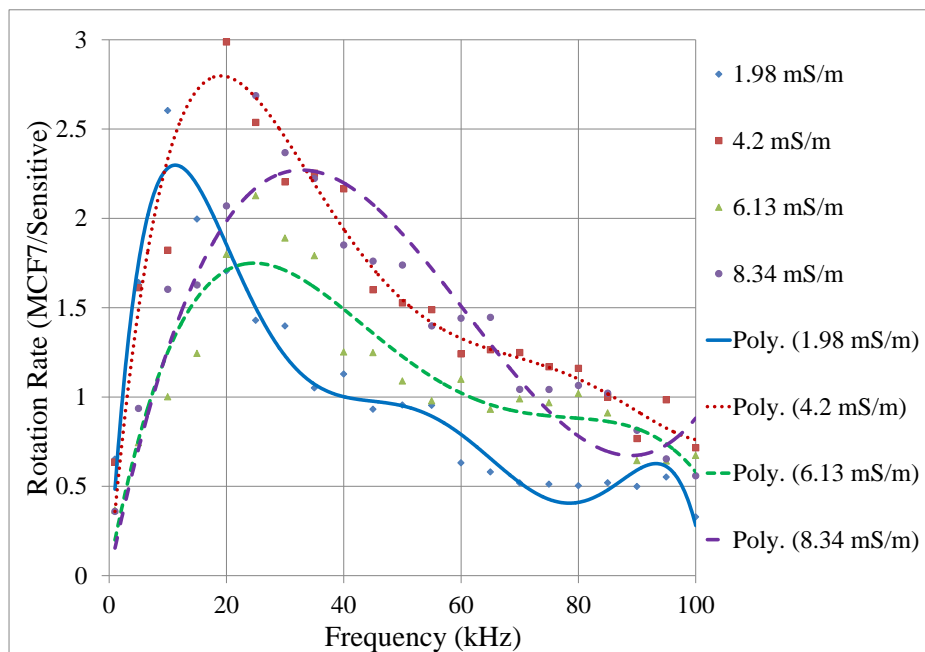


Figure 6. 19: Rotation rates of MCF7/Sensitive cells in the frequency range of 1 kHz to 0.1 MHz, inside four media with different conductivities.

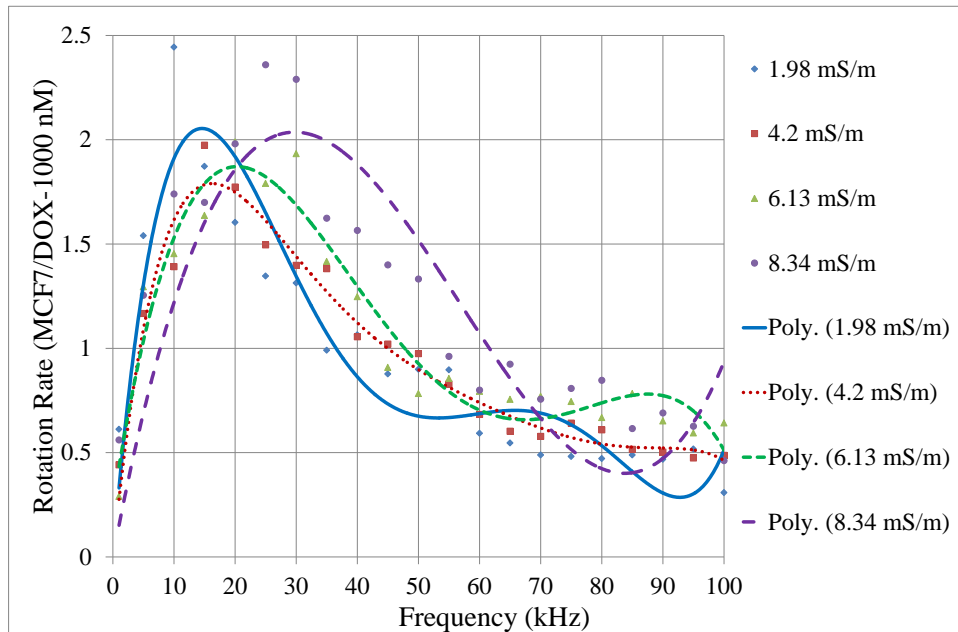


Figure 6. 20 : Rotation rates of MCF7/DOX-1000 nM cells in the frequency range of 1 kHz to 0.1 MHz, inside four media with different conductivities.

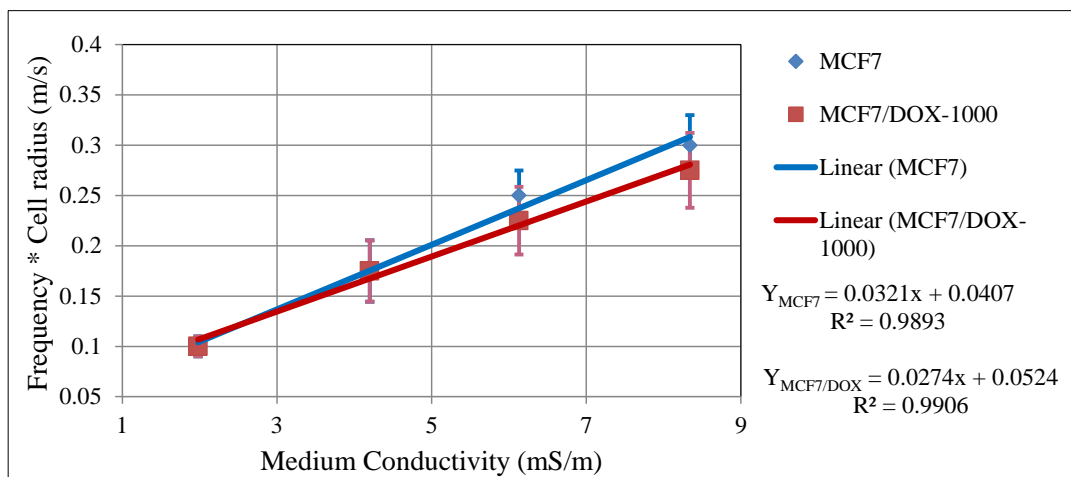


Figure 6. 21 : Straight line fitted to the data points of peak rotation frequency and cell radius versus medium conductivity. For each cell population, the membrane capacitance and effective conductance are calculated using the slope and intercept of the fitted line, respectively.

The slope and the intercept of each cell population were used to calculate the effective conductance and the capacitance of the cell membrane using the slope and intercept method which is discussed in the Chapter 3. Then using the calculated dielectric properties of the cell membrane the interior conductivity of the cell was

determined. All of these calculation steps were embedded in the automated MATLAB program, which was introduced in the Chapter 3.

The calculated dielectric properties of the K562/DOX-0.1, 0.3, and 0.5 μM cells are presented in Table 6.4. These results show variations in cells membrane and interior dielectric properties, as cells develop resistance to the chemotherapeutic drug. An increasing trend is seen in dielectric properties of the cell membrane, as the cells develop resistance to the doxorubicin.

Table 6. 4: Extracted dielectric properties of MCF7 and MCF7/DOX- 1000 nM human breast cancer cells, using ER method.

Cell line	MCF7	MCF7/DOX-1 μM
Properties		
Membrane effective capacitance [mFm^{-2}]	9.92 \pm 0.29	11.76 \pm 1.56
Membrane effective conductance [Sm^{-2}]	253 \pm 2	387 \pm 50
Interior conductivity [Sm^{-1}]	0.50 \pm 0.03	0.43 \pm 0.05
Cells radius [μm]	10 \pm 1	10 \pm 1

However, the interior conductivity of the MDR cells is decreased compared to the drug sensitive MCF7 cells. The same trend was seen in the K562 cells. These variations can be utilized in the design and implementation of the DEP method in separation and detection of MDR in human breast cancer cells.

CHAPTER 7

DIELECTROPHORESIS

This chapter presents the design, simulation, and the fabrication of a MEMS-based dielectrophoresis (DEP) device for separation of the K562 human leukemia cancer cells and its multidrug resistance (MDR) counterparts from the human leukocytes mixture. The introduction about the DEP methods and systems were presented in Chapter 1.3. In this chapter, first the necessary theory of the dielectrophoresis is presented. Second, the simulations and design of the DEP devices will be discussed. Then, the fabrication steps of the devices will be presented. Finally, the FEM analyses of the separation efficiency of the devices will be presented.

7.1 DEP Theory

In the Chapter 2, the dipole model was used to interpret the generated rotational torques on the polarizable particles, due to application of an external electric field. In this chapter, our focus will be directed on the forces exerted to the polarizable particles in the presence of a non-uniform electric field. DEP is the relative motion of the polarized particles and medium, under application of a non-uniform electric field. The time averaged DEP force exerted on the particle of radius R , under a non-uniform electric field of magnitude E , is shown with below expression:

$$\langle F_{DEP} \rangle = 2\pi R^3 \epsilon_m \text{Re}(F_{CM}) \nabla |E^2| \quad (35)$$

where, ε_m is the permittivity of the medium, $Re(F_{CM})$ is the real part of the Clausius-Mossotti factor, and $\nabla|E^2|$ is the gradient of the intensity of the electric field. Clausius-Mossotti factor interprets the polarizability of the dielectric particles compared to the suspension medium and is described using below expression:

$$F_{CM}(\omega) = \frac{\varepsilon_p^* - \varepsilon_m^*}{\varepsilon_p^* + 2\varepsilon_m^*} \quad (36)$$

where, ε_p^* and ε_m^* are the complex permittivities of the particle and the medium, respectively. Complex permittivity describes the frequency dependent response of the particle or the medium with losses in an AC electric field. This factor depends on the conductivity (σ) and permittivity (ε) of the particle/medium and the angular frequency (ω) of the applied electric field. The complex permittivity of the particle and the medium is given by below equation:

$$\varepsilon_n^* = \varepsilon_n - j \frac{\sigma_n}{\omega} \quad (37)$$

where, the subscript n refer to the particle (p) or the medium (m). The polarity of the $Re(F_{CM})$ determines the direction of the motion of the polarized particles in the non-uniform electric field. If the $Re(F_{CM}) > 0$, then the cells are attracted to the region with the higher intensity of the electric field under the positive DEP force (p-DEP). If the $Re(F_{CM}) < 0$, the cells are repelled from the region with high electric field density under the negative DEP force (n-DEP). However, in specific frequencies, the polarization of the particles and the suspension medium can become equal, therefore effective DEP force on the particle will be equal to zero ($Re(F_{CM}) = 0$). This frequency is named as the DEP crossover frequency (f_{co}).

For a multilayered biological cell, the complex permittivity of the particle should be replaced with equivalent of the complex permittivity of the cell (Eq. 18). This expression is utilized to study the frequency dependent responses of the cells. The relative motion of the particle and the medium is the result of the force balance between the hydrodynamic forces and the exerted DEP forces with hydrodynamic drag (or damping) forces inside the medium. The velocity of a particle in a medium with a dynamic viscosity of μ , can be determined using the below equations [108]:

$$v_c = v_m + \frac{\varepsilon_m \operatorname{Re}(F_{CM}) R^2}{3\mu} \nabla|E^2| \quad (38a)$$

$$C_{DEP} = \frac{\varepsilon_m \operatorname{Re}(F_{CM}) R^2}{3\mu}. \quad (38b)$$

In the above equation, v_c and v_m are the velocities of the cells and the medium, respectively. C_{DEP} is the DEP coefficient, determining the ratio of influence of different cells from the gradient of the electric field intensity. The C_{DEP} differs for each cell, depending on the $\operatorname{Re}(F_{CM})$ and the cell radius (R).

7.2 Cell Modeling

The electrical modeling of the cells is essential for studying the DEP separation efficiency of the designed DEP devices. The DEP responses of the cells can be studied by simulation of the real part of the Clausius-Mossotti factor (Eq. 19). The details about the simulation methods were presented in the Section 2.5. We have utilized these methods to extract the frequency dependent response of the leukocytes, human leukemia cancer cell (K562), and its imatinib resistant counterparts (K562/IMA-0.2 μM). In our study, we have investigated the DEP responses of the major subpopulation of the leukocytes which includes granulocytes, T-lymphocytes, B-lymphocytes, and monocytes. In addition, the DEP responses of the erythrocytes are studied, to examine the possibility of implementation of the DEP method in separation of the erythrocytes.

7.2.1 Simulation of DEP Responses of the Cells

For simulation of the real part of the Clausius-Mossotti factor, the dielectric properties of the leukemia cells are adopted from the available data base in the literature [1,71,109]. For simulating the DEP responses of the K562 sensitive and K562/IMA-0.2 cells the reported properties of the cells in this study are utilized [52,53]. The dielectric properties of the cells are presented in Table 7.1. The presented data in the Table 7.1 reflects the average values for the cells. By implementing the above values in the written MATLAB algorithm, the DEP responses of the cells are extracted for the frequency range of $1 - 10^{10}$ Hz. Figure 7.1 shows the MATLAB simulation results for the real part of the Clausius-

Mossotti factor. In these simulations the double layer modeling of the cells were utilized (Eq. 18). The conductivity and relative permittivity of the suspension medium is assumed as 5 $\mu\text{S}/\text{cm}$ and 78, respectively. In the applied electrical frequency of 160 MHz, the human leukemia cells are under p-DEP force, while the cancer cells and erythrocytes experience n-DEP force.

Table 7. 1: Dielectric properties of the utilized cells in this study.

Cell type	σ_i [S/m]	ϵ_i	C_m [mF/m ²]	G_m (S/m ²)	R [μm]
Granulocyte	0.6	150.9	11	-	4.71
T-Lymphocyte	0.65	103.09	10.5	-	3.29
B-Lymphocyte	0.73	154.4	12.6	-	3.29
Monocyte	0.56	126.8	15.3	-	4.63
Erythrocyte	0.52	57	9	-	3
K562	0.32	60	8.93	336	6
K562/IMA-0.2	0.6	60	15.63	2953	6

The following results can be concluded from the presented simulations:

- (1) The erythrocytes and human leukemia cells are under the same type of the DEP force (n-DEP), therefore the separation of these cells from each other is not possible.
- (2) The electrical frequency of 160 MHz can be used in the separation of the cancer cells from leukocytes, due to different type of the DEP forces experienced by the leukocytes and cancer cells.

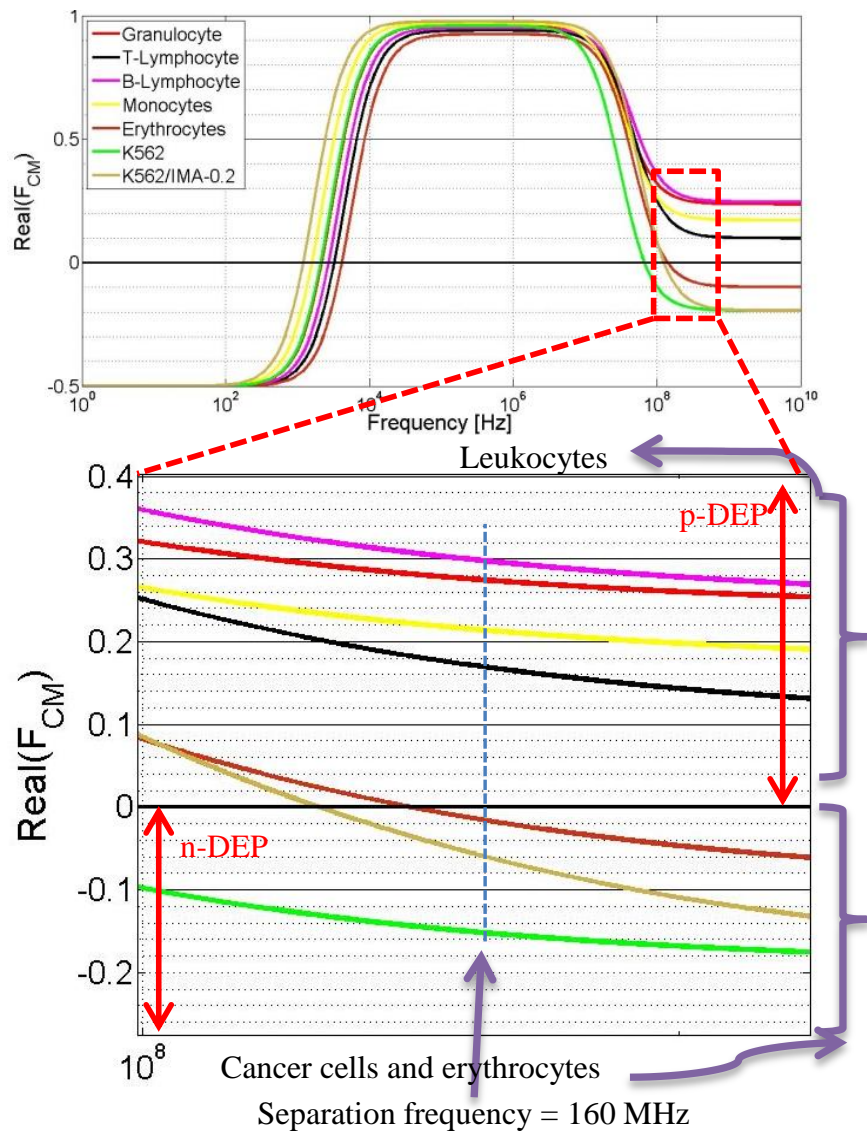


Figure 7. 1: Simulated $\text{Re}(F_{CM})$ for the blood cells and the cancer cells, with magnified view of the proposed separation region at the $f=160 \text{ MHz}$.

7.3 Design Criteria

There are number of important factors that should be determined before designing a DEP device, which are:

1. The application of the DEP device should be specified, which can be such as separation, trapping, focusing, and etc.
2. The electrode type and geometry such as planar (2D), 3D, surface electrodes, bottom and top electrodes, interdigitated, and etc.

3. Design parameters such as pressure, flow rate, applied voltage, channel dimensions, electrode height and size, and etc.

Therefore, before starting to design a DEP platform, the exact application of the DEP device should be defined. In our case, we are aiming to use the DEP device to separate cancer cell from leukocyte mixtures, based on the variations in the dielectric properties of the cells. Therefore, the designed device should be capable of generating high p-DEP regions. In addition, two outlets are essential for collecting the separated leukocytes and the cancer cells. Moreover, to focus the fluidic streamline of the cells in middle of the DEP separation channel, hydrodynamic focusing is utilized, using two lateral inlet channels. The details on the design parameters of the DEP devices are presented in below sections.

7.3.1 Design

As mentioned in above Section, we are aiming to utilize the DEP technique to separate the cancer cells from human leukocyte cell mixture. For this purpose, in addition to the variations in the cell radius, the most important separation criterion is the variations in the dielectric properties of the cells. By modeling of the DEP response of the human leukocytes subpopulation and the K562 human leukemia cells and its MDR counterparts it was found that in the high frequency range (160 MHz), the type of the DEP forces seen by cells differ from each other. Using the MATLAB simulation it was shown that, in the applied frequency of 160 MHz, the K562 cells are experiencing n-DEP force, while the leukocyte cells are under the p-DEP force. Therefore, this frequency was chosen as the separation frequency of our devices.

We have designed the DEP devices with side-wall 3D electrodes. Total of five active electrodes with 30 μm height and 150 μm lengths were used. In addition, 3D potentially floating electrodes were utilized between each pair of the active electrodes to extend the non-uniformity of the electric field in the separation channel. Total of 12 potentially floating electrodes with 30 μm heights and 10 μm length were used for enhancing the separation efficiency of the devices. The schematic view of the designed DEP devices is shown in Fig. 7.2. Utilization of floating electrodes enables use of lower number of active electrodes without

sacrificing the generated DEP force. Successive use of active electrodes leads to an increase in the introduced current density to the microchannel, which can result in cell damage and uncontrolled test conditions due to resistive thermal heating of the test medium.

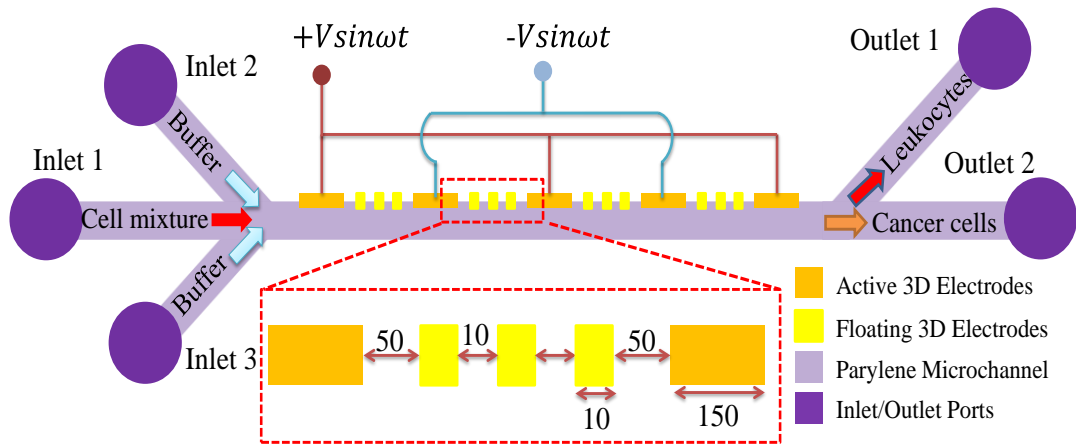


Figure 7. 2: Schematic view of the designed DEP device with 3D isolated electrodes, together with the critical dimension of the device, in μm .

In addition, use of successive active electrodes can lead to the cell stiction (trapping) in the electrode region (high p-DEP region in the vicinity of the active electrodes), which can block the fluidic flow partially or completely. The potentially floating electrodes enhance the separation efficiency of the DEP devices, with extending and distributing the generated electric field gradient in the inter-electrode (active electrodes) region. The designed layouts of the devices together with the critical dimension of the devices are shown in Fig. 7.3. The designed device has two pressure controlled inlets for focusing the cell mixture to the middle of the separation channel (inlets 2 and 3). Buffer medium with optimized pressure is pumped from these inlets. The cell mixture, including cancer cells (K562 human leukemia cells) and the leukocytes cell mixture are pumped into the separation channel with velocity controlled fluid through the inlet 1. Two outlets are available in our devices. The outlet 1 is used for collecting the separated human leukocytes, while the outlet 2 is used for the separated K562 cells and its MDR derivations.

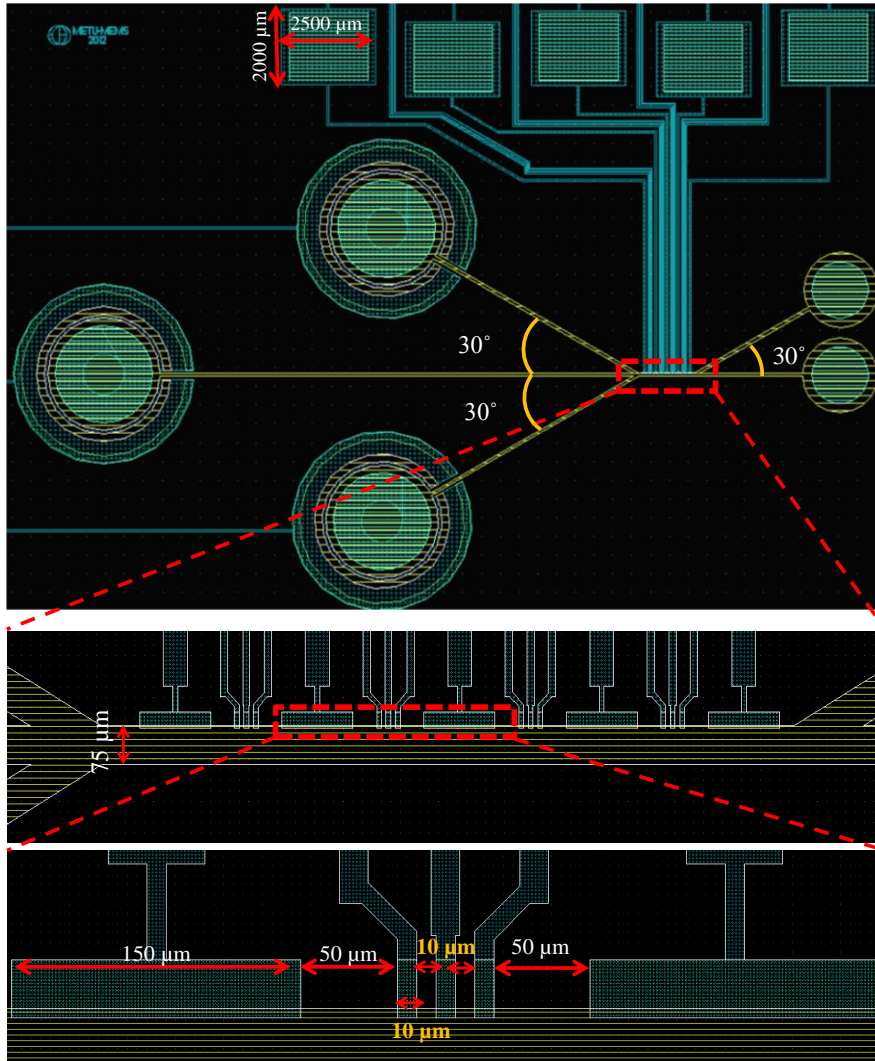


Figure 7. 3: Designed layout of the DEP devices together with the critical dimensions of the devices.

The width of the separation channel is optimized as 75 μm . Although increasing the channel width can increase the flow rate of the device, it can result in ineffective p-DEP force far from the side-wall electrodes. Therefore, the separation efficiency of the devices can drop significantly. The height of the microchannel is optimized as 30 μm , therefore the fabricated 3D electrodes, covers all the channel height. The total length of the separation microchannel is approximately 1450 μm . It was aimed to use the nano-ports in the inlet, therefore to reinforce the inlets; the electroplating was performed in the inlet installation area. However, in the outlets, only reservoirs were utilized. The design parameters of the DEP devices are shown in Table 7.2

Table 7. 2: Design parameters of the DEP devices

Parameters	Values
Active electrode length (μm)	150
Active electrode height (μm)	25-30
Floating electrode length (μm)	10
Floating electrode height (μm)	25-30
Channel width (μm)	75
Channel height (μm)	25-30
Insulating parylene thickness (μm)	0.3
Distance between active electrodes (μm)	150
Distance between the floating electrodes (μm)	10
Distance between floating and active electrodes (μm)	50
Number of active electrodes	5
Number of floating electrodes	12

7.3.2 Simulations

The COMSOL Multiphysics software was utilized for the FEM analyses of the devices. The performed simulations include both electrostatics and incompressible Navier-Stokes simulations. The electrostatics simulations were performed for studying the magnitude of the generated non-uniform electric field, which shows the magnitude of generated p-DEP force. In addition, the incompressible Navier-Stokes simulations were utilized for extracting the fluidic streamline of the cells due to applied electric field.

According to the Eq. 35, the applied DEP force on a particular cell population, with similar size and dielectric properties, depends on the gradient of intensity of the electric field ($\nabla|E^2|$). The $\nabla|E^2|$ is a spatial-dependent term; therefore, the position of the particles is a determining factor in calculation of the effective DEP force on the particles.

$$\nabla|E^2| = \left[\begin{array}{c} \left(\frac{\partial^3}{\partial x^3} + \frac{\partial^3}{\partial y^2 \partial x} + \frac{\partial^3}{\partial z^2 \partial x} \right) \hat{x} \\ \left(\frac{\partial^3}{\partial y^3} + \frac{\partial^3}{\partial x^2 \partial y} + \frac{\partial^3}{\partial z^2 \partial y} \right) \hat{y} \\ \left(\frac{\partial^3}{\partial z^3} + \frac{\partial^3}{\partial x^2 \partial z} + \frac{\partial^3}{\partial y^2 \partial z} \right) \hat{z} \end{array} \right] * V^2 \quad (39)$$

As seen in above expression, the gradient of the electric field depends on the 1st and 2nd derivations of the applied electrical potential along the x, y, and z axis. Eq. 39 was used to study the generated gradient of the intensity of the electric field during the electrostatic simulations with the COMSOL software. 3D simulations were performed for studying the magnitude of the $\nabla|E^2|$ in the separation channel of the DEP devices. Figure 7.4 shows the simulation of the gradient of the electric field intensity in the DEP separation region of the devices. In order to be able to study the electrostatic and microfluidic forces simultaneously, the simulations were performed in two steps. Firstly, the time-dependent electrostatics simulations were performed. Then, the simulation results were stored for the time instant in which the applied DEP force reaches to its maximum value. Finally, the steady-state Navier Stokes simulations were performed with the stored electrostatics results. This method reduces the simulations time significantly. As the next step, the incompressible Navier-Stokes simulations were utilized to extract the streamline of the utilized cells in this study. According to Table 7.1, the dielectric properties of the each cell type differs from the others. Therefore, the DEP coefficient of each cell type will vary (Eq. 38b). For each cell type the C_{DEP} is calculated separately, using the calculated $Re(F_{CM})$, which is presented in Fig. 7.1. Table 7.3 presents the calculated $Re(F_{CM})$ and C_{DEP} for the cells in the separation frequency of 160 MHz. In order to maximize the separation efficiency of the designed DEP device, further optimizations are performed to determine the boundary conditions of the device. These include the pressure of the fluid in the inlets 2 and 3, the velocity of the fluid in the inlet 1, and the amplitude of the applied sinusoidal signals to the active electrodes. The optimized values are presented in the Table 7.4.

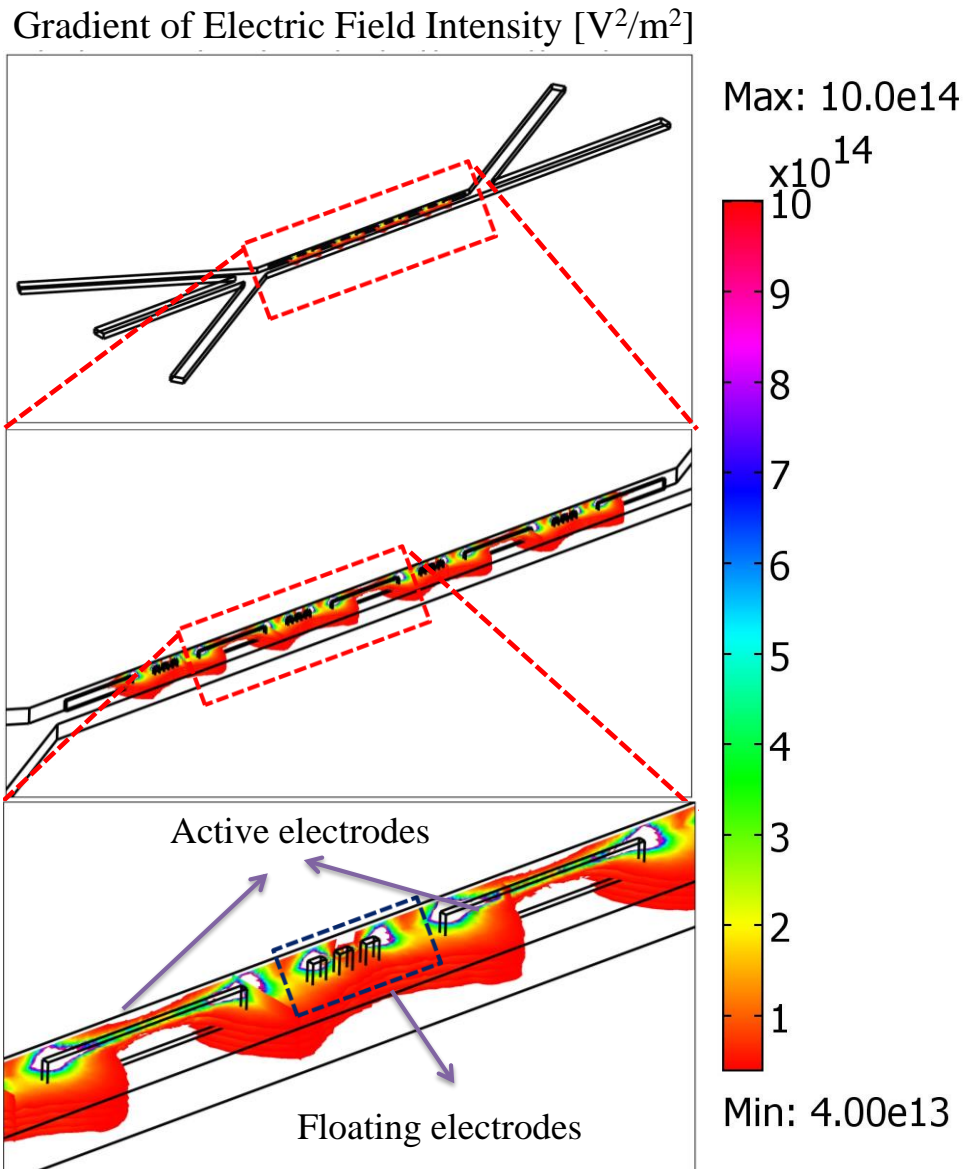


Figure 7. 4: 3D FEM simulation of the distribution of the gradient of the electric field intensity in the DEP separation region of the device.

Table 7. 3: Calculated $Re(F_{CM})$ and C_{DEP} for the cells in the separation frequency of 160 MHz.

Cell type	$Re(F_{CM})$	C_{DEP}	Type of DEP force
Granulocytes	0.2726	1.56E-18	p-DEP
T-Lymphocyte	0.166	4.64E-19	p-DEP
B-Lymphocyte	0.2951	8.24E-19	p-DEP
Monocyte	0.2117	1.17E-18	p-DEP
Erythrocyte	-0.0198	-4.59E-20	n-DEP
K562	-0.1543	-1.43E-18	n-DEP
K562/IMA-0.2	-0.0665	-6.17E-19	n-DEP

Table 7. 4: Optimized boundary conditions for the DEP devices.

	Pressure [Pa]	Velocity [m/s]	Voltage [V_{p-p}]
Inlet 1	-	0.001	-
Inlet 2	25000	-	-
Inlet3	30000	-	-
Electrodes	-	-	10

During the optimizations, the focus was directed to achieve the highest separation efficiency, while avoiding from the cell trapping in the electrode region due the generated high electric field. Under the optimized conditions, the separation efficiency of the each cell type is studied using the FEM analyses (Fig. 7.5).

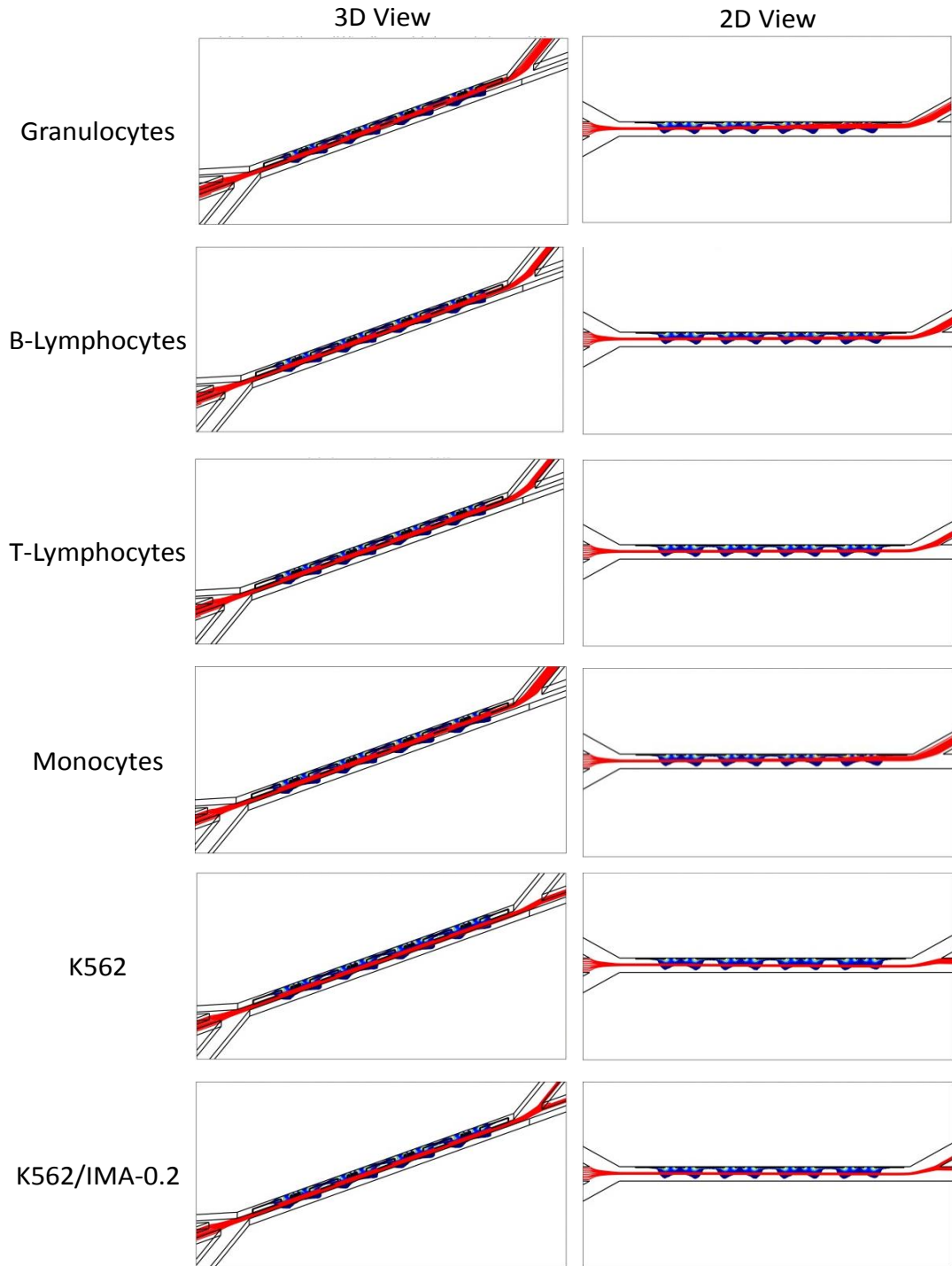


Figure 7. 5: Use of finite element simulations to study the separation efficiency of the cells.

It is aimed to separate the leukocytes to the outlet 1, under the p-DEP force. Similarly, it is aimed to direct the cancer cells to outlet 2, under the n-DEP force. The FEM simulations show that the proposed DEP devices can separate the

leukocytes and sensitive K562 cancer cells with 100% efficiency. However, our devices are able to separate the 65% of the imatinib resistant cells to the outlet 2.

7.4 Fabrication

In the fabrication of the DEP devices four masks were utilized. These DEP devices were fabricated on a common wafer, which was used for the fabrication of the 2nd generation of the ER devices (Section 5.2). The parylene microchannel fabrication process was used in the fabrication of the DEP devices. The fabrication process includes metal sputtering, wet and dry etching, photolithography, electroplating and polymer (parylene) coating steps. The fabrication process of the DEP devices is presented in Fig. 7.6. (See Appendix E for fabrication process flow)

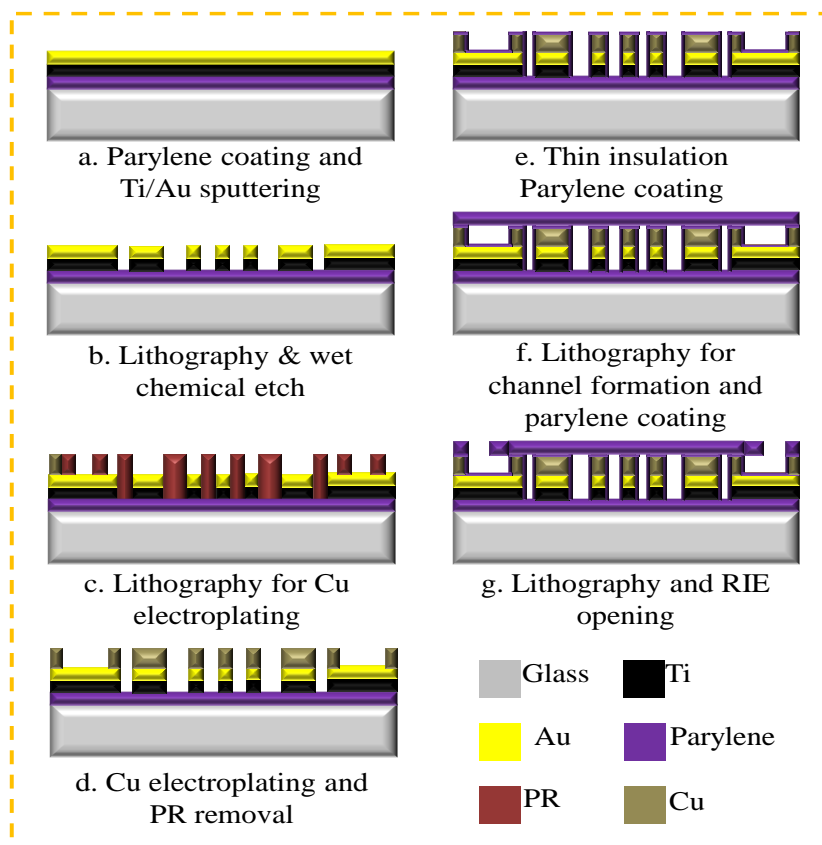


Figure 7. 6: Fabrication process flow of the DEP devices, using four masks.

As the initial step, piranha cleaning of the glass wafers was performed to obtain a polished and rugged surface, which increases the adhesion capabilities of the surface of the wafers. For this purpose, buffered hydrofluoric (BHF) etchant was

used. After cleaning the glass wafer, a thin parylene was coated on the wafer. The parylene coating can be realized by simultaneous use of silane. Silane increases the adhesion of the coated parylene to the glass wafer. The coating parameters of the parylene were optimized in our group. A ratio of 1:2 (thickness in micrometres : parylene weight in grams) was used for the coating purpose. Following the initial parylene coating, Ti and Au were sputtered on the wafer to form a seed layer for the Cu electroplating. Then, mask 1 was utilized for patterning of the Ti/Au seed layer. For this purpose, S1813 photoresist was utilized. S1813 photoresist is generally used for the thin coatings. After this step, the Au layer was etched using commercial Au etchants. For Ti etching an etchant solution was prepared, consisting of 10 ml HF, 10 ml H₂O₂ and 80 ml DI water. After patterning the seed layer, the S1813 photoresist was stripped using acetone. For determining the Cu electroplating area, lithography technique was utilized using the mask 2. The height of the electroplated electrodes was aimed to be 30 µm. Therefore, AZ9260 photoresist was used which is proper for thick coatings. Then, the 3D electrodes were electroplated using the Cu electroplating technique. The process parameters were optimized as 50 mA current for 90 minutes. The aim of the 3D electrodes is to provide a uniform distribution of the electric field by covering the whole cell body. The mask 3 was used for forming the reservoir in the inter-electrode region of the 3D pyramidal electrodes. For this purpose, AZ9260 photoresist was spun and patterned. Then a parylene layer was coated on the wafer to form the reservoir walls. As the final step, RIE was used to open the reservoirs capping and the contact pads. In addition to RIE, manual opening of the inlets and outlets were possible by cutting the capping parylene using a blade. Then the wafer was diced and 9 DEP devices were obtained. In order to compensate the available area on each wafer and increase the number of the fabricated on each wafer, in 8 of the DEP devices, only outlet reservoir was used. Only in one of the DEP devices the nano-port installation area was embedded in the outlets. After opening the reservoir region using the RIE, acetone was used for releasing the photoresist. The fabricated prototype of the DEP devices is shown in Fig. 7.7.

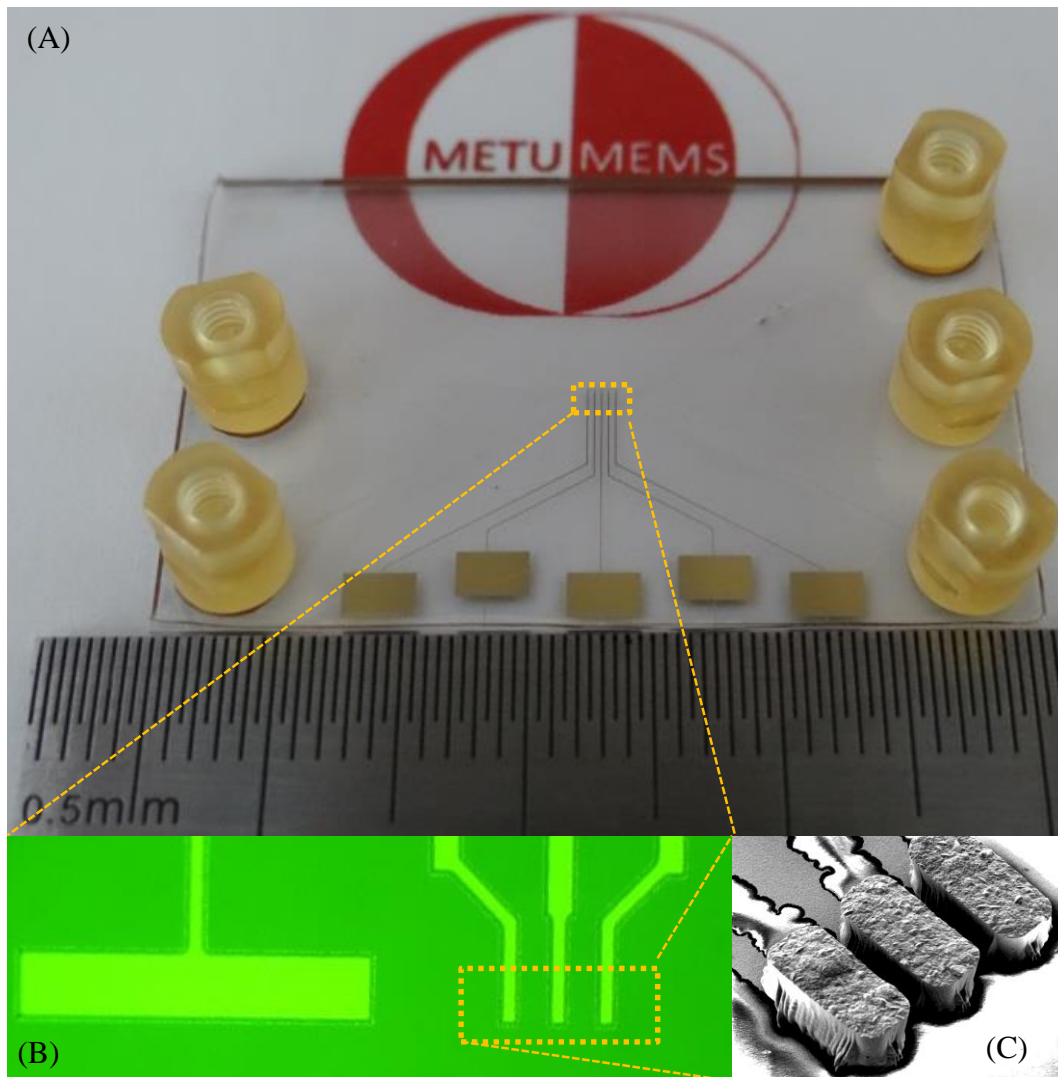


Figure 7. 7: (A) Fabricated prototype of the DEP devices. (B) Magnified view of the sputtered Ti/Au electrodes before electroplating and (C) SEM photograph of the 3D electroplated floating electrodes.

7.5 Conclusion

Design, simulation, and fabrication of a MEMS-based DEP device, for separation of the human leukemia cells from the leukocyte mixture were presented. The fabrication and test process of these devices are continuing. As a part of this thesis, only simulation and fabrication of the devices were presented. However, the further experimental analyses are continuing with these devices.

We have shown that, in addition to active 3D electrodes, floating 3D electrodes can be utilized to enhance the separation efficiency of the DEP devices. FEM analyses

were utilized to show that the proposed devices can achieve 100% efficiency in separation of the human leukemia cancer cells from the leukocytes cell mixture. However, further experimental analyses under the continuous flow regime are necessary to support the statement.

CHAPTER 8

CONCLUSION

The aim of this study was to investigate the possibility of implementation of the DEP method in separation and detection of cancer cells with varying drug resistance levels, from the blood sample. To achieve this goal, an accurate knowledge about the dielectric properties of the cells is essential. However, to that time, there were a few studies, which had subjected the dielectric properties of the MDR cells. Therefore, as the initial step, we have decided to use a method to extract the dielectric properties of the MDR cells, to evaluate the possibility of use of the DEP method in detections and separation of these cells. We have chosen the electrorotation method for dielectric characterization of cancer cells. The ER method is a generally accepted to have the highest accuracy in extracting the dielectric properties of the cells' membrane and interior. In order to use the electrorotation method, three different generation of the ER devices were designed, fabricated, and analyzed. The first generation of the ER devices with 2D planar electrodes was utilized to investigate the possibility of use of the ER method in characterization of the cells. Then, the test setup was designed for the ER measurements. In each generation, the major drawbacks of the previous device were eliminated, and the performance of the devices was enhanced. Different FEM analyses and experimental investigations were utilized in studying the performance of the devices. Finally, the 3rd generation of the ER devices was fabricated, with much easier and rapid fabrication process and higher performance compared to the

previous devices. In the 3rd generation of the ER device, six different electrode geometries were designed and fabricated. Experimental and FEM analyses were utilized to study the performance of the each electrode type. Electrodes were studied from many aspects such as the magnitude and sustainability of the generated rotation torque in 3 dimensional spaces, the uniformity of the generated effective electric field, and the generated effective DEP force. Finally, the ER device with 3D polynomial electrodes was chosen to have the best compromise between the studied factors.

Another challenging part of the ER characterization of the cells was to develop a mathematical methodology to extract the dielectric properties of the cells, from their rotational behavior. Therefore, all the presented methods in the literature were studied carefully. Finally, a precise method was developed to extract the dielectric properties of the cells from their rotational behavior. An automated MATLAB algorithm with GUI interface was designed and developed, based on the utilized expressions and equations. The designed program is capable of calculating the dielectric properties of the membrane and interior of the biological cells, by introducing the peak rotation frequencies of the cells inside the media with varying conductivities.

Using the polynomial electrodes, the dielectric characterization of 9 different cells were carried out, including:

- Drug sensitive K562 human leukemia cells
- Multidrug resistance K562 human leukemia cells, with 0.1, 0.3, and 0.5 μM resistance to doxorubicin.
- Multidrug resistance K562 human leukemia cells, with 0.2, 0.3, and 0.5 μM resistance against the imatinib
- Drug sensitive MCF7 human breast cancer cells.
- Multidrug resistance MCF7 human breast cancer cells, with 1 μM resistance against the doxorubicin.

Simultaneously with the ongoing studies on the ER method, the DEP devices were designed, simulated, and fabricated. The motivation behind the DEP devices was to use these devices in separation of the human leukemia cancer cells and its MDR

counterparts from the human leukocytes mixture. FEM analyses were utilized in design and optimization of the devices. In addition, 3D simulations were utilized to study the separation performance of the devices. The simulation results show 100% separation efficiency for separating the K562 sensitive cells from the leukocytes mixture. The experimental analyses of the DEP devices are continuing with the biological cells.

As the future scope of the work, firstly the ER devices will be improved. In order to increase the throughput of the ER system, an automated setup is essential. Therefore, development of a video processing algorithm seems essential for automated calculation of the rotational rate of the cells. In addition, to minimize the variations of the rotational torque on the cells, it is essential to eliminate lateral movements of the cells. For this purpose, a microfluidic or electrokinetic trapping can be used. All these developments can result in an automated ER setup for dielectric characterization of the biological cells.

In the case of the DEP devices, experimental analyses of the devices will be performed. For this purpose, the tests should be performed under the continuous flow regime. Then, the separation efficiency of the devices can be calculated by cell counting methods in the outlet ports. In addition, to increase the throughput of the DEP devices, the channel volume should increase, without sacrificing the separation efficiency of the devices. The final aim of our study is development of a MEMS based DEP microfluidic platform, with high efficiency and sensitivity in separation and detection of the cancerous cells from the whole blood sample.

REFERENCES

- [1] Becker F F, Wang X B, Huang Y, Pethig R, Vykoukal J and Gascoyne P R 1995 Separation of human breast cancer cells from blood by differential dielectric affinity. *Proc. Natl. Acad. Sci. U. S. A.* **92** 860–4
- [2] Arnold W M, Schwan H P and Zimmermann U 1987 Surface conductance and other properties of latex particles measured by electrorotation. *J. Phys. Chem.* **91** 5093–8
- [3] Gimsa J, Müller T, Schnelle T and Fuhr G 1996 Dielectric spectroscopy of single human erythrocytes at physiological ionic strength: dispersion of the cytoplasm. *Biophys. J.* **71** 495–506
- [4] Yang J, Huang Y, Wang X, Wang X B, Becker F F and Gascoyne P R 1999 Dielectric properties of human leukocyte subpopulations determined by electrorotation as a cell separation criterion. *Biophys. J.* **76** 3307–14
- [5] Pethig R, Jakubek L M, Sanger R H, Heart E, Corson E D and Smith P J S 2005 Electrokinetic measurements of membrane capacitance and conductance for pancreatic beta-cells. *IEE Proc. Nanobiotechnol.* **152** 189–93
- [6] Lei U, Sun P-H and Pethig R 2011 Refinement of the theory for extracting cell dielectric properties from dielectrophoresis and electrorotation experiments. *Biomicrofluidics* **5** 44109(0)–44109(16)

- [7] Malleo D, Nevill J T, Lee L P and Morgan H 2010 Continuous differential impedance spectroscopy of single cells. *Microfluid. Nanofluidics* **9** 191–8
- [8] Jang L-S and Wang M-H 2007 Microfluidic device for cell capture and impedance measurement *Biomed. Microdevices* **9** 737–43
- [9] Cheung K, Gawad S and Renaud P 2005 Impedance spectroscopy flow cytometry: on-chip label-free cell differentiation. *Cytometry. A* **65** 124–32
- [10] Cheung K C, Di Bernardino M, Schade-Kampmann G, Hebeisen M, Pierzchalski A, Bocsi J, Mittag A and Tárnok A 2010 Microfluidic impedance-based flow cytometry. *Cytometry. A* **77** 648–66
- [11] Holmes D, Pettigrew D, Reccius C H, Gwyer J D, van Berkel C, Holloway J, Davies D E and Morgan H 2009 Leukocyte analysis and differentiation using high speed microfluidic single cell impedance cytometry. *Lab Chip* **9** 2881–9
- [12] Gawad S, Schild L and Renaud P H 2001 Micromachined impedance spectroscopy flow cytometer for cell analysis and particle sizing. *Lab Chip* **1** 76–82
- [13] Coulter W H 1956 High speed automatic blood cell counter and size analyzer *Proc Natl Electron Conf* pp 1034–40
- [14] Chin S, Hughes M P, Coley H M and Labeed F H 2006 Rapid assessment of early biophysical changes in K562 cells during apoptosis determined using dielectrophoresis. *Int. J. Nanomedicine* **1** 333–7
- [15] Coley H M, Labeed F H, Thomas H and Hughes M P 2007 Biophysical characterization of MDR breast cancer cell lines reveals the cytoplasm is critical in determining drug sensitivity. *Biochim. Biophys. Acta* **1770** 601–8
- [16] Fatoyinbo H O, Hoettges K F and Hughes M P 2008 Rapid-on-chip determination of dielectric properties of biological cells using imaging techniques in a dielectrophoresis dot microsystem. *Electrophoresis* **29** 3–10

- [17] Gawad S, Schild L and Renaud P H 2001 Micromachined impedance spectroscopy flow cytometer for cell analysis and particle sizing. *Lab Chip* **1** 76–82
- [18] Benazzi G, Holmes D, Sun T, Mowlem M and Morgan H 2007 Discrimination and analysis of phytoplankton using a microfluidic cytometer. *Int Nanobiotechnology* 94–101
- [19] Cheung K C, Di Berardino M, Schade-Kampmann G, Hebeisen M, Pierzchalski A, Bocsi J, Mittag A and Tárnok A 2010 Microfluidic impedance-based flow cytometry. *Cytometry. A* **77** 648–66
- [20] Holmes D, Pettigrew D, Reccius C H, Gwyer J D, van Berkel C, Holloway J, Davies D E and Morgan H 2009 Leukocyte analysis and differentiation using high speed microfluidic single cell impedance cytometry. *Lab Chip* **9** 2881–9
- [21] Gawad S, Schild L and Renaud P H 2001 Micromachined impedance spectroscopy flow cytometer for cell analysis and particle sizing. *Lab Chip* **1** 76–82
- [22] Cheung K, Gawad S and Renaud P 2005 Impedance spectroscopy flow cytometry: on-chip label-free cell differentiation. *Cytometry. A* **65** 124–32
- [23] Cheung K, Gawad S and Renaud P 2005 Impedance spectroscopy flow cytometry: on-chip label-free cell differentiation. *Cytometry. A* **65** 124–32
- [24] Holmes D, Pettigrew D, Reccius C H, Gwyer J D, van Berkel C, Holloway J, Davies D E and Morgan H 2009 Leukocyte analysis and differentiation using high speed microfluidic single cell impedance cytometry. *Lab Chip* **9** 2881–9
- [25] Küttel C, Nascimento E, Demierre N, Silva T, Braschler T, Renaud P and Oliva A G 2007 Label-free detection of Babesia bovis infected red blood cells using impedance spectroscopy on a microfabricated flow cytometer. *Acta Trop.* **102** 63–8

- [26] Breu F X, Guggenbichler S and Wollmann J C 2008 No Title *VASA* **37** 3–29
- [27] Zheng Y, Shojaei-Baghini E, Wang C and Sun Y 2013 Microfluidic characterization of specific membrane capacitance and cytoplasm conductivity of single cells. *Biosens. Bioelectron.* **42** 496–502
- [28] Bousse L 1996 Whole cell biosensors *Sensors Actuators B Chem.* **34** 270–5
- [29] Pancrazio J J, Whelan J P, Borkholder D a, Ma W and Stenger D a 1999 Development and application of cell-based biosensors. *Ann. Biomed. Eng.* **27** 697–711
- [30] Stenger D a, Gross G W, Keefer E W, Shaffer K M, Andreadis J D, Ma W and Pancrazio J J 2001 Detection of physiologically active compounds using cell-based biosensors. *Trends Biotechnol.* **19** 304–9
- [31] McFadden P 2002 Broadband biodetection: Holmes on a chip *Science (80-.)*. 2075–6
- [32] Kovacs G T a. 2003 Electronic sensors with living cellular components *Proc. IEEE* **91** 915–29
- [33] Veiseh M, Wickes B T, Castner D G and Zhang M 2004 Guided cell patterning on gold-silicon dioxide substrates by surface molecular engineering. *Biomaterials* **25** 3315–24
- [34] Lan K-C and Jang L-S 2011 Integration of single-cell trapping and impedance measurement utilizing microwell electrodes. *Biosens. Bioelectron.* **26** 2025–31
- [35] Frazier A B, Chen Z G and Han A 2009 Whole-Cell Impedance Analysis for Highly and Poorly Metastatic Cancer Cells *J. Microelectromechanical Syst.* **18** 808–17

- [36] Cho S and Thielecke H 2007 Micro hole-based cell chip with impedance spectroscopy. *Biosens. Bioelectron.* **22** 1764–8
- [37] Jang L-S and Wang M-H 2007 Microfluidic device for cell capture and impedance measurement. *Biomed. Microdevices* **9** 737–43
- [38] Malleo D, Nevill J T, Lee L P and Morgan H 2010 Continuous differential impedance spectroscopy of single cells. *Microfluid. Nanofluidics* **9** 191–8
- [39] Cho S and Thielecke H 2007 Micro hole-based cell chip with impedance spectroscopy *Biosens. Bioelectron.* **22** 1764–8
- [40] Herbert A Pohl 1951 The motion and precipitation of suspensoids in divergent electric fields *Appl. Phys.* **22** 869–71
- [41] Herbert A Pohl 1958 Some effects of non-uniform fields on dielectrics *J. Appl. Phys.* **29** 1182–9
- [42] Herbert A Pohl 1968 Theoretical aspects of dielectrophoretic deposition and separation of particles *J. Electrochem. Soc.* **115** 155C–61C
- [43] Pethig R 2010 Review article-dielectrophoresis: status of the theory, technology, and applications. *Biomicrofluidics* **4** 1–35
- [44] Jiang K, Liu W, Wan L and Zhang J 2008 Manipulation of ZnO nanostructures using dielectrophoretic effect *Sensors Actuators B Chem.* **134** 79–88
- [45] Seo H-W, Han C-S, Choi D-G, Kim K-S and Lee Y-H 2005 Controlled assembly of single SWNTs bundle using dielectrophoresis *Microelectron. Eng.* **81** 83–9
- [46] Liu W J, Zhang J, Wan L J, Jiang K W, Tao B R, Li H L, Gong W L and Tang X D 2008 Dielectrophoretic manipulation of nano-materials and its application to micro/nano-sensors *Sensors Actuators B Chem.* **133** 664–70

- [47] Kumar S, Yoon S-H and Kim G-H 2009 Bridging the nanogap electrodes with gold nanoparticles using dielectrophoresis technique *Curr. Appl. Phys.* **9** 101–3
- [48] Duncan L, Shelmerdine H, Hughes M P, Coley H M, Hübner Y and Labeed F H 2008 Dielectrophoretic analysis of changes in cytoplasmic ion levels due to ion channel blocker action reveals underlying differences between drug-sensitive and multidrug-resistant leukaemic cells. *Phys. Med. Biol.* **53** N1–7
- [49] Chin S, Hughes M P, Coley H M and Labeed F H 2006 Rapid assessment of early biophysical changes in K562 cells during apoptosis determined using dielectrophoresis. *Int. J. Nanomedicine* **1** 333–7
- [50] Labeed F H, Coley H M, Thomas H and Hughes M P 2003 Assessment of multidrug resistance reversal using dielectrophoresis and flow cytometry. *Biophys. J.* **85** 2028–34
- [51] Pethig R, Jakubek L M, Sanger R H, Heart E, Corson E D and Smith P J S 2005 Electrokinetic measurements of membrane capacitance and conductance for pancreatic b-cells *IEE Proc. Nanobiotechnol.* **152** 189–93
- [52] Bahrieh G, Erdem M, Özgür E, Gündüz U and Külah H 2013 Changes in electric properties of doxorubicin resistant K562 Leukemic cells through electrorotation with 3D electrodes *MicroTAS* pp 1502–4
- [53] Bahrieh G, Koydemir H and Erdem M 2013 Dielectric characterization of Imatinib resistant K562 leukemia cells through electrorotation with 3-D electrodes *IEEE Sensors, 2013* pp 1026–9
- [54] Haapalainen M and Makynen A 2011 Measuring electrical properties of microbeads by dielectrophoretic mobility *2011 IEEE Int. Instrum. Meas. Technol. Conf.* 1–4

- [55] Gascoyne P R C, Huang Y, Pethig R, Vykoukal J and Becker F F 1992 Dielectrophoretic separation of mammalian cells studied by computerized image analysis *Meas. Sci. Technol.* **3** 439–45
- [56] Broche L M, Bhadal N, Lewis M P, Porter S, Hughes M P and Labeed F H 2007 Early detection of oral cancer - Is dielectrophoresis the answer? *Oral Oncol.* **43** 199–203
- [57] Vykoukal D M, Gascoyne P R C and Vykoukal J 2009 Dielectric characterization of complete mononuclear and polymorphonuclear blood cell subpopulations for label-free discrimination. *Integr. Biol. (Camb).* **1** 477–84
- [58] Huang Y, Hölzel R, Pethig R and Wang X B 1992 Differences in the AC electrodynamic of viable and non-viable yeast cells determined through combined dielectrophoresis and electrorotation studies. *Phys. Med. Biol.* **37** 1499–517
- [59] Gascoyne P R C, Huang Y, Pethig R, Vykoukal J and Becker F F 1992 Dielectrophoretic separation of mammalian cells studied by computerized image analysis *Meas. Sci. Technol.* **3** 439–45
- [60] Jones T 2003 Basic theory of dielectrophoresis and electrorotation *IEEE Eng. Med. Biol. Mag.* **22** 33–42
- [61] Jones T B and Washizu M 1996 Multipolar dielectrophoretic and electrorotation theory *J. Electrostat.* **37** 121–34
- [62] Gascoyne P R C, Becker F F and Wang X-B 1995 Numerical analysis of the influence of experimental conditions on the accuracy of dielectric parameters derived from electrorotation measurements *Bioelectrochemistry Bioenerg.* **36** 115–25
- [63] Maswiwat K, Holtappels M and Gimsa J 2006 On the field distribution in electrorotation chambers—Influence of electrode shape *Electrochim. Acta* **51** 5215–20

- [64] Maswiwat K, Holtappels M and Gimsa J 2007 Optimizing the electrode shape for four-electrode electrorotation chips *ScienceAsia* **33** 61–7
- [65] Hughes M P, Wang X-B, Becker F F, Gascoyne P R C and Pethig R 1994 Computer-aided analyses of electric fields used in electrorotation studies *J. Phys. D. Appl. Phys.* **27** 1564–70
- [66] Hughes M P, Archer S and Morgan H 1999 Mapping the electrorotational torque in planar microelectrodes *J. Phys. D. Appl. Phys.* **32** 1548–52
- [67] Hughes M P 1998 Computer-aided analysis of conditions for optimizing practical electrorotation. *Phys. Med. Biol.* **43** 3639–48
- [68] Holzel R 1993 Electric field calculation for electrorotation electrodes *J. Phys. D. Appl. Phys.* **2112**
- [69] Georgieva R, Neu B, Shilov V M, Knippel E, Budde a, Latza R, Donath E, Kiesewetter H and Bäuml H 1998 Low frequency electrorotation of fixed red blood cells. *Biophys. J.* **74** 2114–20
- [70] Han S-I, Joo Y-D and Han K-H 2013 An electrorotation technique for measuring the dielectric properties of cells with simultaneous use of negative quadrupolar dielectrophoresis and electrorotation. *Analyst* **138** 1529–37
- [71] Vykoukal D M, Gascoyne P R C and Vykoukal J 2009 Dielectric characterization of complete mononuclear and polymorphonuclear blood cell subpopulations for label-free discrimination. *Integr. Biol. (Camb)*. **1** 477–84
- [72] Xun Hu, W. Michael Arnold U Z 1990 Alterations in the electrical properties of T and B lymphocyte membranes induced by mitogenic stimulation. Activation monitored by electro-rotation of single cells *Biochim. Biophys. Acta - Biomembr.* **1021** 191–200

- [73] Yang J, Huang Y, Wang X, Wang X B, Becker F F and Gascoyne P R 1999 Dielectric properties of human leukocyte subpopulations determined by electrorotation as a cell separation criterion. *Biophys. J.* **76** 3307–14
- [74] Griffith A W and Cooper J M 1998 Single-cell measurements of human neutrophil activation using electrorotation. *Anal. Chem.* **70** 2607–12
- [75] Berardi V, Aiello C, Bonincontro A and Risuleo G 2009 Alterations of the plasma membrane caused by murine polyomavirus proliferation: an electrorotation study. *J. Membr. Biol.* **229** 19–25
- [76] Becker F F, Wang X B, Huang Y, Pethig R, Vykoukal J and Gascoyne P R 1995 Separation of human breast cancer cells from blood by differential dielectric affinity. *Proc. Natl. Acad. Sci. U. S. A.* **92** 860–4
- [77] Labeed F H, Coley H M, Thomas H and Hughes M P 2003 Assessment of multidrug resistance reversal using dielectrophoresis and flow cytometry. *Biophys. J.* **85** 2028–34
- [78] Cristofanilli M, Gasperis G De, Zhang L, Hung M-C, Peter R. C. Gascoyne A and Hortobagyi G N 2002 Automated Electrorotation to Reveal Dielectric Variations Related to HER-2 / neu Overexpression in MCF-7 Sublines Automated Electrorotation to Reveal Dielectric Variations Related *Clin. Cancer Res.* **8** 615–9
- [79] Hölzel R 1999 Non-invasive determination of bacterial single cell properties by electrorotation. *Biochim. Biophys. Acta* **1450** 53–60
- [80] Fuhr G, Geissler F, Muller T, Hadedorn R and Torner H 1987 Differences in the rotation spectra of mouse oocytes and zygotes *Biochim. Biophys. Acta - Mol. Cell Res.* **930** 65–71
- [81] Asami K, Takahashi Y and Takashima S 1989 Dielectric properties of mouse lymphocytes and erythrocytes *Biochim. Biophys. Acta - Mol. Cell Res.* **1010** 49–55

- [82] Gimsa J, Marszalek P, Loewe U and Tsong T Y 1991 Dielectrophoresis and electrorotation of neurospora slime and murine myeloma cells. *Biophys. J.* **60** 749–60
- [83] Arnold W M, Schwan H P and Zimmermann U 1987 Surface conductance and other properties of latex particles measured by electrorotation *J. Phys. Chem.* **91** 5093–8
- [84] Shibatani S, Minami K, Senda M and Kakutani T 1993 Electrorotation of vacuoles isolated from barley mesophyll cells *Bioelectrochemistry Bioenerg.* **29** 327–35
- [85] Patel P and Markx G H 2008 Dielectric measurement of cell death *Enzyme Microb. Technol.* **43** 463–70
- [86] Chuang C-H, Hsu Y-M and Yeh C-C 2009 The effects of nanoparticles uptaken by cells on electrorotation. *Electrophoresis* **30** 1449–56
- [87] Chuang C, Li C, Yeh C and Hsu Y 2008 Electrorotation of HL-60 cells uptake of metal and dielectric nanoparticles in a stationary AC electric field *2008 3rd IEEE Int. Conf. Nano/Micro Eng. Mol. Syst.* 938–42
- [88] Gasperis G De, Wang X, Yang J, Becker F F and Gascoyne P R C 1998 Automated electrorotation: dielectric characterization of living cells by real-time motion estimation *Meas. Sci. Technol.* **9** 518–29
- [89] Cristofanilli M, Gasperis G De and Zhang L 2002 Automated electrorotation to reveal dielectric variations related to HER-2/neu overexpression in MCF-7 sublines *Clin. Cancer ...* 615–9
- [90] Zhou X, Burt J and Pethig R 1998 Automatic cell electrorotation measurements: studies of the biological effects of low-frequency magnetic fields and of heat shock *Phys. Med. Biol.* **1075**

- [91] Reichle C, Schnelle T, Müller T, Leya T and Fuhr G 2000 A new microsystem for automated electroration measurements using laser tweezers. *Biochim. Biophys. Acta* **1459** 218–29
- [92] Reichle C, Schnelle T, Müller T, Leya T and Fuhr G 2000 A new microsystem for automated electroration measurements using laser tweezers. *Biochim. Biophys. Acta* **1459** 218–29
- [93] Schnelle T, Müller T, Reichle C and Fuhr G 2000 Combined dielectrophoretic field cages and laser tweezers for electroration *Appl. Phys. B* **70** 267–74
- [94] Gasperis G De, Wang X, Yang J, Becker F F and Gascoyne P R C 1998 Automated electroration: dielectric characterization of living cells by real-time motion estimation *Meas. Sci. Technol.* **9** 518–29
- [95] Rowe A and Leake M 2003 Rapid rotation of micron and submicron dielectric particles measured using optical tweezers *J. Mod. Opt.* **50** 1539–54
- [96] Fuhr G R and Reichle C 2000 Living cells in opto-electrical cages *TrAC Trends Anal. Chem.* **19** 402–9
- [97] Reichle C, Müller T, Schnelle T and Fuhr G 1999 Electro-rotation in octopole micro cages *J. Phys. D. Appl. Phys.* **32** 2128–35
- [98] Minerick A R, Zhou R, Takhistov P and Chang H-C 2003 Manipulation and characterization of red blood cells with alternating current fields in microdevices. *Electrophoresis* **24** 3703–17
- [99] Arnold W M, Schwan H P and Zimmermann U 1987 Surface conductance and other properties of latex particles measured by electroration *J. Phys. Chem.* **91** 5093–8
- [100] Jones T B 1995 *Electromechanics of Particles* (Cambridge: Cambridge University Press)

- [101] Huang Y, Hölzel R, Pethig R and Wang X B 1992 Differences in the AC electrodynamics of viable and non-viable yeast cells determined through combined dielectrophoresis and electrorotation studies. *Phys. Med. Biol.* **37** 1499–517
- [102] SCHWAN H P 1957 Electrical properties of tissue and cell suspensions. *Adv. Biol. Med. Phys.* **5** 147–209
- [103] Arnold W M and Zimmermann U 1988 Electro-rotation: development of a technique for dielectric measurements on individual cells and particles *J. Electrostat.* **21** 151–91
- [104] Chan K L, Gascoyne P R, Becker F F and Pethig R 1997 Electrorotation of liposomes: verification of dielectric multi-shell model for cells. *Biochim. Biophys. Acta* **1349** 182–96
- [105] Baran Y, Ural A and Gunduz U 2007 Mechanisms of cellular resistance to imatinib in human chronic myeloid leukemia cells *Hematology* **12** 497–503
- [106] Assef Y a, Cavarra S M, Damiano A E, Ibarra C and Kotsias B a 2005 Ionic currents in multidrug resistant K562 human leukemic cells. *Leuk. Res.* **29** 1039–47
- [107] Idriss H T, Hannun Y A, Boulpaep E and Basavappa S 2000 Topical Review Regulation of volume-activated chloride channels by P_u glycoprotein: phosphorylation has the final say! *J. Physiol.* **524** 629–36
- [108] Cetin B and Li D 2011 Dielectrophoresis in microfluidics technology. *Electrophoresis* **32** 2410–27
- [109] Yang J, Huang Y, Wang X, Wang X B, Becker F F and Gascoyne P R 1999 Dielectric properties of human leukocyte subpopulations determined by electrorotation as a cell separation criterion. *Biophys. J.* **76** 3307–14

APPENDIX A

DOUBLE SHELL CELL MODEL IN MATLAB

The utilized MATLAB algorithm for modeling of the electrical response of the biological particles with double shell model is as below:

```
function varargout = FCM(varargin)

gui_Singleton = 1;

gui_State = struct('gui_Name',    mfilename, ...
                  'gui_Singleton', gui_Singleton, ...
                  'gui_OpeningFcn', @FCM_OpeningFcn, ...
                  'gui_OutputFcn', @FCM_OutputFcn, ...
                  'gui_LayoutFcn', [] , ...
                  'gui_Callback', []);

if nargin && ischar(varargin{1})
    gui_State.gui_Callback = str2func(varargin{1});
end

if nargout
    [varargout{1:nargout}] = gui_mainfcn(gui_State, varargin{:});
else
```

```

gui_mainfcn(gui_State, varargin{:});

end

function FCM_OpeningFcn(hObject, eventdata, handles, varargin)

handles.output = hObject;

guidata(hObject, handles);

function varargout = FCM_OutputFcn(hObject, eventdata, handles)

varargout{1} = handles.output;

function edit1_Callback(hObject, eventdata, handles)

function edit1_CreateFcn(hObject, eventdata, handles)

if ispc && isequal(get(hObject,'BackgroundColor'),
get(0,'defaultUicontrolBackgroundColor'))

    set(hObject,'BackgroundColor','white');

end

function edit2_Callback(hObject, eventdata, handles)

function edit2_CreateFcn(hObject, eventdata, handles)

if ispc && isequal(get(hObject,'BackgroundColor'),
get(0,'defaultUicontrolBackgroundColor'))

    set(hObject,'BackgroundColor','white');

end

function edit3_Callback(hObject, eventdata, handles)

function edit3_CreateFcn(hObject, eventdata, handles)

if ispc && isequal(get(hObject,'BackgroundColor'),
get(0,'defaultUicontrolBackgroundColor'))

    set(hObject,'BackgroundColor','white');

end

```



```

function edit4_Callback(hObject, eventdata, handles)

function edit4_CreateFcn(hObject, eventdata, handles)

if ispc && isequal(get(hObject,'BackgroundColor'),
get(0,'defaultUicontrolBackgroundColor'))

    set(hObject,'BackgroundColor','white');

end

function edit5_Callback(hObject, eventdata, handles)

function edit5_CreateFcn(hObject, eventdata, handles)

if ispc && isequal(get(hObject,'BackgroundColor'),
get(0,'defaultUicontrolBackgroundColor'))

    set(hObject,'BackgroundColor','white');

end

function edit6_Callback(hObject, eventdata, handles)

function edit6_CreateFcn(hObject, eventdata, handles)

if ispc && isequal(get(hObject,'BackgroundColor'),
get(0,'defaultUicontrolBackgroundColor'))

    set(hObject,'BackgroundColor','white');

end

function edit7_Callback(hObject, eventdata, handles)

function edit7_CreateFcn(hObject, eventdata, handles)

if ispc && isequal(get(hObject,'BackgroundColor'),
get(0,'defaultUicontrolBackgroundColor'))

    set(hObject,'BackgroundColor','white');

end

function edit8_Callback(hObject, eventdata, handles)

```

```

function edit8_CreateFcn(hObject, eventdata, handles)

if ispc && isequal(get(hObject,'BackgroundColor'),
get(0,'defaultUicontrolBackgroundColor'))

    set(hObject,'BackgroundColor','white');

end

function edit9_Callback(hObject, eventdata, handles)

function edit9_CreateFcn(hObject, eventdata, handles)

if ispc && isequal(get(hObject,'BackgroundColor'),
get(0,'defaultUicontrolBackgroundColor'))

    set(hObject,'BackgroundColor','white');

end

function edit10_Callback(hObject, eventdata, handles)

function edit10_CreateFcn(hObject, eventdata, handles)

if ispc && isequal(get(hObject,'BackgroundColor'),
get(0,'defaultUicontrolBackgroundColor'))

    set(hObject,'BackgroundColor','white');

end

function edit11_Callback(hObject, eventdata, handles)

function edit11_CreateFcn(hObject, eventdata, handles)

if ispc && isequal(get(hObject,'BackgroundColor'),
get(0,'defaultUicontrolBackgroundColor'))

set(hObject,'BackgroundColor','white');

end

function pushbutton1_Callback(hObject, eventdata, handles)

A=get(handles.edit1, 'String');

```

```
sig_cyto=str2num(A);  
B=get(handles.edit2, 'String');  
sig_mem=str2num(B);  
C=get(handles.edit3, 'String');  
sig_wall=str2num(C);  
D=get(handles.edit4, 'String');  
eps_cyto=str2num(D);  
E=get(handles.edit5, 'String');  
eps_mem=str2num(E);  
F=get(handles.edit6, 'String');  
eps_wall=str2num(F);  
G=get(handles.edit7, 'String');  
r_cyto=str2num(G);  
H=get(handles.edit8, 'String');  
r_mem=str2num(H);  
I=get(handles.edit9, 'String');  
r_wall=str2num(I);  
J=get(handles.edit10, 'String');  
sig_med=str2num(J);  
L=get(handles.edit11, 'String');  
eps_med=str2num(L);  
eps_0= 8.854187817e-12;  
f= logspace(0,8.20411,1e4);  
w=2*pi*f;
```

```

r1= (r_mem / r_cyto)^3;
r2= (r_wall ./ r_mem)^3 ;
for k=1:1e4

    eps_cyto_st = (eps_cyto * eps_0) - (i*(sig_cyto/w(1,k)));
    eps_mem_st = (eps_mem * eps_0) - (i*(sig_mem/w(1,k)));
    eps_wall_st = (eps_wall * eps_0) - (i*(sig_wall/w(1,k)));
    eps_med_st = (eps_med * eps_0) - (i*(sig_med/w(1,k)));

num1 = eps_cyto_st - eps_mem_st ;
den1 = eps_cyto_st + (2*eps_mem_st);
c1 = (num1 / den1) ;
num1_1 = (r1 + (2 * c1));
den1_1 = (r1 - c1);

    eps_eff_1 = eps_mem_st * (num1_1 / den1_1);

num2 = eps_eff_1 - eps_wall_st;
den2 = eps_eff_1 + 2 * eps_wall_st;
c2 = (num2/den2);
num2_2 = (r2 + 2 * c2);
den2_2 = (r2 - c2);

    eps_eff_2 = eps_wall_st * (num2_2 / den2_2);

    CM = (((eps_eff_2 - eps_med_st) / (eps_eff_2 + 2 * eps_med_st)));

FCM(1,k)=(CM);

    css = (sig_cyto - sig_mem) / (sig_cyto + 2*sig_mem);
    sig_eff1 = sig_mem* ((r1 + 2*css) / (r1 - css)) ;
    css2 = (sig_eff1 - sig_wall) / (sig_eff1 + 2*sig_eff1);

```

```

        sig_eff2 = sig_wall* ((r2 + 2*css2) / (r2 - css2));
end
set(handles.axes1,'NextPlot','replace');

axes(handles.axes1);

plot (log10(f(1,:)),FCM(1,:),'-r','LineWidth',2)

hold on

plot (log10(f(1,:)),imag(FCM(1,:)),'-g','LineWidth',2)

ylabel('FCM','FontSize',12);

xlabel('Frequency 10^x Hz','FontSize',12);

title('Clausius-Mossotti Factor','FontSize',12);

line([0 9],[0 0]);

legend ('Real part','Imaginary part','Location','Best')

FCM(1,10000)

grid on

hold on

```


APPENDIX B

AUTOMATED MATLAB BASED SOFTWARE FOR EXTRACTING THE DIELECTRIC PROPERTIES OF THE CELLS USING ELECTROROTATION METHOD

Below MATLAB code is utilized in design and implementation of a software for extracting the dielectric properties of the cells, from the electroration experiments.

```
function varargout = V1gui(varargin)

gui_Singleton = 1;

gui_State = struct('gui_Name',    mfilename, ...
                  'gui_Singleton', gui_Singleton, ...
                  'gui_OpeningFcn', @V1gui_OpeningFcn, ...
                  'gui_OutputFcn', @V1gui_OutputFcn, ...
                  'gui_LayoutFcn', [] , ...
                  'gui_Callback', []);

if nargin && ischar(varargin{1})
    gui_State.gui_Callback = str2func(varargin{1});
end
```

```

if nargin
    [varargout{1:nargout}] = gui_mainfcn(gui_State, varargin{:});
else
    gui_mainfcn(gui_State, varargin{:});
end

function V1gui_OpeningFcn(hObject, eventdata, handles, varargin)
handles.output = hObject;
guidata(hObject, handles);

function varargout = V1gui_OutputFcn(hObject, eventdata, handles)
varargout{1} = handles.output;

function edit1_Callback(hObject, eventdata, handles)

function edit1_CreateFcn(hObject, eventdata, handles)
if ispc && isequal(get(hObject,'BackgroundColor'),
get(0,'defaultUicontrolBackgroundColor'))
    set(hObject,'BackgroundColor','white');
end

function edit2_Callback(hObject, eventdata, handles)

function edit2_CreateFcn(hObject, eventdata, handles)
if ispc && isequal(get(hObject,'BackgroundColor'),
get(0,'defaultUicontrolBackgroundColor'))
    set(hObject,'BackgroundColor','white');
end

function edit3_Callback(hObject, eventdata, handles)

function edit3_CreateFcn(hObject, eventdata, handles)

```



```
if ispc && isequal(get(hObject,'BackgroundColor'),
get(0,'defaultUicontrolBackgroundColor'))
    set(hObject,'BackgroundColor','white');
end
```

```
function edit4_Callback(hObject, eventdata, handles)
function edit4_CreateFcn(hObject, eventdata, handles)
if ispc && isequal(get(hObject,'BackgroundColor'),
get(0,'defaultUicontrolBackgroundColor'))
    set(hObject,'BackgroundColor','white');
end
```

```
function edit5_Callback(hObject, eventdata, handles)
function edit5_CreateFcn(hObject, eventdata, handles)
if ispc && isequal(get(hObject,'BackgroundColor'),
get(0,'defaultUicontrolBackgroundColor'))
    set(hObject,'BackgroundColor','white');
end
```

```
function edit6_Callback(hObject, eventdata, handles)
function edit6_CreateFcn(hObject, eventdata, handles)
if ispc && isequal(get(hObject,'BackgroundColor'),
get(0,'defaultUicontrolBackgroundColor'))
    set(hObject,'BackgroundColor','white');
end
```

```

function edit7_Callback(hObject, eventdata, handles)

function edit7_CreateFcn(hObject, eventdata, handles)

if ispc && isequal(get(hObject,'BackgroundColor'),
get(0,'defaultUicontrolBackgroundColor'))

    set(hObject,'BackgroundColor','white');

end

function edit8_Callback(hObject, eventdata, handles)

function edit8_CreateFcn(hObject, eventdata, handles)

if ispc && isequal(get(hObject,'BackgroundColor'),
get(0,'defaultUicontrolBackgroundColor'))

    set(hObject,'BackgroundColor','white');

end

function edit9_Callback(hObject, eventdata, handles)

function edit9_CreateFcn(hObject, eventdata, handles)

if ispc && isequal(get(hObject,'BackgroundColor'),
get(0,'defaultUicontrolBackgroundColor'))

    set(hObject,'BackgroundColor','white');

end

function edit10_Callback(hObject, eventdata, handles)

function edit10_CreateFcn(hObject, eventdata, handles)

if ispc && isequal(get(hObject,'BackgroundColor'),
get(0,'defaultUicontrolBackgroundColor'))

    set(hObject,'BackgroundColor','white');

end

function edit11_Callback(hObject, eventdata, handles)

```

```

function edit11_CreateFcn(hObject, eventdata, handles)

if ispc && isequal(get(hObject,'BackgroundColor'),
get(0,'defaultUicontrolBackgroundColor'))

    set(hObject,'BackgroundColor','white');

end

function edit12_Callback(hObject, eventdata, handles)

function edit12_CreateFcn(hObject, eventdata, handles)

if ispc && isequal(get(hObject,'BackgroundColor'),
get(0,'defaultUicontrolBackgroundColor'))

    set(hObject,'BackgroundColor','white');

end

function edit13_Callback(hObject, eventdata, handles)

function edit13_CreateFcn(hObject, eventdata, handles)

if ispc && isequal(get(hObject,'BackgroundColor'),
get(0,'defaultUicontrolBackgroundColor'))

    set(hObject,'BackgroundColor','white');

end

function edit14_Callback(hObject, eventdata, handles)

function edit14_CreateFcn(hObject, eventdata, handles)

if ispc && isequal(get(hObject,'BackgroundColor'),
get(0,'defaultUicontrolBackgroundColor'))

    set(hObject,'BackgroundColor','white');

end

function edit15_Callback(hObject, eventdata, handles)

function edit15_CreateFcn(hObject, eventdata, handles)

```

```

if ispc && isequal(get(hObject,'BackgroundColor'),
get(0,'defaultUicontrolBackgroundColor'))

    set(hObject,'BackgroundColor','white');

end

function edit16_Callback(hObject, eventdata, handles)

function edit16_CreateFcn(hObject, eventdata, handles)

if ispc && isequal(get(hObject,'BackgroundColor'),
get(0,'defaultUicontrolBackgroundColor'))

    set(hObject,'BackgroundColor','white');

end

function edit17_Callback(hObject, eventdata, handles)

function edit17_CreateFcn(hObject, eventdata, handles)

if ispc && isequal(get(hObject,'BackgroundColor'),
get(0,'defaultUicontrolBackgroundColor'))

    set(hObject,'BackgroundColor','white');

end

function edit23_Callback(hObject, eventdata, handles)

function edit23_CreateFcn(hObject, eventdata, handles)

if ispc && isequal(get(hObject,'BackgroundColor'),
get(0,'defaultUicontrolBackgroundColor'))

    set(hObject,'BackgroundColor','white');

end

function pushbutton1_Callback(hObject, eventdata, handles)

x1=str2double(get(handles.edit1,'String'));

x2=str2double(get(handles.edit2,'String'));

```

```
x3=str2double(get(handles.edit3,'String'));
x4=str2double(get(handles.edit4,'String'));
x5=str2double(get(handles.edit5,'String'));
y1=str2double(get(handles.edit6,'String'));
y2=str2double(get(handles.edit7,'String'));
y3=str2double(get(handles.edit8,'String'));
y4=str2double(get(handles.edit9,'String'));
y5=str2double(get(handles.edit10,'String'));
df1=str2double(get(handles.edit11,'String'));
df2=str2double(get(handles.edit12,'String'));
df3=str2double(get(handles.edit13,'String'));
df4=str2double(get(handles.edit14,'String'));
df5=str2double(get(handles.edit15,'String'));
r=str2double(get(handles.edit16,'String'));
dr=str2double(get(handles.edit17,'String'));
method=str2double(get(handles.edit23,'String'));

r=r*1e-6;
e_0=8.85e-12;
d=15e-9;
dr=dr*1e-6;

    if x3==0

X=[x1,x2];

F=[y1,y2];

dF=[df1,df2];
```

```

R=[r r];
DR=[dr dr];
n=2;
FR=F.*r;
    elseif x4==0
X=[x1,x2,x3];
F=[y1,y2,y3];
dF=[df1,df2,df3];
R=[r,r,r];
DR= [dr,dr,dr];
n=3;
FR=F.*r;
    elseif x5==0
X=[x1,x2,x3,x4];
F=[y1,y2,y3,y4];
dF=[df1,df2,df3,df4];
R=[r,r,r,r];
DR= [dr,dr,dr,dr];
n=4;
FR=F.*r;
    elseif x5~=0
X=[x1,x2,x3,x4,x5];
F=[y1,y2,y3,y4,y5];
dF=[df1,df2,df3,df4,df5];

```

```

R=[r,r,r,r,r];
DR= [dr,dr,dr,dr,dr];
n=5;
FR=F.*r;
end
for A=1:n
dFR(A)=FR(A)*sqrt((dF(A)/F(A))^2 + (dr/r)^2 );
end
dFR
FR
FRP=dFR+FR
FRN=FR-dFR
FRT=[FR;FRP;FRN];
    c0 = fit(X',FR','poly1');
    c1=fit(X',FRP','poly1');
    c2=fit(X',FRN','poly1');
    cf1=coeffvalues(c0);
    cf2=coeffvalues(c1);
    cf3=coeffvalues(c2);
cfs=[cf1;cf2;cf3];
c_g_m=zeros(5,3);
for i=1:3
    cm(i)=1/(pi*cfs(i,1));
    gm(i)=2*abs(cfs(i,2))*pi*cm(i)*1e-3/(r);

```

```

    e_m(i)=(d*cm(i)*1e-3)/(8.85e-12);

    c_g_m(i,:)=[cm(i),gm(i),e_m(i)];

end

m_cm=mean(cm);

m_gm=mean(gm);

m_em=mean(e_m);

std_cm=std(cm);

std_gm=std(gm);

std_em=std(e_m);

c_g_m(4,1:3)=[m_cm,m_gm,m_em];

c_g_m(5,1:3)=[std_cm,std_gm,std_em];

set(handles.uitable4,'data',abs(cfs));

set(handles.uitable5,'data',c_g_m);

if method==1

    sigma=zeros(5,n+2);

    for i=1:3

        for k=1:n

            [sig]=solve('2*pi*cm(i)*1e-3*FRT(i)=(sig/2)*(1-sqrt(1 - (4/sig)*(2*1e-3*X(k) + gm(i)*r)))','sig');

            sigma(i,k)=eval(sig);

        end

    end

end

if method==2

```



```

sigma=zeros(5,n+2);
for i=1:3
    for k=1:n
        sig=((2*pi*cm(i)*1e-3*FRT(i))^2)/((2*pi*cm(i)*1e-3*FRT(i))+
        4*pi*(78*8.85e-12)*F(k) -gm(i)*r -2*X(k)*1e-3) ;
        sigma(i,k)=(sig);
    end
end
end
end
if method==3

```

```

sigma=zeros(5,n+2);
for i=1:3
    for k=1:n

        sig= -
(1.0*(6.1685027506808491367715568749226*10^35*r^2*FRT(i)*cm(i)^2
*F(k)^2 +
6.1685027506808491367715568749226*10^35*r*FRT(i)*cm(i)*F(k)*(-
(2.0*10^(-78)*(4.8672*10^76*FRT(i)*e_0^2*F(k)^2 +
3.12000000000000000000000000000001*10^71*cm(i)*e_0*r^2*F(k)^3 -
3.12*10^74*FRT(i)*gm(i)*e_0*r*F(k)^2 -
1.9862536897868537903956693668948*10^71*FRT(i)*e_0*F(k)*X(k) -
6.3661977236758134307553507305592*10^65*cm(i)*r^2*F(k)^2*X(k) -
5.0*10^77*FRT(i)*cm(i)^2*r^2*F(k)^2 +
6.3661977236758134307553505366906*10^68*FRT(i)*gm(i)*r*F(k)*X(k)
+
2.0264236728467554288775885162456*10^65*FRT(i)*X(k)^2))/FRT(i))^(
1/2)))/(- 196349540849362077403915211454999.0*cm(i)*r^2*F(k)^2 +

```



```

/(3.125*10^33*X(k) + 1.5625*10^36*r*gm(i) -
1.5315264186250242037505386493488*10^39*e_0*F(k) -
9.8174770424681038701957605727484*10^33*r*cm(i)*F(k));

```

```

sigma(i,k)=(sig);

```

```

    end

```

```

end

```

```

end

```

```

sigma;

```

```

m_sigma_m=zeros(1,n);

```

```

std_sigma_m=zeros(1,n);

```

```

for i=1:n

```

```

    m_sigma_m(i)=mean((abs(sigma(1:3,i))));

```

```

    std_sigma_m(i)=std((abs(sigma(1:3,i))));

```

```

end

```

```

m_sigma_f=zeros(3,1);

```

```

std_sigma_f=zeros(3,1);

```

```

for i=1:3

```

```

    m_sigma_f(i)=mean((abs(sigma(i,1:n))));

```

```

    std_sigma_f(i)= std((abs(sigma(i,1:n))));

```

```

end

```

```

sigma(4,1:n)=m_sigma_m(1,1:n);

```

```

sigma(5,1:n)=std_sigma_m;

```

```

sigma(1:3,6)=m_sigma_f;

sigma(1:3,7)=std_sigma_f;

set(handles.uitable6,'data',abs(sigma))

YY1=cf1(1).*X+ cf1(2);
YY2=cf2(1).*X+ cf2(2);
YY3=cf3(1).*X+ cf3(2);

    axes(handles.axes1);

    cla;

    plot(X,YY1,'-r','LineWidth',2);hold on;plot(X,YY2,'g','LineWidth',2);

hold on;plot(X,YY3,'K','LineWidth',2);

    title('Curve Fitting');

    legend('F','F+df','F-df','Location','NorthWest' );

xlabel('Medium Conductivity (mS/m)');

ylabel('F.R (m/s)');

grid on;

axes(handles.axes2);

cla;

    plot(X,abs(sigma(1,1:n)),'sr','LineWidth',2);

    hold on;

    plot(X,abs(sigma(2,1:n)),'-*g','LineWidth',2);

    hold on;

    plot(X,abs(sigma(3,1:n)),'-+K','LineWidth',2);

    title('Cells Interior Conductivity vs Medium Conductivity');

```

```
    legend('F','F+df','F-df','Location','NorthWest');  
xlabel('Medium Conductivity (mS/m)');  
ylabel('Cells Interior Conductivity (S/m)');  
grid on;  
ave_sigma=mean((abs(sigma(1:3,6))));  
std_sigma=STD((abs(sigma(1:3,6))));  
set(handles.text10,'String',ave_sigma);  
set(handles.text11,'String',std_sigma);
```


APPENDIX C

JOULE HEATING ANALYSES OF THE 3D ER ELECTRODES

The simulation results for the generated joule heating and the current density passing through the 3D electrodes are presented in this section.

The COMSOL Multiphysics is used for the thermal and electrical analyses of the 3D electrodes. For this purpose the Electrostatics, Generalized module of the COMSOL software is used. The conductivity and the relative permittivity of the suspension medium is assumed as 8.5 mS/m and 78, respectively. The applied voltage to the electrodes is assumed to has a peak to peak amplitude of 5 V at frequency of 50 kHz. Figure C.1 shows the current density passing through the electrodes and the medium in the devices with 3D structures.

The applied voltages to the electrodes and resultantly the passing current through the electrodes and the medium is resulted in the joule heating. The generated joule heating in the ER device with 3D polynomial electrodes is shown in the Fig. C2. The comparison between the FEM results for the current density passing through the 2D (Figure 4.4) and 3D electrodes shows that, the current density has reduced by more than 141% in 3D structures. It is due to increased volume of the electrodes in the 3D structures. It is expected that the generated joule heating be reduced in the 3D structures as well. A comparison between the simulation results for the 2D (Fig. 4.3) and 3D structures shows that, the generated heating is reduced by more than 545% in the 3D structures.

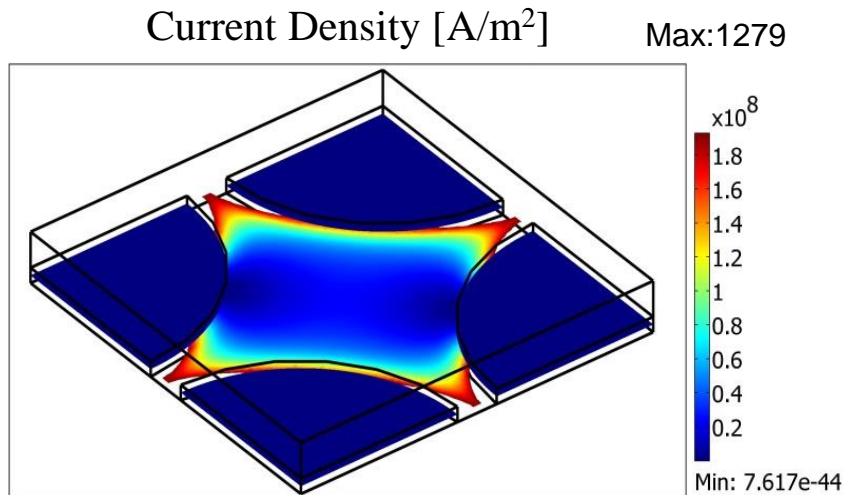


Figure C. 1: Current density passing through the electrodes and medium in the ER devices with 3D electrodes.

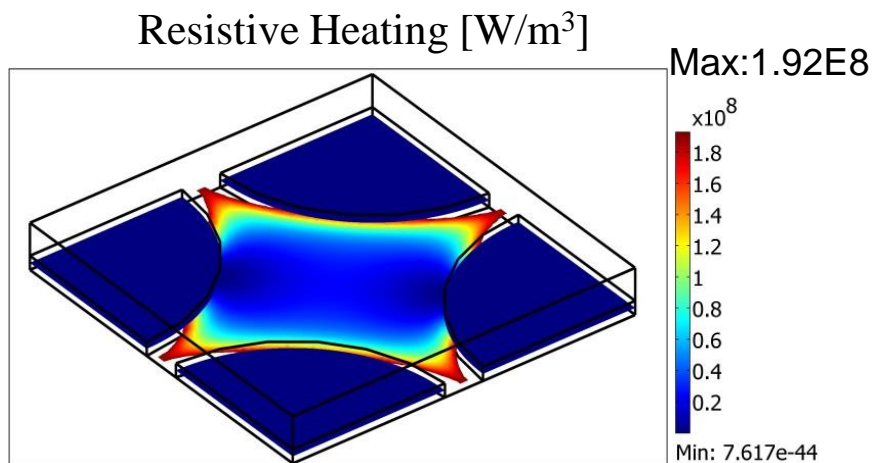


Figure C. 2: Generated joule heating the ER devices with 3D polynomial electrodes.

APPENDIX D

FINITE ELEMENT SIMULATIONS

In this chapter the details about the performed FEM simulations and utilized methods and modules are presented. In this thesis, COMSOL Multiphysics (3.4 and 3.5 versions) is used for the FEM simulations. The performed simulations include both electrostatics simulations and incompressible Navier-Stokes simulations. In the electrostatic simulations the electrical responses of the designed systems are studied. These responses can be the magnitude of the generated electric fields along the different axes, the distribution of the electrical potential, generated joule heating effects, and any other custom equations. In the Navier-Stokes simulations, the microfluidic response of the system is studied. It can be the streamline of the particular cells, pressure or velocity inside the microchannel, and any custom equations. In addition to separately investigations of the electrostatics and microfluidic forces, in the necessary case we have studied the response of the system due to both of the forces. The further details and discussions are presented in below sections.

D.1 DEP Devices

D.1.1 Electrical Model

FEM simulations provide a handy medium to study the electrical characteristics of the fabricated devices. In this thesis, our focus is directed toward the generated electric fields due to application of sinusoidal signals to the electrodes.

The details about the expression of the electrorotation torques and dielectrophoresis forces were presented in Sections 2, 3, and 7. In this section, we have briefly summarized the utilized equation in the simulations, and the methods that we have used to introduce our equation system to the COMSOL software. Firstly, the DEP equations will be presented. Then, the expression related to the electrorotation phenomena will be discussed.

The applied force on a dipole in an electric field is shown with Eq. D.1.

$$\bar{F}_{dipole} = (\bar{p} \cdot \nabla) \bar{E} \quad (D. 1)$$

It should be mentioned that, in this equation the applied higher order multipolar moments except the dipole moments is neglected. This assumption can be satisfied in the moderate non-uniform electric fields. However, in the extreme cases, where the cells are subjected to very strong electric field gradients or the null electric field, the higher order multipolar moments should take into the account, and the DEP expression should be revised accordingly.

The dipole moment on the spherical particle can be shown with below expression:

$$p_{eff} = 4\pi F_{CM} R^3 E \quad (D. 2)$$

By substituting the Eq. D.2 in Eq. D.1, below expression is obtained, which shows the effective DEP force on the spherical particles:

$$F_{DEP} = 4\pi R^3 \epsilon_m Re(F_{CM}) (E \cdot \nabla) E \quad (D. 3)$$

To calculate the $(E \cdot \nabla) E$ term, we will use the vector replacement rules:

$$\nabla (E \cdot E) = 2(E \cdot \nabla) E + 2E \times (\nabla \times E) \quad (D. 4)$$

For the non-rotating electric field the $\nabla \times E$ term is equal to zero therefore, the expression of the effective DEP force can be shown as below:

$$F_{DEP} = 2\pi R^3 \epsilon_m Re(F_{CM}) \nabla |E^2| \quad (D. 5)$$

The same expression can be derived for the effective DEP force, using the Maxwell stress tensor, which includes the both magnetic and electric effects on the cells.

By studying the above equation (Eq. D.5), it can be inferred that for a specific particle with constant dielectric properties, inside a medium with stable electrical characteristic, and under an electric field with constant frequency, the DEP force extremely depend on the $\nabla|E^2|$. This factor shows the gradient of the intensity of the electric field.

For the DEP devices we have studied the both electrostatics and microfluidic (hydrodynamic) forces. The electric field generated by application of AC signals is governed with Laplace equations:

$$\nabla\hat{\phi} = 0 \quad (\text{D. 6})$$

$\hat{\phi}$ is the phasor presentation of the applied electric potential.

Therefore, the utilized FEM module should be capable of solving the Laplace equation for the applied potential inside the microchannel. Moreover, following the discussions in the previous Chapters, in our devices (ER and DEP) we are interested in studying the electrical properties of the devices in presence of a conductive medium. Therefore, the utilized electrical module in the COMSOL software should include number of the electrical properties to satisfy our needs. These factors can be presented as below:

- Electrical conductivity of the fluid passing through the device
- Electrical permittivity of the fluid passing through the device
- Electrical conductivity of the rigid structures
- Electrical permittivity of the rigid structures
- Solving Laplace equation

As discussed before, we have utilized the COMSOL 3.5 software for the FEM analyses. In addition, due to the dimensions of the fabricated devices, which are categorized under the MEMS devices and to apply the scaling factors, we have used the MEMS module of this software. In the MEMS module of the COMSOL and

under the Electrostatics subcategory there are 2 modules for electrical simulations, and under the AC/DC module there are 2 appropriate modules for our case:

- MEMS Module
 - Electrostatics, Generalized
 - Conductive Media DC
- AC/DC Module
 - Statics, Electric
 - Shell, Conductive Media DC
 - Conductive Media
 - Electrostatics
 - Quasi-Statics, Electric
 - Electric Currents
 - Transient Analyses
 - Time Harmonic Analyses
 - Small Signal Analyses

In addition to the 3.5 version, in the 3.4 version of the COMSOL, there was another module, as Electrostatics, Generalized. This module was defined under the MEMS module.

By studying the available parameters in these modules, we have decided that the Electrostatics, Generalized module (Version 3.4) and Electric Currents, Transient Analyses (Version 3.5) can fit to our purposes. Firstly, we are able to define all the essential parameters in the subdomain and boundary sections. Secondly, the equation system of the Electrostatics, Generalized module is based on solving the Laplace equation. Both modules were examined for our devices. The obtained results from both of the modules were in accordance with each other. The presented results in this thesis are from the Quasi-Statics module.

D.1.1.1 Subdomain Conditions

In the Subdomain section of the COMSOL software, generally the used materials are being defined. The designed schematic of the devices is shown in Fig. D.1.

In our systems we are using the gold or copper electrodes. The medium inside the microchannel is a conductive medium, with known electrical properties. The microchannel is fabricated from parylene, which is an insulator polymer.

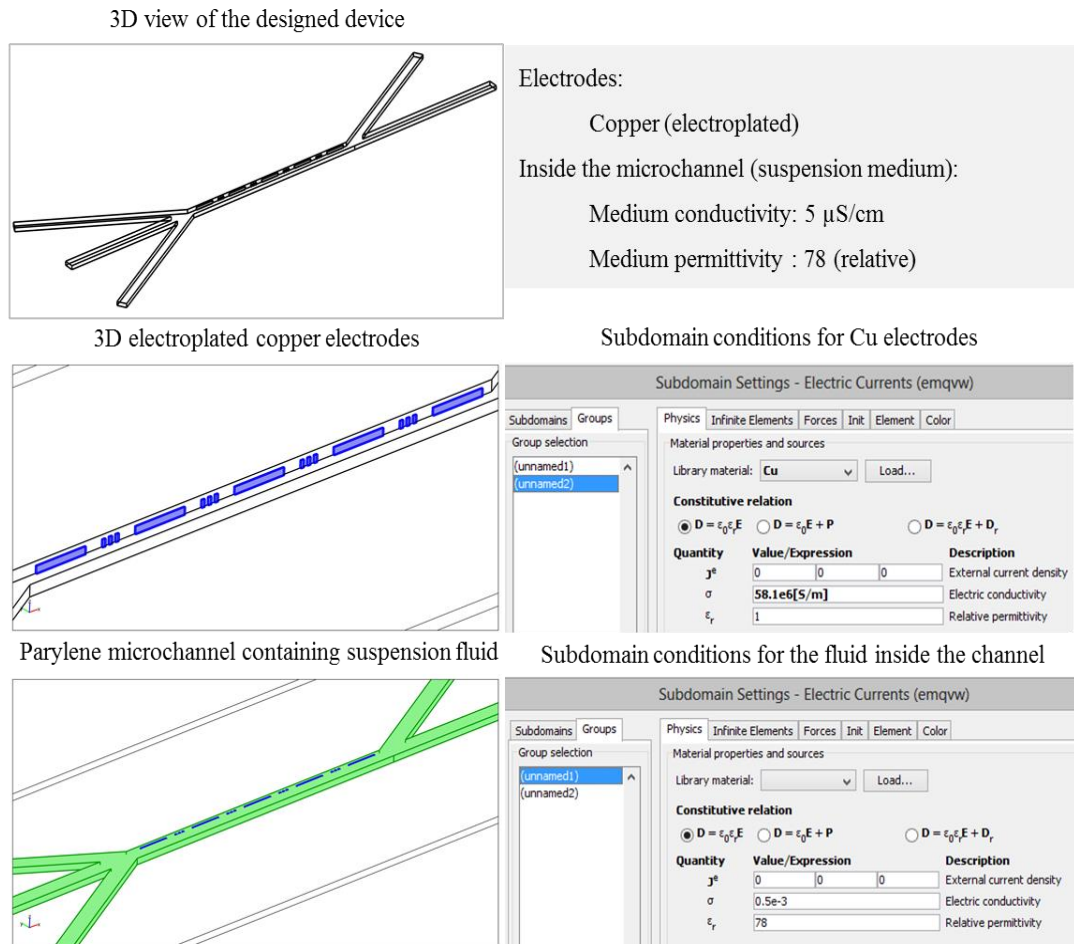


Figure D. 1: Subdomain properties of the DEP devices.

D.1.1.2 Boundary Conditions

In the boundary section, we can define the electrical conditions of each side or section of the device. Below list shows the used boundaries in our devices:

Electric potential is used for defining the applied voltages to the active electrodes.

Floating potential is used for defining the potentially floating electrodes that were used in our devices.

Electric insulation is used for defining the insulating parylene microchannel.

Figure D.2 shows the defined boundary conditions.

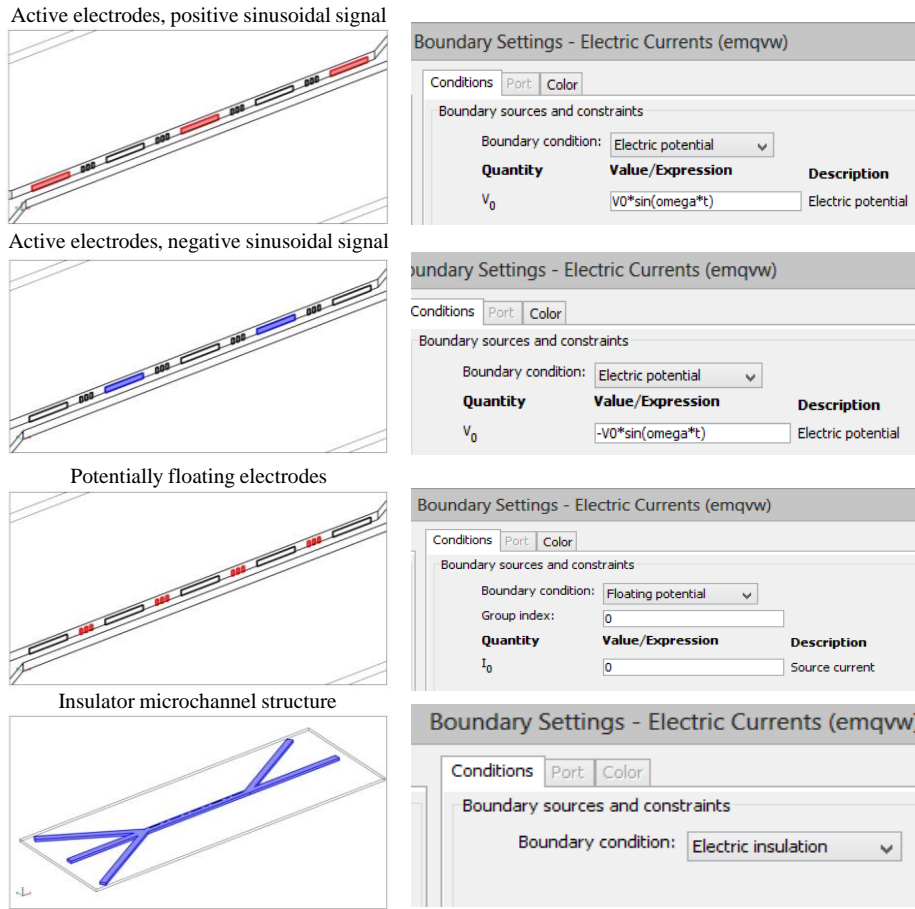


Figure D. 2: Defined electrical boundary conditions for the DEP devices.

The active electrodes were excited with differential sinusoidal signal to generate the non-uniform electric field.

D.1.2 Microfluidic Model

The hydrodynamic forces inside the microchannel are governed by Stokes law. In addition due to channel size, the Reynolds numbers is extremely low, therefore the flow can be assumed as laminar flow. The Stokes equation is as below:

$$-\nabla P + \mu \nabla^2 u = 0 \quad (D. 7)$$

We have chosen the incompressible Navier-Stokes module for the microfluidic simulation. This module is categorized under the MEMS library in the COMSOL. This module is utilized to estimate the microfluidic streamline of the biological particles under the applied DEP force.

D.2.1 Subdomain Conditions

In the subdomain section the properties of the different sections of the device is introduced. This includes the intrinsic properties of the materials and the microfluidic properties such as the dynamic viscosity and density. In the FEM simulations we have assumed the whole microchannel structure (inside the channel structure) as the water. The electrode structures inside the channel is defined as copper with zero dynamic viscosity and high density ($8.9E3$ [kg/m^3]). Figure D.3 shows the assigned subdomain conditions for the devices.

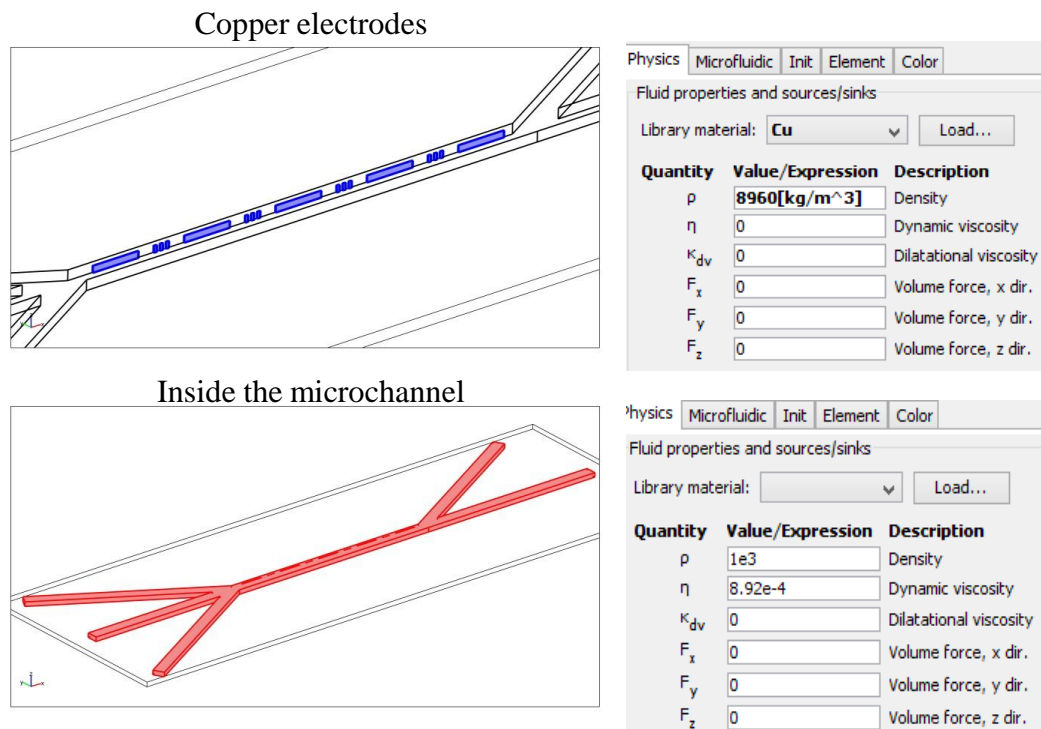


Figure D. 3: Defined subdomain conditions for the DEP devices in the microfluidic module.

D.2.2 Boundary Conditions

The boundary conditions are utilized to define the hydrodynamic activity of the designed structures. As discussed above, due to the channel dimension, velocity of the fluid, and dynamic viscosity of the medium inside the channel, the flow inside the channel is highly laminar. The details of the boundary conditions are presented in Fig. D.4. We will have below boundary conditions in the devices:

- Laminar inflow, with controlled pressure in the buffer inlets.
- Laminar inflow, with controlled velocity in the cell inlet.
- Wall with no slip, for the microchannel walls.
- Outlet, pressure no viscous stress.
- Continuity, for the interior boundaries.

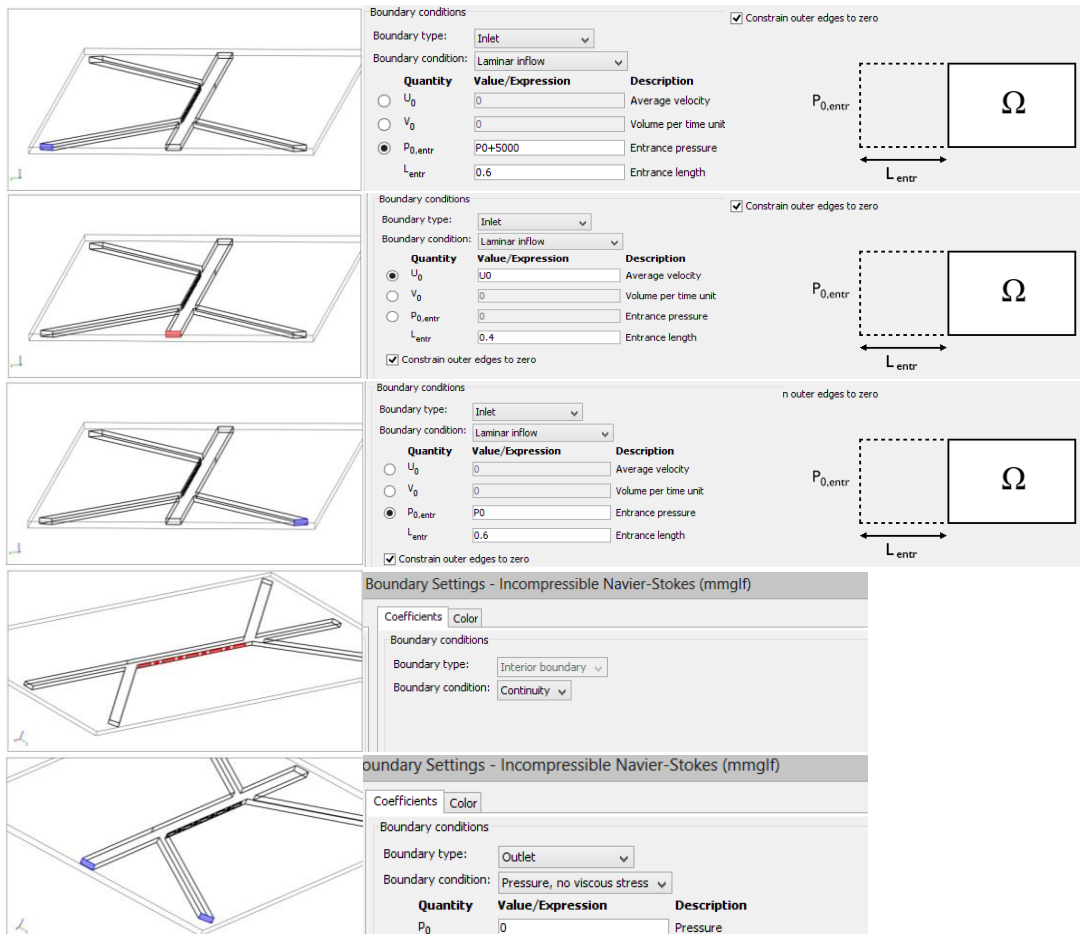
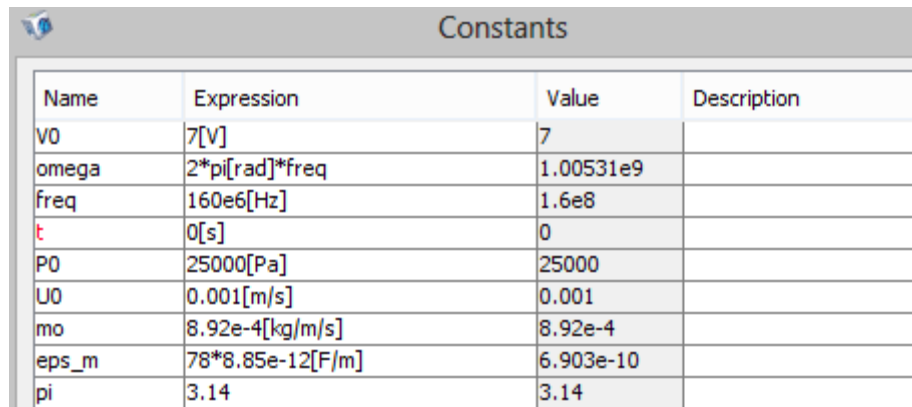


Figure D. 4: Microfluidic boundary settings for the DEP devices.

D.1.3 Constants

The constants section is being used to introduce the global constant values that are being used in the designed FEM model. These can be the amplitude or the frequency of the applied signals, the permittivity or conductivity of a layer or a structure, the pressure and velocity values in the inlet and outlets, and any other values. Below figure shows the defined constants in our model (Fig. D.5).



Name	Expression	Value	Description
V0	7[V]	7	
omega	2*pi[rad]*freq	1.00531e9	
freq	160e6[Hz]	1.6e8	
t	0[s]	0	
P0	25000[Pa]	25000	
U0	0.001[m/s]	0.001	
mo	8.92e-4[kg/m/s]	8.92e-4	
eps_m	78*8.85e-12[F/m]	6.903e-10	
pi	3.14	3.14	

Figure D. 5: Defined constant values for the electric model.

Changing the constant values, don't immediately affect the simulation results, and it is essential to rerun the simulation to see the effects.

D.1.4 Solving

In the DEP devices we are interested in studying the microfluidic behavior of the cells due to application of the hydrodynamic and electrokinetic forces. Therefore, simultaneous solving of the Quasi-Static and Navier-Stokes is essential. However, due to large volume of the calculations simultaneous solving of the modules is not practical and possible. In addition, due to applied sinusoidal signals we are interested in studying the transient response of the system. In the microfluidic simulations, we are interested in the studying the steady-state response of the system to the electrical and hydrodynamic stimulus. Therefore, we are we have used below method in the simulations:

- Simulating the designed FEM structure under the Quasi-Statics time dependent module.

- Storing the simulation results in the time instant that the field gradient intensity is maximized.
- Simulating the microfluidic response of the system under the steady-state incompressible Navier-Stokes module.

Using above method, the stream line of the cells under the DEP and hydrodynamic forces is exerted.

In the post processing section, in order to study the generated electric field gradient intensity, below equation is used.

$$\nabla|E^2| = \left[\begin{array}{c} \left(\frac{\partial^3}{\partial x^3} + \frac{\partial^3}{\partial y^2 \partial x} + \frac{\partial^3}{\partial z^2 \partial x} \right) \hat{x} \\ \left(\frac{\partial^3}{\partial y^3} + \frac{\partial^3}{\partial x^2 \partial y} + \frac{\partial^3}{\partial z^2 \partial y} \right) \hat{y} \\ \left(\frac{\partial^3}{\partial z^3} + \frac{\partial^3}{\partial x^2 \partial z} + \frac{\partial^3}{\partial y^2 \partial z} \right) \hat{z} \end{array} \right] * V^2 \quad (D.8)$$

However, this expression cannot be directly introduced to the COMSOL, therefore we have used below expression, based on the COMSOL variable to study the $\nabla|E^2|$.

$$\nabla|E^2| = \text{sqrt}[2*((V_x*V_{xx}+V_y*V_{yx}+V_z*V_{zx})^2 + (V_x*V_{xy}+V_y*V_{yy} +V_z*V_{zy})^2 + (V_x*V_{xz}+V_y*V_{yz}+V_z*V_{zz})^2)] \quad (D.9)$$

We have shown that the microfluidic behavior of the cells are governed by below expression, under the electrokinetic and hydrodynamic forces:

$$v_c = v_m + \frac{\epsilon_m Re(F_{CM}) R^2}{3\mu} \nabla|E^2| \quad (D.10a)$$

$$C_{DEP} = \frac{\epsilon_m Re(F_{CM}) R^2}{3\mu} \quad (D.10b)$$

To introduce Eq. D.6 to the COMSOL below expression is used.

$$\text{X component} = u + ((C_{DEP})*(2*(V_x*V_{xx}+V_y*V_{yx}+V_z*V_{zx}))) \quad (D.11a)$$

$$\text{Y component} = v + ((C_{DEP})*(2*(V_x*V_{xy}+V_y*V_{yy}+V_z*V_{zy}))) \quad (D.11b)$$

$$\text{Z component} = w + ((C_{DEP})*(2*(V_x*V_{xz}+V_y*V_{yz}+V_z*V_{zz}))) \quad (D.11c)$$

Equation D.7 shows the expression of the microfluidic velocity of the particles in 3D space. We have used this expression to study the separation efficiency of the cell in the DEP devices.

D.2 ER Devices

In the ER device we are not using any hydrodynamic forces. The cells are loaded into the micro-reservoirs using the micropipettes. Therefore, only electrostatic simulations were performed. We have used the electrostatic simulation to study the uniformity of the generated electric field. In addition, the variance in the magnitude of the rotating electric field is studied using the FEM analyses. We have used the 3.4 version of the COMSOL Multiphysics to study the electrical characteristics of the electrorotation devices. The Electrostatics, Generalized module were used for the simulations. This module uses the Laplace equations for simulating the electrical responses of the structures.

In below sections the details about the boundary and subdomain conditions of the 3rd generation of the ER devices are provided. These devices were used in the experimental cell characterizations. The same method was used in the simulations of the 1st and 2nd generations of the ER devices.

D.2.1 Subdomain Conditions

As mentioned in Section 4, six different electrode geometries were fabricated and tested in the 3rd generation of the ER devices. The ER devices with the polynomial electrodes were chosen as the most suitable case for the ER experiments. In this section, we will study the simulation procedure of the ER device with polynomial electrodes. The same procedure was followed in the simulation of the other devices. Figure D.6 shows the designed FEM structure for the polynomial electrodes. The designed FEM structures were the replicates of the fabricated prototypes.

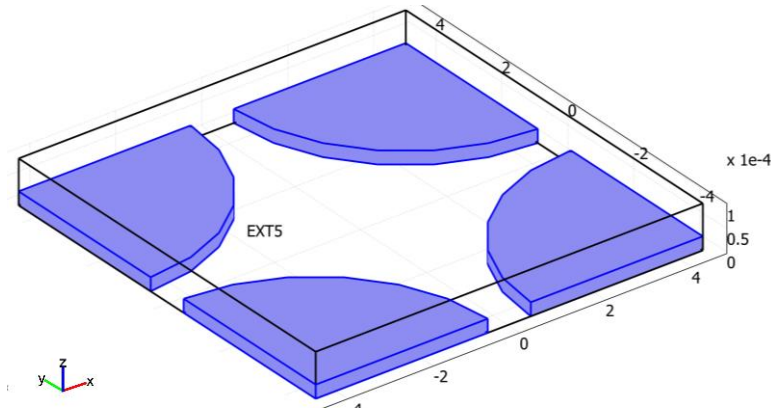


Figure D. 6: Designed FEM module of the polynomial structures.

There are four polynomial electrodes in these devices. In the subdomain section the quadrupole electrodes were introduced as the Au and the 3D region between the electrodes were introduced as the conductive medium with stable electrical conductivity and permittivity. Figure D.7 shows the defined subdomain conditions for the ER devices.

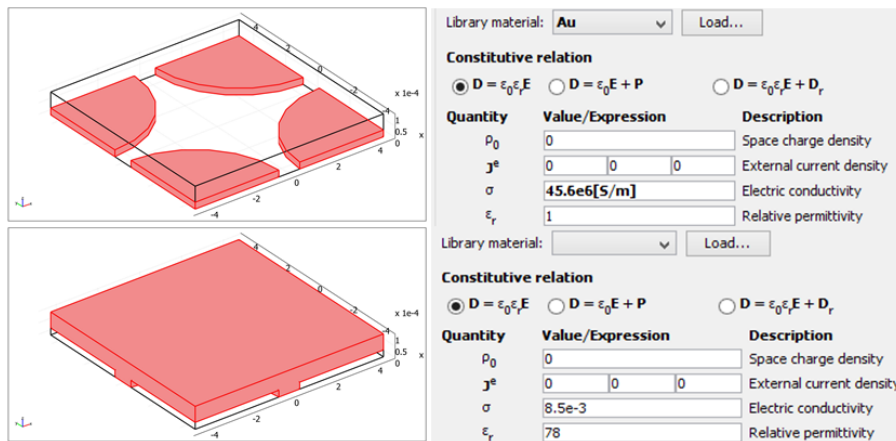


Figure D. 7: Subdomain properties of the ER devices.

D.2.2 Boundary Conditions

In the boundary section the electrodes were defined as the electrical potential. The applied boundary condition to each electrode differs from the others, due to 90° phase shift. The boundary properties of the inter-electrode region were defined as distributed resistance (Fig. D.7).

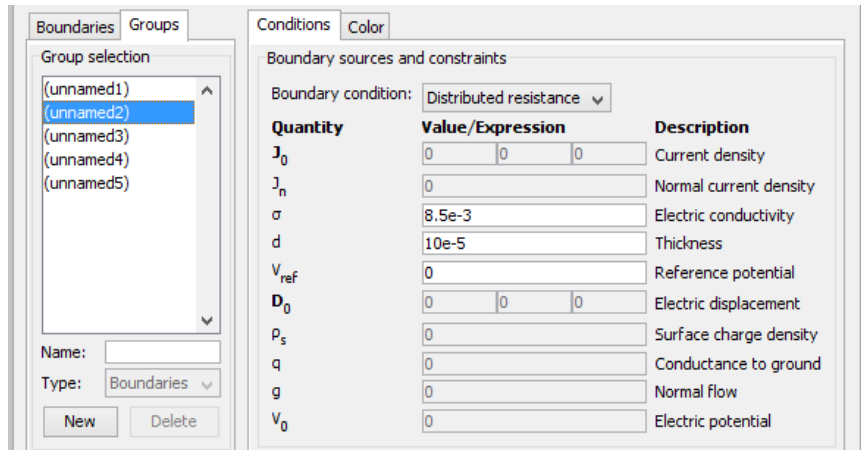


Figure D. 8: Defined boundary condition for the inter-electrode region.

The defined boundary condition for the inter-electrode region is based on the conductivity of the medium. Therefore, it is expected to show variances based on the test condition.

D.2.3 Constants

Following the discussion for the DEP devices, the constants are being used to introduce the global values for a simulation module. For the ER devices, these values are showing the applied voltages and frequencies to the electrodes (Fig. D.9).

Name	Expression	Value	Description
f	50e3[Hz]	50000	
w	2*pi[rad]*f	3.141593e5	
V0	12.5[V]	12.5	
a	V0*sin(w*t)	0	
b	V0*cos(w*t)	12.5	
c	-V0*sin(w*t)	0	
d	-V0*cos(w*t)	-12.5	
t	0[s]	0	

Figure D. 9: Defined constant values for the ER model.

D.2.4 Solving

For solving the simulation, time-dependent simulations were performed. The simulation time was adjusted on the applied frequency to cover two complete cycles.

In our studies, we were interested in the effective electric field magnitude and rotation. Therefore, we have utilized the expression of rotating electric field due to application of sinusoidal signals in phase quadrature.

$$E_{effective}^2 = E_x \times E_y \quad (D.12)$$

To introduce this expression to the COMSOL, we have used below expression:

$$E_{effective}^2 = Ex_{emqv} * Ey_{emqv} \quad (D.13)$$

APPENDIX E

FABRICATION PROCESS FLOW

Fabrication process flow of the 1st generation ER devices is presented in Table D.1.

Table E. 1: Detailed fabrication flow of the 1st generation of the ER devices.

	Fabrication process flow of the 1 st generation of the ER devices.
1	Silicon substrate (4 inches)
2	Dehydration at oven at 110°C for 20 min
3	PECVD oxide growth with mixed frequency for 10 min
4	Dehydration at oven at 110°C for 20 min
5	Ti sputtering as adhesion layer (~20nm) (BESTEC)
	300 W T1:120s T2:70s Distance:135mm Flow:2.5sccm
6	Au sputtering layer (~400 nm) (BESTEC)
	300 W T1:120s T2:400s Distance:130mm Flow:6.2sccm
7	Dehydration at oven at 95°C for 40 min

Table E. 1 (Continued)

8 (Mask 1)	Lithography for Au & Ti etch
	HDMS coating 500 rpm 10s + 4000 rpm 30s
	S1813 500 rpm 10s + 4000 rpm 30s
	Softbake @ 95°C for 90 s hotplate
	Expose UV for 5s vacuum+hard contact
	Develop in MF 319 for 45s
	DI water rinse 1.5min+1.5min
	Dry by N ₂
	Inspection
	Hardbake at oven @ 95°C for 20 min
	Desicator for 5 min
9	Au etch
	Descum in oxygen plasma for 2 min
	Commercial Au etchant for 1.5 min
	DI water rinse 3 cycles
	Dry by N ₂
	Inspection
10	Ti etch
	10ml HF+10ml H ₂ O ₂ +80ml DI water as Ti etchant
	Ti etchant for 30s

Table E. 1 (Continued)

11	Strip photoresist
	In PRS 1000 for 30 min
	DI water rinse 3 cycles
	Inspection
12	Dicing

Fabrication flow of 2nd generation of the ER devices is presented in Table E.2.

Table E. 2: Detailed fabrication flow of the 2nd generation of the ER devices.

	Fabrication process flow of the 2 nd generation of the ER devices.
1	Glass wafer (4")
2	Piranha cleaning (H ₂ SO ₄ :H ₂ O ₂ (800mL:800mL))
	Cleaning in Piranha for 30 min
	DI water rinse 5 cycles
	Dry by N ₂
3	BHF adhesion etch (NH ₄ F:HF (7:1))
	BHF etch for 2 min
	DI water rinse 5 cycles
	Dry by N ₂
	Descum in oxygen plasma for 2 min
4	Dehydration at oven at 110°C for 20 min
5	Parylene coating

Table E. 2 (continued)

	with silane
	4 g for 2 μm parylene thickness
6	Dehydration at oven at 95°C for 40 min
7	Ti sputtering as adhesion layer (~20nm) (BESTEC)
	300 W T1:120s T2:70s Distance:135mm Flow:2.5sccm
8	Au sputtering layer (~400 nm) (BESTEC)
	300 W T1:120s T2:400s Distance:130mm Flow:6.2sccm
9	Dehydration at oven at 95°C for 40 min
10	Lithography for Au & Ti etch
Mask 1	HDMS coating 500 rpm 10s + 4000 rpm 30s
	S1813 500 rpm 10s + 4000 rpm 30s
	Softbake @ 95°C for 90 s hotplate
	Expose UV for 5s vacuum+hard contact
	Develop in MF 319 for 40s
	DI water rinse 1.5min+1.5min
	Dry by N ₂
	Inspection
	Hardbake at oven @ 95°C for 50 min
	N ₂ Desicator for 5 min

Table E. 2 (continued)

11	Au etch
	Descum in oxygen plasma for 2 min
	Commercial Au etchant for 1.5 min
	DI water rinse 3 cycles
	Dry by N ₂
	Inspection
12	Ti etch
	10ml HF+10ml H ₂ O ₂ +80ml DI water as Ti etchant
	Ti etchant for 30s
13	Strip photoresist
	Acetone for 40min
	DI water rinse 3 cycles
	Dry by N ₂
	Inspection
14	Dehydration at oven at 95°C for 40 min
15	Lithography for Cu-electroplating
Mask 2	HDMS coating 500 rpm 10s + 1000 rpm 30s
	AZ9260 500 rpm 15 s + 1000 rpm 60s
	Edge bead removal

Table E. 2 (continued)

	Wait for 15min
	Prebake @ 95°C for 3min at hotplate
	AZ9260 500 rpm 15 s + 1000 rpm 60s
	Edge bead removal
	Wait for 15min
	Hardbake at oven from room temperature to 95°C and 50min @ 95°C
	Cooling at oven from 95°C to 70°C
	Rehydration (3 pipettes of DI water in blue box, minimum 20 hours)
	Expose UV for 30s vacuum+hard contact
	Develop in AZ 826MIF for 10min
	DI water rinse 5min + 3min
	Dry by N ₂
	Expose UV for 30s vacuum+hard contact
	Develop in AZ 826MIF for 12min
	Dry by N ₂
	Inspection
16	Dehydration at oven at 95°C for 10 min
17	Cu electroplating

Table E. 2 (continued)

	100 mA 0.3-0.7 duty cycle 90min for 25 μm Cu thickness
18	Strip photoresist
	Acetone for 60min
	DI water rinse 3 cycles
	Dry by N_2
	Inspection
	O_2 plasma for 5min (can be increased if necessary)
	Inspection
19	Dehydration at oven at 95°C for 40 min
20	Parylene coating
	with silane
	1 g for 0.5 μm parylene thickness
21	Lithography for microchannel (double spin, double expose)
Mask 3	HDMS coating 500 rpm 10s + 1000 rpm 30s
	AZ9260 500 rpm 15 s + 1000 rpm 60s
	Edge bead removal
	Wait for 15min
	Prebake @ 95°C for 3min at hotplate
	AZ9260 500 rpm 15 s + 1000 rpm 60s

Table E. 2 (continued)

	Edge bead removal
	Wait for 15min
	Hardbake at oven from room temperature to 95°C and 50min @ 95°C
	Cooling at oven from 95°C to 70°C
	Rehydration (3 pipettes of DI water in blue box, minimum 20 hours)
	Expose UV for 30s vacuum+hard contact
	Develop in AZ 826MIF for 10min
	DI water rinse 5min + 3min
	Dry by N ₂
	Expose UV for 30s vacuum+hard contact
	Develop in AZ 826MIF for 12min
	DI water rinse 5min + 3min
	Dry by N ₂
	Inspection
22	Dehydration at oven at 95°C for 40 min
23	Parylene coating
	without silane
	40 g for 20 μm parylene thickness
24	Opening lithography

Table E. 2 (continued)

Mask 4	HDMS coating 500 rpm 10s + 1000 rpm 30s
	AZ9260 500 rpm 15 s + 900 rpm 60s
	Edge bead removal with acetone
	Wait for 15min
	Prebake @ 95°C for 3min at hotplate
	AZ9260 500 rpm 15 s + 1000 rpm 60s
	Edge bead removal
	Wait for 15min
	Hardbake at oven from room temperature to 95°C and 50min @ 95°C
	Cooling at oven from 95°C to 50°C
	Rehydration (3 pipettes of DI water in blue box, minimum 20 hours)
	Expose UV for 30s vacuum+hard contact
	Develop in AZ 826MIF for 10min
	DI water rinse 5min + 3min
	Dry by N ₂
	Expose UV for 30s vacuum+hard contact
	Develop in AZ 826MIF for 12min
	Dry by N ₂
	Inspection

Table E. 2 (continued)

25	Parylene etching with RIE
	In RIE (20min+20min+20min)
	Inspection
26	Dicing
27	Strip photoresist
	Acetone for 2 days

Fabrication flow of the 3rd generation of the ER devices and the DEP devices are presented in Table E.3.

Table E. 3: Detailed fabrication flow of the 3rd generation of the ER devices.

	1 st generation devices fabrication flow
1	Silicon substrate (4 inches)
2	Dehydration at oven at 110°C for 20 min
3	PECVD oxide growth with mixed frequency for 10 min
4	Dehydration at oven at 110°C for 20 min
5	Ti sputtering as adhesion layer (~20nm) (BESTEC)
	300 W T1:120s T2:70s Distance:135mm Flow:2.5sccm
6	Au sputtering layer (~400 nm) (BESTEC)
	300 W T1:120s T2:400s Distance:130mm Flow:6.2sccm

Table E. 3 (continued)

7	Dehydration at oven at 95°C for 40 min
8 (Mask 1)	Lithography for Au & Ti etch
	HDMS coating 500 rpm 7s + 3000 rpm 30s
	AZ5214E 500 rpm 7s + 4000 rpm 30s
	Softbake @ 115°C for 70 s hotplate
	Expose UV for 7s vacuum+hard contact
	Softbake @ 120°C for 120 s hotplate
	Flood expose for 14s
	Develop in MF 319 for 50s
	DI water rinse 1.5min+1.5min
	Dry by N ₂
	Inspection
	Hardbake at oven @ 110°C for 1 min
9	Au etch
	Descum in oxygen plasma for 2 min
	Commercial Au etchant for 1.5 min
	DI water rinse 3 cycles
	Dry by N ₂
	Inspection

Table E. 3 (continued)

10	Ti etch
	10ml HF+10ml H ₂ O ₂ +80ml DI water as Ti etchant
	Ti etchant for 30s
11	Strip photoresist
	In PRS 1000 for 30 min
	DI water rinse 3 cycles
	Dry by N ₂
	Inspection
12	Dehydration at oven at 95°C for 40 min
15	Lithography for Cu-electroplating
Mask 1	HDMS coating 500 rpm 10s + 1000 rpm 30s
	AZ9260 500 rpm 15 s + 1000 rpm 60s
	Edge bead removal
	Wait for 15min
	Prebake @ 95°C for 3min at hotplate
	AZ9260 500 rpm 15 s + 1000 rpm 60s
	Edge bead removal
	Wait for 15min
	Hardbake at oven from room temperature to 95°C and 50min @ 95°C

Table E. 3 (continued)

	Cooling at oven from 95°C to 70°C
	Rehydration (3 pipettes of DI water in blue box, minimum 20 hours)
	Expose UV for 30s vacuum+hard contact
	Develop in AZ 826MIF for 10min
	DI water rinse 5min + 3min
	Dry by N ₂
	Expose UV for 30s vacuum+hard contact
	Develop in AZ 826MIF for 12min
	Dry by N ₂
	Inspection
16	Dehydration at oven at 95°C for 10 min
17	Cu electroplating
	100 mA 0.3-0.7 duty cycle 90min for 25 μm Cu thickness
18	Strip photoresist
	Acetone for 60min
	DI water rinse 3 cycles
	Dry by N ₂
	Inspection
	O ₂ plasma for 5min (can be increased if necessary)

Table E. 3 (continued)

	Inspection
19	Dehydration at oven at 95°C for 40 min
20	Electroless Au deposition
21	Photoresist
	HDMS coating 500 rpm 10s + 1000 rpm 30s
	AZ9260 500 rpm 15 s + 1000 rpm 60s
	Edge bead removal
	Wait for 15min
	Prebake @ 95°C for 3min at hotplate
	Hardbake at oven from room temperature to 95°C and 20 min @ 95°C
	Cooling at oven from 95°C to 70°C
22	Dicing
23	Strip photoresist
	Acetone for 1 days